INTERNATIONAL DOCTORAL
SCHOOL OF THE USC

Alexandre
Blanco González

PhD Thesis

The influence of lipid composition on mechano-structural properties of cellular membranes: studies through Molecular Dynamics

Santiago de Compostela, 2024

Doctoral Programme in Materials Science

ESCOLA DE DOUTORAMENTO
INTERNACIONAL DA USC

DOCTORAL THESIS

THE INFLUENCE OF LIPID COMPOSITION ON MECHANO-STRUCTURAL PROPERTIES OF CELLULAR MEMBRANES: STUDIES THROUGH MOLECULAR DYNAMICS

Author

Alexandre Blanco González

Supervisor/s: Rebeca García Fandiño, Ángel Piñeiro Guillén

Tutor: Ángel Piñeiro Guillén

PHD PROGRAMME IN MATERIALS SCIENCE

SANTIAGO DE COMPOSTELA

Contents

LIST OF ABBREVIATIONS

AA . . . . . All Atoms
ABF . . . . . Angle-Based Flattening
AI . . . . . Artificial Intelligence
AMBER . . . . Assisted Model Builder with Energy Refinement
AMOEBA . . . Atomic Multipole Optimized Energetics for Biomolecular Applications
API . . . . . Application Programming Interface
APL . . . . . Area Per Lipid
ATP . . . . . Adenosie Triphosphate
L-BFGS . . . . Limited-memory Broyden–Fletcher–Goldfarb–Shannon
CG . . . . . Coarse Grained
CL . . . . . Cardiolipin
CNT . . . . . Carbon Nanotube
DLPC 1,2-dilauroyl-*sn*-glycero-3-phosphocholine
DMPC 1,2-dimyristoyl-*sn*-glycero-3-phosphocholine
DNA . . . . . Deoxyribonucleic Acid
ELBA . . . . . ELectrostatics BAsed
FA . . . . . Fatty Acid
FFT . . . . . Fast Fourier Transform
GROMACS . . GROningen MAchine for Chemical Simulations
GROMOS . . . GROningen MOlecular Simulation
HIE . . . . . Hydrogen Isotope Exchange
HIFU . . . . . High Intensity Focused Ultrasounds
IQR . . . . . Inter-Quartile Range
LINCS . . . . LINear Constraint Solver
LPS . . . . . Lipopolysaccharide
MD . . . . . Molecular Dynamics
ML . . . . . Machine Learning
OP . . . . . Order Parameter
OPLS . . . . . Optimized Potentials for Liquid Simulation
PA . . . . . Phosphatidic Acid
PC . . . . . Phosphocholine
PBC . . . . . Periodic Boundary Conditions
PDF . . . . . Probability Density Function

PE . . . . . Phosphoetanolamine
PG . . . . . Phosphoglycerol
PI . . . . . Phosphoinositol
PM . . . . . Plasmatic Membrane
PME . . . . . Particle-Mesh Ewald
POPC 1-palmitoyl-2-oleoyl-*sn*-glycero-3-phosphocholine
POPE 1-palmitoyl-2-oleoyl-*sn*-glycero-3-phosphoetanolamine
POPG 1-palmitoyl-2-oleoyl-*sn*-glycero-3-phosphoglycerol
POPS 1-palmitoyl-2-oleoyl-*sn*-glycero-3-phosphoserine
PS . . . . . Phosphoserine
PSR . . . . . Poisson Surface Reconstruction
PUFA . . . . . Poly-Unsaturated Fatty Acid
RC . . . . . Reaction Coordinate
RNA . . . . . Ribonucleic Acid
STFT . . . . . Short-Time Fourer Transform
SVD . . . . . Sinfular Value Decomposition
UA . . . . . United Atoms
US . . . . . Ultrasound

Agradecementos

A meus pais, Lola e Adrián, por terme apoiado en todo momento dende cativo cas miñas lideiras científicas e quererme de maneira incondicional. A meus avós, Argentina e Jesús, Mucha e Manolo; meus tíos Mari e Camilo (alí onde estés, que conmigo por sempre has de vir), e meus curmáns Ari, Miguel e Iván; pois fixéstesme e facédesme ser quen son.

A Enrique e Xurxo, os meus irmáns aínda sen compartirmos pais, por seren diáfanas ventás ás que asomarme cara as Humanidades e as Artes. A Joaquín, por saber apaixoarme pola Ciencia e aceptar o pasar de ser un profesor un amigo. A Ana, por ser a miña mellor amiga en todas e cada unha das circunstancias. A Sara, (por suposto que non só) polas tantísimas horas en Lordran arranxando o mundo até altas horas da madrugada. A Helena, pola súa inquebrantable amizade e apoio ao longo de xa tantos anos. A Andrés, por ser o primeiro camarada que fixen na carreira, e tras case dous lustros seguir sen verlle data de caducidade. A Javi, que non tardou moito máis en chegar á miña vida, e me axudou a baleirar unhas poucas botellas de Coto de Imaz no piso.

A todos os do despacho, por levar anos aturándome e escoitándome saturar cando algo non me sae, que é a meirande parte do tempo. A Fabián, por sempre tentar entender as miñas ideas de bombeiro e ser o meu compa de butaca no Numax. A Alfosno, por ser o firme pilar de cordura no parque de bólas que é o P1-D11. A Dani, máxima expresión da serenidade e a calma. A Paula, que cun sorriso e un encollerse de ombreiros é capaz de arranxar calquera burrada que se diga. A Álex, ca súa constante vontade de axudar aos demais. A Marta, por ensinarme o que é ser investigador e o significado da palabra perseverancia. A Anxo, pola súa infinita actitude de positividade e facer que non me esqueza de cando en vez de tamén *vivir*. Pese a xa non compartirmos despacho, a Martín, Pablo e David, meus mentores durante os primeirísimos pasos, fontes inagotables de ideas e paciencia. A todo aquel no grupo de Juan Granja, por sufrirme durante tantos seminarios. A todas estas marabillosas persoas, en xeral, por facer que o traballo e a xenuina amizade estivesen sempre en tan próximo contacto.

Por suposto, a Rebeca e a Ángel, por apostaren por min dende o primeiro momento e aceptar ser os meus directores de tese. A Juan Granja, por aínda non sendo o meu director estar sempre disposto axudar e a facer preguntas para que me decate do que realmente é importante. A Syma Khalid e Siewert-Jan Marrink, por acollérenme tan amablemente nos seus respectivos grupos de investigación.

A todo aquel que, valentemente, decida meterlle o dente a este traballo que estou a pique de presentar, espero non decepcionarvos. Moitas grazas, e vou xa pedindo desculpas polo que está por vir.

0 SUMMARY

As Gregor Samsa awoke one morning from uneasy dreams he found himself transformed in his bed into a gigantic insect.

–Franz Kafka,
The Metamorphosis.

0.1 Versión Completa en Galego

O corpo desta presente Tese versa sobre as membranas lipídicas, estruturas esenciais para a Bioloxía e, por ende, a vida. Este traballo foi levado a cabo a través dun prisma computacional, no canto de usar técnicas experimentais, para investigar a auto-organización e a resposta a estímulos mecánicos externos destas entidades biolóxicas. Desta maneira enmarcámonos nunha interfase entre a Física, a Química, a Bioloxía e a Computación; remarcando a importancia da interdisciplinariedade na Ciencia en xeral, e sendo un claro exemplo do contexto no que se densenvolve a Investigación a día de hoxe.

A tese comeza proporcionando unha perspectiva histórica, prestando especial atención á evolución do pensamento no relacionado á Computación e as Ciencias da Vida, dando unha visión xeral de como ao longo dos séculos as condicións materiais foron evoluíndo e dándolle forma á sociedade occidental e, polo tanto, aos avances técnico-científicos que esta foi producindo. Isto sérvenos de introdución e xustificación para as subsecuentes investigacións que tratan sobre o obxecto central desta tese: as membranas celulares. O noso entendemento destas estruturas tamén foi modificado e mellorado ao longo da historia, levándonos dunha interpretación simplificada que as vía como simples barreiras a unha visión moito máis completa que as mostra como as estruturas multifuncionais e complexas que en verdade son.

As primeiras evidencias científicas sobre as membranas lipídicas remóntanse a medidas da presión osmótica nos glóbulos vermellos, observándose que estes medraban ou se encollían dependendo de cambios na forza iónica da matriz líquida na que se atopasen suspendidos, falándonos por vez primeira da semipermeabilidade das membranas. Estas observacións deron en modelos que co paso do tempo foron sendo refinados, producíndose un momento de inflexión en 1925 cando Gorter e Grendel postulan a estrutura da bicapa como a morfoloxía fundamental das membranas. Esta interpretación segue a ser, a día de hoxe, a pedra angular do noso entendemento delas e das funcións que cómpren a nivel celular, sobre a cal novos avances técnicos ao longo do século XX permitiron construír modelos máis e máis sofisticados que nos proporcionan unha visión máis completa das súas características.

Así, ao longo do primeiro capítulo desta tese, explórase a composición molecular das membranas lipídicas. Por suposto e coma o seu nome indica, o compoñente fundamental e principal causante do seu ser, son os lípidos. En breve, os lípidos son moléculas anfóteras, é dicir, presentan unha anisotropía estrutural que os dota de rexións ben diferenciadas segundo a súa querencia por interaccionaren ca auga. Esta diferenciación leva aos lípidos a autoensamblarse, como tantas outras biomoléculas, baixo determinadas condicións físico-químicas, dando lugar deste xeito ás membranas. Así mesmo, introduciremos como os lípidos en si poden ser agrupados en distintas categorías en tanto en canto teñan certas características e cumpran segundo que función nas membranas. Por outra banda, e no canto das outras especies moleculares que se poden atopar

nunha membrana, de especial relevancia son as proteínas, e tanto é así que nun contexto de rigor biolóxico nin as membranas poden ser entendidas sen as proteínas nin as proteínas sen as membranas, pois existen necesarias relacións fundamentais entre elas para o seu correcto funcionamento. Ademais das proteínas, os azucres tamén xogan papeis de gran importancia nas membranas celulares. Veremos deste xeito que estes roles teñen especial peso para certos organismos como as bacterias gram-negativas, nas cales polisacáridos unidos covalentemente a motivos lipídicos conforman case de maneira íntegra a monocapa externa das súas membranas celulares.

Sentadas as bases da composicón das membranas, mostrando como diferentes tipos de biomoléculas son necesarias para a súa esencia e forma, procédese a continuación no capítulo da Introdución a discutir os dous modelos básicos usados para interpretalas: o modelo de mosaico fluído e o modelo de balsas de lípidos (fluid mosaic model e lipid raft model, en Inglés). Antes de detallar sobre estes dous modelos concretos, dase un repaso polas tentativas previas de capturar as membranas lipídicas a nivel conceptual, cos avances e interpretacións que cada unha delas proporcionou, así coma cas súas limitacións e fallos. Construíndo sobre estes modelos non de todo correctos, introdúcese como en 1971 Singer e Nicolson propoñen por primeira vez o modelo de mosaico fluído. Este modelo interpreta as membranas como 'unha solución dous-dimensional, orientada e viscosa de proteínas anfipáticas xunto con lípidos, nun equilibrio termodinámico instantáneo'. Con esta definición, usando as propias palabras dos investigadores que a formularon, queda pois capturada tanto a xeometría xeral das membranas, como a súa composición heteroxénea e a súa natureza intrínsecamente dinámica, e segue a ser o modelo máis aceptado incluso varias décadas máis tarde, con sólidas evidencias científicas a respaldalo. A continuación deste, o concepto de dominio no contexto das membranas celulares é discutido, conlevando isto a introdución do modelo de balsas de lípidos. Este modelo, o cal non está carente de certa controversia debido a evidencias contraditorias sobre a súa corrección, é unha extensión do modelo de mosaico fluído que postula que especies concretas de lípidos teñen tendencias a asociarse entre elas xunto con outras entidades como determinadas proteínas, creando unidades cohesionadas, especialmente ordenadas e localizadas no espazo (é dicir, dominios) con implicacións para o correcto funcionamento de varios procesos celulares.

Queda evidente deste xeito a complexidade das membranas lipídicas no que ás súas unidades básicas e á súa organización xeral se refire, e resulta axeitado a continuación falar en máis profundidade das diversas funcións que estas poden cumprir nunha célula calquera. O rol principal destas, e a través do cal tradicionalmente foron e son interpretadas, é o de barreira física que compartimentaliza tanto varios orgánulos, como delimita a célula en si mesma. Malia esto, resultaría agora comprensible sospeitar que dada a súa variabilidade composicional e natureza dinámica os roles que estas membranas poden tomar non se restrinxan sómentes aos de barreira. En efecto, e tal e como se introduce no primeiro capítulo da tese, as membranas lipídicas están intimamente relacionadas ca función das proteínas, ca transmisión e transdución de sinais celulares, co transporte tanto pasivo como activo de materia entre os distintos compartimentos das células e mailo seu entorno, e ca capacidade das células para cambiar de forma e moverse, entre moitos outros exemplos. Así pois, e con istoutra capa de complexidade adicional para as membranas, pásase a discutir a continuación as distintas variedades destas que se poden observar e os factores que infúen na súa diferenciación. Distínguense pois na súa composición molecular as membranas lipídicas segundo a que organismo pertenzan, ou a que tecido estén dando lugar nun mesmo organismo. Tamén son de relevancia para esta diferenciación procesos de enfermidade ou incluso o envellecemento.

Dadas estas diferenzas das membranas segundo os factores anteriormente discutidos, adícase unha sección no primeiro capítulo da tese á relación que estas gardan para cos diversos procesos de enfermidade e as terapias contra estas. Faise así especial fincapé nas terapias de lípidos de membrana (MLT polas súas siglas en Inglés), por estaren estas dirixidas a modificar o perfil lipídico das membranas do paciente, e o foco que esta Tese pon na composición lipídica das membranas estudadas. A principal hipótese na que estes métodos se fundamentan é que, en base ás diferenzas entre membranas, estas poden ser fixadas como obxectivos de axentes terapéuticos. En efecto, na introdución desta tese enuméranse e danse exemplos dunha serie de campos como o da oncoloxía, o das enfermidades cardiovasculares ou as enfermidades neurodexenerativas; nos que xa existen tratamentos ou polo menos se atopan en fases avanzadas de probas, para os cales as membranas e a súa composición lipídica son a súa diana terapéutica. Mais aló da MLT, no primeiro capítulo deste documento tamén se dá un repaso ao uso de terapias con base mecánica, no canto do uso máis tradicional de axentes químicos, para o tratamento e a cura de enfermidades. De especial relevancia para este traballo é o uso de ultrasóns, cuxos efectos sobre as membranas celulares versa unha boa parte dos resultados obtidos durante as investigacións levadas a cabo neste doutoramento; dándose así un resumo das súas aplicacións no campo médico e as potenciais relacións que existen entre estes mailas membranas. En particular, fálase do concepto de sonoporación e como este, a través do uso de ondas de presión é capaz de inducir rupturas nas membranas celulares, creando desta maneira un vínculo entre potenciais terapias, as membranas e mailas súas propiedades estruturais e mecánicas.

Con isto, a introdución pasa seguidamente a discutir a ferramenta computacional usada para o desenvolvemento desta tese: a dinámica molecular (MD polas súas siglas en Inglés). Esta sección comeza dando unha descrición xeralista das súas principais aplicacións e usos, entre os cales se atopan a busca conformacional de biomoleículas, a axuda a técnicas experimentais para a determinación estrutural de compostos de caracterización complexa e, máis notoriamente, o estudo de procesos dinámicos en gran multitude de sistemas, por suposto a nivel molecular. A continuación, o foco torna cara a aplicación da MD para o estudo de membranas lipídicas, o cal é un campo tamén amplamente prolífico. Esta discusión comeza falando das primeiras simulacións levadas a cabo neste contexto, máis simples pero pioneiras no seu campo e aínda con actual vixencia, as cales sentaron as bases para multitude de estudos que hoxe por hoxe se levan a cabo de maneira rutinaria. Seguidamente, introdúcese o paso cara a simulacións de membranas complexas, con sistemas que incorporan lípidos de distintos tipos xunto con outras biomoléculas, usualmente proteínas. Estes estudos, debido á súa maior sofisticación, requiren asimesmo de técnicas máis avanzadas para tratar de evitar os problemas que xorden derivados do maior grado de complexidade dos sistemas. Esto serve de precedente para falar da crecente necesidade de obter parametrizacións eficientes e precisas dun número cada vez maior de distintos tipos de moléculas entre os cales, por suposto, os lípidos forman parte. De feito, o desenvolvemento de campos de forza, pois iste é o nome que reciben os conxuntos de parámetros que describen as interaccións inter e intramoleculares nunha simulación de MD, é un campo en constante bulir, así como o das comparacións sistemáticas entre eles. Deste xeito, adícase un apartado da introdución da tese a unha revisión bibliográfica dos estudos feitos tanto para o desenvolvemento de parametrizacións de lípidos así como para a súa comparación. Disto conclúese que, a pesares da actual abundancia de opcións, cada unha delas ten vantaxes pero tamén inconvintes, pois ningunha consegue capturar de maneira totalmente fiel nin ca mesma exactitude as diversas propiedades que se poden determinar para as membranas lipídicas, e delegan deste xeito no investigador as labores interpretativas e de toma de decisión á hora de seleccionalos para un

determinado traballo.

A continuación, as dúas seguintes seccións do capítulo da introdución tratan estudos nos que se tentan desenvolver modelos realistas de membranas, así como a traballos que tentan modelar sistemas próximos ás células na súa completitude. Pola banda dos modelos realistas, menciónase que gran parte dos esforzos estiveron dirixidos ao desenvolvemento de modelos fieles ás membranas plasmáticas de células eucariontes, tendo os máis complexos da orde de decenas de diferentes tipos de lípido e sendo capaces de capturar a aparición de dominios de escala nanométrica. Ademais dos modelos de membrana plasmática, outros considerados de grande relevancia son os de membrana bacteriana, os cales tamén recibiron moita atención nas últimas dúas décadas. O termo de 'membrana bacteriana' non é máis que un que encompasa, en realidade, unha gran cantidade de modelos diferentes con cadansúas particularidades, xa que as membranas das procariotas soen ser altamente complexas, combinando capas de membranas lipídicas con outras estruturas como 'muros' de peptidoglicán, sumerxidos en substancias de gran viscosidade, o cal converte o seu estudo nunha tarefa non trivial. Ademais, malia non ter tanta prominencia como os exemplos citados anteriormente, discútense certos modelos de orgánulos, principalmente para as mitocondrias. Con esto, séntanse as bases para o actual estado-do-arte no modelado de sistemas de membrana altamente complexos. Estes recentes traballos enmárcanse principalmente na modelación e simulación de partículas víricas completas, así como de algúns orgánulos e, finalmente, a creación dun modelo completo de 'célula mínima' ainda a pesares de non ser polo de agora, en rigor, simulable.

A derradeira parte do capítulo de introdución da presente tese está adicada á determinación de propiedades mecánicas e magnitudes derivadas de ou relacionadas con estas nas membranas lipídicas, xa que unha boa parte do traballo desenvolto neste doutoramento está intimamente ligado a elas. Discútese en primeiro lugar como as propiedades mecánicas das membranas son considerados factores de gran relevancia dende polo menos os anos 90 para a MD, e dende os anos 70 a nivel teórico co desenvolvemento do Hamiltoniano de Helfrich. A continuación dáse unha relación de estudos os cales ao longo dos anos foron refinando os métodos para o cálculo destas propiedades, así como introducindo modificacións ao Hamiltoniano anteriormente mencionado, principalmente para ter en conta os graos de liberdade internos das membranas, isto é, a orientación molecular dos lípidos. Con isto, pásase seguidamente a discutir traballos que, sen calcular directamente as constantes fenomenolóxicas relacionadas cas propiedades mecánicas das membranas, estudan o comportamento destas fronte a aplicación de estímulos mecánicos. Agrúpanse estes traballos en tres grandes grupos: os que estudan a enerxía necesaria para crear un poro na membrana, os que estudan a enerxía necesaria para deformar membranas ao longo do plano que as contén, e os que estudan os efectos dos ultrasóns e/ou cavitación sobre as membranas. Os primeiros céntranse sobre todo no desenvolvemento de coordenadas de reacción axeitadas para capturar o proceso de poración e a súa natureza metaestable, sendo o grupo do Prof. Jochen Hub de referencia neste contexto. Os traballos sobre as deformacións uni e bi-axiais das membranas están dirixidos, principalmente, ao estudo de como a velocidade á que se aplica esta deformación afecta ao comportamento das membranas, asimesmo de como a composición desta modula os observables das simulacións. Por último, e en relación aos traballos estudando a influencia dos ultrasóns sobre as membranas celulares, menciónanse os esforzos feitos para o modelado e a simulación de efectos de cavitación de nano e micro burbullas de aire en auga, as cales se teoriza que son capaces de crear correntes supersónicas de líquido arredor delas ao colapsar, causando danos nos tecidos circundantes. No canto da simulación da interacción directa dos ultrasóns con membranas, en ausencia de burbullas, discútense as contribucións pioneiras

do grupo de Phillippe Derremaux, no cal desenvolven a técnica fundamental para aplicar ondas de son dentro do algoritmo de MD, e estudan o seu efecto con diferentes sistemas nos que hai membranas celulares presentes.

Desta maneira, procédese a continuación no documento da tese a dar unha breve descrición dos obxectivos que esta se propón, de maneira xeral e para cada un dos traballos realizados. Estes son, respectivamente, contribuír ao coñecemento da biofísica das membranas lipídicas debido á súa relevancia para a bioloxía, así como para os seus potenciais usos terapéuticos; e avaliar aspectos técnicos das simulacións de MD de membrana como a precisión de diversos campos de forza, estudar a organización estrutural de membranas de gran tamaño e propor un esquema xerárquico mediante o cal entendelas e, finalmente, facer un estudo sistemático e pormenorizado da influencia da composición lipídica das membranas sobre como estas reaccionan ás deformacións impostas polos ultrasóns.

Con esto en mente, procédese a continuación a dar unha descrición detallada dos métodos usados para o traballo desenvolto nesta Tese. Comeza este capítulo introducindo a técnica principal e sen a cal este doutoramento non é posible: a dinámica molecular. Introdúcese primeiramente o seu fundamento físico básico: a segunda lei de Newton e a derivación das forzas que actúan sobre o sistema a partires dun campo escalar conservativo. Isto serve de base para a continuación entrar en detalle sobre as características que este campo toma, o cal recibe o nome de campo de forzas, por motivos obvios. Dáse a continuación unha relación dos distintos termos que comunmente son utilizados dentro dun campo de forzas para capturar as interaccións relevantes a nivel molecular, como os termos de distancia e ángulos de enlace, as interacións de tipo Van der Waals ou as interaccións electrostáticas. Unha vez dados estos exemplos, pásase a discutir outro concepto fundamental das parametrizacións de moléculas na MD: o seu nivel de resolución. Deste xeito discútese como para un mesmo sistema, este pode representarse a nivel atomístico se cada átomo ten un equivalente en partícula no campo de forzas; cuase atomístico se os hidróxenos non polares se agrupan nunha única partícula no campo de forzas xunto co heteroátomo ao que estén unidos; ou en gran groso no caso de facer agrupacións de varios heteroátomos nunha partícula única. Fálase deste xeito das vantaxes e inconvintes que cada un destes niveis de resolución ten, estando principalmente relacionados co aforre de custos computacionais dos modelos de menor resolución, ca conseguinte perda de precisión á hora de representar os sistemas.

Descríbense despois os algoritmos principais á hora de implementar un motor de simulación de MD. Fálase deste xeito dos integradores, os cales son os encargados de resolver numericamente as ecuacións diferenciais pertinentes ao método, que ou ben minimizan a enerxía dun sistema ou ben obteñen o movemento das súas partículas ao longo do tempo, a través do anteriormente mencionado campo de forzas. Dáse unha descrición tamén de como se calculan certas magnitudes de relevancia como a enerxía cinética e a relación que esta ten ca temperatura e ca presión do sistema, servindo isto de precedente para introducir como, en función de que magnitudes concretas se decidan manter constantes nunha simulación, esta se atopa en colectividades termodinámicas diferentes. Así, dáse unha descrición xeral dos algoritmos e aparatos matemáticos que unha simulación de MD usa para manter estas magnitudes constantes, facendo especial fincapé nos que resultaron de maior relevancia para o desenvolvemento dos traballos realizados durante o doutoramento. Por último, e unha vez completada esta visión do funcionamento interno da MD, propóñense unha serie de pasos xerais que o algoritmo global segue para producir unha simulación calquera.

O capítulo adicado aos métodos torna a continuación aos aspectos técnicos de como se obtiveron as medidas de certas magnitudes calculadas con frecuencia ao longo dos diversos estudos

levados a cabo durante o doutoramento. Comézase deste xeito por unha descrición do aparato matemático usado para obter medidas nunha membrana lipídica de tal xeito que as posibles deformacións desta non introduzan artefactos. Apoiándonos no traballo desenvolto no grupo do Prof. Markus Deserno e a súa descrición das membranas lipídicas a través da xeometría diferencial, faise unha proposta dun sistema de referencia local (LFR polas siglas en Inglés) que permite obter medidas de diversas magnitudes nas membranas de maneira agnóstica ás súas desviacións da absoluta planaridade. Dado que este método depende de calcular as derivadas espaciais de varias magnitudes definidas sobre a superficie da membrana, adícase un apartado a introducir dous esquemas de discretización espacial que permitan calcular as devanditas operacións. Os esquemas discutidos son o esquema de Euler, que divide o espazo en gradillas regulares; e o método Lagranxiano, o cal se basea en teoría da interpolación e permite avaliar as derivadas en calquera punto arbitrario do espacio.

O seguinte paso neste capítulo tómase na dirección de introducir e explicar o xeito concreto no que se mediron as diferentes propiedades das membranas lipídicas determinadas de relevancia para o desenvolvemento desta tese. Para cada unha delas, explícase a súa importancia e mailo fundamento que se usou para estimalas a partires dunha simulación de MD. Estas propiedades son o grosor da membrana, as funcións de distribución radial, os enlaces de hidróxeno entre distintas especies na simulación, os coeficientes de difusión, a área por lípido, a inclinación das colas dos lípidos con respecto á superficie da membrana, os parámetros de orde dos enlaces CH dos lípidos, e a permeación de moléculas como a auga nas membranas.

A sección que segue a anteriormente descrita adícase aos diversos aspectos relacionados ca implementación do protocolo de simulación de ultrasóns no motor de MD. Comézase por calcular, de maneira teórica, o límite inferior para o tamaño da zona na que unha onda de son pode ser focalizada, idealizando en gran medida o seu comportamento e tratándoa como un feixe de radiación coherente. Unha vez calculado este límite, que se determina 5 a 6 ordes de magnitude superior ao tamaño de calquera sistema simulable a través da MD, procédese a explicar a modificación introducida no algoritmo de control de presións para reproducir os efectos derivados da presenza dunha onda de son nunha simulación. Por último neste contexto, e xa que gran parte do traballo desenvolto versou sobre a determinación de como diversas membranas reaccionan ás deformacións mecánicas impostas por unha onda ultrasónica, adícase unha sección deste capítulo á explicación do método desenvolto para cuantificar o alcance destas reaccións. Este método está baseado en tratamento de sinais dixitais, e conleva o centrado da sinal producida na membrana polo ultrasón a través dun filtro Savitzky-Golay, e unha conseguinte transformada de Fourier para obter a amplitude da oscilación, a cal é directamente proporcional á reacción da membrana.

A continuación adícanse uns apartados ao tratamento estatístico non estándar dos datos obtidos das simulacións levadas a cabo durante os traballos realizados ao longo da tese. En concreto, faise referencia ao método desenvolto para a identificación de magnitudes non redundantes usadas para a proposta de organización xerárquica das membranas lipídicas. Este método fundaméntase nunha descomposición en autovectores dunha matriz de datos orixinal, a través da cal se identifican pares de propiedades acopladas entre si e que codifican información equivalente, permitindo obviar unha delas obtendo así unha representación mínima do estado mecánico da membrana. Dáse tamén unha explicación do algoritmo de *clustering* de datos utilizado para agrupar e comparar o comportamento das membranas no traballo referido ás diferenzas producidas pola composición lipídica das membranas sobre a reacción desta aos ultrasóns. A última sección do capítulo dos métodos está adicada aos aspectos técnicos da construción dos sistemas

e os parámetros de simulación concretos usados en cada traballo.

Pásase así ao capítulo dos resultados, nos cales se presentan os achados máis relevantes das investigacións levadas a cabo ao longo do doutoramento. Este capítulo subdivídese á súa vez en catro apartados, os cales tratan cada bloque diferenciado de traballo realizado. O primeiro bloque trata a comparación de campos de forza para a simulación de modelos simples de membrana de bacteria. Neste, unha serie de propiedades son medidas nas simulacións para as membranas propostas no estudo, representadas nos distintos campos de forza, e os valores obtidos para cada unha destas simulacións comparados con valores determinados experimentalmente. Esta comparación permite avaliar a proficiencia de cada parametrización á hora de reproducir as devanditas propiedades, e de especial relevancia neste estudo foi a colaboración con investigadores expertos en espectroscopía RMN, os cales proporcionaron de maneira orixinal os parámetros de orde dos lípidos das composicións de membrana concretas que foron usadas neste traballo. A través deste estudo conclúese que a día de hoxe a labor da elección dun campo de forzas para a simulación de membranas lipídicas a través da MD segue a ser unha labor altamente interpretativa, na cal o investigador ha de tomar a decisión dependendo das caracterísitcas do traballo a realizar, xa que ningunha das parametrizacións testadas se erixiu como a claramente superior fronte as outras, tendo cada unha vantaxes e inconvintes.

O seguinte bloque de traballo presentado no capítulo de resultados céntrase no estudo das propiedades estruturais das membranas celulares e na proposta de organización xerárquica derivada destas. Deste xeito, postúlase unha equivalencia entre os modelos tipicamente usados para as proteínas ou os ácidos nucleicos e a proposta feita nesta tese, tamén nunha estrutura primaria, secundaria, terciaria e cuaternaria. Así, a estrutura primaria dunha membrana celular relaciónase co perfil lipídico que a compón, do mesmo xeito que a estrutura primaria dunha proteína é a súa secuencia concreta de aminoácidos. A estrutura secundaria no caso das membranas serían as morfoloxías autoensambladas dos lípidos, dando lugar a bicapas, monocapas, micelas, etc., de maneira análoga ás morfoloxías en, por exemplo, hélices ou láminas observadas no caso das proteínas. O nivel terciario de organización require dunha análise máis pormenorizada no caso das membranas, e identifícase como a existencia de dominios localizados no espazo e no tempo nos cales hai un comportamento coordinado e coherente en grupos de lípidos próximos entre si, os cales poden interaccionar entre eles e evoluir de maneira cambiante. Esto faise en analoxía a como os motivos secundarios mencionados con anterioridade para o caso das proteínas poden agruparse e interaccionar entre eles, dando lugar a cambios conformacionais na biomolécula. Por último, o nivel cuaternario de organización identifícase como os cambios morfolóxicos na estrutura das membranas debido á interación destas con outras macromoléculas como as proteínas ou entidades máis exóticas como nanotubos de carbono. Con esta proposta, preténdese crear un marco teórico preliminar que equipare as membranas celulares a outras entidades biolóxicas as cales foron historicamente consideradas de maior relevancia.

Os seguintes e últimos dous bloques presentados no capítulo de resultados da tese versan sobre a reacción das membranas celulares ante deformacións mecánicas impostas por unha onda de ultrasóns. O primeiro deles estuda o comportamento de dez composicións de membrana diferentes frente a un tipo único de ultrasón, e pretende comprobar a viabilidade do método, así como a adecuación dun campo de forzas de gran groso para levar a cabo este tipo de estudos. Para facer isto, os resultados deste último campo de forzas valídanse contra os obtidos de simulacións equivalentes usando unha parametrización atomística e, malia requerir dun factor de corrección en magnitudes relacionadas co tempo, as predicións de ambos considéranse equivalentes. Con isto en mente, realízanse simulacións máis longas usando as representacións a gran groso dos

sistemas seleccionados e determínanse para todas elas unha serie de propiedades relevantes para o estado mecánico das membranas, como a área por lípido, o grosor, ou a curvatura, entre outras. Aplicando o método desenvolto para estudar o alcance da deformación mecánica imposta, obsérvase que a composición lipídica xoga un papel fundamental á hora de ditar como unha membrana reacciona ante o devandito estímulo, sendo certos lípidos dominantes sobre outros dada a súa maior capacidade de modular o comportamento da membrana que conforman.

Este anterior estudo senta pois as bases para o traballo levado a cabo no que se describe no derradeiro bloque do capítulo de resultados. Neste, no canto de usar dez composicións lipídicas diferentes e un único tipo de ultrasón, avalíanse os efectos de cen combinacións diferentes de parámetros da onda sonora (frecuencia e presión máxima alcanzada) sobre catro composicións simples de membrana. Este estudo permite obter, de maneira sistemática, superficies de resposta para as membranas celulares estudadas como función do espazo paramétrico xerado polos ultrasóns. Determínase deste xeito que as combinacións de frecuencias baixas con sobrepresións elevadas son capaces de alterar profundamente a morfoloxía das membranas, observándose para estes casos en todas as composicións estudadas a perda da estrutura de bicapa nos ciclos de presión negativa, malia que esta se recupera na súa totalidade nos ciclos de presión positiva da onda. Ademais disto, e fóra dos rexímenes de perda da estrutura nominal, obsérvase que para a meirande parte das propiedades medidas, a presión do ultrasón ten un efecto máis acentuado que a frecuencia concreta elixida, aínda que existen sutilezas dependendo da propiedade que se esté a medir e da composición concreta estudada. No canto das diferenzas entre composicións obsérvase de novo que estas son estatísticamente significativas na gran maioría dos casos estudados, pero non necesariamente sistemáticas, variando en función da propiedade medida ou dos parámetros do ultrasón concretos a comparar. Deste xeito, os resultados mostran un panorama altamente complexo, no cal a composición da membrana, as propiedades específicas que se determinen para estas e os parámetros seleccionados para o ultrasón, se inflúen mutuamente á hora dos resultados producidos polas simulacións.

Remata así o documento cun capítulo final de conclusións, no que se dá unha derradeira visión xeral dos contidos discutidos ao longo do texto, así como das principais aportacións que emanan da presente tese. Con este traballo, pretendeuse contribuir ao entendemento das membranas lipídicas, estruturas bioquímicas fundamentais para a vida, mais tradicionalmente relegadas a un segundo plano en favor das proteínas e ácidos nucleicos. Usando ferramentas computacionais, e nunha constante interfase entre varias disciplinas, leváronse a cabo tanto estudos sobre sobre temas técnicos no relativo á simulación, como con enfoques no plano da bioloxía ou no de potenciais terapias médicas. Espérase que os resultados obtidos e as conclusións ás que nos levaron ao longo desta tese aporten novas perspectivas sobre a biofísica das membranas lipídicas, e subliñen as intrincadas sinerxias entre o seu perfil lipídico, as súas propiedades mecano-estruturais e, polo tanto, as súas respostas a estímulos externos.

0.2 Reduced English Version

The body of this Thesis focuses on lipid membranes, which are essential structures in biology and thus crucial for life. This work was conducted computationally, rather than using experimental techniques, to investigate the self-organisation and mechanical responses of these biological entities to external stimuli. This interdisciplinary approach bridges physics, chemistry, biology, and computation, emphasising the importance of such synergy in modern scientific research.

The Thesis begins with a historical overview, highlighting how material conditions have shaped technical and scientific advancements, leading to a deeper understanding of cellular membranes. Initially seen as simple barriers, membranes are now recognised as multifunctional and complex structures. Early scientific evidence, like osmotic pressure measurements on red blood cells, pointed to the semipermeability of membranes, which later evolved into the bilayer model proposed by Gorter and Grendel in 1925 - a cornerstone of our current understanding of membranes.

In the first chapter, the molecular composition of lipid membranes is explored, with lipids being the fundamental component due to their amphiphilic nature. This structural anisotropy allows lipids to self-assemble into membranes under specific conditions. The discussion also covers proteins and sugars, essential molecular species within membranes, emphasising the interdependence several relevant families of molecules for proper biological function. This chapter also introduces two key models: the fluid mosaic model and the lipid raft model, each offering a conceptual framework for understanding membrane structure and dynamics.

The complexity of lipid membranes extends beyond their basic units and organisation, as they perform various cellular functions, including acting as physical barriers and being involved in signal transmission, material transport, and cell motility. Different types of membranes, influenced by factors like organism type, tissue specificity, disease processes, and aging, are then discussed.

A section is dedicated to membrane lipid therapy (MLT), which targets lipid compositions in membranes as potential therapeutic approaches. Examples from fields like oncology, cardiovascular disease, and neurodegenerative conditions demonstrate the therapeutic potential of targeting membrane lipids. Mechanical therapies, especially the use of ultrasound, are also discussed, given their relevance to the results obtained in this Thesis, particularly regarding the concept of sonoporation, where pressure waves induce membrane disruptions, linking these mechanical stimuli to the structural and mechanical properties of membranes.

The introduction then shifts to the computational tool used throughout the Thesis: molecular dynamics (MD). This method is described in detail, from its physical basis in Newton's second law to the use of force fields for simulating molecular interactions. The discussion includes the development of molecule parameterizations and particularly for lipids, reviewing current methods and concluding that while many options exist, none fully capture the complexity of lipid membranes, leaving interpretation and decision-making to the researcher.

Further sections in the introduction focus on realistic membrane models and the simulation of complex systems, such as bacterial membranes and eukaryotic plasma membranes. Recent efforts in modelling entire viral particles, organelles, and the 'minimal cell' are also discussed. Finally, the mechanical properties of lipid membranes and how they respond to mechanical stimuli are explored, with significant attention given to studies on pore formation, membrane deformations, and the effects of ultrasound and cavitation.

The Thesis then moves to its objectives, which are to contribute to the understanding of lipid membrane biophysics, assess technical aspects of MD simulations, study the structural organi-

sation of large membranes, and examine how lipid composition influences membrane responses to ultrasound-induced deformations.

In the methods chapter, the fundamental physics of MD simulations are introduced, followed by descriptions of the force fields, resolution levels, and algorithms used to simulate membrane systems. Special attention is given to the methods for calculating relevant membrane properties, such as membrane thickness, lipid tail orientation, diffusion coefficients, and hydrogen bonding. The chapter also details the protocol for simulating ultrasound effects on membranes, including the modification of pressure control algorithms to simulate sonic waves in MD simulations.

Results are presented in four sections. The first compares force fields for bacterial membrane models, concluding that the choice of force field remains interpretive, with no single one proving superior. The second section proposes a hierarchical organisation of membranes, analogous to protein structure models, introducing primary, secondary, tertiary, and quaternary levels of structure for lipid membranes. The final two sections focus on membrane responses to ultrasound. One examines how ten membrane compositions respond to a single ultrasound type, while the other assesses the effects of different ultrasound parameters on four membrane compositions, revealing a complex interplay between lipid composition, ultrasound parameters, and membrane properties.

The Thesis concludes by summarizing the key contributions, underscoring the relevance of lipid membranes in biology and potential therapeutic applications. Using computational tools, this work offers new perspectives on the biophysics of lipid membranes, highlighting the intricate relationships between lipid profiles, mechanical properties, and external stimuli responses.

1 INTRODUCTION

To understand the "real", we must compare it with what is commonly understood as virtual.

–Yuk Hui,
On the Existence of Digital Objects

1.1 A Brief Historical Perspective

This work delves into the realm of lipid membranes, a fundamental biological structure, their self-organisation, and their response to specific physical stimuli. In particular, this research did not occur in a traditional laboratory. Instead, it happened within microprocessors, hard drives, wires, and cables, observing a biological subject under the light of a computational prism. I believe that the most intriguing things happen at the interfaces, where boundaries blur and elements intermingle. Additionally, I advocate that to truly understand a scientific concept, one must consider its historical and philosophical roots, tracing the journey to our current understanding.

1.1.1 On Computation

The history of computation is deeply intertwined with that of humanity. So much so that I believe the latter can scarcely be understood without the former. From the dawn of consciousness, most surely predating *homo sapiens*, we have sought to decipher our world. More than mere survival, our goal has been to understand and interpret the world around us.

Figure 1.1: The Antikythera Mechanism, considered among the earliest mechanical computers. Source: Wikimedia Commons[1], distributed under a Creative Commons licence

We have filled our minds and imaginations with models (*i.e.*, abstract representations of reality), enriched with variables and parameters, adjusted until they align well enough with the phenomena we observe. The early models were simple, such as numbers and numerals for precise counting beyond vague terms such as *'no'*, *'many'*, or *'a lot'*. This precision was especially beneficial for the management of communal affairs. Then, as the models became more complex, the need for **computation** arose. According to the Cambridge Dictionary, computation is *'the act or process of calculating an answer or amount using a machine'*. This mention of a *machine* is specially interesting to me, as it highlights a return to the tangible world after abstract modelling, in a process where the thesis of a concrete occurrence is faced with the antithesis of the abstraction, and these are then synthesised by the use of a tangible machine which returns a result, again in the abstract plane priming the cycle once more.

Thus, computation became particularly significant when we invented machines for, well, *computing*. The first examples include Sumerian counting tablets, precursors of the abacus, dating from 2700 to 2300 BC[2]. A couple of millennia later, the Antikythera Mechanism (Figure 1.1), from Ancient Greece, was used to track the planetary positions, representing one of the first mechanical computers.

Islamic scholars like Al-Khwarizmi advanced mathematics and algebra in the early Middle Ages, building upon Greek knowledge which led to sophistication and perfection of computing devices such as the astrolabe[3]. These developments later permeated into late Medieval European society, fostering the mechanistic worldview, sparking the era of analog computing. This period saw the advent of mechanical clocks and Blaise Pascal's Pascaline, a precursor to more complex mechanical calculators like Leibniz's Step Reckoner[4, 5].

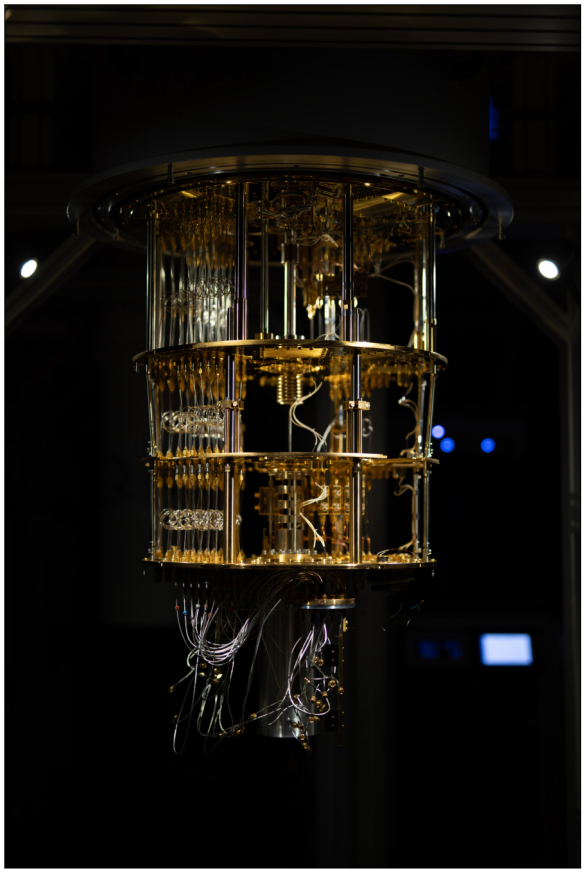

Figure 1.2: A functioning IQM Quantum Computer in Espoo, Finland. Image sourced from Wikimedia Commons[6], distributed under a Creative Commons licence.

The industrial revolution further propelled these developments, introducing programmable machines. Charles Babbage's work, notably the Difference Engine, and later the Analytical Engine, birthed the first programmable, general-purpose, Turing-complete (decades before we even knew what Turing-complete meant!) mechanical computer, thanks to the contributions of Ada Lovelace[7]. In that same century, George Boole's boolean algebra laid the mathematical foundation for computer logic, representing a significant step towards modern digital computing. Boole, who was a complete theoretician, encoded Aristotle's syllogistic logic in binary equations, unknowingly laying the foundations for the design of digital circuits[8].

It was in the beginning of the twentieth century that Claude Shannon's insights into combining switches for symbolic logic operations and Alan Turing's theoretical work on computation accelerated the development of digital computers[5]. These early computers, initially using relays, then vacuum tubes and eventually transistors, performed complex mathematical and arithmetic operations. World War II further spurred technological advancements, leading to the miniaturisation of digital computers in the later half of the twentieth century, turning them into essential tools for modern life.

Today, our existence is deeply interwoven with the digital realm; one may argue that our mode of existence is no longer separable from the digital world. Computation permeates virtually every aspect of modern life, from industrial production to financial decision making, and, significantly for this Thesis, the simulation of physical phenomena. We are also potentially at the threshold of the most significant computational revolution since the invention of the transistor.

The horizon for computing and simulation technology is bright and ever-expanding.

On the software front, concepts like cloud computing are rapidly gaining prominence and traction[9, 10], supported by the explosive growth of the internet over the last two decades. In parallel, Artificial Intelligence (AI) and Machine Learning (ML) algorithms have evolved from theoretical concepts to practical tools, propelled by the appearance of Big Data[11–13]. However, these rapid advances in AI have sparked both enthusiasm and caution. Some experts express concern about excessive optimism[14, 15] and the ethical implications of these emerging technologies[16, 17], given our lack of experience and regulatory frameworks to ensure their responsible use[18].

Hardware advancements have kept pace, with significant improvements in transistor-based microprocessors and the introduction of specialised hardware accelerators, such as Graphics Processing Units (GPUs), which are particularly effective in training AI models[19]. Furthermore, the computational landscape is being reshaped by emerging technologies like Quantum Computing[20] (Figure 1.2), which takes advantage of quantum phenomena; and Biocomputing, with the aim of harnessing biological systems for information processing[21].

As we continue to push the boundaries of computation, we venture into a future where the possibilities are as vast as our collective imagination and ingenuity. The implications of these advances for fields like lipid membrane research, as discussed in this Thesis, are profound and far-reaching, bridging the gap between the abstract and the tangible in our quest for knowledge and understanding.

1.1.2 On Life Sciences

The object of work for this Thesis, even while using computational methods, pertains to the field of life sciences. Of course, for as long as we have been thinking about computation and building machines to aid us with it, we still struggled with disease, death, or simply just pondered what does it mean for something to be alive. Thus, the roots of this topic grow deeply buried in time. However, life sciences have been shrouded in mysticism up until not that long ago. As we shall see in the following section, prayer, rituals, and alchemy will be the accompanying concepts until recently.

Figure 1.3: An arybalos depicting a physician treating a patient, ca. 480-470 BC, Louvre Collection. Image sourced from Wikimedia Commons[22], released into the public domain.

In addition to interest in surgical procedures, most surely due to necessity, for which we have solid evidence as early as the Mesolithic and proto-Neolithic[23, 24]; and the beginning of agriculture dating back to 12000 - 11000 years ago[25], the formal study of life in the western world (it is known that the ancient Chinese civilisations, as well as those of the Indian subcontinent, were proficient in the study of life sciences[26]) can be traced back to Ancient Greece (Figure 1.3). Philosophers like Aristotle and later his disciple Theophrastus con-

tributed extensively to the empirical understanding of nature, especially the habits and attributes of plants and animals in the world[27].

The legacy of classical Greece during antiquity was crystallised in the Alexandrian era, under Ptolemies' rule. The Library of Alexandria emerged as a cultural hub, parallel to what we now understand as a university, concentrating knowledge in a single institution. Its unfortunate demise led to a yet-present gap on what we know about ancient times. Moreover, it seems that life sciences at that point were still more a matter of conjuration of spirits than of empirical evidence[26]. A change of paradigm, although maybe not recognised at that time, happened in the Roman era, with Galenus of Pergamun, who developed the theory of humours. This theory, despite still falling on the mysticism side by today's standards, challenged the contemporary worldview that relied mainly on divination[26, 28].

Subsequently, the Middle Ages did not see much improvement in understanding the life sciences, besides the continuation and preservation of the Greek and Roman doctrines by the Islamic civilisation in their golden age. In Europe, scholasticism flourished with the appearance of universities, although they focused mainly on philosophy and theology at that time[26]. A notable exception is Albertus Magnus, who produced works on minerals[29] (he is known to be the discoverer of the element Arsenic) and animals[30], making him a pioneer on the matter.

The European Renaissance, spanning approximately from 1300 to 1650, was a period of transition between the decaying Middle Ages and Modernity. It was a pivotal period in the evolution of western science and culture, where mobility between different human groups and cultures brought about a rediscovery and advance of Greek philosophy, art and science[26, 31]. This increased movement of people was probably one of the main culprits for the bubonic plague of 1348, which put pressure on the realm of science and medicine, even if not immediately, leaving a profound impact on the mentality of the contemporaries because of the pandemic that killed a third of the European population[32].

This was a time of groundbreaking anatomical discoveries and philosophical shifts. Art and anatomy became involved and mixed within each other, with artists like Leonardo da Vinci taking up meticulous studies to enhance the realism in their art, symbolising the era's blend of scientific inquiry and artistic endeavor[26]. Some notable landmarks in this advancement were Andreas Vesalius' works, specifically his *De Humani Corporis Fabrica*, which challenged the widely accepted Galenic doctrines, reforming the anatomical understanding of his age, while at the same time granting him many critiques and a death that is still shrouded in mystery[33, 34]. Furthermore, the period was enriched by explorations in alchemy and natural magic, with figures such as Paracelsus contributing to early chemistry[26]. Moreover, the work of William Harvey on the discovery of blood circulation culminated in the dismantlement of Galenic theories, significantly advancing the understanding of human physiology[35].

After the Rennaisance, the 17th century continued this transformative period in the evolution of scientific thought and practice, characterised by a departure from traditional Aristotelian academia towards a new paradigm of experimental and practical investigation. This shift was catalysed by figures such as Galileo, Newton, and Harvey, whose contributions illuminated natural philosophy and guided European society from its agrarian roots to an urban and industrial future[26]. The establishment of scientific societies, such as the Accademia del Cimento in Firenze and the Royal Society in London, clearly symbolise this transformation. These institutions, often supported by government charters and wealthy patrons, created an environment conducive to experimental science, distancing scientific exploration from the constraints of university doctrines of the time[36]. Simultaneously, this era witnessed significant intellectual contributions from

philosophers like Francis Bacon and René Descartes, who, despite their contrasting approaches (Bacon stood up for experimentation while Descartes rooted for rationalism), collectively reshaped the scientific method. Furthermore, advances in microscopy, particularly through the work of Antoni van Leeuwenhoek[37], unveiled a whole new world, revolutionising our biological understanding and challenging existing scientific paradigms.

This synthesis between empiricism and rationalism allowed for rapid advancements in the sciences (and in particular the life sciences) on subsequent times, through the development and gradual perfection of the scientific method. In the XVIII century Anton Lavoisier set the bases for modern Chemistry enunciating the conservation of mass law[38] and introduced the chemical nomenclature[39] still widely in use today. This fathered a scientific discipline which was separate from the 'magical thinking' approaches of Alchemy and grounded a systematic science which, as we will mention in a few paragraphs, was mandatory for the revolution of Biology that happened in the following centuries. At the same time, Jean-Baptiste Lamarck laid the first foundations for the theory of Evolution with his theory of the inheritance of acquired characteristics[40].

The XIX century was, then, a time of great advancements that were built upon previous discoveries. Especially remarkable is Darwin's *On the Origin of Species*[42], which formulated for the first time the Theory of Evolution, postulating that life and speciation are a continuous process, rather than something that happens because of direct divine intervention. At the same time and while studying plant hybridisation, Gregor Mendel set, probably without realising, the basics of genetics[43]. At this point, Biology was just beginning to approach its molecular rationalisation. In order for that to occur, two important realisations had to be introduced: first, John Dalton's theory of atoms[44] postulating, in a curious reminiscence to ancient times, that matter is composed of microscopic particles forming the different elements and that it is them that (re)-combine in chemical reactions; and the idea of the periodicity of the elements mainly developed and attributed to Dmitri Mendeleev[45].

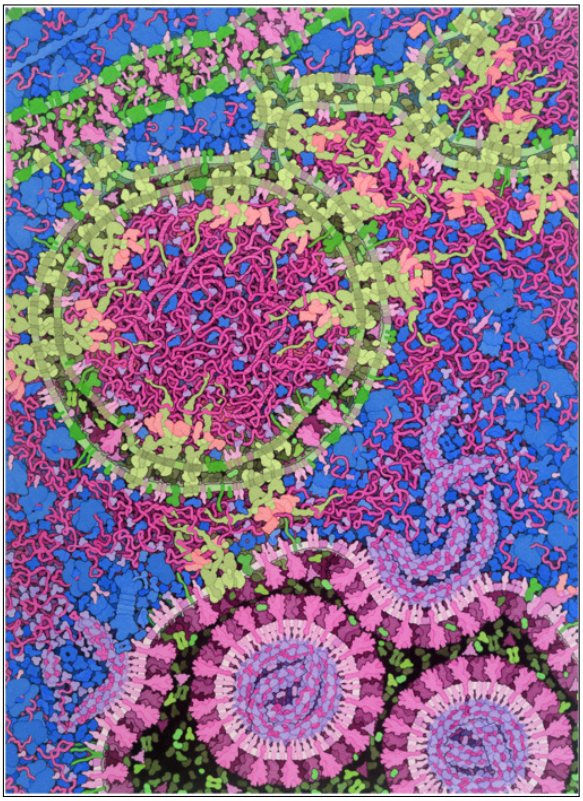

Figure 1.4: A computer render of a cross-section through a cell infected with a coronavirus. The cell's molecules are shown in blue and green, and viral molecules are shown in red and purple. Image reproduced from David. S.Goodsell *et al*.[41], under a Creative Commons Licence.

All of these ideas and discoveries created the perfect environment for the almost miraculous advances of the twentieth century. Then and there, the discoveries occurred not only fast, but at an accelerated rate. Of paramount importance was the advent of modern synthesis, the paradigm developed by Fisher, Haldane, and Wright that merged the ideas of Darwin and Mendel into a unified mathematical framework[46]. This mixing of mathematics and biology is

a clear example of a key characteristic of the XX century, that is, the intermingling of different areas of science as we start to become aware of the grand scheme of things. In fact, with the advance of other disciplines we realised that the bases for Biology are of molecular nature.

But, of course, the elephant in the room for the past century is none other than the discovery of the double helix structure of DNA, by Rosalind Frankin, James Watson, and Francis Crick[47–49], another great example of how Biology benefited from technical advances in other scientific fields, as this discovery was made possible by the development of X-ray diffractometry. This discovery, followed by Fred Sanger's publication of the first aminoacid sequence of insuline in 1955[50], revolutionised our understanding of how genetic information is stored and translated to the molecular machinery that are proteins, paving the way for the advent of genomics and proteomics.

The last part of the XX century was characterised by a surge in technological advances which, in fact, were deeply tied to the advent of microprocessors and personal computing, discussed in the previous section. Specifically, bioinformatics was established as a discipline of its own[51], combining Biology, Computer Science, and Information Technology. This marked a new era, one in which huge amounts of data are produced and a shift in research is observed towards finding patterns hiding in it, aided by computers.

It is in this context where this present work is contextualised. At an interface where Biology, Chemistry, Physics, and Computer Science mix with each other. We have provided a quick look at how technology and with it society (or maybe how society and thus technology) have evolved, shaping our world through the millenia. Starting from two perspectives that occasionally seem to clash with each other, the at times impersonal computation and the down-to-earth life sciences, we found connections between them time and time again. It seems that we are at a moment when that connection is particularly strong, and let us hope it stays that way for a long time. Now, for the actual work.

1.2 The Relevance of Lipid Membranes

In the previous section we gave a fast, yet hopefully comprehensive, discussion of the main general topics this Thesis versed on, and which were the historical advances that led to them. However, a specific biological structure has been the focus of this work: lipid membranes. Our understanding of lipid membranes has evolved significantly over the years. Central to them is the lipid bilayer model, which views the membrane as two oil-water monolayers, back-to-back. We now know that, within a cell, there are many such membranes, but we will focus on the plasmatic membrane, which was the first of the biological membranes to be studied. Its main function is to act as a barrier that separates the interior of the cell from the external environment[52] although, as we will see in the following sections, it plays many other relevant roles. Early key contributors to the study of membranes include William Hewson, who in 1773 demonstrated osmotic swelling and shrinkage of red blood cells, deducing from this the existence of a cell membrane[52, 53]. C.H. Schultz in 1836 used iodine staining to estimate the thickness of the erythrocyte membrane[52], further advancing the understanding of membrane structure despite the limitations of microscopic techniques of his time.

Later contributions included Karl von Nägeli's studies on osmotic behaviour in plant cells and Wilhelm Pfeffer's membrane theory, proposing that the plasma membrane was thin and semi-permeable[52]. Charles Ernest Overton's permeability studies in the late nineteenth century suggested the presence of a lipid barrier in membranes, linking membrane permeability to lipid solubility[52, 54]. It was the landmark work of E. Gorter and F. Grendel in 1925 which provided

experimental evidence for the structure of the lipid bilayer of membranes[52, 55], a conclusion drawn from their studies on erythrocytes. These findings were foundational for the modern understanding of membrane structure.

1.2.1 The Building Blocks of Lipid Membranes

In this section, we shall give an explanation of the primary biochemical constituents composing lipid membranes. As will be discussed, multiple species of diverse nature participate in the construction of these biochemical structures, each imparting unique properties that collectively contribute to the formation of one of the most integral components of any living cell.

1.2.1.1 Lipids: the Basic Unit

As one can already imagine by their name, lipid membranes are constituted, mainly, by lipids. The word 'lipid' is derived from the Greek *lipos*, which means 'fat'. Thus, lipids are, by definition, insoluble in water. This is of course due to their molecular structure, having lipids long hydrocarbon chains (nonpolar and hydrophobic) and are usually scarcely decorated with polar and hydrophylic motifs. The subset of lipids that are of relevance for membrane formation take this to an extreme, having two clearly distinguishable segments, one that is polar and prefers solution into water and another which is completely nonpolar and avoids water at all costs. Such types of molecules are called amphipathic.

'Lipid' is really just an umbrella term to describe a family of molecules that have similar molecular motifs, sharing structural characteristics that make them behave in an analogous way. Therefore, the family of molecules that fall into the lipid category is overwhelmingly diverse[56]. It has been estimated that any typical animal cell can contain in the order of one thousand *major* lipid types. However, this number becomes even larger when considering minor lipids. Some studies show that in human tears, at least thirty thousand individual lipid types coexist with each other[52, 57].

So, with such great variability in their molecular nature, what are the functions that lipids can play? It is obvious that Nature does not waste resources; as Albert Einstein said, 'God does not play dice', even though he was talking about something completely different when he formulated his celebrated quote. In general, lipid function can be divided into three main categories[52], storage, structural, and active. Storage lipids are generally nonpolar and appear as densely packed biochemical energy sources in lipid droplets, most of which do not form part of lipid membranes. Structural lipids form the amphipathic matrix of the membranes discussed in this Thesis. Active lipids come in many different forms and are also found in membranes but at much lower levels than structural ones.

With so many different lipids, many classification systems have been proposed[52, 58, 59]. The method proposed by Fahy and co-workers is based on the idea of *lipidomics*, a term introduced at the beginning of the twenty-first century in analogy to the much more developed fields (at the time and now) of genomics and proteomics; but in this case it relates to the study of the relationships between the lipid contents of an organism, their physical properties and their biological activities[60]. This classification, despite being useful and convenient for the era of informatics, is far too complex for membrane studies, as only a small fraction of the lipids contained there are relevant for the formation of lipid membranes[52].

Probably the most relevant building blocks found in membrane-forming lipids are Fatty Acids (FA). Upon hydrolysis, a lipid is deemed 'complex' if a FA is released, and deemed 'simple' otherwise. Interestingly, free FAs are known to be detrimental to membranes[61] and are found

only at very low levels; while the main components are sterified FA derivatives. In general, a FA is 'a monocarboxylic acid usually with a long unbranched aliphatic tail that may be saturated or unsaturated'[52], but this is just a scaffold upon which many changes can occur. In fact, much of the variation in lipids comes from variations in the FA chains. The detailed disparities in lipids from their FA motifs are outside the scope of this work, and we refer the reader to the excellent book by William Stillwell, which is being used as a reference to build this section for an in-depth discussion. In summary, chain length, degree of usaturation, the location and isomerism of said unsaturations, and even possible ramifications of the acyl chains are all relevant factors for the derivatisation of FAs that lead to different lipid species.

1.2.1.2 Membrane Forming Lipids

As we discussed in the previous section, free FAs are not the main constituent of a lipid membrane, in fact, they have a detergent effect and are able to disrupt membranes. Thus, the lipid molecules found in membranes show derivatisations in the FA building blocks. These commonly imply the connection of acyl chains to other motifs. As can be seen in Figure 1.5, this connection is usually an ester bond, although amides and even thioesters are not uncommon[52].

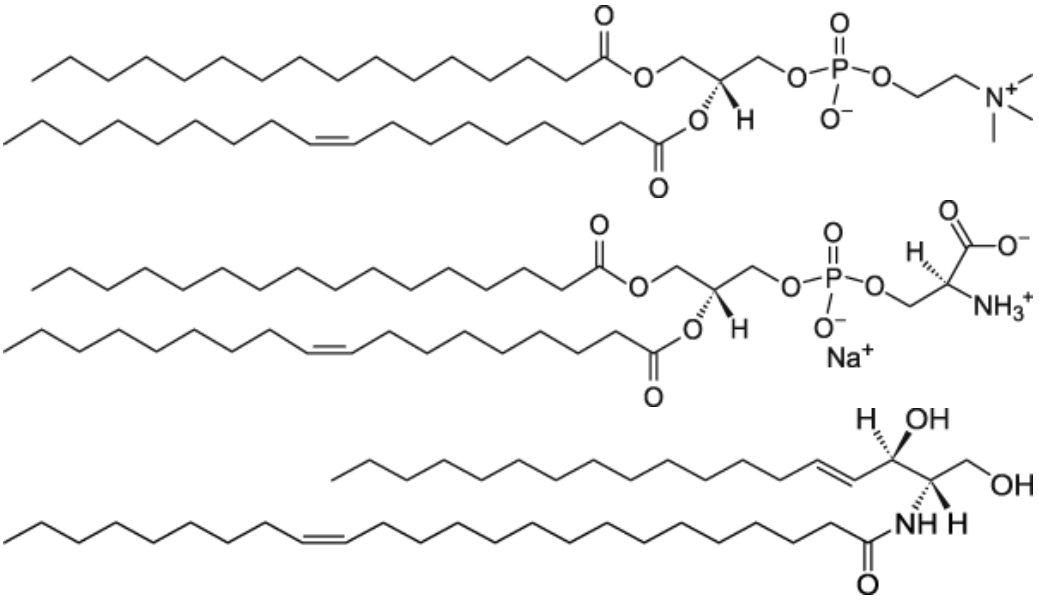

Figure 1.5: Molecular structure of three typical lipids. From top to bottom, POPC, POPS and 16:0 ceramide. Note how all the structures have a large nonpolar region comprised of acyl chains, and a polar region with hydrophilic heteroatoms. Note too how different lipids have different substitutents in their polar heads, and how also the acyl chains have different levels of unsaturation and length.

These bonds link FAs and are hydrolisable, such as esters or amides. In fact, the hydrolisis of such bonds is known as *saponification*, and has been a process understood for millennia (not at the molecular level, of course), used to produce soaps[62, 63]. However, some lipids have stronger linkage bonds, making them much more resistant to hydrolisis. Interestingly, these lipids are present mainly in primitive organisms such as those in the *Archea* kingdom, which are known to have a tendency to develop their lives under extreme environmental conditions, where a typical ester or amide would be easily broken[52].

In any case, the main kind of lipids that pertain to the work in this Thesis are glycerophospholipids (first two structures in Figure 1.5), following the nomenclature proposed by Fahy and colleagues. They are made up of one glycerol, one phosphate, two FAs, and an alcohol. In general, phospholipids are understood as having two different regions, a 'polar head' spanning from the ester linkage, up the glycerol, to the end of the alcohol motif; and the 'apolar tails', which comprise the acyl chains of the FAs.

The glycerol moiety acts as a linker between the apolar tails and the polar head. This molecule, which on its own is not optically active, becomes a chiral centre once it is esterified by the different groups that make up a phospholipid. The biologically occurring form is the D-isomer[52]. The C1 and C2 carbons of the glycerol are esterified by FA molecules, and these positions are known as the *sn*-1 and *sn*-2 positions, respectively. In general, and for mammalian lipids, the *sn*-2 position contains unsaturations. The C3 position of the glycerol is esterified by the phosphate group.

Most of the common phospholipids for animals have their phosphate motif doubly esterified. This results in the presence of only one OH group in the phosphate, whose pK_a is 2.1, which, at physiological pH, is deprotonated and thus creates a net negative charge in the phosphate. There are seven main classes of phospholipids for mammals[52], of which all are amphipathic. Some of them are zwitterionic in nature, having alcohol-derived motifs with a net positive charge that neutralise the phosphate; and others are anionic where the phosphate charge is not countered.

The general nomenclature of phospholipids is based on the different alcohol moieties that are esterified to the phosphate group. Again, we believe that an in-depth discussion of the different groups that can be attached at this phosphate position is beyond the scope of this Introduction chapter, and we refer the reader once more to the work of William Stillwell for a detailed explanation[52]. In summary, the main lipid types are those derived from Phosphatidic Acid (PA), an anionic lipid in which the phosphate is only esterified to the glycerol; from Phosphatidyletanolamine (PE), the main phospholipid for bacterial membranes, zwitterionic, in which the phosphate is esterified to an etanolamine group; from Phosphatidylcholine (PC), the main phospholipid for animal membranes, zwitterionic, in which the phosphate is esterified to a choline group; from Phosphatidylserine (PS), a mainly present in animals and anionic lipid in which the phosphate is esterified to the serine amino acid, known to be involved in functions other than structural within a membrane[64]; Phosphatidylinositol (PI), an anionic lipid where the phosphate group is esterified to inositol (a naturally occurring sugar), which has special presence in the brain and is also involved in non-structural functions[65, 66]; Phosphatidylglycerol (PG), another anionic lipid with great presence in bacterial membranes, in which the phosphate group is esterified to another glycerol moiety thus producing two chiral centers per lipid; and Cardiolipin (CL), which is basically a dimer of PG lipids linked by the same terminal glycerol moieties on their polar heads, and found primarily in the mitochondrial membrane[67].

Although phospholipids constitute the main class of membrane-forming lipids, two additional families are crucial to maintaining the integrity of lipid membranes: sphingolipids and sterols. Sphingolipids are a diverse family of molecules found in human membranes, all share the core structure of the C18 amino alcohol sphingosine (see the upper tail of the third structure of Figure 1.5). More than 60 variants exist[52], differing mainly by the groups attached to the C1 alcohol. FAs can be esterified with nitrogen in C2 and form amide bonds, making one hydrophobic tail (sphingosine) fixed and non-hydrolysable, while the other variable tail is nitrogen bonded. Sphingolipids have a polar head group and hydrophobic tails, similar to those of phospholipids but with structural differences including a trans double bond in sphingosine

and variable chain saturation. The main types include sphingomyelin (with phosphocholine or phosphoethanolamine head), cerebrosides (single sugar head), globosides (multiple sugars) and gangliosides (oligosaccharides with sialic acid)[52].

On the other hand, sterols are vital components of animal, plant, and fungal membranes but are absent in prokaryotes, where hopanoids serve a similar role. The primary sterols are cholesterol in animals, ergosterol in fungi, and β-sitosterol in plants, which differ slightly in their structures. These molecules have three distinct parts: a polar OH group for membrane anchoring, hydrophobic sterol rings that control membrane fluidity, and a flexible tail of uncertain function[52, 68]. Cholesterol is especially notable in animal membranes, often comprising more than 50% of the lipids in the plasma membrane and playing a role in structural integrity, membrane organisation, and cell signaling through lipid rafts (more on this in subsequent sections). Cholesterol is also a precursor for steroid hormones, bile salts, and vitamin D, and can be stored or modified for various, sometimes detrimental functions[52].

1.2.1.3 Other Membrane Constituents

So far we have discussed the fundamental building blocks of lipid membranes, and the ones that actually give them a name. However, in the biological scenario, membranes are also populated by other molecules and macromolecules that confer them with their specific function. The main two families of molecules that can be found in lipid membranes are proteins and sugars.

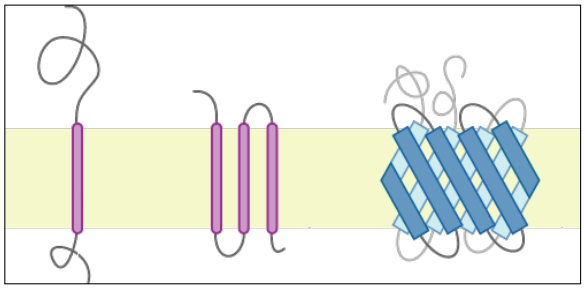

Figure 1.6: Schematic representation of several types of motifs found in transmembrane proteins. α-helices are shown in magenta, the β-sheets are shown in cyan, and the membrane region is shown in yellow. Image adapted from Wikimedia Commons[69], under a Creative Commons Licence.

Although lipids are the main constituents of membranes by number, if this metric is changed to weight, we may find that up to 75% of a lipid membrane can be composed of proteins, as is the case for the inner mitochondrial membrane[52]. Membrane proteins are classified into three broad types: peripheral, amphitropic, and integral proteins. Peripheral proteins are bound to the membrane surface through electrostatic or hydrogen bonds and can be easily removed by altering the pH or ionic strength of the surrounding medium[70]. A good example of a peripheral protein is the myelin basic protein, which adheres to the membrane surface of neurones through electrostatic interaction with anionic phospholipids[71].

On the other hand, integral proteins penetrate the hydrophobic core of the membrane and require more drastic methods, such as detergents, to extract them from their membrane matrix. Approximately 20 to 30% of the cellular proteins are integral to the lipid membranes[52]. These types of proteins have hydrophobic domains that embed into the membrane core, securely anchoring them. These proteins are then subdivided into endo/ecto-proteins and transmembrane proteins. The first kind are proteins that do not fully traverse the lipid membrane but are just anchored to it either on the extracellular matrix side (ecto) or on the cytosolic side (endo). An example of such proteins is cytochrome b_5, which is involved in electron transport[72]. Then, the transmembrane proteins (Figure, 1.6) completely traverse the lipid membrane with segments exposed both to the outside and to the inside aqueous spaces of the membranes[52]. Transmembrane proteins can use different motifs to anchor themselves to the membrane matrix, the most

common structures being single or multiple α-helices[73] or β-barrels[74]. Moreover, some of these transmembrane proteins can be covalently linked to fatty acids, such as myristic acid[75] or palmitoic acid[76]; whose long acyl hydrophobic chains serve as an anchor to the membrane in which they are embedded[52].

Finally, amphitropic proteins are a class of proteins that display the ability to alternate between soluble and membrane-bound states[77], coexisting their globular and bound form due to their reversible interactions with membranes. This transformation is induced by phosphorylation, acylation, or ligand binding, which exposes membrane binding sites, depending on the modification they suffer. These proteins usually participate in cell signaling and include examples such as the Src kinase, protein kinase C, or phospholipase C. Amphitropic proteins also include channel-forming toxins such as colicin A and α-hemolysin[52].

After lipids and proteins, sugars (that is, water-soluble carbohydrates) are also a major component of the lipid membrane. Sugars do not have large hydrophobic motifs, so they lie on the surface of the membranes, especially on the outer surface of the plasma membrane; and also have no known enzymatic activity. Therefore, their primary role involves engaging with the cell's external environment, safeguarding membrane proteins from degradation by proteases, contributing to cell identification, recognition, and adhesion, offering immunological characteristics, and functioning as receptors[52].

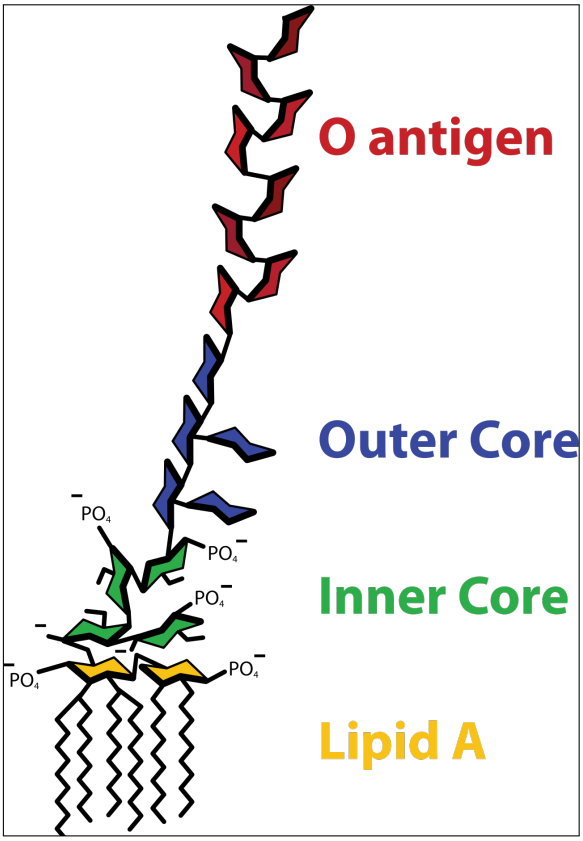

Figure 1.7: Molecular representation of Lipopolysaccharide. Image adapted from Wikimedia Commons[78], under a Creative Commons License.

Sugars can also be found covalently attached to lipids, giving rise to a family of molecules known as glycolipids. In animals, the main glycolipids are sphingolipids, which include cerebrosides, globosides, and gangliosides. Gangliosides contain complex sialic acid oligosaccharides and are significant in the lipid content of the brain and the structure of the neuronal membrane. These glycolipids are essential for cell signaling and serve as receptors for various signaling proteins and bacterial toxins. They are involved in cell recognition and immunology, but are absent outside the animal kingdom[52]. In addition, lipopolysaccharide (LPS, Figure 1.7) is a crucial component of the outer membranes of gram-negative bacteria, where it predominantly forms the outer leaflet[79]. Full-length LPS consists of lipid A, core oligosaccharides, and highly variable O-antigen polysaccharides. The length of LPS varies between different bacterial strains, even within the same species. LPS can participate in multiple noncovalent interactions due to its complex biochemistry; its acyl tails participate in hydrophobic interactions, while its sugars form hydrogen bonds and electrostatic interactions[80]. The interaction between LPS molecules, the crosslinking by divalent cations, and the large mass of the molecule limit the lateral mobility

of LPS, which reduces the permeability of bacterial outer membranes to antimicrobials[81].

1.2.2 The Structures of Lipid Membranes

We have discussed the most relevant building blocks for the formation of lipid membranes. It is now time to introduce the main biologically relevant structures they form and what forces drive their assembly.

1.2.2.1 The Driving Force

Lipid membranes, as many other biochemical structures, are self-assembled entities. As we discussed in Sections 1.2.1.1 and 1.2.1.2, membrane-forming lipid molecules are amphipathic molecules, with hydrophobic and hydrophilic parts. Thus, when lipids are put into water (the basic solvent for life) in sufficient concentration, they will arrange themselves in such a way that some criteria are met such that the energy of the system is minimised.

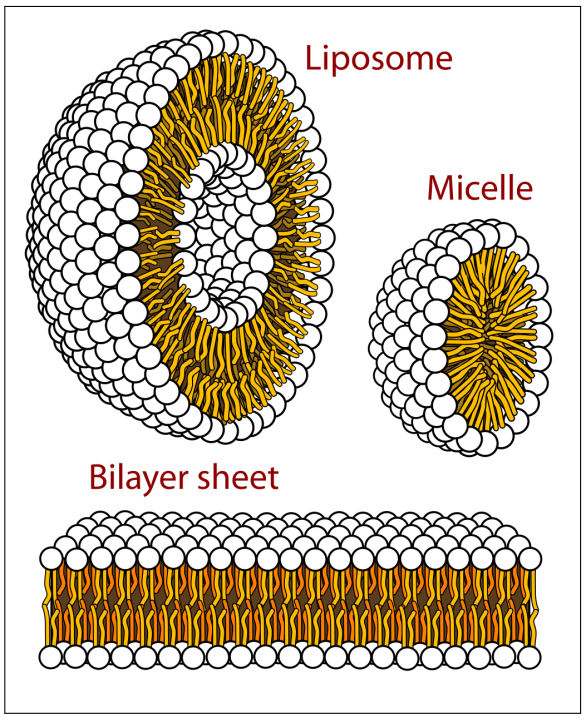

Figure 1.8: Schematic representation of the most typical self-assembled structures of lipids in water. The circles are the hydrophilic heads and the wavy lines are the fatty acyl side chains. Figure taken from Wikimedia Commons[82], released into the public domain.

In fact, one could argue that water, rather than lipids, is responsible for membrane formation due to its notable capability to create Hydrogen bonds with itself. Under normal conditions of pressure and temperature, water is liquid, and each water molecule in the bulk will be able to form a total of four Hydrogen bonds, two as a donor and two as an acceptor. Moreover, the energy of these bonds is greater than the expected kinetic energy of a collision between any two water molecules under the same conditions[52]. This favourable energetics results in the formation of clusters consisting of dozens of water molecules, which together create an interconnected web of Hydrogen bonds.

Thus, when a molecule containing a hydrophobic motif (in our particular case acyl chains) is introduced into water, this network of Hydrogen bonds will be disrupted, as water is not able to establish this kind of interaction with CH groups, having Carbon and Hydrogen practically the same affinity for electrons. Therefore, in the region immediately surrounding the acyl chain, the water molecules will not be able to form the four previously mentioned Hydrogen bonds. This phenomenon, known as the hydrophobic effect[83], is the main driving force behind membrane self-assembly and also responsible for the insolubility of oils in water. Moreover, recalling the amphipathic nature of lipids, it should now be obvious that their acyl chains will bunch together moving away from the body of water, and hence orient the hydrophilic head of the lipids in the direction of the water bulk. These hydrophilic motifs in the lipid molecules are able to form Hydrogen bonds with water, further stabilising the formed structure. The interactions between

the different lipids are also mainly favourable. The polar heads of the lipids can interact with each other through dipole interactions, and the acyl chains can further coalesce through van der Waals forces. The unfavourable forces at play are mainly entropic in nature. The packing of the lipids in the membranes reduces their effectively available degrees of freedom, leading to unfavourably caged tails; and the mere coalescence of several lipids to form a semi-ordered material is also non-favourable in an entropic sense. However, the energetic penalties that these effects entail are clearly outweighed by the favourable interactions mentioned above.

In general, the resulting structures of the self-assembly of lipids in water are bilayers (see Figure 1.8). This disposition renders two layers of acyl chains facing each other, which protects them from the bulk of the water solvent. This solvent in turn interacts with the polar headgroups of the phospholipids. These bilayers can also present different specific topologies, but most commonly form water-enclosing, roughly spherical compartments called vesicles or liposomes. When these are sufficiently large (*i.e.* the size of the vesicle is orders of magnitude larger than the size of a lipid), the bilayers can be understood as patches of locally flat surfaces. Under certain conditions, structures other than bilayers are formed. For example, when working with lipids that have a single acyl chain, micelles can form (see Figure 1.8). In these structures, rather than having a double layer of lipids, a spherical conformation is adopted, pointing the acyl chains inward towards the centre of the micelle, allowing the polar heads to interact with the surrounding water. Monolayers of lipids can also be formed on the interface of water with another medium, such as air, where the polar heads face the bulk of water and the acyl chains point toward the gaseous phase.

1.2.2.2 The Fluid Mosaic and Lipid Raft Models

Now that we have introduced the basic principle under which lipid membranes assemble resulting in their most canonical structure, the lipid bilayer, we can discuss the most significant bilayer models that are still in use nowadays, in the biological context. We are talking about the fluid mosaic model and the lipid raft model. As we mentioned in previous sections, there are many more species other than lipids forming a typical, biologically relevant, lipid membrane. These two models try to capture and explain this complex landscape. However, to get to them, some previous steps had to be taken.

Interestingly, the development of complex lipid membrane models was influenced, at least in part, by research on proteins. At the start of the twentieth century, many measurements of surface tension for different interfaces were being performed. It was known at that time that the surface tension of water could be greatly reduced by including phospholipids, and, when proteins were added, the surface tension was reduced even more. Remarkably, it was reduced to the values of a biological membrane[52]! Of course, the conclusion was that proteins had to play a relevant role in membrane structure, since membranes were known to be semipermeable but, at the time these measurements were made, it was still unknown exactly how this characteristic was achieved[84].

Thus, in 1935 Danielli and Davidson proposed their Pauci-molecular membrane model[85]. They seemed to have reached the conclusion of the lipid membrane independently of Gorter and Grendel, who ten years earlier had already hinted at the existence of a membrane surrounding cells[55], although they had not proposed any specific model. Danielli and Davidson were, then, the first to include proteins in the membrane landscape, suggesting that proteins were loosely attached to the surface of the membranes and that the bilayers had thin, peptide-lined transmembrane channels to explain their semipermeability.

The Pauci-molecular model was further refined in the end of the 1950s and beginning of the 1960s by Robertson with his unit membrane model[86, 87]. Following electron micrography experiments, he measured his 'unit membrane' to be approximately 75 Å thick. He proposed that all membranes shared this characteristic, and this measurement was his sole addition to the Pauci-molecular model, which was agnostic to any membrane dimensions. Furthermore, at the end of the 1960s the lipoprotein membrane models were proposed by Benson and Green[88, 89]. At the time, these two scientists were not supporters of the lipid bilayer disposition proposed by the Pauci-molecular or the unit membrane models. Instead, their models, which were not based on typical (*e.g.* the plasmatic) membranes due to these scientists' main academic focus, proposed that membranes were, in fact, formed by coalescing proteins interlocked by phospholipids acting as anchors between them.

All of the previous descriptions failed to capture several important attributes of lipid membranes; specifically, their dynamic nature as opposed to the static representation given by the first two models, and the inadequacy of the last model to accurately describe the properties of more common membranes, such as the cytoplasmic membrane. These caveats were finally overcome by the fluid mosaic model (Figure 1.9) proposed by Singer and Nicolson in 1971[90]. This model is still widely accepted and used to reason about lipid membranes even today. In Singer and Nicolson's own words, the membrane is 'an oriented, two-dimensional viscous solution of amphipathic proteins (or lipoproteins) and lipids in instantaneous thermodynamic equilibrium'. A natural consequence of the fluid-mosaic taking into account the dynamical nature of lipid membranes, where lipids and proteins are dispersed through the membrane, is the idea of heterogeneous segregated membrane patches called 'domains'[91, 92]. These domains are able to evolve and change with time as the basic molecular units that build a membrane laterally diffuse through it.

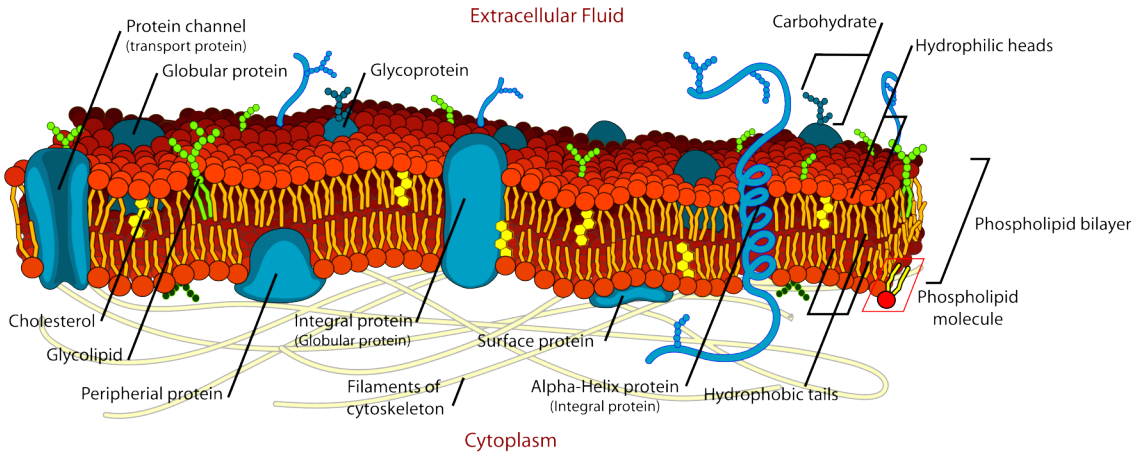

Figure 1.9: Detailed schematic representation of the fluid mosaic model. A lipid bilayer embedded with proteins, sterols, and carbohydrate-derived molecules can be seen. Figure taken from Wikimedia Commons[93], released to the public domain.

Nevertheless, the original fluid mosaic model did not explicitly account for domains, although in the 1970s studies were beginning to report that lipid clusters of the membrane may be common features of biological membranes[52]. The concept of a 'domain' was first introduced by Karnovsky and Klausner in 1982[91], in light of studies that showed that cholesterol had a tendency to aggregate with sphingomielin even in model membranes that contained no

proteins[94, 95]. However, it was not until 1997 when Kai Simmons introduced the concept of 'lipid raft'[96] that a seemingly endless cosmos (the paper has 12126 reported citations in Google Scholar as of July 2024!) of studies on lipid domains was sparked into existence.

William Stillwell defines lipid rafts as 'phase-separated cholesterol and sphingolipid-rich liquid-ordered microdomains'[52], while suggesting that perhaps the exorbitant interest in lipid rafts could be due, at least partly, to their very flashy name. In any case, lipid rafts are believed to exist in the liquid-ordered (l_o) thermodynamic phase, an intermediate state between the liquid-disordered (l_d) and gel phases, typical of lipid membranes. This l_o phase, characteristic of lipid rafts, would be produced by an increased level of saturation in acyl chains, as they are enriched in sphingomyelin compared to non-raft domains, which would favour tighter packing of lipid tails. It is believed that these lipid rafts are further held together by cholesterol, as its concentration is twice as high as in non-raft regions. Moreover, lipid rafts would commonly be packed with specific proteins involved in cellular signaling events[52]. The typical size for naturally occurring rafts is believed to be rather small, on the order of 10-200 nm[97].

It should also be noted that despite the great interest in the study of lipid rafts, there are also doubts about their actual existence[98, 99]. The main argument against their existence is their small size, well below the diffraction limit of a light microscope, so direct evidence is scarce[52, 99]. Additionally, several methods employed to obtain indirect evidence of lipid rafts have been criticized for generating results considered 'artificial', and some of the most sophisticated techniques, which should theoretically provide direct proof, have produced negative outcomes[98].

Furthermore, despite the compelling nature of lipid rafts, other kinds of 'microdomains' may exist on a functional lipid membrane. In addition, even lipid rafts, should their existence be definitely proven to be true, may also be composed of other subdomains[52]. Two types of these non-raft membrane domains have been suggested: ceramide-rich platforms[101] and microdomains rich in polyunsaturated fatty acids (PUFA)[102]. On the side of ceramides, these significantly impact membrane structure and functionality at relatively low concentrations and, akin to lipid rafts, produce l_o thermodynamic phases. However, they differ in that they are enriched in C-24 fatty acids and have much lower cholesterol levels. These platforms are believed to be formed by the aggregation of distinct stress-induced signaling proteins associated with ceramides[52].

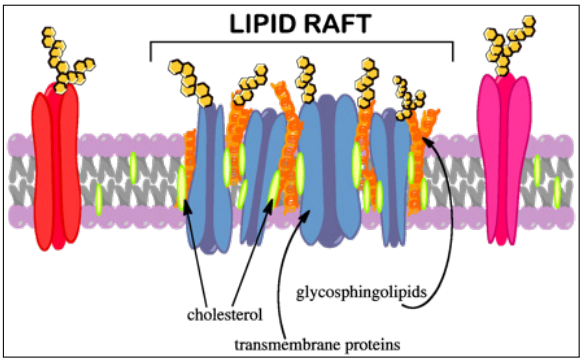

Figure 1.10: Schematic representation of the lipid raft model. Figure taken from Wikimedia Commons[100], released into the public domain.

On the other end of the spectrum of properties for lipid rafts lie PUFA-rich domains. These molecules, such as docosahexaenoic acid, are highly flexible and rapidly isomerise between their different *cis* and *trans* isomers, making their packing very inefficient and leading to disordered membrane states[102]. Moreover, docosahexanoic acid is known to have a low affinity for cholesterol, making its presence in the raft domains highly unlikely[103]. Thus, these PUFA rich domains would be 'the antithesis of lipid rafts and so would support non-raft cellular functions', in William Stillwell's own words[52].

1.2.3 The Functions of Lipid Membranes

It should now be evident that, given of the complexity of lipid membranes, their role will not be limited to just that of a wall, or barrier, for any given cell. In fact, we have already discussed that some non-lipid molecules insert themselves in the lipid bilayer, so acting as anchoring points is already an evident extra role for them. Moreover, we will also see that, depending on the type of cell one is observing, the composition of the membrane and thus its purpose will also be different.

1.2.3.1 More than Simple Barriers

When we typically think of a lipid membrane we picture a barrier that envelops a cell, keeping inside what must not come out and outside that that must not come in. And although this is true, this view falls very short of reality. Indeed, lipid membranes act as barriers for cells, but these structures can also be found **compartmentalising** organelles[104] (the 'organs' of a cell). In fact, several organelles are known to have been incorporated into eukaryotic cells through symbiogeneses, a process in which formerly free-living prokaryotes were absorbed and integrated inside other simple organisms, occurring somewhere down the evolutionary tree. Some of such organelles are the famous mitochondrion[105], the chloroplast[106], or the recently discovered nitroplast[107]. Thus, as these new organelles were integrated into higher-order beings, they carried with themselves their own membranes, with their characteristics and particularities that can still be seen today.

In addition to partitioning functions, membranes have a say in many other vital cellular processes. We have already discussed how proteins associate with the lipid bilayer in Section 1.2.1.3. As a matter of fact, the field of **lipid-protein interaction** is very prolific and it is becoming increasingly clear that bilayers play a very important role in the regulation of the many tasks performed by proteins[108]. Furthermore, proteins are known to be assembled in the endoplasmic reticulum (which is a lipid membrane in and of itself), and theories that pose lipids as essential chaperones for proper protein folding have been gaining traction as of late[109].

It is only reasonable to think, then, that due to the large number of proteins that are associated in some way with the lipid bilayer, and being one of the functions of proteins the transduction of signals in cells; that lipid membranes will also be to some extent related to **signal modulation**. In fact, we would be right to think so. The tendency of lipids to form domains within a membrane, as discussed in Section 1.2.2.2, can have the effect of bringing proteins togeter, or pulling them apart, which in its turn has the effect of controlling the signal transduction carried by said proteins[110]. In addition, certain kinase proteins, essential molecular components responsible for phosphorylating various molecules and playing a critical role in the transmission of cellular signals, are known to exert their influence directly on lipid molecules. Thus, membranes are believed to be crucial for their effectiveness[111]. Additionally, the paradigmatic biological mechanism for the transmission of information, the synapse, is mediated by the release of chemicals in the neuronal interstice, a process that occurs in the surroundings of the cell's lipid membrane and is facilitated by endosomes[112].

Membranes are involved in not only regulating the activity of proteins related to signal transduction inside a cell, but also in that of transport proteins, which are in charge of the exchange of substances between cells (or organelles) and their immediate environment. As some lipids are specifically bound to transport proteins, they can modulate their function, from the bulk of the bilayer[113]. Even when not modulating protein activity, the lipid bilayer itself plays a role in the **transport of matter**, as it is known to be a semi-permeable barrier, capable of selectively

differentiating between molecules that are able to passively diffuse through it and those that are not[114].

The shape of a cell is ultimately determined by the shape of its surrounding membrane, especially in the absence of other structures such as cell walls found in plants and certain bacteria. This shape is known to be related to many aspects of normal biological function, such as tissue development, wound healing, cell division, and **motility**, that is, the ability of a cell to move and change shape. This process is, in turn, mediated by the assembly and disassembly of actin filaments[115]. This dynamic process occurs in close proximity to the plasma membrane, as actin assembly factors are membrane-bound. Although the lipid bilayer has traditionally been considered just a mere scaffold upon which the actin filaments grew and disassembled, more recent findings suggest that the dynamics of cytoskeleton rearrangement is closely related to the mechanics of the cell membrane[116].

These have been but just a few mentions of all the multifaceted roles lipid membranes can play within a cell, despite traditionally being just interpreted as barriers. From organelle compartmentalisation to cell motility, this has not been an exhaustive list of membrane functions, as they are also known to be involved in, for example, energy storage[117] or metabolism regulation[118], among a myriad of other processes, some of which may even be yet unknown. This section serves to point out to the reader the versatility and importance of these structures, which, as innocent as they may seem at first, are vital for life.

1.2.3.2 No Two Equal Membranes

We have given a fast review of some of the multiple functions a lipid bilayer can have within the inner workings of a cell. It is now sensible to question whether membranes that play different functions, be it because they belong to different cell types or because they are in different locations within the same cell, will look different too at a molecular level. The short answer to this question is a rotund YES.

The main constituents of a lipid membrane, or at least the most relevant, are, of course, lipids. Hence, the lipid composition of a membrane is known to change depending on several factors. Within the same organism, the lipid profile found in membranes will be different depending on the type of cell (for example, a fibroblast *vs.* a red blood cell), will also depend on the specific organelle of a given cell (the plasma membrane *vs.* the mitochondria membranes) and even the composition of each leaflet for the same bilayer will not be the same[119].

The differences go beyond those of different types of cells within the same organism. We have already hinted at disparities between organisms when we talked about how lipopolysaccharide was an integral part of the outer cell membrane of gram-negative bacteria, in Section 1.2.1.3. Indeed, different organisms can have radically different membranes. For instance, a typical mammalian cell has its plasma membrane enriched with PC-type lipids[119], while a typical gram-negative outer membrane will mainly display PE and PG-type phospholipids[120]. Fungal lipid membranes are mainly composed of PC and PE-type lipids, but also have a non-negligible proportion of PS and PI-type phospholipids[121]. Interestingly, some fungal strains can modify the PS:PI ratio in response to external stimuli, which shows that the lipid composition of a given membrane can also be actively altered by an organism depending on its environment[122].

Other factors can also modulate the composition of the lipid membranes that an organism expresses in its cells, such as, for example, disease. A clear example is how cancerous cells in mammals lose their compositional asymmetry between the leaflets of the plasma membrane. A healthy mammal cell, although enriched in PC-type phospholipids, also has a relevant amount

of PS-type lipids, but these face the cytoplasmic side of the cell. However, when a cancerous process occurs, this asymmetry is lost and the PS lipids will also face the outside of the cell[123], which confers it with an outward facing negatively charged environment, since PS is anionic. In addition, pathogenic diseases are also known to have an effect on the lipid membranes of their hosts. In the life cycle of a typical virus, the lipid membrane of the infected host is known to play a role in several relevant steps, such as the attachment and fusion of viral particles, the synthesis of the molecular machinery needed to produce more viruses, and finally the release of new virions into the media to continue the cycle of infection[124]. All of this interplay between the virus life cycle and the inner workings of the infected cell is known to leave a mark on its lipid bilayers, not just in the plasma membrane but profoundly affecting organelles like the endoplasmic reticulum[125].

Even non-disease factors, at least not in the traditional sense, can have an impact on the composition of a lipid membrane. The age of an organism, for example, is known to modify the lipid content of cellular membranes[126]. Most of the research efforts on this specific topic have been done for the loss of neuronal function with age and the interplay between lipid composition and neuronal plasticity[127]. Lipid peroxidation has also been found to be associated with age and to have an effect on the mechanical rigidity of neurone cells[128]. Interestingly, these modifications in the lipid composition of the cellular membrane of neurones have been linked to changes in the gut microbiota[129] (*i.e.* microorganisms living in a symbiosis with ourselves in our intestines), which have also been linked to the correct development of the brain in infants[130] as well as, in general, to various cognitive processes[131].

This section of the Introduction chapter does not aim to be an all-encompassing review of every different factor that can affect the lipid composition of a cellular membrane, either. As in the previous section discussing membrane function, we aim to give a general outlook to the reader, showing how these biological structures are not static, but dynamical entities surrounded by nuances and complexities.

1.2.3.3 Membranes as Therapeutic Targets

We have now discussed some of the most relevant roles a lipid membrane can take, as well as some factors that change their lipid profile. Thus, the picture is as follows: different membranes in different places doing different things. It then stands to reason that because of these disparities, one could tell membranes apart and wonder if, because of differences in membrane function, one could target a specific membrane, with a specific composition and playing a specific function.

In fact, the use of lipid membranes as a therapeutic target has gained traction in the last couple of decades, in which, particularly, the group of Professor Pablo Escribá has been very prolific[132, 133]. Conventionally, drugs have been designed to affect the proteic or genetic machinery of an organism, since disease is typically understood as malfunctions in these systems. However, even if perhaps inadvertently, humans have been using drugs that alter the properties of lipid membranes, specifically as anaesthetics[89], for quite a long time, among which the intoxicating effects of alcohol can be included[133].

Naturally occurring antimicrobial peptides (AMPs) are also particularly relevant due to their interaction with lipid membranes, which is a primary mechanism of their antimicrobial activity. AMPs typically target the lipid bilayer of microbial cell membranes, exploiting the differences between microbial and host cell membranes[134]. These peptides can bind to and disrupt microbial membranes through various mechanisms, such as forming transient or permanent pores or

causing membrane thinning. This disruption can lead to cell lysis and death by compromising the structural integrity of the microbial cell membrane, allowing leakage of cellular contents[135, 136]. The effect of AMPs is rapidly felt in their target pathogens, which often occurs within seconds of contact with the microbial cell membrane[136, 137]. Their ability to affect lipid membranes differentiates them from traditional antibiotics, which often target specific intracellular pathways, reducing the likelihood of resistance development[134].

On the side of rational design, 2-hydroxyoleic acid was the first molecule created with the intention of modulating the lipid composition and structure of the membrane[133]. From there, a new field of therapies has been created, coined under the term of Membrane Lipid Therapy (MLT). We can distinguish five types of MLT[133], depending on the specific mode of action of the drug: Type 1 acts directly on the lipid membranes, type 2 acts through indirect regulation of sphingomyelin syntase 1[138], type 3 acts through lipid interaction with DNA transcription factors, type 4 acts by changing membrane microdomains, altering protein-protein interactions of membrane proteins; and type 5 regulates enzymes that catalyse the addition of lipid anchors to membrane proteins[139].

Thus, MLT has found its place in many fields of the treatment of disease. For example, the aforementioned 2-hydroxyoleic acid has applications in **oncology**. It is a type 2 drug, according to the previous definition, and has the effect of modulating the lipid composition of the cancer membrane, which causes the migration of an oncogenic protein from the membrane to the cytoplasm, disrupting signaling pathways, and producing apoptosis[140, 141]. In addition, 2-hydroxylinoleic acid (a PUFA lipid) is being tested as an anticancer drug. It is a type 4 drug that binds to the membrane and disrupts the l_o thermodynamic phase (see Section 1.2.2.2) that is theorised to exist within lipid rafts[133]. This causes a desregulation of protein function specifically in cancer cells and leads to cell autophagy[142].

MLT has applications not only in the treatment of cancerous processes, but also in **neurodegenerative disorders**, as these are linked to lipid alterations in the central nervous system[143, 144]. Specifically, Alzheimer's disease, which is known to be at least partially produced by the coalescing of amyloid microfibrils in the brain, is also related to cholesterol homeostasis. In fact, cholesterol and other raft-forming lipids can revert insoluble amyloid peptide fibrils back to their toxic soluble oligomeric forms[145]. In addition, PUFAs and PE-type lipids have also been found to appear at significantly lower levels for patients with Alzheimer[146–148]. This deregulation of normal lipid levels causes relevant changes in the corresponding lipid membranes[149, 150]. Thus, treatment with 2-hydroxy-docohexanoic acid has been found to restore PE and PUFA levels in mice expressing human Alzheimer's disease genes, as well as to reinstate their cognitive abilities[151, 152]. Other ailments such as Parkinson's disease, sclerosis, or even spinal chord injuries could also potentially benefit from MLT[133].

Inflammatory processes are also well known to be mediated by molecules derived from PUFAs[153], which can modify the lipid membrane composition and the activity of several transcription factors. Thus, analogues of these molecules could be used to treat inflammation and, in fact, some specific examples such as 2-hydroxy arachidonic acid has been proven effective at doing so[154]. Some native PUFAs have also been suggested to be useful at treating patients with chronic inflammation, following *in vitro* studies[155]. Furthermore, it has been found that a balanced fatty acid diet reduces inflammatory effects, when compared with a high carbohydrate intake diet[156, 157].

Following on the intake of lipids through the diet, it is known that they can modulate the composition of the cellular membrane, and this can then have an effect on **cardiovascular**

health[158, 159]. For example, high cholesterol and low levels of phospholipids are associated with hypertension and altered G protein activity[159]. Cholesterol, when paired with sphingolipids, plays an important structural role, due to its ability to create microdomains in cells, as introduced in Section 1.2.1.2. The modification of the biophysical properties of lipid membranes induced by cholesterol-driven domains is believed to be one of the main factors for atherosclerosis and elevated blood pressure[160]. In contrast, the intake of 2-hydroxy oleic acid or diets rich in linoleic acid (an essential constituent of olive oil) are known to reduce blood pressure[161, 162]. The effectiveness of these molecules is believed to be related to their ability to change the lipid composition of cellular membranes and thus control the activity of membrane-bound signaling proteins[163, 164].

Metabolic diseases are also known to be affected by the lipidic profile of their patients. For example obesity, having reached an epidemic level in industrialized countries[165, 166], is linked to dietary fats, with cis oleic acid being associated with a lower body mass index[167]. Olive oil, which is rich in oleic acid, has been found to reduce body weight in rats, while its *trans* isomer, elaidic acid, does not have this effect[168, 169]. Within this context, analogues of oleic acid have been shown to aid in weight reduction through two well-established mechanisms: influencing the mitochondrial inner membrane thus altering the metabolic cycle to produce heat rather than ATP; and leading to a reduced food intake[168]. Rising diabetes rates parallel those of obesity and are linked to dietary fats too, with higher saturated-to-*cis*-unsaturated fatty acid ratios observed in type 2 diabetes patients[170–172]. A high intake of oleic acid improves glycemic status and reduces saturated fatty acid levels[173], plus treatments containing *cis*-unsaturated fatty acids, and derivatives, may also help against diabetes[173, 174].

We have now provided a general review on the clinical importance of lipid membranes contextualised in a series of families of diseases. Specifically, this section focused on Membrane Lipid Therapy, and we refer the reader to the outstanding work of Professor Escribá[132, 133, 139, 159] and collaborators for an in-depth discussion on this topic.

1.2.3.4 Beyond Membrane Lipid Therapy.

The reader may notice, however, that all of the therapies discussed in the previous section are mostly biochemical in nature, seeking to influence metabolic pathways in order to achieve a desired effect. One can argue that MLT of type 1 and type 3 also have a mechanical basis, as they rely on modulating the biophysical properties of the lipid membranes. Despite this, the cascading effects that are sought with them are still, in essence, biochemical. Therefore, in this Section, we will look into mechanotherapy applied to lipid membranes, as one of the main topics of this Thesis will revolve around it.

It is now understood that some cells have the ability to sense mechanical forces due to, for example, the ability of muscle precursors to respond to mechanical stretching and differentiate into actual muscular tissue[175, 176]; or endothelial cells to change gene expression patterns due to shear forces applied by blood flow in the arteries[177]. One of the mechanisms proposed to explain this is the direct morphological changes in the lipid bilayers of these cells, caused by the applied mechanical forces, which in turn would produce a conformational transformation in membrane-bound proteins[178, 179], and generate a signal that the organism can then recognise[180]. This explanation is the currently accepted answer to, for example, how sound is perceived in the cochlea[181] or the mechanism behind the opening and closing mechano-gated pores[182].

Thus, in light of the fact that cells can react to mechanical stimuli, mechanotherapy has

appeared as an alternative to conventional drug-driven therapies[183–185]. Mechanotherapy already comes in several different flavours, from negative pressures applied to wounds that accelerate the healing process[186], through subcutaneous tissue expanders that promote angiogenesis[187] to the use of extracorporeal shockwaves[188]. All of these techniques have in common the application of an external mechanical deformation to a tissue, which then reacts to it, producing the desired effects.

Of special interest for this Thesis is the use of external shockwaves as mechanotherapy. These mechanical stimuli can be either produced by pulsed electromagnetic waves or by pressure waves (*i.e.*, sound)[184], and play a putative role in modulation of natural inflammatory pathways, upregulation of growth factors and protein synthesis[189–191]. In particular, shockwave therapy has already found use in the treatment of sports injuries such as plantar fasciitis[192], and in the regeneration of soft and hard tissues[193, 194].

However, the exact molecular mechanisms behind the effect of shockwave therapies are not yet completely understood[184]. The mode of action is implied to occur through a 'wear-and-tear' mechanism in which microdamage is induced in the tissue. The body then regenerates this damage, mimicking the effects of physical activity and exercise[195], but a precise molecular picture is still elusive in this model, for which we have to turn to the study of sonoporation[196].

Although sonoporation has not been studied in direct relation to the therapies mentioned above that use shockwaves, it is the closest molecular model that links mechanotherapy, lipid membranes, and sound waves. Sonoporation, as the name says, produces pores in the lipid membrane through pressure waves in the ultrasound range[197, 198]. Most of the time, the effects of the ultrasound are enhanced by including gas-filled microbubbles, sometimes stabilised by a lipid, protein, or polymer shell; which, when interacting with the ultrasound wave, can undergo stable or inertial cavitation[196]. In the case of stable cavitation, the microbubbles do not collapse but create a liquid flow around them, a so-called 'micro stream', which induces shear stresses in nearby lipid membranes[199, 200] that can potentially lead to loss of membrane integrity. On the side of inertial cavitation, which occurs at higher ultrasound intensities[196], the microbubbles collapse and can cause a shockwave accompanied by a hypersonic jet of fluid in the direction of collapse, capable of perforating the membranes of living cells[201, 202]. In recent years, sonoporation techniques that do not require microbubble injection have been developed, as bubble-mediated techniques are more prone to produce unwanted side effects such as irreversible cell damage[203]. Due to its ability to effectively poke holes into cells, sonoporation is primarily researched as a cargo delivery technique[204, 205], with potential applications in cancer treatment[206].

Beyond sonoporation, ultrasounds have also found applications in, for example, stimulation of the central and peripheral nervous systems[207, 208] whose effects are believed to be mediated by modulating the activity of mechanosensitive transmembrane ion chanel proteins[209, 210]. Of special interest for this work, however, is the use of High Intensity Focused Ultrasounds (HIFU)[211, 212]. This particular technique is capable of focussing an ultrasound beam, in the range of the MHz, on a localised zone in a tissue[213]. HIFU already has existing applications in the ablation of both malignant[214–216] and benign[217, 218] tumours; or in the treatment of other disorders such as essential tremor[219] or Parkinson's disease[220]. The basic principles believed to be behind the effect of HIFU are, primarily, energy deposition on the irradiated tissue in the form of heat and mechanical effects due to the oscillating pressure wave[213]. It is believed that, if the ultrasound intensity is high enough, HIFU can induce cavitation without the need for microbubble injection[221].

With this, we have given a review of the current state-of-the-art in non-drug-derived therapies that use lipid membranes as their targets or in which the structure and functions of membranes are believed to be involved. We also finalise the section of the Introduction Chapter discussing the relevance of lipid membranes. We aimed to provide a comprehensive discussion of the basic aspects surrounding these fundamental structures for life, and hopefully convince the reader of the relevance of basic research on them.

1.3 Molecular Dynamics and Lipid Membranes

The work carried in this thesis was, essentially, computational in its approach to understand several aspects of lipid membranes. In particular, we have used Molecular Dynamics (MD, more on this in Section 3.1), a family of techniques that are widely used in biophysical research, from which lipid membranes are not unfamiliar.

Thus, we are now tasked with giving an introductory discussion on how MD has been used to investigate lipid membranes, what the most relevant advances have been made in doing so, and what the current state of the art is. With this in mind, our objective is to provide a comprehensive review of the previous work that served as the foundation for this thesis.

1.3.1 A General View of Molecular Dynamics

MD simulations, in essence, predict how every atom in a given molecular system will move over time, based on a general model of the physics governing interatomic interactions[222]. This technique is already several decades old, with the first MD simulation, which calculated the phase transitions of a simple gas model, dating back to the late 1950s[223]; and the first MD simulation of a protein being done in the 1970s[224]. Today, MD is routinely used to answer many biophysical questions.

MD simulations have become much more present and relevant in the last few decades, frequently appearing in structural biology papers[225]. This is due to their ability to probe spatio-temporal resolutions that are yet unattainable with conventional wet-lab protocols. Although nowadays there is no shortage of chystalographic data of various types of biomolecule and, more recently, ML-assisted tools to predict their structure have appeared[226, 227]; the determination of the full 3D conformation of some of them, especially in their native biological state, is still not a trivial task. The available chrystalographic and / or predicted data can then serve as a starting point for MD, which can provide a more complete dynamical picture of the systems[225].

Moreover, with the advent of the Information Technology (IT) era and the rapid growth in numbers and power of personal computing, MD has become much more potent and accessible. MD is a field with many free and open source software alternatives[228–230], which are very well documented so that even nonexperts can get introduced to them. The appearance of new hardware technologies, particularly GPUs, is making simulations more accessible to run locally, rather than depending on the availability of supercomputing centres[231].

MD comes in many flavours and can be used to answer different types of question (Figure 1.11). Maybe the most straightforward application is to probe the mobility of a biomolecular system around thermal equilibrium, investigating the flexibility of its different regions. Taking as a starting point, for example, the averaged structure of a biomolecule provided by crystalographic determination, a simulation can then be conducted to evaluate the extent of the movement of the system, and to identify the various types of structural fluctuations it experiences while at the same time revealing the dynamics of the solvent or ions around it[232–234]. Thus, these aforementioned starting models can be refined using MD simulation. X-ray structures are commonly

polished using a simulated annealing protocol that fits the experimental data while maintaining a reasonably realistic structure[235], which has been shown to be a better alternative than the least-squares fitting method. MD is also routinely used to build atomistic structures from 3D density maps produced by cryo-EM[236, 237], or to recover the conformational ensembles of molecules from NMR data[238].

Another of the most widespread applications of MD simulation is probing how a biomolecular system responds to some perturbation. This includes, but is not limited to, testing how the conformation of a protein changes when a ligand is removed from its structure[239, 240], predicting the effects of mutations[241], phosphorylation[242] or protonation states[243] in a protein sequence; or directly applying forces to simulate mechanical strain[244]. With this, MD strives to observe biomolecular processes in action, allowing us to answer questions about the structural basis of events that are difficult to address experimentally.

However, sometimes a single MD simulation at equilibrium is not enough to capture the relevant events that one may be interested in. This can happen because the timescale at which the events occur is much longer than what is attainable in a conventional simulation; or because the potential energy surface governing the event has several local minima, and thus the system becomes kinetically trapped in a potential well. Several variations of MD have been proposed to solve such cases and fall under the category of enhanced sampling techniques[245], such as umbrella sampling[246], metadynamics[247], on-the-fly probability enhanced sampling[248, 249], parallel tempering[250] or deep learning-based sampling methods[251], to name a few.

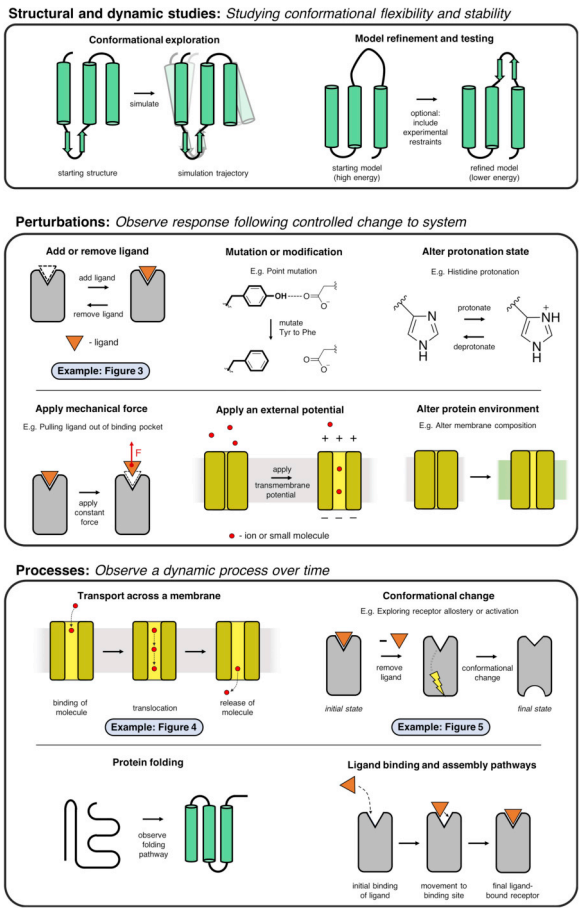

Figure 1.11: Some of the applications of Molecular Dynamics Simulations. Image reproduced from the work of Dror *et al*.[225], Licence L1, copyright by Elsevier.

1.3.2 Computational Modelling of Lipid Membranes

We have given a general outlook on MD and its uses, and a more detailed explanation of its algorithmic pipeline can be consulted in the Methods Chapter, Section 3.1. In the Section above, we mainly cited studies involving proteins in one way or another, however, modelling lipid membranes is also one of the fundamental tasks performed via MD[252, 253]. The first MD simulations of lipids or surfactants date back to the 1980s[254, 255], not many years after the first MD simulation of a protein[224]. From these first studies, very modest in size, complexity, and time scales, where an average simulation consisted of a bilayer containing approximately 120 lipids and lasted a few hundred picoseconds; a vast field in its own right has emerged, with

typical studies using several (relatively) large simulations of complex systems spanning several microseconds[252].

1.3.2.1 Basics of Simulation of Membrane Models

The scientific literature is, quite literally, plagued by thousands of studies on lipid membranes, many of which simulate basic systems with a single phospholipid type forming the lipid bilayer[256]. Despite their simplicity, these early simulations provided crucial foundational insights into the structure and dynamics of lipid membranes. Key research focused on the orientation of lipid headgroups and their interactions with the surrounding water, shedding light on the dynamics of lipid molecules[257, 258]. A significant breakthrough by Lindahl and Endholm was the first estimate of relaxation times for undulatory and peristaltic modes within a large (according to those day standards) lipid bilayer[259], which advanced the study of the mechanical properties of lipid membranes. The simulations at that time also aimed to calculate mechanical parameters such as the area compressibility and the bending modulus of lipid bilayers[260]. Efforts were made to align simulation results with experimental data, for example, using lipid movement correlation functions to replicate NMR NOESY spectra[261] and calculating order parameters for lipid molecules that could be directly compared with NMR data[262, 263].

Although those early simulations may seem simple from our point of view, they laid the groundwork for many current studies. Order parameters remain a key measure in MD simulations and are considered the gold standard for comparison with experimental results[264, 265], so much so that this metric is crucial for the largest collaborative project on lipid membranes to date, the NMRLipids initiative[266, 267]; and for the development of new forcefields[268, 269]. Furthermore, the calculation of mechanical properties of lipid membranes continues to be an active area of research, with studies that examine theoretical aspects[270], solid phases of lipid bilayers[271], and free energies of membrane deformation[272].

1.3.2.2 Simulation of Complex Membrane Models

Nowadays, many of the efforts put into the molecular simulation of lipid membranes are focused in obtaining a realistic model that captures the many relevant interactions happening for them. As we have mentioned in this Introduction Chapter, in Section 1.2.2, a typical cellular membrane is formed by literally thousands of different types of phospholipid, countless different proteins, and many other biomolecular entities. Moreover, membranes do not exist isolated from their context; they are highly dynamic structures that can be curved and deformed, interacting with components of their surrounding medium such as the cytoskeleton, neighbouring organelles, or other cells.

Essential to the concept of complexity and realism is testing the existence and behaviour of nanodomains (recall the sometimes disputed concept of lipid rafts). Low resolution Coarse-Grained (CG, refer to Methods Chapter, Section 3.1.2 for an explanation) have proved very useful to probe this, capturing the spontaneous formation of l_o and l_d (refer to Section 1.2.2.2)domains[273]. After this pioneering study, many others followed, constructing ternary phase diagrams[274], studying the influence of temperature[275], or mechanical stresses[276] on the existence of lipid domains. The spatial sorting of proteins between the different lipid domains has also been studied by MD simulations, revealing that the inclusion of peptides in the membrane disrupts the tight packing of lipids in the l_o domain and thus provides an enthalpic contribution for their migration to the l_d domain[277]. Furthermore, lipid anchors in proteins were found to provide a counter force to this effect[278].

In addition to this, the interaction between proteins and lipid membranes has also been extensively studied through MD simulations. The determination of binding sites for lipids within a protein and the obtaining of a quantitative descriptor of such interaction is a routine task today. This is best demonstrated by the many MD studies that confirm the existence of experimentally deduced binding pockets, as is the case for the recognition of singular sphingomyelin molecules by a protein transmembrane domain[279], or through various works on the binding pockets for cholesterol in G protein-coupled receptors (GPCRs)[280–282]. MD has not only been used to confirm anticipated experimetally binding sites, but also to predict new ones[283–285], or to study nonspecific lipid binding[286, 287] that were found to induce long-range complex perturbation patterns in the lipid membrane[288].

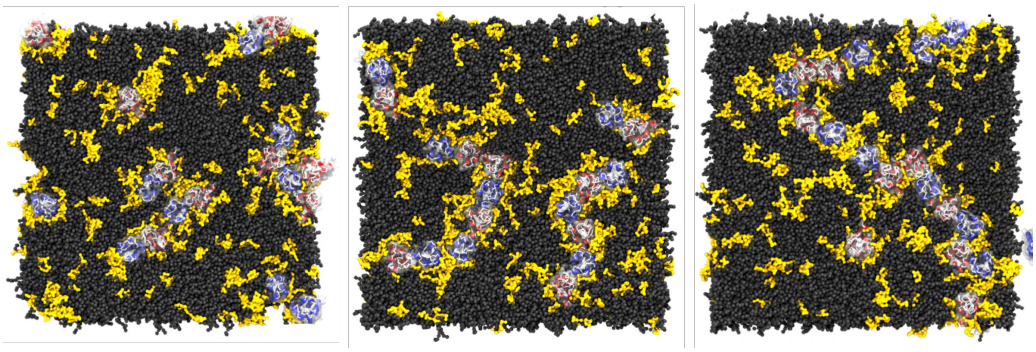

Figure 1.12: Snapshots showing protein (semi-transparent surfaces) clustering mediated by omega-3 lipids (highlighted in yellow) in a cellular membrane. Figure adapted from the work of Guixà-González and coworkers[289], distributed under a Creative Commons 4.0 license.

The oligomerisation of proteins mediated by the lipid membrane (Figure 1.12) is also a hot topic researched using MD simulations. For example, the oligomerisation of GPCRs has been followed by free MD simulations, capturing their self-assembly process[290–292], which has been found to be mediated and modulated by the lipids of the membrane in which they are embedded. However, such self-assembly simulations are well known to suffer from poor sampling issues, especially when the molecular systems represented therein are of moderate to high complexity. To address this, biasing methods such as umbrella sampling, metadynamics, and others can be employed to predict binding interfaces and gain understanding of the thermodynamics of the process. Nevertheless, these approaches still present challenges, often necessitating lengthy simulation periods and the implementation of CG models to ensure convergence[252]. In any case, such methods have been used to study the dimerisation of WALP peptides in a membrane[293], concluding that the helix–to-helix peptide association is enthalpically favourable in all cases, while the entropic contribution appears favourable only in the presence of significant positive hydrophobic mismatch. Other examples include simulations of glycophorin A dimers embedded in different membrane environments[294], where oligomerisation was driven mainly by peptide tilt or perturbations in the local membrane thickness.

The morphology of the membrane and, in particular, its curvature (whether spontaneous or induced) is also a relevant factor to capture when simulating a realistic cellular membrane. This magnitude is known to be involved in membrane remodelling processes, such as fusion and fission, and the shaping of internal cellular compartments[295–297]. Curvature can be induced by asymmetries in leaflets that form a bilayer, the inclusion of non-lamellar forming lipids such as

DOPE, or the action of specialised proteins[252]. Some studies testing the influence of proteins on membrane curvature include the investigation of membrane bending forces on the Denge virus envelope[298], showing that a heterotetramer protein complex serves as the molecular machinery for the deformation of the viral membrane, being able to migrate lipid molecules between leaflets of the bilayer and hence imposing a curvature stress. Other works studied the influence of short antimicrobial peptides on membrane morphology[299], showing that they can induce positive curvature in the bilayer, which is sensitive to molecular interactions[300]. Furthermore, several studies have been performed on the effect of the lipid distribution and composition on membrane curvature. For example, the addition of gangliosides was found to be able to curve the membranes[301] and, conversely, membrane curvature has been found to induce lipid sorting[276, 302, 303].

Membrane fusion and fission, which are processes that involve a significant amount of curvature, have also been investigated with MD simulation. Protein-free fusion pathways are fairly well understood and established[304], indicating that the repertoire of topologies available for lipid aggregates in aqueous solvent is limited, as they appear to depend only on the hydrophobic-hydrophilic volume ratio and the thickness of the hydrophobic core of the systems. Current efforts in the field are mainly focused on the study of the influence of molecular migration during fusion events[305], the energetics of transition states in these processes[306, 307], or the influence that other molecules, such as peptides[308], have.

1.3.2.3 Comparative Studies of Forcefields for Lipid Membranes

As can be deduced by the previous two sections, the effective simulation of lipid membranes requires precise modelling of molecular interactions, making the choice of forcefield (refer to Section 3.1.2 in the Methods chapter) critical for the accuracy of MD simulations. CHARMM (Chemistry at HARvard Macromolecular Mechanics) is a popular option due to its availability of parameters for various lipids and detailed modelling of lipid-protein interactions[230]. The GAFFlipid (General AMBER Force Field) was specifically created to model phospholipid membranes at the atomistic level, refining previous versions[309, 310]. Similarly, the newer Lipid14 with subsequent Lipid21 forcefields (also developed for use with AMBER[268, 311]), and Slipids[269] focused primarily on the atomistic parameterisation of lipid molecules.

The OPLS (Optimised Potentials for Liquid Simulations) forcefield, initially proposed in 1988 for cyclic peptides[312], has been updated to include representations of lipids and is frequently used in mixed lipid systems to capture thermodynamic properties such as membrane compressibility[313, 314]. The GROMOS (GROningen MOlecular Simulation) forcefields[315–318] are known for their efficiency in simulating complex membrane systems, focussing on phase transitions and structural properties[314]. A United Atoms (UA, refer to Section 3.1.3) variant, GROMOS-CKP[319], offers faster simulations at the expense of spatial resolution.

CG models such as the ELBA (ELectrostatics BAsed) forcefield[320] and the Martini family of forcefields[321–323] also play a very significant role in simulations of lipid membranes. Their lower resolution allows the study of slower dynamic processes, such as self-assembly and lipid reorganization[314]. The Martini2 force field includes a Dry-Martini variant[324], which treats the solvent implicitly, greatly reducing computational costs; and the Polarisable Martini model[325], that tries to better capture electronic polarisability effects while still retaining the benefits of a low spatial resolution.

Thus, as the complexity and diversity of lipid membrane simulations have grown, so has the

importance of understanding the strengths and limitations of the different available forcefields. Several comparative studies have been conducted to evaluate the performance of various forcefields in reproducing experimental observations and capturing essential membrane properties. Here we give a general and non-exhaustive overview of some of the relevant works on this topic conducted until today.

Piggot and colleagues performed a comparison of five freely available forcefields commonly used for PC-type membrane simulations: GROMOS 43A1-S3, GROMOS 53A6$_L$, Berger, GROMOS-CKP, and CHARMM36[319]. Their study revealed that, while all force fields reasonably reproduced many experimental properties, there were significant variations in their predictions. For example, CHARMM36 and Berger showed better agreement with the experimental deuterium order parameters, while they produced slightly higher diffusion coefficients than those determined by experiments, where the UA forcefields tested performed better[319].

A study by Paloncýová et al. compared the performance of five forcefields (Berger, Slipids, CHARMM36, GAFFlipid, and GROMOS 43A1-S3) and the implicit COSMOmic method to predict the partition coefficients of 11 molecules into DMPC membranes[326]. Their results showed that Slipids performed best, closely followed by COSMOmic and CHARMM36. The study highlighted the importance of careful forcefield selection based on the specific properties of interest in membrane simulations.

On the other hand, another comparative study by Pluhackova *et al.* focused on the structural and dynamical properties of model DMPC, POPC, and POPE bilayers using four atomistic lipid forcefields; GROMOS54a7, CHARMM36, Lipid14, and Slipids[314]. Their results highlighted that the parameterisations tested generally describe the structural characteristics of phospholipid bilayers well. The all-atom forcefields accurately described lipid diffusion and water permeability, but all forcefields have some shortcomings in reproducing various observables. GROMOS54a7 underestimated lipid self-diffusion and struggled with membrane melting characteristics, making it less suitable for studies of dynamical lipid behaviour. Slipids performed well for membrane studies near melting temperature, while Lipid14 and CHARMM36 excelled in describing well-ordered membrane structures and cooperative phase transitions. Slipids and Lipid14 best reproduced the order parameters and scattering form factors, with CHARMM36 being better for lipid volume and bilayer thickness. Lipid14 was found to be the most computationally efficient all-atom force field and did not produce artefacts with shorter radii for non-bonded interactions[314].

The importance of electrostatic interactions in simulations of lipid membranes, with a special emphasis on lipid peroxidation levels, was underscored in a study by Siani and co-workers, comparing CG forcefields Martini and ELBA[327]. The ELBA forcefield, with its more accurate treatment of electrostatic interactions, was found to better resolve conflicts between experiments and simulations, particularly in reproducing experimentally observed properties[327].

More recently, Antila and colleagues evaluated the performance of polarisable lipid force fields, specifically parameters based on CHARMM-Drude and AMOEBA, against high-fidelity experimental data and compared them with the top performing non-polarisable models[328]. Their results indicate that current polarisable models need improvements to match the best non-polarisable forcefields. CHARMM-Drude models improve molecular conformations and dynamics but predict an overly ordered membrane core and slow headgroup dynamics, affecting convergence. AMOEBA-based models struggle with lipid acyl chain ordering but handle headgroup conformations and dynamics reasonably well. Ion binding simulations with sodium and calcium reveal improvements with CHARMM-Drude in distinguishing calcium's stronger bind-

ing compared to sodium, but neither CHARMM-Drude nor AMOEBA perfectly match the experimental binding depth and affinity. These inaccuracies are related to other detected issues in the conformations of the lipids and the order of the membrane[328].

An innovative approach to forcefield comparison and development was presented by Kirikki *et al.* in their work on the NMRlipids Databank[267, 329]. This community-driven, open-to-all database provides programmatic access to quality-evaluated atom-resolution MD simulations of cellular membranes. The Databank enables rapid comparison of different forcefields and facilitates the development of data-driven and machine learning applications to predict membrane properties. This approach represents a significant step towards more systematic and comprehensive evaluations of lipid membrane forcefields.

These comparative studies highlight ongoing challenges and progress in forcefield development for lipid membrane simulations. They emphasise the importance of careful selection of the forcefield based on the specific properties and phenomena of interest in a given study, as no single forcefield excels in all aspects of membrane behaviour. Furthermore, the emergence of tools such as the NMRlipids Databank suggests a future where forcefield development and comparison can be more systematic, data-driven, and community-oriented.

1.3.2.4 Simulation of Realistic Membrane Models

The examples of simulations given so far, although already complex, do not completely capture all the nuances that an actual, biologically relevant membrane displays. Thus, several efforts to build realistic computational models to simulate cellular membranes with MD have been made in the past few years.

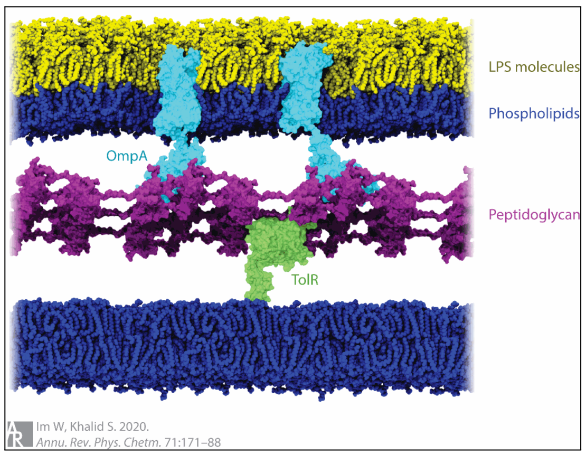

Figure 1.13: A multicomponent *Escherichia coli* cell envelope system composed of the outer membrane, inner membrane, and a single-layered cell wall. Reproduced from the work of Wonpil Im and Syma Khalid[330], Licence L2, copyright by Annual Reviews, Inc.

In cells, the **plasma membrane** (PM) defines the boundary, separating the interior of the cell from the outside environment. Eukaryotic PMs typically contain a non-negligible fraction of cholesterol or sterol derivatives and are asymmetric in their leaflet composition. Typically, the outer leaflet is primarily composed of saturated lipids and is enriched in sphingolipids and glycolipids. The inner leaflet is usually enriched in anionic and unsaturated lipids. The eukaryotic PM has historically been modelled as a pure POPC or DOPC bilayer. However, it should now be evident that this is a very simplistic approximation. More recently, models have been developed to better capture a realistic PM. Ingólfsson *et al.* have developed an 'average' mammalian PM model containing just phospholipids and cholesterol, with 63 different lipid types, divided into 14 different head groups and 11 different lipid tails, and an asymmetric distribution of lipids between leaflets[331]. Other efforts include the seven-component model by Koldsø *et al.*[332], which was able to capture many of the same properties as the model mentioned above, such as the appearance of nanodomains. Furthermore, this model was used to test the effects of curvature and protein inser-

tion, which were found to affect lipid sorting and organisation, as well as lipid clustering and diffusion. This model and some of the subsequent variants were used in other studies to explore protein clustering[333], the effect of GPCRs on membrane dynamics[334] and lipid binding to several protein complexes[335, 336]. Many other models have been built trying to capture different types of PM, such as the carcinogenic thymocyte model of Ueoka and coworkers[337]; or the human neuronal PM model built by Ingólfsson and coworkers[331].

As we have already discussed, the composition of the membranes also varies greatly depending on the **organelles**, which are significantly under-represented in the MD literature on lipid membranes[252]. In this sense, the organelles that are the most studied are the mitochondria. Their lipid membranes are known to be enriched in cardiolipin[338], and have typically been modelled as binary or ternary mixtures of PC or PC:PE with cardiolipin. These membranes have been used to study the binding of cardiolipin to respiratory chain protein complexes[339], the rotor of metazoan ATP syntase[340], or to study the specific properties of the membrane as a function of cardiolipin tail peroxidation[341]. Some efforts have also been made to model the lipid membranes of chloroplasts, endoplasmic reticulum, and Golgi apparatus[342–344].

The **bacterial membrane** is one of the Holy Grails of computational modelling in the context we are discussing. Gram-negative bacteria have, in fact, an inner and an outer cellular membrane, which is separated by a viscous periplasm[345] (Figure 1.13), making accurate modelling of such systems a rather non-trivial task. As we have discussed in Sections 1.2.1 and 1.2.3, bacterial membranes are mainly constituted by PE and PG-type phospholipids, and the outer leaflet of the outer membrane is composed primarily of LPS.

Thus, a large number of bacterial membrane models have been built over the years, with the earliest examples dating back to the work of Lins and Straatsma in 2001[346], simulating a rough LPS bacterial outer membrane. From there, models grew in complexity and have been used to study the structure and electrostatics of membranes[347], electroporation mechanisms[348], their interaction with exotic macromolecules such as fullerenes[349], the dynamics of transporter proteins embedded in such membranes[350], or the effect that an antimicrobial peptide has on them[81], among many other. Other bacterial membranes have also been modelled; for example, Lim and Klauda have made efforts to build the membranes of the elementary body and the reticular body of *C. trachomatis*[351]; or the development of an inner membrane model for *E. coli* containing cyclopropane moieties in the aliphatic chains of lipids[352]. More recently, simulations have been carried out that model both outer and inner bacterial membranes, studying the binding of TolR and OmpA protein complexes to the peptidoglycan layer[353]; or how the diffusion and morphologies of the inner and outer membranes are affected by the size of the embedded proteins[349].

Of course, the realistic models mentioned in this section come at a price. Their increasing complexity requires sampling times of orders of magnitude larger than those of a simplified membrane[252]. This effect is particularly notable for the diffusion of the different molecules, especially in systems that are very crowded[354–356]. In addition, for realistic asymmetric membranes, determining the lipid concentration in each leaflet is not a simple task, due to the lack of reliable experimental data[252]. Thus, to build such models, some criteria must be imposed, such as matching the area per lipid[357] or the surface tension between the two leaflets[358]. Furthermore, realistic bilayer simulations also face complexities due to the significant deformations that occur, which require larger simulation boxes to accommodate their natural undulations and extended simulation times to capture the slowest modes and the migration of lipids due to such deformations[303, 332]. It is obvious, then, that these added layers of complexity require

more sophisticated analyses that must account for all the particularities of a realistic membrane model.

1.3.2.5 Simulation of Complete Cell Models

Beyond the simulation of very realistic cellular membranes, the ultimate barrier for MD is the simulation of a complete cell. Of course, *classical* MD will never be able to simulate the basic unit of life, as the myriad of biochemical processes involved meddle deep into the quantum-mechanical world. However, a minimal representation of a cell is an interesting objective to strive for.

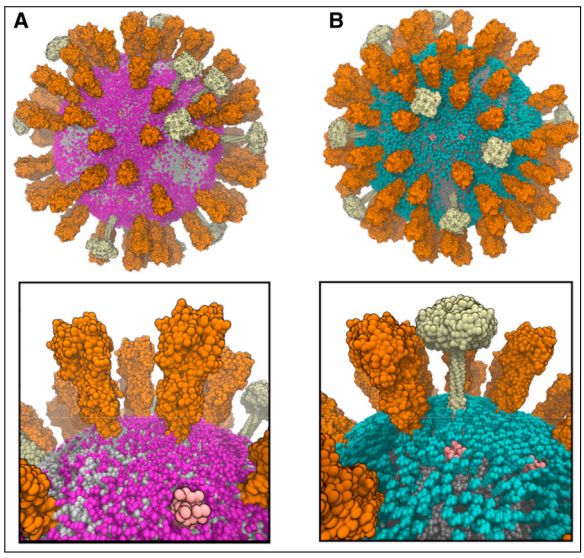

Figure 1.14: Molecular representations of the virion particles built by Reddy and co-workers[359], reproduced under a Creative Commons licence.

In fact, that objective may not be that far away. Using CG and multiscale approaches, large-scale simulations of viral envelopes have already been performed. Reddy and co-workers combined X-ray structures with cryo-EM, NMR, and lipidomics data to build a complete model of the influenza-A virion particle[359] (Figure 1.14), performing several simulations under different conditions, providing a computational platform to probe the structural and biophysical stability of the virion in water. The influenza-A envelope proteins were found to diffuse slowly within the viral membrane, which matched previous NMR measurements. Marzinek and colleagues have also taken steps to build a complete viral particle model for the Dengue virus, consistent with cryo-EM data, which allowed adding details regarding the nature of key protein-lipid interactions and the stability of the virion paricles[360, 361]. Subsequently, Reddy and Samson also modelled the Denge virus, observing that the dense packing of transmembrane protein domains, along with the encapsulation of the outer leaflet of the lipid bilayer within a protein shell, led to a diffusion regime for lipids similar to that seen in the influenza-A virus, despite the fact that cholesterol is absent from the Dengue virion particle[362]. Dommer and colleagues made the most recent state-of-the-art advances in virus modelling, building an integrative multiscale model of the complete SARS-CoV-2 virus aerosolised in deep lung fluid[363]. Their simulation, containing more than 1 billion particles, captures the intricate chemical and biological complexities within a respiratory aerosol, while setting a first-of-its-kind work paving the way for the simulation of similar systems.

Various organelles have also been constructed and simulated in its (close to) totality via MD. For example, Shingharoy and co-workers reported a 100 million particle simulation of a bacterial chromatophore[364]. In this study, they probed the influence and effect of the integral proteins within the chromatophore, which conferred it with its characteristic curvature, extended their simulations using Brownian dynamics of small molecules within the organelle, and studied the charge transfer mechanism that would lead to the synthesis of ATP through sunlight. In a study conducted by the Marrink group and led by W. Pezeshkian, a tool was developed to

build simulation-ready CG models from structures originating from mesoscale simulations[365]. They demonstrated that such a tool can be used to build, for example, a complete representation of mitochondrial membranes at almost-atomistic resolution. Moreover, although not typically considered an organelle *per se*, an atomistic model of the bacterial cytoplasm has also been developed, in order to study different protein-protein interactions within[366].

All of these studies have, in some way or another, paved the way to the recent publication led by J. Stevens, also from the Marrink group, of the first model of an entire minimal cell[367]. In this pioneering study, despite not being able to actually run an MD simulation due to the gargantuan size of the reportedly built system, they provided a pipeline through which the constructions of such complex systems can be achieved.

1.3.3 Mechanical Properties of Lipid Membranes

So far we have discussed some of the most fundamental aspects of MD simulation, as well as the evolution of how cellular membranes have thus been modelled along the last decades. As we have mentioned previously, lipid membranes play many different roles within a living cell. It should be obvious that for some of those roles, like their ability to compartmentalise a cell or their entity as a matrix through which other biomolecules diffuse, the mechanical properties of the membranes are of paramount importance. We now turn to taking a closer look at the study of such properties, as these are of relevance for this Thesis, especially for the two works discussing the effects of ultrasonic waves on the structure of lipid bilayers, discussed in Sections 4.3 and 4.4.

1.3.3.1 Classical Mechanical Properties

Fundamentally, the mechanical properties that are routinely measured are phenomenological (*i.e.*, they are not derived from first principles) constants that affect the energetics of the many deformations that can happen to a lipid membrane. Thus, over the years, many energy functionals have been developed that model the behaviour of membranes at a theoretical level. Of particular importance is the Helfrich Hamiltonian[368], developed in the 1970s and still widely used today. In general, and without going into much detail, the Helfrich Hamiltonian states that the energy of a lipid membrane is dependent on its surface tension and curvature. This level of theory assumes that the thickness of the bilayer is infinitesimally small, that is, the bilayer is by far much wider than it is thick. Thus, the Helfrich Hamiltonian only applies rigorously as a large-scale theory.

After the Helfrich theory of membrane elasticity, other functional forms have been developed, taking into account the internal degrees of freedom of the lipid membranes. In particular, these theories suggest that the orientation of the lipid tails contributes to the energetics of the membrane. In fact, Hamm and Kozlov[369] showed that the energy density of a lipid membrane depended on the tilt of the lipids within the membrane through a quadratic term in the energy functional. More than a decade later, Watson and co-workers showed that to better explain measurements of the energy spectra of lipid bilayers another term had to be considered, related to the twist of the lipid tails through another quadratic term in the energy functional[370]. In recent years, Terzi et al. have shown that the splay of the lipids, that is, how the tails of different lipids diverge from one another, is also coupled with their tilt[371, 372], adding yet another term to the energy functional.

Thus, for each of those contributions to the energy, a phenomenological constant can be measured, namely: the area compressibility modulus, the bending modulus, the lipid tilt modulus,

the lipid twist modulus and the lipid splay-twist modulus, respectively. The area compressibility modulus and the bending modulus are, by far, the ones that are most commonly measured. However, the group of Markus Deserno is quite prolific in both theoretical studies and measurements of these magnitudes for lipid membranes.

The area compressibility modulus for lipid membranes has been calculated through MD simulations since the mid 1990s. Feller, Zhang and co-workers developed methods to evaluate this magnitude based on fluctuations in the area of lipid membranes using singular MD simulations at constant pressure and temperature[260]; or with a series of MD simulations at constant area[373, 374]. In recent years, Doktorova and co-workers postulated that these two approaches have some fundamental problems. First, the method based on the fluctuations of the area is known to be prone to errors and outliers, and second, these methods are rigourous only for symmetric bilayers. Thus, they proposed a method that is able to calculate the compressibility modulus of each bilayer leaflet separately[375] in a robust manner. In general, when measured in a MD simulation, the compressibility modulus of a lipid bilayer is in the range of 200 to 300 dyn/cm with standard errors of approximately 10%, and different lipids produce different values with good statistical significance[376]. However, the compressibility modulus value that a specific membrane has is known to be highly dependent on simulation metaparameters, such as the treatment of long-range interactions[376].

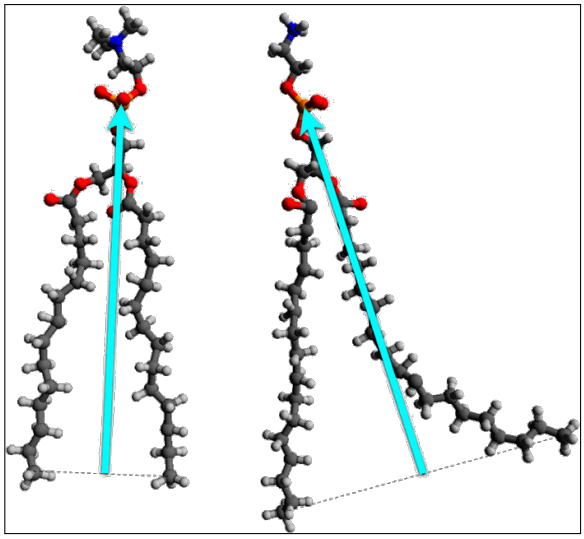

Figure 1.15: Representation of the lipid director (cyan arrow), defined from the midpoint between same-level tail-carbons to the phosphorus atom in the head group. The right snapshot illustrates how the molecular director averages the orientations of the two individual tails. Reproduced from the work of M. F. Ergüder *et al.*[377], Licence L3, copyright by AIP Publishing.

The bending modulus for lipid membranes has also been calculated with MD since at least the mid 1990s. Based on the Helfrich Hamiltonian, Safran shows that the bending modulus can be obtained, in principle, through the Fourier power spectrum of the membrane topography[378]. However, and because this method is based on the basic Helfrich approximation, in which the bilayer is treated as a structureless thin film, this is only valid for membranes whose simulation box is more than 10 times larger than their thickness, rendering it impractical for atomistic simulations. Even then, only the longest wavelength modes can be analysed[376, 379].

Thus, as we introduced in the above paragraphs, several corrections were introduced to the Helfrich model. Watson and co-workers propose that the bending modulus can be calculated from the Fourier power spectrum of the longitudinal component of the vector field of the lipid director, taking into account the internal structure of the membrane[380]. With this method, deviations from the theory are only seen for the shortest wavelengths (three times shorter than the thickness of the bilayer), and simulations containing only 288 lipids proved enough to calculate this constant[381]. In contrast to the area compressibility modulus, the bending modulus fluctuates by around a factor of three depending on the membrane studied. Polyunsaturated lipids give the lowest values,

while saturated acyl chains tend to produce a higher bending modulus[376].

Another advantage of using the method proposed by Watson and co-workers is that it also allows one to calculate the lipid tilt and twist moduli[380]. Both magnitudes are related to the Fourier power spectra of the transversal component of the vector field of the lipid director, rather than the longitudinal one, and have been experimentally calculated in the last decade[382, 383]. In general, the tilt modulus does not vary much from one membrane to another, being in the range of 4 to 8.5 (10^{-20} J/nm^2). Unsaturated lipids give lower values, while saturated ones produce higher tilt moduli. The twist moduli show a less compact behaviour depending on the membrane, ranging from 1 to 4.75 (10^{-20} J), while the effect of chain unsaturation remains the same as for the tilt moduli[376].

Finally, data for the twist-splay modulus of lipid membranes is still scarce, as the models that incorporate it into the energy functional of a lipid membrane are still relatively new[371, 372]. Terzi and co-workers propose that this modulus can be calculated by simultaneously fitting the Fourier power spectra of both the longitudinal and transversal components of the lipid director vector field. The values reported in their study find that the splay-tilt moduli for various lipid membranes range from 13 to 30 k_BT. Completely unsaturated chains produce lower values, and lipids containing unsaturation in their chains report higher splay-tilt moduli[372]. To date, the only experimental measurement for the splay-tilt moduli comes from a very recent paper led by Ergüder, also from the Deserno group[384].

1.3.3.2 Mechanical Perturbations and Lipid Membranes

Beyond calculating the elastic parameters mentioned above, MD simulations have also been extensively used to test the resistance of lipid membranes to mechanical deformation. Typical studies on the field of membrane mechanical deformation usually cover the topics of pore formation, uniaxial/biaxial strain and/or shear stresses, the effects of cavitation close to the membrane surface, and the influence of ultrasounds on the lipid membrane.

Earlier studies of pore formation used external stimuli on lipid membranes, either by mechanical means[385] or by applying an electric field[348, 386]. The use of such techniques requires controlled perturbations in the simulation, which complicates the task of obtaining a free-energy landscape of the process. Pore formation is known to involve two highly distinct conformational transitions: pore nucleation, that is, the establishment of the pore itself through a process of membrane thinning; and pore expansion, whose name is self-explanatory[387]. In order to reproduce such phenomena, efforts have been made to define Reaction Coordinates (RCs) for enhanced sampling simulations. Some of the simplest RCs include the radius of the pore[388], which is known to be incapable of capturing pore nucleation; RCs that steer lipids away from the centre of the pore[389]; or the density of the solvent along a cylinder that traverses the membrane[390]. Despite the abundance of pore-forming RCs, a comparative analysis carried out by Awasthi and co-workers, in the group of Jochen Hub, found that none of the examined RCs accurately represented the metastable nature of membrane pores, which is one of their key characteristics[391]. Thus, also in the same group, a new method was developed to obtain the free energy of pore formation (Figure 1.16). The proposed RC consists of two different terms, or sub-RCs. The first term drives pore nucleation, by following water occupancy and connectivity in a membrane-spanning cylindical region[392]. The second term kicks in once complete connectivity is achieved in said cylinder and drives pore expansion by following the number of water particles inside it[393], since the radius of the pore is directly proportional to that magnitude. This new RC proved to be capable of correctly capturing both pore nucleation

and expansion, as well as pore metastability[393]. When tested for different membrane models (endoplasmic reticulum, Golgi apparatus, plasma membrane, *etc.*), a clear dependency on membrane composition was found, which the authors hypothesise to reflect biological function[394].

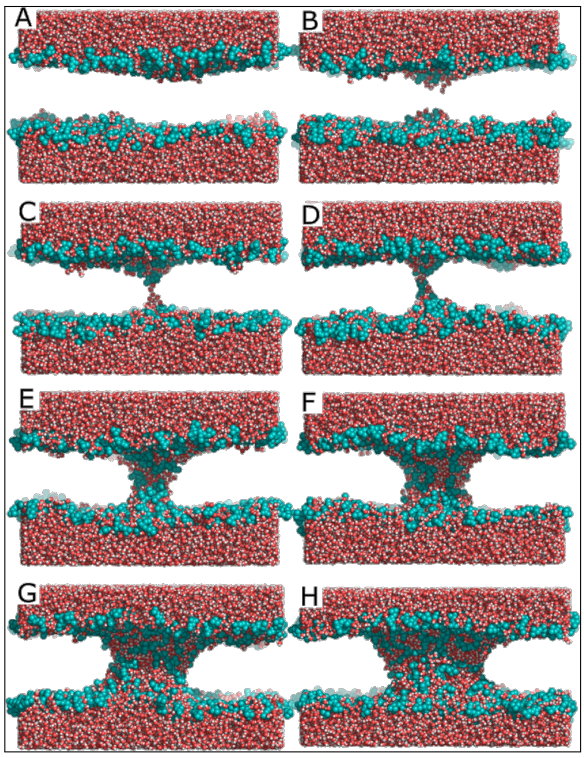

Figure 1.16: Typical snapshots during pore nucleation and expansion, taken from the final frames of umbrella sampling windows, reproduced from the work of J. S. Hub[393], Licence L4, copyright 2024 American Chemical Society.

Membrane rupture can be followed by applying strain, that is, stretching the membranes along a given direction at a constant rate. Such MD simulations have been performed for several decades, with Peter Tieleman pioneering the work[385], and thereafter many studies have emerged applying this technique. Thus, several factors that govern membrane rupture have been studied when strain is applied. The effect of the type of deformation applied to a POPC bilayer was followed, showing that biaxial (stretching the membrane in two directions at the same time) deformations produce higher stresses on the membrane at lower strains, compared to uniaxial deformations[395]. The effect of strain rate (the speed at which the membrane is stretched) was also studied[396], for a pure DPPC and a DPPC:Cholesterol membrane. The results indicate that the strain at which the membrane ruptures is directly proportional to the strain speed, that is, faster stretch rates require a higher strain to produce a defect in the membrane. The addition of cholesterol to the membrane was found to accentuate this fact[396]. On the side of complex membranes, a study was carried out for a pure POPC bilayer and that same bilayer with flexible and rigid inclusions of proteins and lipids, through a multiscale framework. These inclusions served as idealised representations for stiffened biomolecular complexes in cell membranes[397]. The different membranes were then subjected to uniaxial strains at different rates. This study postulated that the reactions of the pure membrane as well as those of the membrane with the soft protein embedded in it are virtually independent of the strain rate applied, although the membrane-protein system was found to be slightly less resistant. Moreover, rigid inclusions within the membrane had the effect of facilitating membrane rupture[397]. Another study focused on the effect of lipid oxidation on the resistance of POPC-derived membranes to uniaxial strain, finding that higher oxidation levels produce less resistant membranes (Figure 1.17)[398]. The more technical side of MD simulation was also tested, with a very recent study evaluating the results obtained with different forcefields when a POPC membrane was subjected to biaxial deformations[399]. The study was carried out at three levels of resolution and showed that the strain at which the membrane ruptured was similar for all of them. Nevertheless, lower resolution levels produced lower yield stresses (the stress at which the material finally ruptured) required for defect formation[399].

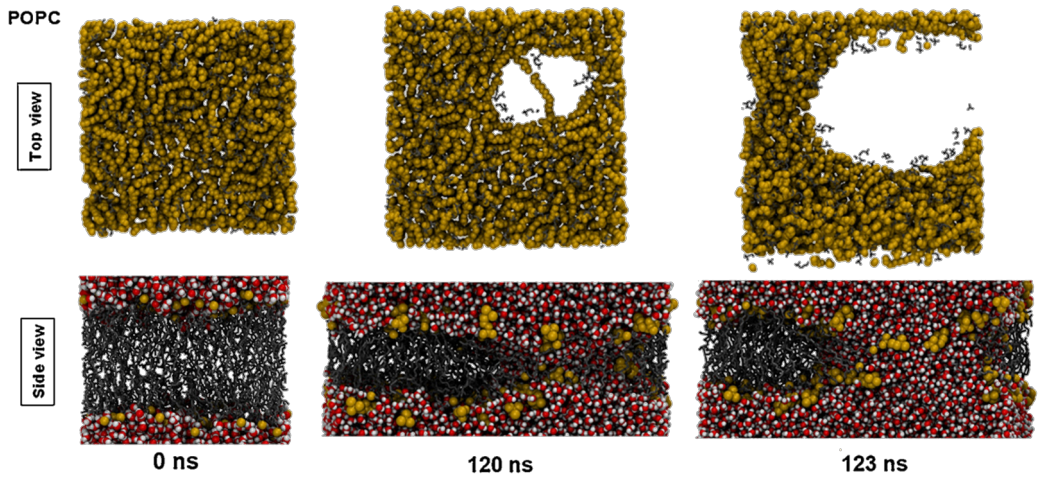

Figure 1.17: Snapshots from the stretching of a POPC membrane, starting from the equilibrated membrane. Water molecules and headgroups are represented as van der Waals spheres with red/white and yellow colours, respectively. The *sn*-1 and *sn*-2 chains are represented by grey lines. Reproduced from the work of M. C. Oliveira *et al*.[398], Licence L5, copyright by Elsevier.

The effects of ultrasounds or ultrasound-induced phenomena on lipid membranes have also been studied through MD simulation, due to their potential therapeutic applications, as we introduced in Section 1.2.3.4. The interest in the computational modelling such processes dates back almost two decades, with pioneering studies by Koshiyama, Kodama, and co-workers[400, 401]. After simulating a single shockwave traversing a DPPC bilayer, they found that the fluidity and spatial organisation of the lipids were greatly affected[400]. In a consecutive study, despite not modelling a cavitation bubble within the MD pipeline, a numerical model was applied to calculate the size of the microbubble depending on the intensity of the shockwave, showing that such bubbles would be able to damage the membrane from a distance larger than 5µs[401]. In recent years, Ganzenmüller and co-workers studied the effect of shocwkaves on a larger flat, very rough coarse-grained lipid membrane[402]. The shockwave was generated using the momentum mirror method[403], thus creating a flat hypersonic wavefront. The simulations were tested for various shockwave velocities, and found that after a threshold of about 3 km/s, a total loss of membrane shape was observed, with no recovery of the nominal structure[402]. On the other hand, Sliozberg and Chantawansri conducted a similar study, but focussing on the effect of a shockwave impact upon a spherical lipid vesicle[404]. The vesicle was composed of a coarse-grained representation of DMPC, and water was modelled at the mesoscale resolution. Their results indicate that the liposomes are fairly insensitive to the compression produced by the shockwave, but the following negative pressure phase has a strong effect on them. The structural integrity of the vesicles was compromised for showckwave impulses greater tha 5 Pa·s. Direct poration was observed for the tensile portion of the shockwave but only for very high negative pressures exceeding -120 MPa[404].

However, most of the interest regarding the effects of shockwaves on lipid membranes has revolved around the cavitation of water followed by the collapse of the bubble. While sonoporation was studied as a cargo delivery method within living cells, it was found that the addition of microbubbles improved the efficiency of the process, and it was demonstrated that the ultrasound caused said bubbles to collapse, generating water jets[405, 406]. Choubey and colleagues performed, to the best of our knowledge, the first study to model microbubble collapse followed

by a hypersonic stream in the presence of a lipid bilayer[407]. The procedure was very similar to what we described above, using the momentum mirror method for shockwave generation but, in this case, a spherical cavity was formed by removing solvent particles to emulate a microbubble next to a DPPC bilayer, modelled at the coarse-grained level. Thus, when the shock front hits the proximal side of a nanobubble, water molecules from its periphery accelerate toward the centre and form a nanojet. The size of the nanojet was found to depend both on shockwave velocity and on the size of the bubble. The following impact of the water jet on the lipid bilayer caused poration, and the thermodynamic phase of the membrane was found to influence the extent to which the pore was formed. The velocity of the shockwave was found to influence the poration process and no pores were observed below 0.4 km/s. Many studies followed the pioneering work of Choubey and co-workers, for example the work of Santo and Berkowitz conducting a systematic study on the influence of microbubble size and shockwave velocity on the poration of a pure DPPC and a DPPC:Cholesterol membrane[408]. This study also tested the ability of the membranes to recover once a pore was formed. As expected, the extent of membrane rupture is dependent on the shockwave and microbubble parameters, as these dictate the velocity of the water nanojet. The presence of Cholesterol was found to make the membranes more resistant, requiring faster shockwaves to produce poration. In addition, all pores were found to heal with time[408]. Other works focused on testing the effect of lipid composition on the resistance of the membrane to the impact of these water nanojets. This is the case in the work of Wei and colleagues, with their study testing the effect of lipid peroxidation on a DOPC membrane subjected to a microbubble collapse procedure as the ones described above[409]. Their results indicate that, indeed, lipid peroxidation makes the cellular membranes less resistant to these mechanical perturbations[409]. Beyond the use of shockwaves to induce hypersonic water jets, Fu and co-workers studied the effects of microbubble collapse in the absence of shockwaves[410]. By using simulations at the atomistic and coarse-grained levels of resolution, they found that just the flux created by the bubble collapsing over itself was enough to induce a deformation on the lipid bilayers, although no poration was observed[410]. The effect of stable cavitation of a microbubble located close to a coarse-grained DPPC lipid membrane was studied recently by Man and colleagues, showing that their bubble model oscillating in the nanosecond timescale produces shear stresses comparable to those of experimental results. Moreover, their model was not able to induce poration suggesting that stable cavitation is not the main mechanism through wich membranes are ruptured[411].

Finally, the main efforts to simulate through MD the direct interaction of ultrasounds with lipid membranes have been led by the group of Philippe Derreumaux. In a paper led by Man and co-workers, they proposed a method to simulate ultrasounds within the MD pipeline[413]. Their approach enabled the application of an oscillating pressure wave in a localised zone of the lipid bilayer, emulating a focused ultrasound. Although not completely rigorous, since the area in which their ultrasound wave is focused is well below the diffraction limit of a wave with such characteristics (we prove this in the Methods chapter, Section 3.4.1.1), their method was a first of its kind in modifying a pressure control algorithm to model a sound wave[413]. In a follow-up study, Man and co-workers used an atomistic minimal model of the blood-brain barrier, composed of two lipid bilayers, mimicking two portions of neighbouring cells, connected by a tight junction formed by a pair of two cis dimers of the claudin-5 protein. Their results showed that high-intensity ultrasounds are capable of pulling leaflets away from each other, thus facilitating potential translocation of molecules through the blood-brain barrier[414]. The last work to date by Man and co-workers which focused on the interaction of an ultrasonic wave with

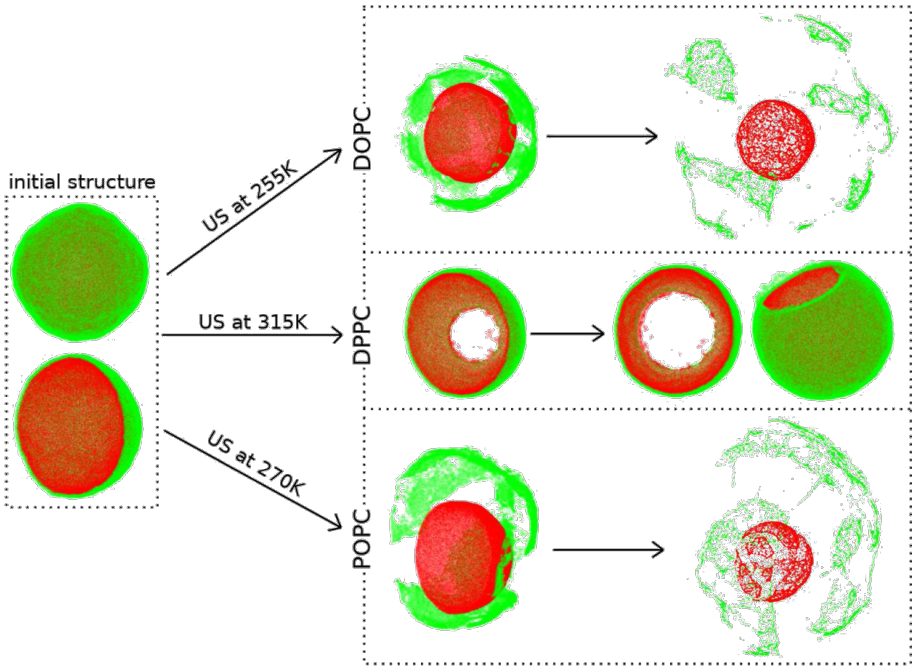

Figure 1.18: Initial structure (left) and snapshots of three liposomes (DOPC, DPPC, and POPC) obtained from after US irradiation. The inner and outer leaflets are shown in red and green, respectively. Reproduced from the work of V. H. Man *et al*.[412], Licence L6, copyright 2024 American Chemical Society.

lipid membranes involved simulating several vesicles of different compositions at the atomistic and coarse-grained level under different ultrasound conditions (Figure 1.18)[412]. The study found two different liposome-damaging mechanisms, a pore formation pathway and a monolayer detachment pathway, depending on the membrane composition. For cholesterol-enriched liposomes, the monolayer detachment pathway was preferred. The specific thermodynamic phase of the lipid membrane was also found to play a role in the preferred pathway, as well as the intensity of ultrasound[412]. Beyond the work of the group of Derreumaux, a very recent paper published by Li and colleagues tested the influence of an ultrasound wave on atomistic DPPC bilayers and micelles[415]. Their ultrasound model was much simpler than the proposal of the group of Derreumaux, despite being able to capture equivalent phenomena such as the influence of the pressure wave on the thickness of the membrane. The partition of CO_2 molecules between the lipid and the solvent phase was also studied, showing that carbon dioxide tended to enter the bilayer in the low pressure cycle, although this was observed only for waves with sufficiently long periods[234].

2 OBJECTIVES

Cando vou pro fiandeiro
non vou por fiar na roca
vou por toca-lo pandeiro, ai!
que esta noite a min me toca.

–Galician folk song.

The primary goal of this doctoral Thesis was to enhance our understanding of lipid membrane biophysics through computational methods. This, in turn, deepening our understanding of these structures, is expected to provide valuable insights that could inform both basic research and practical applications, contribute to the development of more accurate computational models, and hopefully pave the way for more advanced applications. Lipid membranes are essential components of biological cells, playing key roles in preserving cellular integrity, enabling communication, and facilitating various biochemical processes, as discussed in the Introduction chapter. Although considerable advancements have been made in this field, many aspects of lipid membrane behavior remain elusive due to their microscopic and dynamic nature. This research, thus, aimed to address these knowledge gaps by concentrating on three main objectives: assessing Molecular Dynamics forcefields, examining equilibrium properties and structural organization of lipid membranes, and exploring the effect of ultrasound waves on these biological structures. The specific objectives are detailed as follows:

2.1 Evaluation and Comparison of Molecular Dynamics Forcefields

The first objective of this Thesis was to conduct a thorough evaluation of various MD forcefields in their ability to simulate lipid membranes, and to perform a rational comparison between them. This involved a series of simulations using different freely available sets of parameters. We focused on and measured relevant biophysical properties including membrane thickness, area per lipid, lateral diffusion coefficients, and Hydrogen bonding patterns. When possible, we compared these properties with experimental data, aiming to identify which forcefield, if any, provided the most accurate and reliable results for lipid membrane simulations. Of particular relevance to this latter point was the experimental determination of deuterium order parameters through NMR for the tested models, enabling a direct comparison with simulation results. A comparison of different simulation meta-parameters was also carried out, testing the influence of the underlying algorithms working behind each forcefield. The end goal was to understand how different approaches in the representation of inter- and intramolecular forces affect the results produced by an MD simulation. This involved an assessment of the strengths and weaknesses of each parameterisation.

This piece of work is hoped to provide a valuable resource for researchers in the field, guiding the selection of forcefields and facilitating educated choices for potential future simulations. The findings of this study are also expected to contribute to the development of more advanced and accurate forcefields for biological simulations, ultimately enhancing our understanding of lipid membranes and their role in cellular processes.

2.2 Membrane Properties and Hierarchical Organization

The second objective of the present Thesis was to investigate the average value of some structural properties in equilibrated, unperturbed systems of large lipid membranes and their structural organization, with a particular focus on possible hierarchies in their structure. In this work, we aimed to apply advanced methods to accurately measure relevant physical properties within a membrane, taking into account the natural fluctuations that their spatial arrangement can incur in. The study also explored the concept of hierarchical structural organisation in parallel to the well-established hierarchical structures of proteins or nucleic acids. This postulate began with an analysis of the primary structure, relating it to the individual lipid molecules within a membrane, and their interactions. From there, we progressed to the secondary structured, relating it to how lipid molecules self-assemble into their canonical membrane structures such as bilayers or micelles. The tertiary structure was proposed by referring to large-scale organisation patterns, or domains, that spontaneously appear in the membranes, creating potential functional regions. Finally, the quaternary structure is explored as the interactions between a lipid membrane and other biomolecules, as well as their integration into more complex cellular structures.

This investigation aimed to reveal some of the fundamental principles that dictate the self-assembly and arrangement of lipid membranes. By applying precise measurements and providing a theoretical framework similar to that used for other biomolecules, this research hopes to offer a deeper understanding of the elements that affect membrane stability, flexibility, and functionality. The findings of this study are expected to have implications for various fields, such as cell biology, biophysics, and materials science.

2.3 The Influence of Ultrasound Waves on Membrane Structure

The third objective of this Thesis was to study the impact of ultrasonic waves on the structure and behaviour of lipid membranes. Ultrasounds are increasingly used in the medical field; therefore, understanding their effects on biological structures is of paramount importance for the development of new, safer, and more effective applications. To achieve our goal, we implemented and validated a protocol to simulate the effects of an ultrasound wave within an MD pipeline. Our research systematically studied how different membrane compositions reacted to exposure to ultrasonic irradiation, identifying how specific membrane properties reacted to such stimuli. In a follow-up work, a wide range of ultrasound parameters (overpressure and frequency) were also explored to determine how these affect and influence membrane dynamics and integrity.

With this in mind, our objective was to provide a comprehensive understanding of the physical responses of a lipid membrane to ultrasound and to provide insights into their underlying mechanisms. We expect our findings to be relevant for the optimisation of ultrasound-related applications in the medical field, such as drug delivery, non-invasive diagnostics, and other therapeutic applications. Moreover, we hope that our results may lead to the development of potential new technologies that exploit ultrasound-membrane interactions with applications in biotechnological and materials science.

3 METHODS

If mathematical analysis should ever hold a prominent place in chemistry – an aberration which is happily almost impossible – it would occasion a rapid and widespread degeneration of that science.

–Auguste Comte,
Philosophie Positive

Throughout this chapter, the methods employed to conduct the work for this PhD will be explained. A detailed description of the simulation technique used, Molecular Dynamics, will be provided to facilitate a rational understanding of its inner workings. The mathematical methods used to perform the various measurements relevant to a lipid membrane will also be explained and, additionally, a comprehensive overview of the ultrasound model employed in this work, as well as its implementation in the simulation engine, will be presented.

3.1 Molecular Dynamics

At the core of this work lays a computational technique, Molecular Dynamics (MD). Generally speaking, these are computer simulations that model and study the movement of molecules over time. MD relies on numerical integration of the equations of motion for a large number of atoms forming said molecules or, in a more general case, particles. Those equations of motion are derived from a potential functional encoded in the so-called forcefield, and several other algorithms are applied to ensure that the simulations behave in the way the researcher desires and thus produce meaningful and interpretable results. A deeper examination of these concepts will be presented in the following sections. The reader should note that the explanations given here are just the basic backbone for MD, and the actual computation of the following magnitudes involves a more detailed and nuanced process. The specifics of such computation are beyond the scope of this Thesis; however, it is deemed useful to understand the basics. There are several works that cover the MD pipeline in great detail; the reader is encouraged to consult the exceptional works of Benedict Leimkuhler and Charles Matthews[416], and Daan Frenkel and Berend Smit[417], which were utilised in the writing of this section. Furthermore, the GROMACS online documentation[418] serves as an excellent resource for gaining a good understanding of the topic. In the following sections, an in-depth account of some of the techniques used will be given, as they are of special relevance to this Ph.D.

3.1.1 The Physical Fundament

MD is, fundamentally, a classical technique. By this, it is meant that the framework within which it operates is Newtonian Mechanics. Consequently, anything of quantum nature falls outside its boundaries, despite the existence of some flavours (QM/MM and Car-Parrinello MD, for example) that incorporate quantum effects.

Thus, within the Born-Oppenheimer approximation, it is stated that the motion of the atomic nuclei and that of their electron clouds can be treated separately. It is therefore assumed that the electron clouds adjust their dynamics instantly when the atomic positions change, and that they always remain in the ground state. Taking this into account, we can write Newton's second law

as follows:

$$m_i \frac{\mathrm{d}^2 \mathbf{r_i}}{\mathrm{d}t^2} = \mathbf{F_i} \tag{3.1}$$

$$\mathbf{F_i} = -\nabla U(\mathbf{r_i}) \tag{3.2}$$

Where m_i is the mass of the i^{th} particle in the simulation, $\mathbf{r}_i$ is the position of the particle, *t* symbolises time, $\mathbf{F}_i$ is the force acting on the particle and *U* is the potential functional. Since the forces are conservative, they are calculated as the negative spatial derivatives, *i.e.* the negative of the gradient of the potential: $\nabla U = \left(\frac{\partial U}{\partial x}, \frac{\partial U}{\partial y}, \frac{\partial U}{\partial z}\right)$. Both equations are solved simultaneously for small increments in time, called timesteps. More details can be found in Section 3.1.5.1.

3.1.2 The forcefield

The forcefield is, simply put, the set of parameters that shape the potential functional. In general, it can be expanded as follows:

$$U(\mathbf{r}) = U_{bonded}(\mathbf{r}) + U_{non-bonded}(\mathbf{r}) \tag{3.3}$$

The potential is split into two main groups of contributions: bonded interactions, representing the energies acting upon particles that are directly linked via chemical bonds; and non-bonded interactions, representing the energies acting between particles that are not directly connected.

More generally, a complete force field is made up of two basic components: the set of equations used to generate the energies and the parameters that modulate those equations. Note that no precise mathematical form is provided in Equation 3.3. This is because the bonded (Equation 3.4) and non-bonded (Equation 3.5) contributions can be further divided:

$$U_{bonded}(\mathbf{r}) = U_{bonds}(\mathbf{r}) + U_{angles}(\mathbf{r}) + U_{proper\ dihedral}(\mathbf{r}) + U_{improper\ dihedral}(\mathbf{r}) \tag{3.4}$$

$$U_{non-bonded}(\mathbf{r}) = U_{VdW}(\mathbf{r}) + U_{electrostatic}(\mathbf{r}) \tag{3.5}$$

The specific mathematical expression of each contribution can change depending on the parameterisation approach and desired characteristics of the forcefield. In the following sections, a basic explanation of each will be provided.

3.1.2.1 Bond Stretching

Represents the stretching or compression movement along the axis defined by the bond between two particles (Figure 3.1). In the forcefileds used in this work (refer to Section 3.1.3), a harmonic potential is used to represent this contribution, taking the form of Equation 3.6:

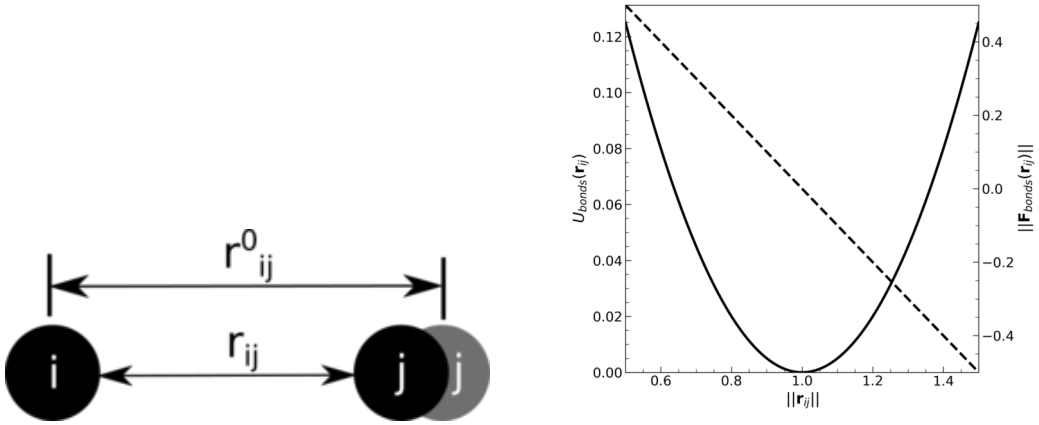

Figure 3.1: Schematics of the stretching action between two bonded particles (left) along with graph of the potential (solid line, left axis) and signed force norm (dashed line, right axis) as a function of particle distance (right). Graph is in arbitrary units.

$$U_{bonds}(\mathbf{r}_{ij}) = \frac{1}{2}k_{ij}(||\mathbf{r}_{ij} - \mathbf{r}^0_{ij}||)^2 \tag{3.6}$$

Where $\mathbf{r}_{ij}$ is the the vector connecting particles *i* and *j*, k_{ij} is the force constant and $\mathbf{r}^0_{ij}$ is the equilibrium bond distance. Thus, in this case, k_{ij} and $\mathbf{r}^0_{ij}$ are the forcefield-specific parameters.

Note that other mathematical expressions can be used to represent this contribution, such as Morse potentials, when anharmonic behaviour is desired, or cubic bond-stretching potentials, which are simpler than Morse potentials and still yield reasonable results.

3.1.2.2 Bond Angle

An example of the potential acting on the angle formed by the bond between three consecutively connected particles is represented in Figure 3.2. In the forcefields utilised in this study, a harmonic potential is employed to model this contribution. The mathematical expression for this is provided in Equation 3.7.

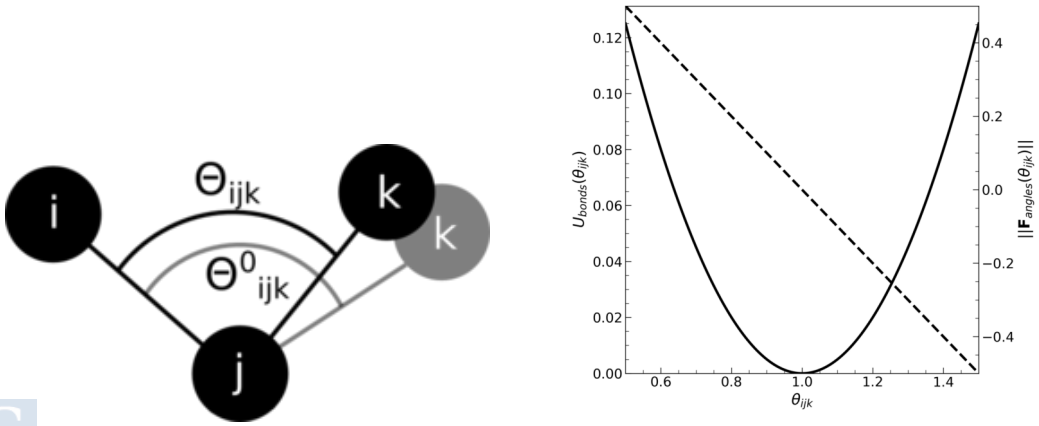

Figure 3.2: Schematics of the angle bending action between three bonded particles (left) along with graph of the potential (solid line, left axis) and signed force norm (dashed line, right axis) as a function of the angle (right). Graph is in arbitrary units.

$$U_{angles}(\theta_{ijk}) = \frac{1}{2}k_{ijk}(\theta_{ijk} - \theta^0_{ijk})^2 \tag{3.7}$$

Where θ_{ijk} is the angle formed by three consecutively bonded particles at any given instant, k_{ijk} is the force constant for this contribution and the specific trio of particles, and θ^0_{ijk} is the equilibrium angle. Thus, in this case, k_{ijk} and θ^0_{ijk} are the forcefield-specific parameters.

Other possible functional forms include cosine-based angle potentials (*i.e.*, using the cosine of the angle instead of the angle itself as an input variable) or the quartic angle potential, which uses a fourth-order polynomial to describe this contribution.

3.1.2.3 Proper Dihedral Angles

The bending along a proper dihedral angle defined by four consecutively connected particles is illustrated in Figure 3.3. The most common form of dihedral angle bending, which appears in all the force fields used in this study, is of periodic type, as described by Equation 3.8.

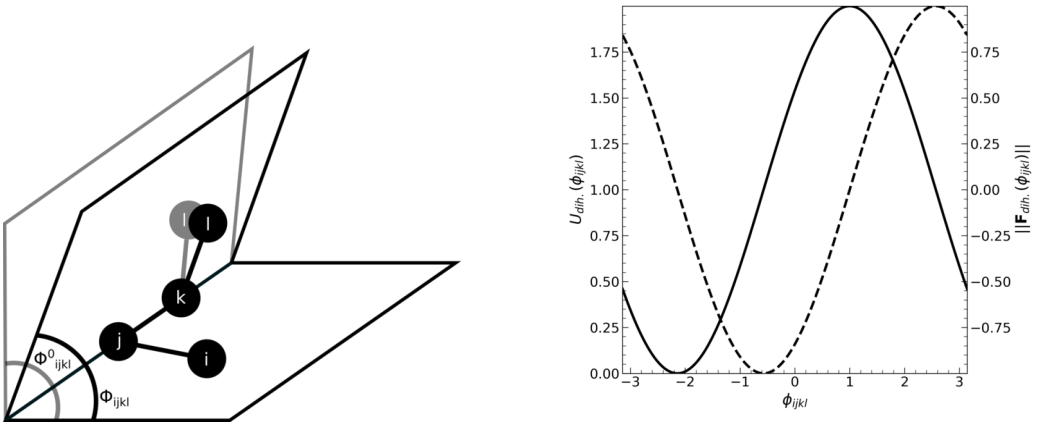

Figure 3.3: Schematics of the dihedral angle bending action between four bonded particles (left) along with graph of the potential (solid line, left axis) and signed force norm (dashed line, right axis) as a function of the proper dihedral angle (right). Graph is in arbitrary units.

$$U_{proper\ dihedral}(\phi_{ijkl}) = k_{ijkl}(1 + cos(n\phi_{ijkl} - \phi^0_{ijkl})) \tag{3.8}$$

Where ϕ_{ijkl} is the dihedral angle between four consecutively connected atoms, defined as the angle between the planes formed by the atoms *ijk* and *jkl*; k_{ijkl} is the force constant for this contribution, n is the dihedral multiplicity and ϕ^0_{ijkl} is the equilibrium value for the proper dihedral angle. Therefore, the forcefield-specific parameters in this case are k_{ijkl} and ϕ^0_{ijkl}.

There are other possible functional forms this interaction can take, such as the Ryckaert-Bellemans function, which is used to manually favour some conformations over others, or Fourier series, to name a couple.

3.1.2.4 Improper Dihedral Angles

This type of dihedrals is used to maintain, or to prevent, coplanarity for a group of four bonded particles (Figure 3.4). The most common mathematical form taken is also harmonic, as shown in Equation 3.9.

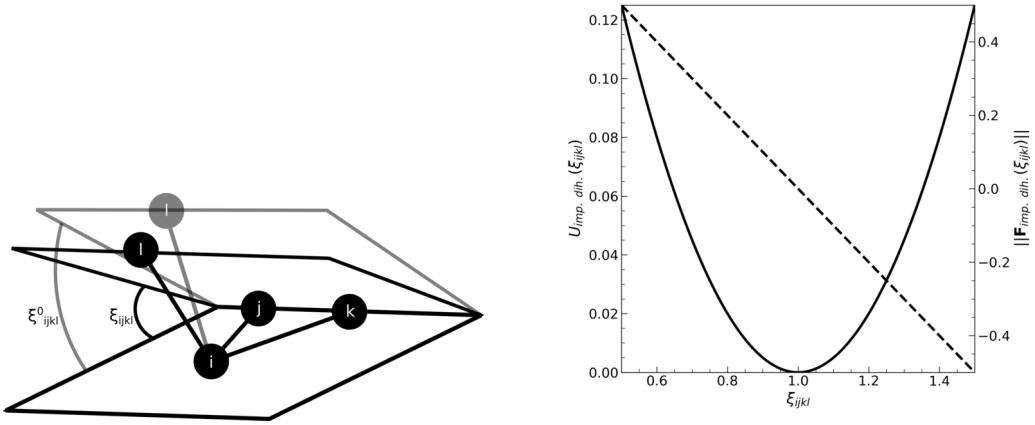

Figure 3.4: Schematics of the dihedral angle bending action between four bonded particles (left) along with graph of the potential (solid line, left axis) and signed force norm (dashed line, right axis) as a function of the improper dihedral angle (right). Graph is in arbitrary units.

$$U_{improper\ dihedral}(\xi_{ijkl}) = \frac{1}{2}k_{ijkl}(\xi_{ijkl} - \xi^0_{ijkl})^2 \tag{3.9}$$

Where ξ_{ijkl} is the improper dihedral angle between four bonded atoms, defined as the angle between the planes formed by the atoms *ijk* and *jkl*. The term k_{ijkl} represents the force constant for this contribution, and ξ^0_{ijkl} denotes the equilibrium value of the improper dihedral angle. Consequently, the forcefield-specific parameters in this context are k_{ijkl} and ξ^0_{ijkl}.

3.1.2.5 Van der Waals Interactions

A type of non-bonded interaction that describes the intermolecular forces acting between particles. The most commonly used potential is the Lennard-Jones potential, which consists of both an attractive and a repulsive term. It is formulated as follows in Equation 3.10:

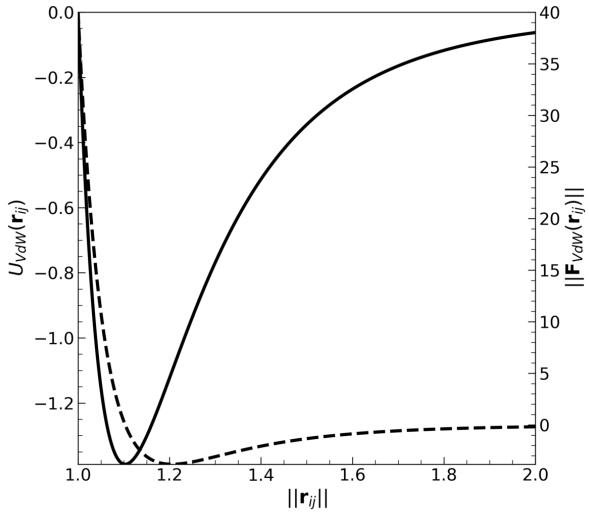

Figure 3.5: Graph of the Lennard-Jones potential energy (solid line, left axis) and signed force norm (dashed line, right axis) as a function of particle distance. Graph is in arbitrary units.

$$U_{VdW}(\mathbf{r}_{ij}) = 4\varepsilon_{ij}\left(\left(\frac{\sigma_{ij}}{||\mathbf{r}_{ij}||}\right)^{12} - \left(\frac{\sigma_{ij}}{||\mathbf{r}_{ij}||}\right)^{6}\right) \tag{3.10}$$

Where ε_{ij} represents the depth of the potential well, σ_{ij} dictates the distance at which the van der Waals potential between the two interacting particles is at minimum and $||\mathbf{r}_{ij}||$ is the distance between the pair of particles. Thus, ε_{ij} and σ_{ij} are the forcefield-dependent parameters in this case. Another approach to describe van der Waals forces is the Buckingham potential, which is more accurate than the Lennard-Jones function but at the expense of increased computational cost.

3.1.2.6 Electrostatic Interactions

The coulomb potential dictates how (partially) charged particles interact via the electrostatic interactions. The potential takes the form:

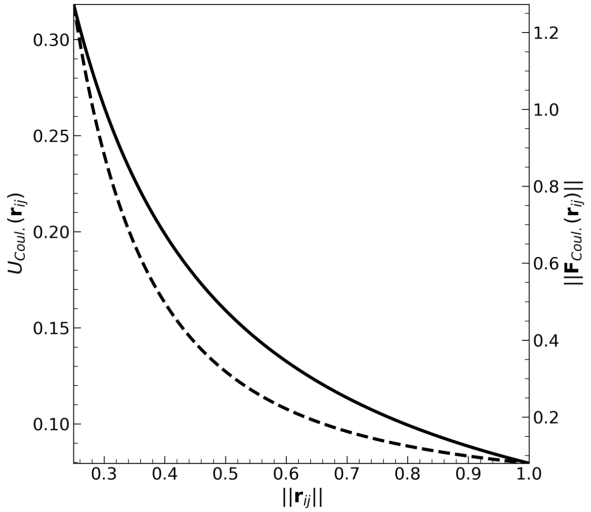

Figure 3.6: Graph of the Coulomb potential energy (solid line, left axis) and signed force norm (dashed line, right axis) as a function of particle distance. Graph is in arbitrary units.

$$U_{electrostatic}(\mathbf{r}_{ij}) = \frac{q_i q_j}{4\pi\varepsilon_0\varepsilon||\mathbf{r}_{ij}||} \tag{3.11}$$

where q_i and q_j are the electric charges of the two interacting particles, ε_0 and ε represent the dielectric constant of vacuum and the simulation medium, respectively, and $||\mathbf{r}_{ij}||$ is the distance between the pair of particles. For electrostatic interactions, the forcefield-dependent parameters are the charges q.

It should be noted that, in MD simulations, the calculation of long-range electrostatic interactions is computationally expensive. To address this, the Particle-Mesh Ewald (PME) method[419] is commonly employed. This technique splits the Coulomb potential into short-range and long-range contributions:

$$\frac{1}{||\mathbf{r}_{ij}||} = \frac{\text{erfc}(\beta||\mathbf{r}_{ij}||)}{||\mathbf{r}_{ij}||} + \frac{\text{erf}(\beta||\mathbf{r}_{ij}||)}{||\mathbf{r}_{ij}||} \tag{3.12}$$

where erfc and erf are the complementary error function and error function, respectively, and β is the Ewald convergence parameter.

In the PME method, the charge distribution is discretised onto a grid, allowing for efficient computation of the long-range interactions. The structure factor $S(\mathbf{m})$ is defined as:

$$S(\mathbf{m}) = \sum_{j=1}^{N} q_j \exp(2\pi i \mathbf{m} \cdot \mathbf{r}_j) \tag{3.13}$$

where $\mathbf{m}$ are the reciprocal lattice vectors, defined as $\mathbf{m} = m_1\mathbf{a}_1^* + m_2\mathbf{a}_2^* + m_3\mathbf{a}_3^*$, with m_1, m_2, m_3 being integers and $\mathbf{a}_i^*$ the reciprocal lattice basis vectors.

The total electrostatic energy in the PME method can be expressed as the sum of three terms:

$$U_{electrostatic} = U_{dir} + U_{rec} + U_{corr} \tag{3.14}$$

$$U_{dir} = \frac{1}{2} \sum_{n}^{*} \sum_{i,j=1}^{N} \frac{q_i q_j \text{erfc}(\beta ||\mathbf{r}_j - \mathbf{r}_i + \mathbf{n}||)}{||\mathbf{r}_j - \mathbf{r}_i + \mathbf{n}||} \tag{3.15}$$

$$U_{rec} = \frac{1}{2\pi V} \sum_{\mathbf{m} \neq 0} \frac{\exp(-\pi^2 \mathbf{m}^2 / \beta^2)}{\mathbf{m}^2} S(\mathbf{m}) S(-\mathbf{m}) \tag{3.16}$$

$$U_{corr} = -\frac{\beta}{\sqrt{\pi}} \sum_{i=1}^{N} q_i^2 \tag{3.17}$$

Here, U_{dir} is the direct sum in real space, U_{rec} is the reciprocal sum in Fourier space, and U_{corr} is a correction term. The asterisk in the direct sum indicates that terms with $i = j$ when $\mathbf{n} = 0$ are omitted.

The PME method approximates the structure factors using B-spline interpolation and evaluates the reciprocal sum using Fast Fourier Transforms (FFT)[420]. This approach significantly improves computational efficiency, especially for large systems, while maintaining high accuracy. The computational complexity of PME scales as $\mathcal{O}(N \log N)$, where N is the number of particles, making it more efficient than the standard Ewald summation for systems with many particles.

3.1.3 Levels of Resolution in Forcefields

In the previous section, the term *particle* was used instead of *atom*. This choice was deliberate. Fundamentally, forcefields are discrete mathematical representations of physical systems, and these descriptions are not necessarily atomistic.

Forcefields can be categorised based on their level of resolution, or more specifically, what the particles in the forcefield represent: atoms or groups of atoms. This section discusses three commonly used resolution levels in MD simulations and describes the specific forcefields utilised in this Thesis.

3.1.3.1 All Atoms: CHARMM 36M & Slipids

The highest level of resolution in a classical Molecular Dynamics simulation that neglects electron effects is achieved when each particle in the simulation represents an individual atom. Forcefields falling under this category are known as atomistic or All Atoms (AA) forcefields.

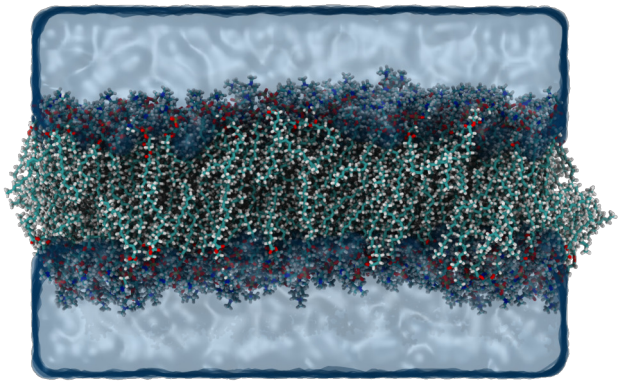

Figure 3.7: Molecular representation of a POPC membrane at the AA level. Carbon atoms are shown in cyan, Hydrogen atoms in white, Oxygen atoms in red, Phosphorus atoms in brown, and Nitrogen atoms in blue. Water is shown as a transparent blue surface.

CHARMM 36M[421] (Figure 3.7) is a widely used example of an AA parameterisation, employed for the general-purpose simulation of biological systems, from proteins to nucleic acids and lipids. It is an additive forcefield, using the potential energy forms described in Section 3.1.2. This set of parameters was employed for the comparison of multicomponent lipid membranes (Sections 2.1 & 4.1) and in the study of the effects of ultrasound waves on the structure of different membrane compositions (Sections 2.3 & 4.3).

Slipids[269], on the other hand, is another AA parameterisation specifically designed for simulations of lipid systems, originally developed to be compatible with AMBER. The forcefield was developed by tuning it to accurately reproduce X-ray and neutron scattering experiments, as well as deuterium order parameters from NMR studies. This set of parameters was used in the comparison of multicomponent lipid membranes (Sections 2.1 & 4.1).

3.1.3.2 United Atoms: GROMOS-CKP & GROMOS-H2Q

The next level of resolution corresponds to forcefields that do not explicitly represent all of the atoms in the system to be simulated, but instead group non-polar Hydrogens with the heavy atoms they are attached to, creating a single particle that represents that grouping. Polar Hydrogens, however, are still represented individually as distinct particles. These are called

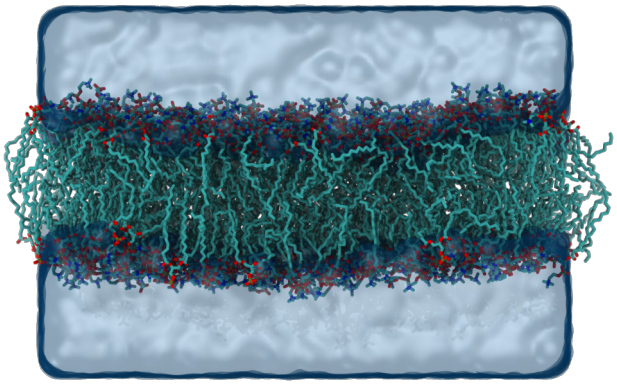

Figure 3.8: Molecular representation of a POPC membrane at the UA level. Aliphatic motifs are shown in cyan, Oxygen atoms in red, Phosphorus atoms in brown, and Nitrogen atoms in blue. Water is shown as a transparent blue surface

United Atoms (UA) forcefields. This approach significantly reduces the degrees of freedom of the system, thus speeding up computation, at the cost of spatial resolution and accuracy (further discussed in subsequent sections).

GROMOS-CKP[319] exemplifies a UA parameterisation. It is specifically designed for simulations of lipid systems based on the GROMOS 54a7 general-purpose forcefield. This set of parameters was used in the comparison of multicomponent lipid membranes (Sections 2.1 & 4.1).

GROMOS-H2Q[422, 423] refers to the utilisation of the isotope exchange technique (Hydrogen to Quadium, H2Q) to increase the simulation speed. By substituting all polar Hydrogens with the four-fold heavier Quadium, the vibrational frequency associated with the bond where the substitution has occurred is greatly reduced, thus allowing for larger timesteps (further discussed in subsequent sections). This variant of the GROMOS parameters was employed for the comparative study of multicomponent membranes (Sections 2.1 & 4.1).

3.1.3.3 Coarse Grained: Martini 2 & 3

Finally, when a forcefield groups several heavy atoms and their attached Hydrogens into a single particle, it falls under the category of Coarse Grained (CG) parameterisations. The particle in this context is typically referred to as a *bead*. This approach, similar to the UA approach, greatly reduces the degrees of freedom in the system representation, significantly reducing computational costs, but again at the expense of spatio-temporal resolution.

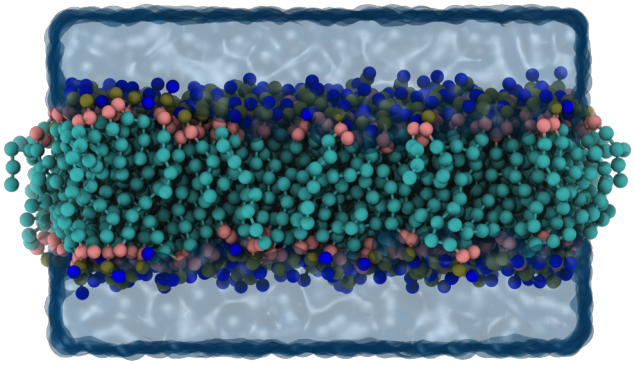

Figure 3.9: Molecular representation of a POPC membrane at the CG level. Aliphatic motifs are shown in cyan, glycerol groups in salmon, phosphate groups in brown, and choline groups in blue. Water is shown as a transparent blue surface.

Martini 2 and Martini 3[321–323] are among the most well-known CG forcefields for general-use simulations of biological systems. Their parameterisation clusters, on average, four heavy atoms with their attached Hydrogens (if present) into a single bead, producing particles that represent complete functional groups. The philosophy behind their parameter set development was to maintain partition free energies consistent with their AA counterparts.

In the present Thesis, these CG forcefields were employed in the work involving the search for hierarchical structures in lipid membranes (Sections 2.2 & 4.2) and for all the work involving ultrasound-induced deformations (Sections 2.3, 4.3 & 4.4).

3.1.4 Boundary Conditions

In Molecular Dynamics simulations, boundary conditions play a crucial role in mimicking the behaviour of large systems while using a computationally manageable number of particles. The most commonly employed boundary condition is the Periodic Boundary Condition (PBC).

In PBC, the simulation box is replicated infinitely in all directions. When a particle moves out of the primary simulation box, it re-enters from the opposite side. This approach effectively eliminates surface effects and allows the simulation of bulk properties using a relatively small number of particles. Mathematically, for a cubic box of length L, the position $\mathbf{r}$ of a particle is adjusted as:

$$\mathbf{r}_{\text{adjusted}} = \mathbf{r} - L \cdot \text{round}\left(\frac{\mathbf{r}}{L}\right) \tag{3.18}$$

Here, the round function rounds each component to the nearest integer. While PBC is widely used, it is important to note that it presents some limitations: the system size must be larger than the range of any relevant interactions to prevent the particles from interacting with their own periodic images and, additionally, PBC can suppress long-wavelength fluctuations, which may be important in some systems, particularly those near phase transitions.

Other boundary conditions exist, such as rigid walls for simulating confined systems or stochastic boundaries for simulating systems coupled to a thermal bath. The choice of boundary condition depends on the specific system and properties being studied.

3.1.5 The Algorithms

The Molecular Dynamics pipeline requires more than equations and their parameters. Instructions must be provided to the computer regarding the handling of these mathematical objects to produce the desired results. This section examines the most relevant algorithms within an MD simulation, with a detailed explanation of those utilised in this Thesis research.

3.1.5.1 Integrators

Among the most fundamentally relevant algorithms in the Molecular Dynamics pipeline are the integrators. As simulation is, at its core, obtaining the solution for differential equations, these algorithms perform precisely that function. They are responsible for evolving systems in time, transforming a potential energy landscape into moving particles, and minimising the system's energy in the preliminary steps before putting a simulation into production.

For energy minimisation, one of the most widely used algorithm is the steepest descent[424] scheme. It takes the form:

$$\mathbf{r}_{n+1} = \mathbf{r}_n + \frac{-\nabla U(\mathbf{r}_n)}{\max\left(||-\nabla U(\mathbf{r}_n)||\right)} h_n \tag{3.19}$$

This algorithm updates the positions of the system particles in the n^{th} step, $\mathbf{r}_n$, by computing the negative gradient of the potential energy $-\nabla U(\mathbf{r}_n)$ (*i.e.*, the Force), normalises it by dividing by the maximum calculated computed force, and then multiplies it by the maximum allowed permissible displacement h_n. Additionally, a criterion is added to dynamically update the maximum allowed step based on the potential energy:

$$\begin{cases} h_{n+1} = 1.2h_n & \text{if } U(\mathbf{r}_{n+1}) < U(\mathbf{r}_n) \\ h_{n+1} = 0.2h_n & \text{if } U(\mathbf{r}_{n+1}) \geq U(\mathbf{r}_n) \end{cases}$$

Other integrators used for energy minimisation include the Conjugate Gradient method[425], which uses optimised minimisation directions not to interfere with each other instead of using

the potential energy gradient, and the L-BFGS[426, 427] method, which uses an estimation of the potential's Hessian to compute the minimisation directions. A detailed explanation of both methods is beyond the scope of this work.

On the other hand, to evolve the system over time an integrator is required to solve the second-order differential equation 3.2, introduced in Section 3.1.1. One of the most widely used algorithms, and the one consistently employed in this Thesis, is the Leap-Frog algorithm[428]. It takes the form:

$$\mathbf{v}(t + \frac{1}{2}\Delta t) = \mathbf{v}(t - \frac{1}{2}\Delta t) + \frac{-\nabla U(\mathbf{r}(t))\Delta t}{m} \tag{3.20}$$

$$\mathbf{r}(t + \Delta t) = \mathbf{r}(t) + \Delta t \mathbf{v}(t + \frac{1}{2}\Delta t) \tag{3.21}$$

The name of this integrator derives from the fact that the positions **r** and velocities **v** of the system particles are updated in interlacing timesteps, that is, they are staggered. It should be noted that the velocity at the previous half-step is required to compute the velocity at the next half-step, which is then used to update the positions to the next whole step. The Leap-Frog algorithm belongs to the family of symplectic integrators, allowing for the conservation of the system's energy and being time-reversible, making it an excellent choice for computing the evolution of dynamical systems.

It should be noted that this integrator is stable as long as $\Delta t < \frac{2}{\omega}$, with ω being the frequency associated with the fastest mode present in the simulation. This relates to the discussion in Section 3.1.2. When explicit Hydrogens are present, the fastest mode of the simulation will be the vibration related to their bonds. Thus, if these Hydrogens are represented implicitly in a single particle with their accompanying heavy atom, those modes disappear from the simulation, and the next fastest modes will have a lower frequency, which allows for larger Δt. Moreover, as their frequency is proportional to their mass, artificially increasing the mass of the remaining polar, explicit Hydrogens also reduces the frequency, therefore also allowing for greater timesteps. The reader is referred to the work by K. A. Feenstra and co-workers[429] for an in-depth discussion of this topic.

Another example of an integrator for the equations of motion is the velocity-Verlet integration scheme[430]. This is a variant of the Leap-Frog algorithm with synchronous position and velocities, but requiring an extra step to calculate the gradient of the potential, twice for each integration cycle.

3.1.5.2 Calculators of Quantities

Some basic magnitudes were of special interest for the development of this Thesis, and therefore are deserving of a section explaining how they are computed within the MD pipeline. The magnitudes referred to are the kinetic energy (and thus the temperature), and the pressure of the simulated system.

Starting with the computation of the kinetic energy, it can be retrieved in its tensorial form as:

$$\mathbf{E}_{\text{Kin}} = \frac{1}{2}\sum_{i}^{N} m_i \mathbf{v}_i \otimes \mathbf{v}_i \tag{3.22}$$

Where the sum is over each particle of the total N particles in the system, m_i is the mass of the i^{th} particle and $\mathbf{v}_i$ is its velocity vector. The tensorial product $\otimes$ in this equation is crucial for capturing the directionality of the kinetic energy. For two vectors **a** and **b**, their tensorial (or outer) product is defined as:

$$\mathbf{a} \otimes \mathbf{b} = \mathbf{a}\mathbf{b}^T = \begin{pmatrix} a_x b_x & a_x b_y & a_x b_z \\ a_y b_x & a_y b_y & a_y b_z \\ a_z b_x & a_z b_y & a_z b_z \end{pmatrix} \tag{3.23}$$

In the context of kinetic energy, using the tensorial product $\mathbf{v}_i \otimes \mathbf{v}_i$ instead of the scalar product $\mathbf{v}_i \cdot \mathbf{v}_i$ preserves information about the direction of motion for each particle. This is particularly important when dealing with anisotropic systems or when analysing the system's behaviour along specific directions. Hence, the resulting kinetic energy tensor $\mathbf{E}_{\text{Kin.}}$ contains information about the kinetic energy contributions in all spatial dimensions and their cross-terms.

From the kinetic energy, we can retrieve the temperature of our system as:

$$T = \frac{2\text{Tr}\left[\mathbf{E}_{\text{Kin}}\right]}{N_{\text{df}} k_{\text{B}}} \tag{3.24}$$

Here, N_{df} represents the number of degrees of freedom of the system and k_{B} is Boltzmann's constant. The number of degrees of freedom is calculated as:

$$N_{\text{df}} = 3N - N_{\text{c}} - N_{\text{COM}} \tag{3.25}$$

Where N is the number of particles in the system, N_{c} is the number of constraints that might be applied to the system and $N_{\text{COM}} = 3$, as we remove the overall motion of the centre of mass of the whole simulated system.

Next, using the definition of the kinetic energy shown in Equation 3.22, we can retrieve the pressure tensor for our system. However, we must first define the Virial:

$$\boldsymbol{\Xi} = -\frac{1}{2} \sum_{i<j} \mathbf{r}_{ij} \otimes \mathbf{F}_{ij} \tag{3.26}$$

In this context, $\mathbf{r}_{ij}$ is the vector that connects the particles i and j, $\mathbf{F}_{ij}$ is the force arising from the interaction of the same two particles, and the sum is taken over every pair of particles. We can then use this definition to compute the pressure as:

$$\mathbf{P} = \frac{2}{V} \left(\mathbf{E}_{\text{Kin.}} - \boldsymbol{\Xi}\right) \tag{3.27}$$

3.1.5.3 Conservators of Magnitudes

After introducing these two magnitudes, some of the algorithms more commonly used to maintain them around a constant value during a simulation will be examined. In general, different magnitudes can be kept constant, permitting simulations under different thermodynamic ensembles. If the number of particles (N), the volume (V) and the total energy (E) of the system are kept constant, the simulation is said to be carried out in the microcanonical ensemble (NVE). In this case, since a symplectic integrator is used, the MD pipeline does not require further modification.

However, if the temperature (T) is to be kept constant instead of the energy, the canonical ensemble (NVT) is being used, entering the realm of thermostats. Thermostats are the family of algorithms that keep the simulation temperature constant, or more precisely around a constant value. Although many algorithms exist for this purpose, this manuscript will focus on one of the most frequently employed thermostats, applied throughout this Thesis: the Velocity-Rescale thermostat[431].

The V-Rescale thermostat is a variation of the Berendsen thermostat[432]. The latter is a weak first-order (with respect to temperature) coupling scheme and thus does not reproduce the canonical ensemble correctly, as it suppresses the natural fluctuations of the kinetic energy. To address this, the V-Rescale scheme adds a stochastic term, taking the form:

$$\mathrm{d}E_{\text{Kin}} = (E^0_{\text{Kin}} - E_{\text{Kin}})\frac{\mathrm{d}t}{\tau_T} + 2\sqrt{\frac{E_{\text{Kin}}E^0_{\text{Kin}}}{N_{\text{df}}}}\frac{\mathrm{d}W}{\sqrt{\tau_T}} \tag{3.28}$$

Where $E_{\text{Kin}} = \text{Tr}\left[\mathbf{E}_{\text{Kin}}\right]$ is the instantaneous kinetic energy of the system, E^0_{Kin} is the reference Kinetic energy for a given desired temperature (recall Equation 3.24 for their relation), $\mathrm{d}t$ is the simulation timestep, τ_T is the thermostat coupling constant, N_{df} are the degrees of freedom of the system and $\mathrm{d}W$ represents a Wiener process[433], which fundamentally models a stochastic random walk (think of, for example, Brownian motion).

The implementation of the fluctuations, represented by the Wiener process $\mathrm{d}W$, is crucial for the correct sampling of the canonical ensemble. As detailed in the original paper by Bussi *et al.*[431], the stochastic term is constructed to ensure that the kinetic energy distribution converges to the correct canonical distribution. This is achieved by drawing the new kinetic energy from the distribution:

$$P(E_{Kin}) \propto (E_{Kin})^{0.5N_{\text{df}}-1}\, e^{-\beta E_{Kin}} \tag{3.29}$$

where $\beta = \frac{1}{k_B T}$, with k_B being the Boltzmann constant and T the target temperature.The actual implementation involves generating a random number c according to:

$$c = (1-\alpha)R_1 + \alpha R_2 \tag{3.30}$$

where $\alpha = e^{-\Delta t/\tau_T}$, R_1 is drawn from a chi-square distribution with N_{df} degrees of freedom, and R_2 is drawn from a Gaussian distribution with zero mean and unit variance. The new kinetic energy is then computed as:

$$E^{new}_{Kin} = E^0_{kin}\frac{c^2}{N_{\text{df}}} + E_{Kin}(1-c) \tag{3.31}$$

This procedure ensures that the kinetic energy fluctuations are correctly represented, allowing the system to sample the canonical ensemble while maintaining the efficiency of the Berendsen thermostat in relaxing the system to the target temperature. This method scales the velocity of the atoms in the system through the kinetic energy (recall their relation through Equation 3.22) for a given temperature, hence the name.

On the other hand, when a constant pressure (P) and temperature are maintained allowing a variable volume, the isothermal-isobaric ensemble (NPT) is employed. This is typically the choice for most unbiased simulations performed within an MD framework, as it represents conditions commonly encountered in traditional laboratory setups. Thus, an algorithm to maintain constant pressure, that is, a barostat, is needed. This section focusses on two particular cases of interest. The first is the Berendsen barostat[432], which follows a first-order coupling scheme according to:

$$\frac{\mathrm{d}\mathbf{P}}{\mathrm{d}t} = \frac{\mathbf{P} - \mathbf{P}^0}{\tau_P} \tag{3.32}$$

It then scales the positions of the particles in the system through a scaling matrix, as follows:

$$\mathbf{R}' = \boldsymbol{\mu}\cdot\mathbf{R} \tag{3.33}$$

$$\mu_{ij} = \delta_{ij} - \frac{n_{\text{PC}}\Delta t}{3\tau_P}\beta_{ij}\left(P^0_{ij} - P_{ij}\right) \tag{3.34}$$

Here, $\mathbf{R}$ represents the vector of particle positions and $\boldsymbol{\mu}$ is the scaling matrix. This is a consequence of the fact that the pressure is a tensorial magnitude, according to Equation 3.27, where each element of the matrix is $\mu_{ij} = \mu_{ji}$. This allows for an independent control of the pressure of the simulation box for each spatial dimension. Thus, each component of the scaling matrix depends on the isothermal compressibility modulus β_{ij}, the instantaneous pressure felt along a given dimension P_{ij}, and the pressure to be maintained along that same dimension P^0_{ij}. Moreover, the Berendsen barostat also depends on two global parameters: n_{PC} representing the number of simulation steps after every barostat activation; and τ_P, which is the barostat coupling time constant.

The Berendsen barostat is ideal for equilibrating systems, as its first-order kinetics makes it robust against conditions deviating from equilibrium. However, equivalently to the Berendsen thermostat, this weak coupling scheme does not capture pressure dispersion properly, and thus does not represent the isothermal-isobaric ensemble faithfully, so it should not be used in production runs of free MD simulations. Despite this, the scheme is described here as subsequent sections will include modifications to it which were central to some of the work carried out in this Thesis.

Instead, other schemes have been developed for NPT simulations which conform to the required thermodynamic ensemble. The one used during this work was the Parrinello-Rahman barostat[434, 435]. It is a second-order scheme with respect to the simulation box vectors. These vectors now also have an equation of motion:

$$\frac{\mathrm{d}^2\mathbf{b}}{\mathrm{d}t^2} = V\mathbf{W}^{-1}\mathbf{b}^{\mathbf{T}^{-1}}\left(\mathbf{P} - \mathbf{P}^0\right) \tag{3.35}$$

Here, V is the volume of the system, $\mathbf{b}$ is the matrix of box vectors, and $\mathbf{W}$ is a matrix parameter that determines the strength of the coupling. This matrix takes the form:

$$\left(\mathbf{W}^{-1}\right)_{ij} = \frac{4\pi^2\beta_{ij}}{3\tau_P^2 L} \tag{3.36}$$

The parameters β_{ij} and τ_P have already been described, and in this case L represents the largest element of the box matrix. The addition of the equation of motion of the box vector implies that the conserved Hamiltonian is modified, which becomes:

$$\mathcal{H} = E_{\text{pot}} + E_{\text{kin}} + \sum_i P_{ii}V + \sum_{ij}\frac{1}{2}W_{ij}\left(\frac{\mathrm{d}b_{ij}}{\mathrm{d}t}\right)^2 \tag{3.37}$$

In this equation two additional terms are present, $\sum_i P_{ii}V$, which takes into account the work done by the barostat; and $\sum_{ij}\frac{1}{2}W_{ij}\left(\frac{\mathrm{d}b_{ij}}{\mathrm{d}t}\right)^2$ which is a term akin to the kinetic energy carried by the box vectors. Hence, when the equations of motion for the particles are derived from the previous Hamiltonian, a modification to what was described in Equation 3.2 is arrived at, adding an extra first-order term that appears as a fictitious friction, a consequence of the Parrinello-Rahman barostat being defined with respect to the box vectors:

$$\frac{\mathrm{d}^2\mathbf{r}_i}{\mathrm{d}t^2} = \frac{-\nabla U(\mathbf{r}_i)}{m_i} - \mathbf{M}\frac{\mathrm{d}\mathbf{r}_i}{\mathrm{d}t} \tag{3.38}$$

$$\mathbf{M} = \mathbf{b}^{-1}\left[\mathbf{b}\frac{\mathrm{d}\mathbf{b}^T}{\mathrm{d}t} + \frac{\mathrm{d}\mathbf{b}}{\mathrm{d}t}\mathbf{b}^T\right]\mathbf{b}^{T^{-1}} \tag{3.39}$$

3.1.5.4 Minimal Description of the Molecular Dynamics Pipeline

After introducing and discussing some of the most fundamental aspects of a Molecular Dynamics simulation, a typical MD pipeline can be summarised in the following steps:

1. **Initialisation:** Set up the initial configuration of particles, assign initial velocities (often from a Maxwell-Boltzmann distribution), and define simulation parameters.

2. **Force Calculation:** Compute the forces acting on each particle based on the potential energy function (forcefield).

3. **Integration:** Update particle positions and velocities using an integration algorithm (*e.g.*, Leap-Frog or Velocity Verlet).

4. **Thermostat/Barostat Application:** Adjust velocities and/or positions to maintain desired temperature and/or pressure.

5. **Periodic Boundary Conditions:** Apply boundary conditions to keep particles within the simulation box.

6. **Data Collection:** Calculate and store relevant physical quantities (*e.g.*, energies, temperatures, pressures).

7. **Repeat:** Iterate steps 2-6 for the desired number of timesteps.

8. **Analysis:** Process the collected data to compute properties of interest.

This basic pipeline is typically implemented within a loop structure, where each iteration represents a single timestep of the simulation. The specific implementation details may vary depending on the MD software package used and the particular system being studied.

This section has described some of the algorithms and mathematical tools deemed most relevant for the work carried out for this Thesis. While this is but a superficial look at what the MD pipeline truly entails, it is hoped that it provides the reader with an understanding of its general outlook.

3.2 Measurements in the Presence of Deformations

As discussed in Section 2.2, one of the main objectives of this Thesis was to study the self-organisation of lipid membranes in equilibrium. The work was designed to simulate rather large membrane patches, which presented a challenge to overcome: deviations from planarity. The membranes were so large that their natural undulations and deformations became a non-negligible effect. Moreover, the challenge of highly deformed membranes was even more stringent in the following works dealing with ultrasound-induced deformations.

Hence, during the development of this study, a framework was devised to carry out measurements which are agnostic to such deformations, namely a Local Frame of Reference (LFR). Using this tool, different properties that characterise the mechanical state of a membrane are measured.

3.2.1 Membrane Parameterisation

The first step to obtaining a deformation-agnostic frame of reference for a planar membrane (or in fact any surface) is parameterisation. This does not refer to a forcefield but rather to a

way of mathematically describing a surface based on some parameter. For this work, the Monge gauge was chosen (Figure 3.10), building on the excellent work developed by Markus Deserno and colleagues[377, 436].

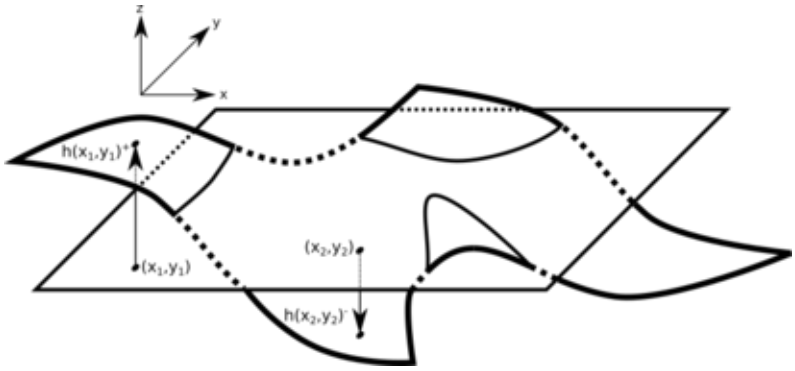

Figure 3.10: A schematic of Monge gauge applied over a square(ish) surface. Here, an arbitrary surface is overlaid over a flat, square plane such that a height function h can be taken for each (x, y) point.

Essentially, Monge Gauge parameterises a surface by a height function over the 'flat' configuration. Thus, for a square membrane patch, a flat plane that spans $X \cdot Y$ can be taken at an arbitrary Z position, which can be chosen as the Z component of the centre of mass of the bilayer. Then, a reference particle, or groups of particles, is chosen for each lipid and used to define the surface of the membrane. In the square bilayer shape, the height function is $h(x, y) = R_Z - COM_Z$, where R_Z is the Z position of the reference particle(s) taken.

To define this height function, the raw simulation data were read using the MDAnalysis[437, 438] package, and subsequent mathematical handling was performed through the NumPy library[439], in scripts written in Python 3.x.

3.2.2 Local Frame of Reference

With this in hand, a frame of reference can be built for each point in the bilayer. This is a set of orthonormal vectors $\{\mathbf{X}', \mathbf{Y}', \mathbf{Z}'\}$ that give a basis for the orientation of the membrane at each point on its surface. The construction begins as follows, first defining the local tangent vectors to the surface as:

$$\mathbf{e}_x = \left(1, 0, \frac{\partial h}{\partial x}\right); \ \mathbf{e}_y = \left(0, 1, \frac{\partial h}{\partial y}\right) \tag{3.40}$$

Then, the normal vector to the surface can be computed such as:

$$\mathbf{n} = \frac{\mathbf{e}_x \times \mathbf{e}_y}{|\mathbf{e}_x \times \mathbf{e}_y|} = \mathbf{Z}' \tag{3.41}$$

On the other hand, the total curvature of the surface can be computed as:

$$K = -\nabla \cdot \frac{\nabla h}{\sqrt{1 + (\nabla h)^2}} \tag{3.42}$$

Here, $\nabla \cdot \mathbf{f} = \dfrac{\partial f_x}{\partial x} + \dfrac{\partial f_y}{\partial y}$ is the divergence of a vector-valued function $\mathbf{f} = (f_x, f_y)$; and

$(\nabla h)^2 = \left(\frac{\partial h}{\partial x}\right)^2 + \left(\frac{\partial h}{\partial y}\right)^2$ refers to the square of the norm of the gradient of the aforementioned height function.

To obtain the LFR, the gradient of the curvature must first be considered. Let us begin by defining the partial derivatives of the curvature with respect to x and y:

$$\frac{\partial K}{\partial x} = K_x, \quad \frac{\partial K}{\partial y} = K_y \tag{3.43}$$

These components form a vector in the xy-plane:

$$\nabla_{xy} K = (K_x, K_y) \tag{3.44}$$

To extend this to a full three-dimensional gradient, we need to consider how the curvature changes along the surface normal. This can be approximated by projecting $\nabla_{xy} K$ onto the surface gradient ∇h:

$$K_n = \nabla_{xy} K \cdot \nabla h \tag{3.45}$$

Here, K_n represents the rate of change of curvature in the direction normal to the surface. Now, we can express the full gradient of the curvature as:

$$\nabla K = (K_x, K_y, K_n) \tag{3.46}$$

Hence, this magnitude indicates the direction along which the curvature of the membrane changes the most, *i.e.* its Anisocurvature. However, there is no guarantee that this direction is perpendicular to the normal vector. This can be resolved by taking a slight detour. If the direction of Isocurvature is defined as:

$$\mathbf{X}' = \frac{\mathbf{n} \times \nabla K}{|\mathbf{n} \times \nabla K|} \tag{3.47}$$

It is ensured that it is now perpendicular both to the normals and to the direction gradient of the curvature, which must point in the direction of least (or equal) curvature of the surface. Complementarily, Anisocurvature can be redefined as:

$$\mathbf{Y}' = \frac{\mathbf{n} \times \mathbf{X}'}{|\mathbf{n} \times \mathbf{X}'|} \tag{3.48}$$

All the mathematical operations involved in the calculation of these magnitudes were handled using Python 3.x scripts, using the NumPy library[439]. This approach was implemented for the HierarchyMem library[440] used in this Thesis, as well as in some generalist scripts, available in Github[441].

3.2.3 Eulerian vs. Lagrangian Discretisation of Surface Magnitudes

The previous section laid out the mathematical foundation to obtain the height function, normal vectors, curvature and a LFR for an arbitrary square surface. The mathematical framework deals with continuous surfaces; however, lipid membranes in general, and particularly in MD simulations, are discrete, composed of individual lipids. Thus, discretisation schemes are needed to compute the properties described in Equations 3.40 to 3.48. Two different schemes may be chosen, each with its advantages and disadvantages.

3.2.3.1 Eulerian Discretisation

Eulerian discretisation is perhaps the most straightforward scheme. It involves dividing the space into a regular grid, computing the desired magnitude for each point in the grid, where derivatives become a finite difference scheme. After defining said grid, a point of reference for each individual lipid is defined (usually an atom or atom group like the Phosphate), and a search is performed to decide which lipid falls within each grid cell. Then the average of the magnitude of interest (*e.g.* the position) for the found lipids is stored in the grid cell. For a grid spanning x and y, with cell indices $\{i, j\}$, where the grid cells have an area $\Delta x \cdot \Delta y$ and a function f needs to be differentiated at each cell of the grid, the finite difference scheme becomes:

$$\frac{\partial f(i,j)}{\partial x} \approx \frac{f(i+1,j) - f(i-1,j)}{2\Delta x}; \quad \frac{\partial f(i,j)}{\partial y} \approx \frac{f(i,j+1) - f(i,j-1)}{2\Delta y} \tag{3.49}$$

The advantages of this approach are that the regular grid facilitates differentiation on a computational level, as this becomes a highly parallelisable problem. On the other hand, the definition of the grid, namely the size of each grid cell, can be quite arbitrary or difficult to decide. If cells are too small, some may be empty as no lipids fall within the region they define; whereas if they are too large, a lot of spatial resolution can be lost and the finite-difference scheme becomes more imprecise. Moreover, the mere definition of a 2D grid to obtain the height function for Monge Gauge implies the loss of one spatial dimension, which is why some gradients can be ill-defined, as is the case for the curvature when using this discretisation scheme.

In this present Thesis, when this approach was used all mathematical handling was done with the NumPy library[439], and parallelisation schemes were built by leveraging the powerful Numba package[442], all in scripts written in Python 3.x. This approach was used in the HierarchyMem[440] library developed for this Thesis, as well as in some generalist scripts, also available in Github[441].

3.2.3.2 Lagrangian Discretisation

Alternatively, a Lagrangian approach to discretisation can be used. It has its basis in interpolation theory and has applications in other simulation fields like Smoothed-Particle Hydrodynamics[443]. The basic assumption is that the value of a function f at a point $\mathbf{x}'$ can be known by calculating the following integral, using the Dirac delta sifting property:

$$f(\mathbf{x}') = \int_{\Omega} f(\mathbf{x})\delta(\mathbf{x}' - \mathbf{x})\mathrm{d}^n\mathbf{x} \tag{3.50}$$

Here $f(\mathbf{x}')$ is a smooth function defined in the domain $\Omega \subseteq \mathbb{R}^n$ and evaluated at an arbitrary point $\mathbf{x}' \in \Omega$. The $\delta(\mathbf{x}' - \mathbf{x})$ is a Dirac delta, and this distribution is, in practice, approximated by a kernel function:

$$\langle f(\mathbf{x}')\rangle = \int_{\Omega} f(\mathbf{x})W(|\mathbf{x}' - \mathbf{x}|, h)\mathrm{d}^n\mathbf{x} \tag{3.51}$$

Now $\langle f(\mathbf{x}')\rangle$ is the expected value of $f(\mathbf{x}')$ and W is the interpolation smoothing kernel, with a smoothing length h. Desirable kernels must comply with a normalisation condition such that:

$$\int_{\Omega} W(|\mathbf{x}' - \mathbf{x}|, h)\mathrm{d}^n\mathbf{x} = 1 \tag{3.52}$$

They must also be even functions such that $W(|\mathbf{x}' - \mathbf{x}|, h) = W(|\mathbf{x} - \mathbf{x}'|, h)$, must be equal to the Dirac delta in the limit $h \to 0$, must be positive definite, monotonically decreasing and,

ideally, many times differentiable. This last condition is of special interest for the topic discussed here, as it can be shown that:

$$\langle \nabla f(\mathbf{x}') \rangle = \int_{\Omega} f(\mathbf{x}) \nabla W(|\mathbf{x}' - \mathbf{x}|, h) \mathrm{d}^n \mathbf{x} \tag{3.53}$$

This means the expected value of the gradient (and therefore any other derivative, as per the chain rule) of the function f is given by integrating said function times the gradient of the kernel, over the complete domain.

However, so far the discrete scheme has not been addressed. To do that, the previous integrals must be turned into discrete sums. More specifically, instead of integrating, a reference point for each n^{th} lipid will be selected, as in the previous case (again, the Phosphate group, for example), and the function of interest will be evaluated there giving f_n; then a discrete sum over all N lipids will be performed:

$$\langle f(\mathbf{x}') \rangle \approx \sum_{n}^{N} f_n W(|\mathbf{x}' - \mathbf{x}|, h) \tag{3.54}$$

$$\langle \nabla f(\mathbf{x}') \rangle \approx \sum_{n}^{N} f_n \nabla W(|\mathbf{x}' - \mathbf{x}|, h) \tag{3.55}$$

The advantage of Lagrangian discretisation is that it no longer relies on defining a grid over the membrane. This is particularly useful when dealing with membranes that deviate significantly from planarity or when their nominal shape is other than a square patch, as in the case of vesicles. This method also allows for the retention of spatial resolution, as the function of interest can be evaluated at any arbitrary position, and it does not intrinsically entail the loss of a spatial dimension. The downsides come from its interpolative foundations, as a satisfactory kernel must be chosen, and its smoothing length must be decided, which can be a difficult decision. Moreover, if no spatial decomposition scheme is applied, the sum over all lipids evaluated at each point scales with the worst case $\mathcal{O}(N^2)$, making it computationally expensive. However, this can be alleviated by using a spatial partitional algorithm, such as a kd-tree, as is the case of the present work, so the complexity can potentially be reduced to a best-case scenario of $\mathcal{O}(N \log(N))$. In all cases where this approach was used in this Thesis, the implementation was done through Python 3.x scripts using the NumPy library[439] for general mathematical handling, and using scikit-learn[444] for the kd-tree decomposition. This approach was used in the SurfParam library developed for this Thesis, available on Github[445].

3.3 Properties of Interest in a Lipid Membrane

Throughout this Thesis, several magnitudes were repeatedly determined, even for different objectives, as they characterise the mechanical state of a membrane at any given point in time. This section describes these magnitudes and provides insights into how they are computed from MD simulation data.

3.3.1 Thickness

Thickness is a fundamental property of any lipid bilayer. It characterises its width, and thus has implications for the mechanical properties of the bilayer and other processes, such as its resistance to permeation by other molecules. There are different ways to measure the thickness of a membrane, and two methods will be described here.

3.3.1.1 Using Phosphate Lateral Density

This method begins by choosing an atom or group of atoms, most commonly a Phosphate group, and calculating its lateral density along the Z dimension. This is calculated by dividing the simulation box into a given number of bins along Z, typically of the order of 1 Å in length, and computing a mass histogram on them, which in turn can be normalised into a probability density function (PDF) $p(Z)$. From this, a distribution appears showing two peaks. The histogram can be split at its midpoint to obtain two distributions: distribution A with bin midpoints Z^A and PDF $p(Z^A)$ related to the Phosphates of one leaflet; and distribution B with bin midpoints Z^B and PDF $p(Z^B)$, related to the Phosphates of the other leaflet. The target function for the thickness T is the distance between the two distributions $|A - B|$. Its expected value can be obtained as:

$$T = \langle |A - B| \rangle \approx \sum_{ij} |Z_i^A - Z_j^B| p(Z_i^A) p(Z_j^B) \tag{3.56}$$

Conversely, the variance of the thickness can be obtained as:

$$Var(T) = \langle |A - B|^2 \rangle - \langle |A - B| \rangle^2 \tag{3.57}$$

$$\langle |A - B|^2 \rangle \approx \sum_{ij} |Z_i^A - Z_j^B|^2 p(Z_i^A) p(Z_j^B) \tag{3.58}$$

Thus, this is a robust method to calculate the thickness of a bilayer as it provides both an average value and its dispersion, without making many assumptions about the underlying distributions governing lipid positions, as everything is numerically calculated from histograms. However, this method breaks down when deformations in the membrane are non-negligible, which happens frequently when working with bilayers from moderate to large sizes.

When implementing these techniques for the present Thesis, the reading of the simulation trajectory data was done through the MDAnalysis library[437, 438], and subsequent mathematical operations were handled through the NumPy package[439], all written in Python 3.x scripts. Examples of programs using this approach can be found in a Github repository[441].

3.3.1.2 Accounting for Deformations

Deformation-derived effects can be prevented by using the LFR, using the approach of discretising the membrane in a regular grid. Figure 3.11 shows a diagram depicting the relevant geometric parameters to correct the calculation of the thickness for a curved membrane.

In this approach, a normal vector at each discrete cell for each leaflet can be obtained by applying Equation 3.41. Then, the height function, which is parameterised as the average Z position of the Phosphates in each grid cell, as described in Section 3.2.3.1, can be corrected; and the thickness T can be calculated as:

$$h' = h \cdot (-\mathbf{N} \cdot \hat{\mathbf{Z}}) \tag{3.59}$$

$$T = h'_A - h'_B \tag{3.60}$$

Where the subscripts A and B refer to the corrected height function of each leaflet of the membrane. Note that by using this approach, statistical information about this magnitude can still be obtained, as per the discrete nature of the method, T can be computed for each pair of aligned grid cells for each leaflet, thus obtaining average and variance values.

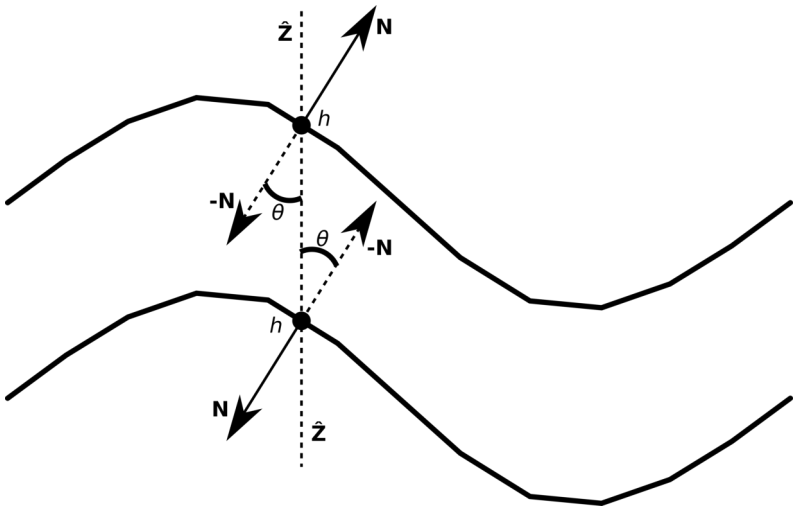

Figure 3.11: Diagram depicting the geometry of the cross-section of a curved membrane, discretised using a regular grid. The normal vector is represented as N, the vertical basis vector $\{0, 0, 1\}$ is represented as $\hat{\mathbf{Z}}$, the angle between those vectors is represented as θ, and the height function is represented as h.

In all cases where this approach was used, such as in its implementation for the HierarchyMem package[440]; or in generalist scripts[441] used through this present Thesis, MDAnalysis[437, 438] was used to read raw trajectory data and NumPy[439] was used to handle mathematical operations.

3.3.2 Radial Distribution Function

The Radial Distribution Function (RDF) between particles of type A and type B is defined as:

$$g_{AB}(r) = \frac{1}{\langle \rho_B \rangle_{local}} \frac{1}{N_A} \sum_{i \in A}^{N_A} \sum_{j \in B}^{N_B} \frac{\delta(r_{ij} - r)}{4\pi r^2} \tag{3.61}$$

Where $\langle \rho_B \rangle_{local}$ is the particle density of type B averaged over all spherical regions around all particles of type A with a radius r_{max}, $\delta(r_{ij} - r)$ is a Dirac delta (which is effectively approximated as a histogram for particle positions), and r_{ij} is the distance between the i^{th} particle of type A and the j^{th} particle of type B. The averaging is also performed over time.

The RDF is essentially a measure of the correlations between particles (or groups of particles) and can be interpreted as the probability of finding a particle at a given distance r from a reference particle, providing structural information about the system under study. In practice, for the specific case of lipid membranes, the RDFs are most commonly computed using the centres of mass of the PO_4 groups as reference particles. In all cases the RDFs were calculated the *gmx rdf* utility, available with the GROMACS simulation engines.

3.3.3 Hydrogen Bonds

Hydrogen Bonds (HBonds) are one of the most important ways two molecules or chemical groups can interact with each other in biological systems. Therefore, computing them in MD simulations is of great relevance. The method to do so is based purely on geometrical constraints. In this work, a HBond donor D and an acceptor A were defined to be participating in a hydrogen bond if:

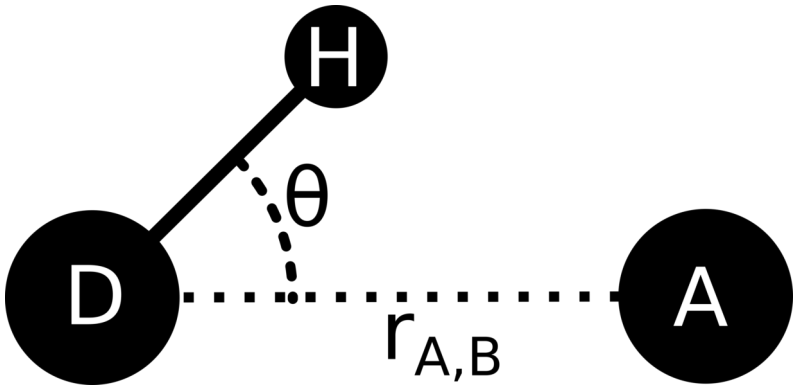

Figure 3.12: Schematic representation of the geometry of a Hydrogen Bond between a Donor (D) with its Hydrogen (H) and an Acceptor (A).

$$r_{AB} \leq r_{HB} = 0.35 \text{ nm} \tag{3.62}$$

$$\theta \leq \theta_{HB} = 30^{\circ} \tag{3.63}$$

In this Thesis, HBonds were calculated using the *gmx hbond* tool, available through the GROMACS simulation engine.

3.3.3.1 Normalisation of Hydrogen Bonds

Moreover, HBonds were calculated not only between different molecules (*e.g.* lipids and solvent) but between different chemical groups within the same molecule, namely: the headgroups of the lipids, defined to span from the Phosphorus atom of the Phosphate to the most external atom on the lipid head; and the glycerol of the lipids, defined to span from their Oxygen connecting to the Phosphate to the ester motifs of the aliphatic tails.

Because different lipid types have different chemical groups, with a varying number of Hydrogen bonding capabilities (not all of the groups have the same donors and/or acceptors), and because the solvent molecules exist in a far greater number than lipids in an MD simulation, a normalisation criterion is needed to account for these different amounts of molecules and their respective bonding capabilities. This normalisation of HBonds between groups A and B is calculated as:

$$N_{norm}(A,B) = \frac{N_{obs}(A,B)}{N_{max} \cdot [P(A) + P(B)]} \tag{3.64}$$

Where $N_{obs}(A,B)$ is the observed number of H-bonds between types A and B, and N_{max} represents the total number of H-bonds that could *a priori* exist within the entire system. The probability of molecule A or B forming an H-bond, denoted as $P(A)$ or $P(B)$ respectively, is derived from their relative abundances and bonding capabilities. For instance, in a simulation with various molecule types, let's assume that there are n_i molecules of the molecule i, each capable of forming χ_i HBonds, thus:

$$N_{max} = \sum_i \chi_i \cdot n_i \tag{3.65}$$

where i iterates over the total number of different molecule types in the system. The probability for the type A can be defined as:

$$P(A) = \frac{\chi_A \cdot n_A}{N_{max}} \tag{3.66}$$

This approach yields a dimensionless metric, effectively correcting for biases related to the diverse H-bonding capacities and varying molecule quantities across different species. It should be noted that this approach involves setting maximum H-bond counts for different atomic species: neutral Oxygen atoms can form two H-bonds based on two lone electron pairs, negatively charged Oxygen atoms up to three due to an extra lone pair, and each polar Hydrogen atom can form one H-bond as a donor.

The normalisation of HBonds was done through Python 3.x scripts, handling mathematical operations with the NumPy library[439]. Examples of this approach can be found in a Github repository[441] with generalist scripts used in this Thesis.

3.3.4 Diffusion Coefficients

The diffusion coefficients of the lipids within a bilayer relate to its fluidity and mechanical properties. They are, simply put, a measure of how fast lipids move and change position in the membrane. The method used in this work was proposed by Perttu S. Niemelä and colleagues[286], implemented in a Python script available in the generalist Github repository[441], and is described below.

Assuming that the lipids are distributed on an almost flat membrane spanning the XY plane, the lateral displacement l_{xy} of a lipid with position $\mathbf{r}(t) = \{x(t), y(t), z(t)\}$ is calculated for a time window Δt as follows:

$$l_{xy} = \sqrt{(x(t+\Delta t) - x(t))^2 + (y(t+\Delta t) - y(t))^2} \tag{3.67}$$

This magnitude is calculated for all of the lipids and for a given period of time, obtaining a set of lateral displacements. From this set, a probability density function $P(l_{xy}, \Delta t)$ can be estimated using a histogram. Niemelä *et al.* propose that this probability density function can be fitted to a 2D random walk equation:

$$P(l_{xy}, \Delta t) = \frac{l_{xy}}{2 \cdot D \cdot \Delta t} \exp\left[-\frac{l_{xy}^2}{4 \cdot D \cdot \Delta t}\right] \tag{3.68}$$

Where D represents the observed diffusion coefficient for a given Δt. Thus, by numerically fitting Equation 3.68, a diffusion coefficient can be estimated for the molecules in the system.

3.3.5 Area per Lipid

Area per Lipid (APL) is one of the most relevant properties that can be measured for a lipid bilayer. It is a measure of the lipid packing and is directly related to the thermodynamical phase of the membrane, and thus to its mechanical properties. Furthermore, it can be experimentally estimated in wet-lab protocols, making it a direct link between simulation and the real world.

The simplest way to obtain the APL from a bilayer simulation is by dividing the simulation box area in XY by the number of lipids in each leaflet:

$$APL = \frac{X \cdot Y}{N_L} \tag{3.69}$$

This approach to calculate the APL was implemented in Python 3.x scripts, available in Github[441], where the simulation box areas were read through the pyedr package[446], and mathematical operations were handled using NumPy[439].

However, this method is inadequate for bilayers with significant deformations or membranes with shapes that deviate from a flat square, such as vesicles. To address this limitation, alternative methods have been developed. This section describes a technique based on the work of

H. Bhatia and colleagues[447], and implemented in the SurfParam Python package developed during this Thesis[445]. The method employs Poisson surface reconstruction, followed by UV parameterisation of the resulting surface to obtain a conformal map. Subsequently, a Delaunay triangulation is performed on the original points projected onto the conformal map. This process yields a precise measure of the area per lipid, even for complex membrane geometries.

3.3.5.1 Poisson Surface Reconstruction

Poisson Surface Reconstruction[448] (PSR) is a technique mainly used in computer graphics to obtain a smooth, 'water tight', surface from a point cloud. If the surface of a leaflet from a bilayer is considered to be arising from, for example, the previously used Phosphate groups, a point cloud in 3D space is already available. However, PSR requires that each point have an associated normal vector. To obtain these, Equation 3.41 can be used, in combination with a Lagrangian approach to differentiation discussed in Section 3.2.3.2. This requires a parametric function h for the surface, which can be difficult to obtain for bilayer shapes that deviate significantly from nominal shapes. Thus, it is preferable to have a method to estimate the normal vector at each point that is agnostic to the overall shape of the surface.

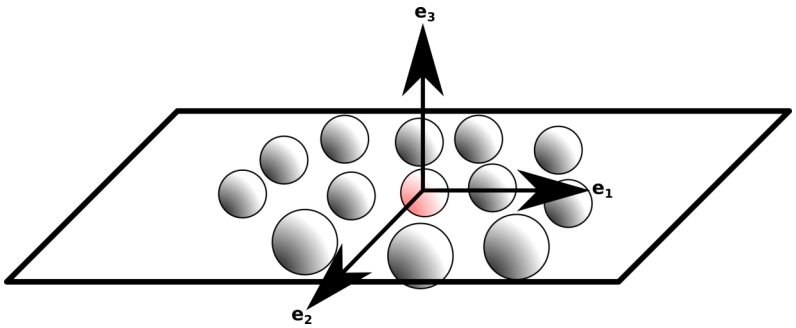

Figure 3.13: Diagram showing the principal components of a small point cloud. The central point (red hue) is surrounded by K neighbours (grey hue). After applying PCA a best-fitting plane (black square) is found with three orthonormal vectors $\{\mathbf{e_1}, \mathbf{e_2}, \mathbf{e_3}\}$, pointing in the directions of most to least variance, respectively.

For this purpose, a method based on estimating the principal components (*i.e.*, the eigenvectors) of a subset of points that form a local point cloud can be applied, as schematically depicted in Figure 3.13. First, for each point for which the normal vector is to be calculated, its K nearest neighbours can be obtained. Consideration must be given to selecting K, as too large a value will render a subset of points with too many non-local effects (they could define a curved surface), whereas too small a value will make the points not aligned with any particular flat plane, thus not having any particular normal vector. A suitable choice is usually on the order of tens of neighbours. There are many algorithms and implementations for this, and the scikit-learn Python package[444] was used in this work. Using this subset of points, a Principal Component Analysis (PCA) can be performed over the matrix defined by their 3D position vectors. Many different methods exist for this too, and the NumPy[449] package was used in this work. Hence, the eigenvector with the associated smallest eigenvalue will be an estimation of the normal vector (labelled $\mathbf{e_3}$ in Figure 3.13), since it is the direction of least variance.

Once a normal vector for each point is calculated, a vector field $\mathbb{N}$ is obtained. Thus, the Poisson equation in this context states that:

$$\nabla^2 \varphi = \nabla \cdot \mathbb{N} \tag{3.70}$$

This means that the Laplacian $\nabla^2 := \frac{\partial^2}{\partial x^2} + \frac{\partial^2}{\partial y^2} + \frac{\partial^2}{\partial z^2}$ of a scalar field φ is equal to the divergence of the normal vector field $\mathbb{N}$. Therefore, solving the Poisson equation involves finding the best-fitting scalar field given a set of points with their respective normals. Then, once φ is computed, an isosurface is obtained at its zero level, via a marching-cubes[450] algorithm. These two steps were handled using the Open3d[451] Python library. This isosurface will be the best-fitting surface for the input points, and it is guaranteed that there will be no holes in it. It should be noted that the surface will not necessarily pass through the input points, but will be a smooth interpolation of them. When the surface is constructed with an *in-memory* representation in a computer, it will be stored as a collection of polygons sharing vertices and thus connected by their sides. Because the reconstructed surface is a smooth interpolation of the input points, there is no guarantee that there will be as many vertices in the surface as there are input points. The usual case will have a reconstructed surface with many more vertices than input points. Therefore, a numerical projection method of the input points over the smooth surface is required.

3.3.5.2 UV Mapping

As mentioned in the beginning of Section 3.3.5, at the core of this method to compute the APL lies a Delaunay triangulation. However, although this triangulation can be defined on 3D points, for this particular case it needs to be performed solely over the surface of the membrane, thus collapsing one dimension and working in 2D. This is a rather non-trivial task, as it depends on the original geometry of the points defining the surface.

Fortunately, primarily due to research in computer graphics, several tools exist to solve this problem. UV mapping (Figure 3.14) comprises a family of techniques that unwrap a mesh defining a surface, closed or not, and map it to a lower-dimensional space, similar to what an atlas is to a globe. In this context, UV mapping refers to the process of projecting the 3D Poisson surface of the membrane onto a 2D plane. The letters 'U' and 'V' represent the coordinates in this 2D space, analogous to how 'X', 'Y', and 'Z' represent coordinates in 3D space. This mapping allows for the complex 3D geometry of the membrane to be represented and analysed in a simplified 2D form while preserving essential geometric properties.

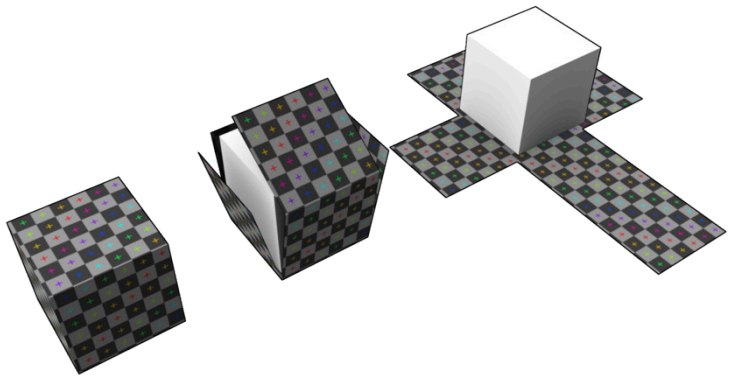

Figure 3.14: Schematic representation of a UV map of a mesh wrapping a cube. Image by Zephyris, licensed under a Creative Commons License, via Wikimedia Commons[452].

Specifically, this work utilises Angle-Based Flattening (ABF)[453] to construct UV maps of the Poisson surfaces built as described in the previous section. ABF is a technique that operates on triangular meshes and is particularly useful since it preserves, as much as possible, the angles defining the faces of the original mesh. This prevents distortion when mapping to the 2D plane and preserves the internal geometry of the points. At the core of this technique lies the solution of a nonlinear system of equations that minimise the distortion of the mesh angles in each face. The actual implementation of this step was carried out through the Blender Python API[454].

3.3.5.3 Point projection on UV map

Once the mesh is unwrapped as described in the previous section, a 2D representation of a 3D surface is obtained. However, it must be remembered that a Poisson surface is a smooth interpolation of the input points, which will not necessarily have its vertices in the same position as them. Therefore, the original points need to be projected onto the UV map to allow for the ensuing triangulation step.

To project the original points in the UV space, a series of operations are followed, the first of which is computing the centroids for all the triangular faces of the Poisson surface. Next, for each original point, the centroid (and therefore the face) closest to it is calculated. Let the triangular face ΔABC be defined by the vertices A, B and C; and let the point to project be P. Barycentric coordinates can be used to express the point as:

$$P = \alpha A + \beta B + \gamma C \tag{3.71}$$

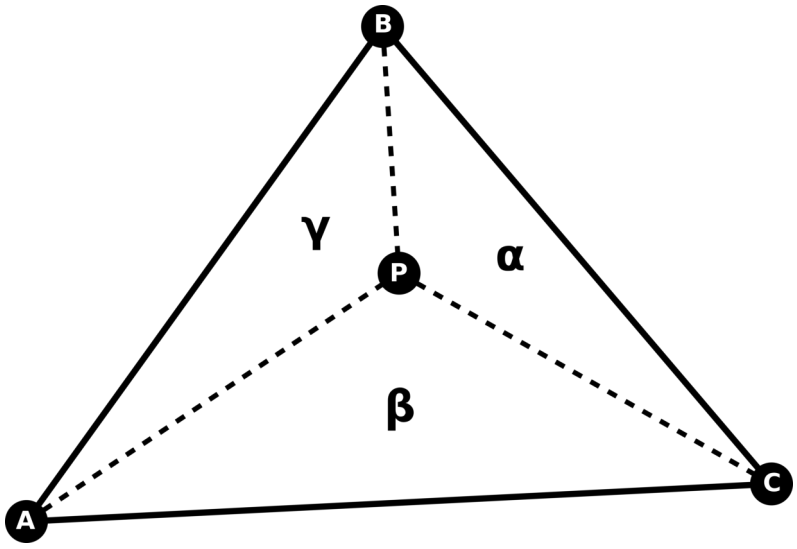

Figure 3.15: Schematics showing the barycentric coordinates of a point P in a triangle ΔABC.

The barycentric coordinates are proportional to the area of the subtriangle formed by the point P and the opposite side of the vertex corresponding to that coordinate (Figure 3.15). These coordinates are normalised such that $\alpha + \beta + \gamma = 1$. Furthermore, if P lies within ΔABC, all barycentric coordinates are equal to or greater than zero; if the point lies on any of the edges, one or more coordinates will be exactly zero; and if the point lies outside the triangle, one or more coordinate will be negative.

This property can be exploited to project the point onto the plane defined by the triangle by clamping α, β and γ, forcing them to be positive and their sum to add up to 1. For instance, if α is negative, $\alpha' = 0$ is set and the rest of the coordinates renormalised:

$$\beta' = \frac{\beta}{\beta + \gamma} \tag{3.72}$$

$$\gamma' = \frac{\gamma}{\beta + \gamma} \tag{3.73}$$

$$P' = \alpha' A + \beta' B + \gamma' C \tag{3.74}$$

Therefore, P' is ensured to lie perfectly aligned with ΔABC. However, the point must be projected onto the UV map. The fact that by performing an Angle-Based Flattening the internal geometry of the faces has been maintained can be exploited, and hence the barycentric coordinates remain the same. Let triangle ΔABC have coordinates A_{UV}, B_{UV}, C_{UV} on the UV map, the projection of P onto it is given by:

$$P'_{UV} = \alpha' A_{UV} + \beta' B_{UV} + \gamma' C_{UV} \tag{3.75}$$

3.3.5.4 Delaunay Triangulation

The Delaunay triangulation is a mesh-generation method that takes a set of points $\mathbb{P} = \{P_1, P_2, ..., P_n\}$ and outputs a mesh where its faces are defined by triangles $\Delta = \{P_i, P_j, P_k\} \in \mathbb{P}$ subdividing the convex hull (the smallest shape that can fully enclose all the points, akin to stretching a rubber band around them) of $\mathbb{P}$. This triangulation method is of particular interest as the circumcircles of the triangles do not contain any other points, and it maximises the smallest angle of the triangles.

In the method described here, the Delaunay triangulation is performed over the UV coordinates of the input points. Subsequently, the connectivity of the mesh is retrieved, that is, the

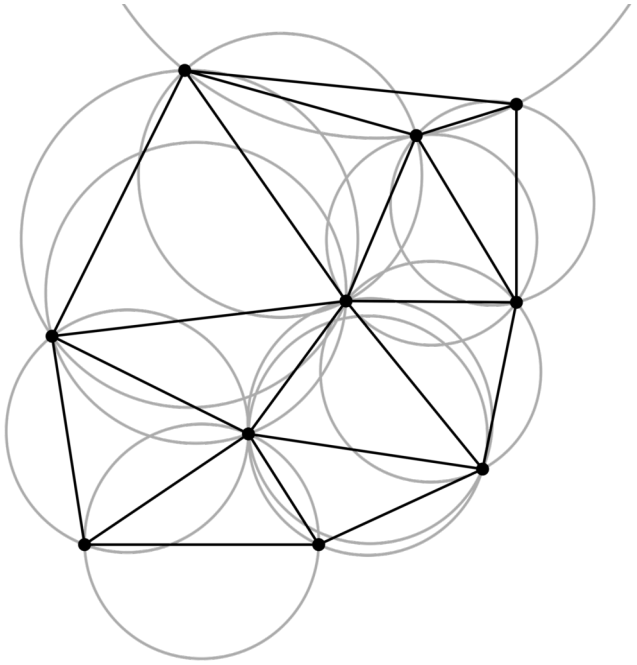

Figure 3.16: Schematic representation of a Delaunay triangulation of a set of points (black dots, black lines) and their corresponding circumcircles (grey circles). Image by Gjacquenot, licensed under a Creative Commons License, via Wikimedia Commons[455].

edges connecting the points, and used to connect the input points in their original space, thus effectively wrapping the Delaunay triangulation over the surface they define. The implementation of the triangulation in the SurfParam package was handled through the SciPy Python library[456] as a wrapper to the Qhull algorithms[457].

3.3.5.5 Area Computation

One of the main advantages of this method is that it allows the computation of the APL at each individual lipid, which is feasible because every lipid is located at a specific vertex of the triangulation described in previous sections. To compute the APL this way, first, the incident triangles at each vertex (lipid) are subdivided into polygons by connecting the midpoints of their three edges with their circumcentre (Figure 3.17). The area surrounding the vertex is then computed as the sum of the corner areas corresponding to the given vertex, in all the triangles incident on it.

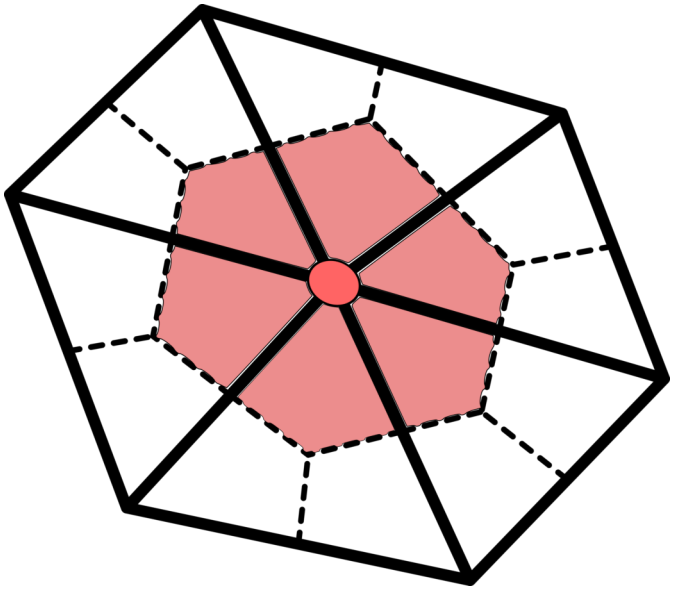

Figure 3.17: Schematic representation of the subdivision of the incident triangles on a given vertex (red circle), and which are the sub-polygons (shaded red) that are taken into account to calculate the individual Area Per Lipid.

Mathematically, these corner areas are computed with the use of barycentric coordinates of the circumcenter of each incident triangle. Let $\{\mathbf{x_0}, \mathbf{x_1}, \mathbf{x_2}\}$ be the vertices of a given triangle Δ, $\mathbf{x}$ be its circumcentre, and let its edges be indexed with respect to the opposite vertex such that $\mathbf{e_0} = \mathbf{x_2} - \mathbf{x_1}$, $\mathbf{e_1} = \mathbf{x_2} - \mathbf{x_0}$ and $\mathbf{e_2} = \mathbf{x_1} - \mathbf{x_0}$; and $l_k = ||\mathbf{e_k}||$ represent the length of edge k. The barycentric coordinates of the circumcenter can be computed as:

$$\mu_k = l_k \cdot \left(l_{(k+1)\%3} + l_{(k+2)\%3} - l_k\right) \tag{3.76}$$

In Equation 3.76, the % symbol represents the modulo operator, to enforce the cyclic nature of a triangle. The resulting coordinates are then normalised such that their sum is equal to 1, and the area of the corner k in the triangle Δ is given by:

$$A(\Delta, k) = \frac{\mu_{(k+1)\%3} + \mu_{(k+2)\%3}}{2} \cdot A(\Delta) \tag{3.77}$$

Here $A(\Delta)$ represents the area of the incident triangle, which can be computed as $A(\Delta) = \frac{||\mathbf{e_0} \times \mathbf{e_1}||}{2}$. Finally, the Area Per Lipid is calculated as:

$$APL(\mathbf{x_j}) = \sum_{i=0}^{m} Area(\Delta, k_{ij}) \tag{3.78}$$

The mathematical operations in this last step implemented in the SurfParam package were handled using NumPy[439].

3.3.6 Tail Tilt

The tilt of the lipids (Figure 3.18), that is, how slanted they are with respect to the surface of the membrane, is another relevant property to measure in an MD simulation. This property is correlated with the thickness of the membrane and can change depending on, for example, the thermodynamic phase of the membrane or its molecular composition.

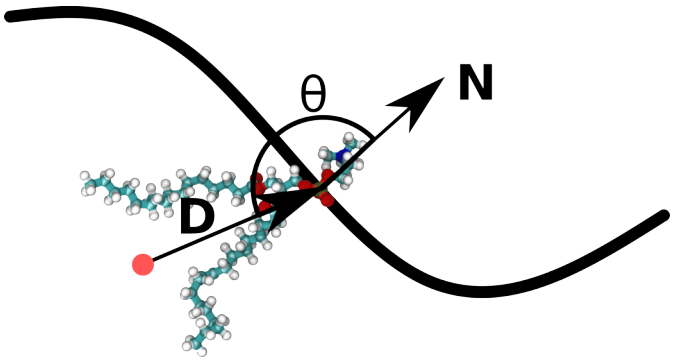

Figure 3.18: Schematic representation of the tail tilt measured in a typical MD simulation of a lipid membrane. The angle θ is calculated between the normal vector to the surface, N, and the lipid director vector, D, defined to point from the phosphate centre of mass (green circle) to the midpoint of the lipid tail tips (red circle).

To compute this magnitude, a lipid director vector **D** is first defined, as proposed by Ergüder and colleagues[377]. This is a vector that points from the Phosphate group to the centre of mass of the last Carbon atoms of each tail. Then, using the normal vector **N** computed as Equation 3.41, or if the membrane is flat enough assuming that $\mathbf{N} = \{0, 0, \pm 1\}$, the angle between the Director and the Normal can be calculated as:

$$\theta_{Tilt} = \arccos\left(\frac{\mathbf{N} \cdot \mathbf{D}}{||\mathbf{N}||\ ||\mathbf{D}||}\right) \tag{3.79}$$

For this Thesis, an implementation of this method can be found in the HierarchyMem package[440], as well as in generalist Python scripts used for different works[441]. Both the package and the scripts were built using Python 3.x, using the MDAnalysis library[437, 438] to read raw trajectory data, and mathematical operations were handled using NumPy[439].

3.3.7 Order Parameters

The Order Parameters (OP) of a lipid are a very relevant magnitude to measure in a simulation, as they can be obtained through wet-lab experiments, providing a robust link between the real and the virtual world. In essence, they are a measure of (dis-)order and orientation of the

lipids inside a lipid membrane. They are, in a way, complementary to the tail tilt as the angle of the lipid with respect to the Normal vector of the membrane is of relevance for their computation. However, OPs give finer information as they can be computed for each Carbon atom in the lipid.

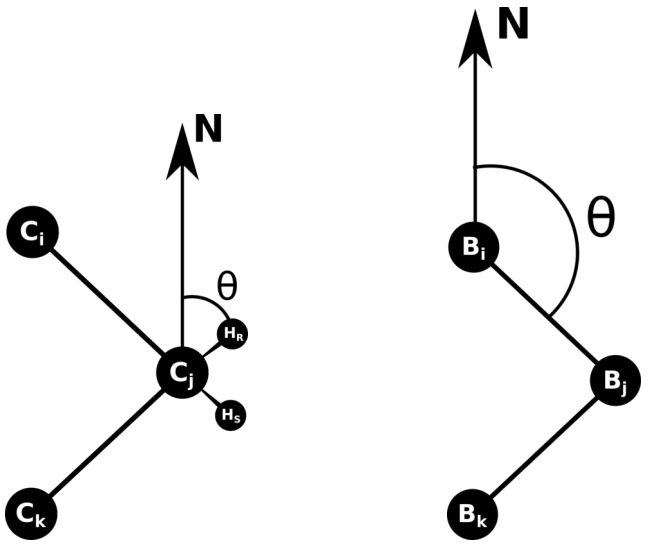

Figure 3.19: Schematic representation of the angles used to calculate the Order Parameters. Left-hand graph shows the angle calculated for an AA simulation, between the membrane Normal and the Carbon-Hydrogen vector. Right-hand graph shows the angle calculated for a CG simulation, between the membrane Normal and the Bead-Bead vector.

A distinction must be made when working with AA or CG simulations (see Figure 3.19), as the latter do not have explicit Hydrogen representation, thus the OPs are not directly comparable with experiment. On the other hand, the AA case can be calculated as follows:

$$\theta_{CH} = \arccos\left(\frac{\mathbf{CH}\cdot\mathbf{N}}{||\mathbf{CH}||\,||\mathbf{N}||}\right) \tag{3.80}$$

$$S_{CH} = \frac{1}{2}\left(3\cos\left(\theta_{CH}\right)^2 - 1\right) \tag{3.81}$$

For CG systems, the formula for OPs would remain the same, except that the angle taken into account is defined by the vector formed by connecting two consecutive beads and the membrane normal vector. This makes the OPs of CG simulations not directly comparable to either AA simulations or wet-lab experiments. The equations are:

$$\theta_{BB} = \arccos\left(\frac{\mathbf{BB}\cdot\mathbf{N}}{||\mathbf{BB}||\,||\mathbf{N}||}\right) \tag{3.82}$$

$$S_{BB} = \frac{1}{2}\left(3\cos\left(\theta_{BB}\right)^2 - 1\right) \tag{3.83}$$

The calculation of order parameters was implemented in Python 3.x scripts, available in Github[441], where raw trajectory data was read using the MDAnalysis library[437, 438], and mathematical operations were handled using NumPy[439].

3.3.8 Molecule Permeation

The ability of a membrane to take up molecules within its hydrophobic core is of great relevance, as it can modulate its mechanical properties. For instance, if a membrane presents a large number of water molecules hydrating it, this may cause a fluidification effect. Thus, having a robust method to account for embedded molecules inside a membrane is of paramount importance.

The method proposed here relies on computing lateral densities, as described in Section 3.3.1.1, but instead of obtaining PDFs $p(Z)$ from the mass distributions, expressing them as number of molecules per bin $n(Z)$, a transformation which is straightforward if the mass of the molecule to study is known. This method proposes to obtain such distributions for the Glycerol groups of the lipids, $n_{Glc}(Z)$, which will define the region from which the membrane core starts; and, of course, the distributions for the molecules which are of interest to calculate the permeation for, $n_{Mol}(Z)$.

$n_{Glc}(Z)$ can then be split at its midpoint ($n_{Glc}(Z^A)$ and $n_{Glc}(Z^B)$) and Z^i_{Max} obtained where $n_{Glc}(Z^i) = \max[n_{Glc}(Z^i)]$. These values can then be used as limits for an integral that will allow the computation of the number of molecules of interest inside the region defined as the membrane core:

$$\mathrm{N}_{Mol} = \int_{Z^A_{Max}}^{Z^B_{Max}} n_{Mol}(Z)dZ \tag{3.84}$$

It is important to note that in practice, as the data is obtained from MD simulations, the distribution $n_{Mol}(Z)$ is actually a discrete histogram rather than a continuous function. Therefore, the integral in Equation 3.84 is more accurately represented as a finite sum over the histogram bins. The actual computation can be expressed as:

$$\mathrm{N}_{Mol} = \sum_{i=i_A}^{i_B} n_{Mol}(Z_i)\Delta Z \tag{3.85}$$

where i_A and i_B are the indices of the histogram bins corresponding to Z^A_{Max} and Z^B_{Max} respectively, Z_i is the centre of the i-th bin and ΔZ is the width of each bin. This approach was implemented in Python scripts, available in Github[441]. The raw data from the MD trajectories was read with the MDAnalysis library[437, 438], and all mathematical operations were handled using NumPy[439].

3.4 Ultrasounds in Molecular Dynamics

One of the main objectives of this work, as presented in the Objectives chapter, section 2.3, was to study the effect of ultrasonic pressure waves upon their interaction with a lipid membrane. In the following segment, we will give an explanation on how the ultrasound (US) wave was rationalised and implemented, as well as insight on the methods used to compute how the US waves impacted the membranes.

3.4.1 Ultrasound Implementation

The type of ultrasounds that were modeled in this work were, specifically, High Intensity Focused Ultrasounds[458] (HIFU), chosen as they already have applications in the medical field. The basic principle relies on the use of a piezoelectric transducer that delivers the US beam to a localised area of the patient. Thus, to model the US wavefront, we must first investigate the

theoretical limit of diffraction for a wave of its characteristics, as if the systems to study (in our case lipid membranes) were to be much bigger than the smallest possible area of energy deposition, local effects should be taken into account as well as the potential effects of curved wavefronts.

3.4.1.1 Theoretical minimum focal point

The assumption that the focalised ultrasound (US) acts as a coherent beam (all waves are in-phase), akin to laser light, is employed. This very idealised scenario provides a lower limit to the degree of focalisation, despite its deviation from real-life US applications. By treating the US wave as a laser beam, the well-known mathematical modelling of Gaussian beams can be utilised to rationalise the diffraction limit.

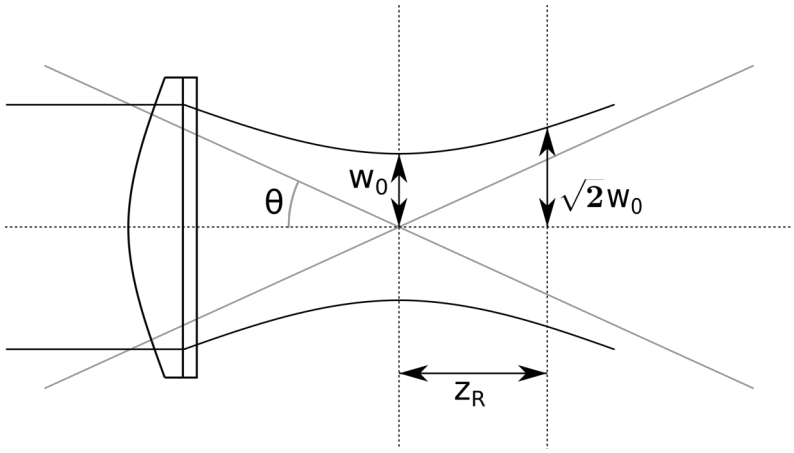

Figure 3.20: Schematic representation of a focused Gaussian beam. The beam envelope is depicted with black solid lines, while asymptotes to the hyperbolic part of the envelope are shown with grey solid lines.

Figure 3.20 illustrates the focalisation of a Gaussian beam. These beams are modelled to focus to a circular region of radius (or width) w_0. The focal width w_0 is related to the convergence of the lens θ and the Rayleigh length of the beam Z_R, defined as the length after the focal point at which the beam width equals $\sqrt{2}w_0$. The relevant relations, derived from online lectures by the Chair for Laser Technology of RWTH Aachen University[459, 460], are:

$$Z_R = \frac{w_0}{\theta} \tag{3.86}$$

$$Z_R = \frac{\pi w_0^2}{\lambda} \tag{3.87}$$

where λ represents the wavelength. Thus, w_0 can be expressed as a function of the wavelength and beam convergence:

$$w_0 = \frac{\lambda}{\theta\pi} \tag{3.88}$$

An additional assumption is made that the beam converges perfectly and immediately, placing the focal point of the US wave directly after the transducer. In this scenario, the convergence $\theta = \pi$, which allows the focal width to be expressed solely as a function of wavelength.

HIFU typically operates in the range of 0.5-12 MHz. Given that wavelength λ is related to frequency ν and wave propagation speed v through $\lambda = \frac{v}{\nu}$, and considering that the human

body is predominantly water (with a speed of sound of approximately 1480 m/s), the wavelength range can be estimated. For the lowest frequencies, the wavelength is approximately 3 mm, while for the highest frequencies, it is around 0.1 mm. Substituting these values into Equation 3.88 yields focal widths of approximately 0.3 mm and 0.01 mm for the lowest and highest frequencies, respectively.

As the focal width is 5 to 6 orders of magnitude larger than the simulated systems (which are in the nanometre range), the US wave can be modelled as acting on the entire system simultaneously, neglecting any *a priori* local effects. Furthermore, the wavefront can be modelled as a planar wave propagating along a single dimension.

3.4.1.2 Modification of a Barostat

Section 3.1.5.3 introduced barostats, algorithms used to maintain constant pressure. Given that US are essentially pressure waves, it is logical to revisit these algorithms. As demonstrated in the previous section, an US wave with the desired characteristics will have a wavefront several orders of magnitude larger than the simulated biological systems, and this wavefront will be planar, travelling along a single direction. Recalling the Berendsen barostat (Equation 3.34), where a factor μ_{ij} scales the atomic positions in the simulation box, the expression for this factor can be modified as follows:

$$\mu_{ij} = \delta_{ij} - \frac{n_{PC}\Delta t}{3\tau_P}\beta_{ij}\left(P_{ij}^0 - P_{ij}(t) - P_{ij}^{osc}(t)\right); \tag{3.89}$$

$$P_{ij}^{osc}(t) = P_{ij}^{max}\sin\left(2\cdot\pi\cdot\nu\cdot t\right) \tag{3.90}$$

This modification introduces an additional term, $P_{ij}^{osc}(t)$, to the Berendsen barostat, which represents the pressure wave. This term can be modelled as a sinusoidal function with overpressure P_{ij}^{max} and frequency ν. By selecting appropriate indices $\{i, j\}$ for non-zero overpressure, the propagation direction of the US wave can be controlled.

The implementation of this was performed by modifying the source code of the GROMACS 2021.5 MD simulation engine. The modified code is available on Github[461], and comes with a bash wrapper to recompile the code with the desired modification to the overpressure and frequency of the oscillating pressure control algorithm.

3.4.2 Measuring deformation

The determination of how the ultrasound (US) wave affects membrane structure is central to this part of the work. Section 3.3 introduced a series of properties that can be measured for a given membrane at any point in time, but a method to quantify how each property reacts to the US is necessary. The proposed method, described in this section, is based on signal analysis and Fourier analysis. The method is implemented in Python 3.x scripts, available on Github[441].

3.4.2.1 Normalisation of the properties

Consider an arbitrary property $X(t)$, which can be measured for a lipid membrane as a function of time t. With the exception of thickness, the described properties can be measured independently for both leaflets. Thus, the property can be divided into $\mathrm{E}\left[X_{up}\right](t)$ and $\mathrm{E}\left[X_{down}\right](t)$, denoting the expected value of the property X for the upper or lower leaflet, respectively, as a function of time. For each simulation in the presence of US, a short (in the order of tens of nanoseconds) free simulation was also performed. From this, the equivalent quantities $\left\langle X_{up}^{eq}\right\rangle$ and $\left\langle X_{down}^{eq}\right\rangle$ are obtained, where the angular brackets denote the time average of the properties

from the free simulation for each leaflet. $X(t)$ can then be normalised as:

$$X^0(t) = \frac{1}{2} \cdot \left(\frac{\mathrm{E}\left[X_{up}\right](t)}{\langle X_{up}^{eq} \rangle} + \frac{\mathrm{E}\left[X_{down}\right](t)}{\langle X_{down}^{eq} \rangle} \right) - 1 \tag{3.91}$$

This yields a dimensionless magnitude related to the original property X, combining both leaflets and centring it around 0, because if $\mathrm{E}\left[X_{leaf}\right](t) \approx \left\langle X_{leaf}^{eq} \right\rangle$ then $\frac{\mathrm{E}\left[X_{leaf}\right](t)}{\left\langle X_{leaf}^{eq} \right\rangle} \approx 1$.

3.4.2.2 Zero frequency removal

Despite applying Equation 3.91, the normalised magnitude may not be properly centred around 0 at all times, potentially causing issues in subsequent steps. This bias to the signal, sometimes referred to as a DC offset, appears as a zero frequency when performing Fourier analysis. This masks the actual signal to be analysed and must be eliminated.

To achieve this, $X^0(t)$ is further post-processed. First, a filtered signal is obtained by applying a Savitzky-Golay filter[462], $\mathrm{SG}\left[X^0(t)\right]$. This technique smooths data by successively fitting low-order polynomials via least squares to subsets of adjacent data points, called windows. The applied filter was of order 3, with a window length long enough to span 4 full oscillation cycles of the US wave. The advantage of the Savitzky-Golay filter is that it produces a vector of exactly the same length as the input vector. Therefore, the signal can be properly zeroed as:

$$X^*(t) = X^0(t) - \mathrm{SG}\left[X^0(t)\right] \tag{3.92}$$

By subtracting the filtered signal from the unfiltered one, any offset to the time series is eliminated, thus removing the zero frequency. The implementation in Python scripts was done using the NumPy library[439] to handle general mathematical operations, and through the SciPy library[456] to apply the Savitzky-Golay filter.

3.4.2.3 Fourier analysis

The amplitude of an oscillation is directly proportional to the intensity of the peak corresponding to said oscillation in its Fourier spectrum. For this work, the short-time Fourier transform[463] (STFT) was used (Figure 3.21). This variation of the Fourier transform allows to obtain a spectrogram, which is a time-resolved spectrum. The STFT takes the form:

$$\mathrm{STFT}\left[X^*(t)\right](\tau, \nu) = \int_T X^*(t) \cdot w(t-\tau) \cdot e^{-i \cdot 2\pi\nu \cdot t} dt \tag{3.93}$$

Where $X^*(t)$ is the function to be transformed, $w(t-\tau)$ is a window function, ν is the frequency, and τ is the time variable along which the spectrum is calculated. The STFT effectively divides the signal into shorter segments and computes the Fourier transform for each segment, allowing the analysis of how the frequency content changes over time.

The choice of window function is crucial in STFT analysis. For this work, a Hann window function was selected. The Hann window, named after Julius von Hann, is defined as:

$$w(n) = 0.5 \left(1 - \cos\left(\frac{2\pi n}{N-1} \right) \right) \tag{3.94}$$

Where N is the window length and n is the current sample index ($0 \leq n \leq N-1$). The Hann window was chosen for its good frequency resolution and reduced spectral leakage compared to a rectangular window.

The window length N is a critical parameter in the STFT analysis. It determines the trade-off between time and frequency resolution. A longer window provides better frequency resolution but poorer time resolution and vice versa. In this study, the window length was set to encompass four full oscillation cycles of the US wave, balancing the need for good frequency resolution with the desire to capture temporal changes in the signal.

Another important parameter is the overlap between consecutive windows. An overlap of 50% between adjacent windows was used, which is a common choice that provides a good balance between computational efficiency and smooth spectrogram results.

The STFT analysis allows one to determine the intensity of the oscillation of the property $X^*(t)$ at each time τ. To focus specifically on the effects of the US wave and avoid considering contributions from other sources, only the harmonic series of the fundamental frequency of the US was considered. The intensity of the oscillation for the property X^* was thus defined as:

$$\mathrm{I}\left[X^*\right](\tau) = \sum_{i=0}^{n} \int_{\nu_i-\delta\nu}^{\nu_i+\delta\nu} \left|\mathrm{STFT}\left[X^*(t)\right](\tau,\nu)\right|^2 d\nu \tag{3.95}$$

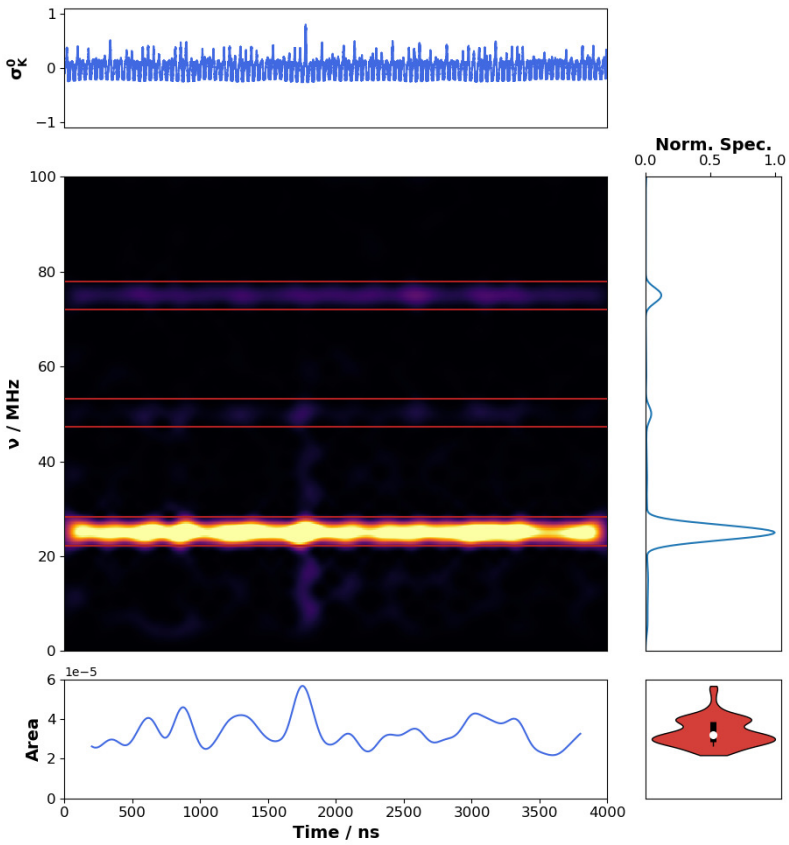

Figure 3.21: View of the timeseries of the normalised curvature of a POPC membrane (top inset), its spectrogram (central inset), time-averaged Fourier spectra (middle-right inset), area of the integrated peaks (bottom inset) and violin plot of the integrated areas (bottom-right inset). Red horizontal lines in spectrogram indicate the regions where the peak areas are obtained from.

Here, the power spectrum $\left|\mathrm{STFT}\left[X^*(t)\right](\tau,\nu)\right|^2$ is integrated over the harmonic series $\{\nu_0,\ \nu_1 = \nu_0 \cdot 2,\ \ldots,\ \nu_n = \nu_0 \cdot (n+1)\}$, where ν_0 is the fundamental frequency of the US. The

integration range $\nu_i \pm \delta\nu$ accounts for the width of each spectral peak, where $\delta\nu$ was chosen to be 5% of the fundamental frequency. This approach captures the main frequency components induced by the US, while excluding unrelated spectral content.

In practice, the summation in Equation 3.95 was limited to $n = 2$, including only up to the third harmonic. This limitation is justified because the intensity of higher-order harmonics typically diminishes rapidly, with second-order effects generally being the highest-order significant contributions in this context.

This was implemented in Python 3.x scripts using the NumPy library[439] to handle general mathematical operations and the SciPy library[456] to perform STFT analysis.

3.5 Statistical Analyses

Throughout this Thesis, accurate measurements and meaningful data extraction with significance were required. To this end, mathematical and statistical tools were employed to reason about the findings. This section of the Methods chapter introduces the statistical formalisms used in this work, explaining their fundamentals, application, timing, and purpose.

3.5.1 Minimal Set of Non-Redundant Properties

As explained in Section 2.2, a series of hierarchical organisational structures characterising lipid membranes in a manner akin to proteins or nucleic acids is postulated. Specifically, it is proposed that the tertiary structure of a lipid membrane would correspond to correlations between a minimal set of relevant properties, which is a behavioural rather than a structural definition. The implementation of the following methods can be found in the HierarchyMem package, available on Github[440]. An Eulerian discretisation of the membrane surface (see Section 3.2.3.1) is first applied, dividing it into a 21x21 grid. In each cell of this grid, a series of properties are measured. The initial set of magnitudes chosen for inclusion in the study were:

- Height function (topography) of the leaflets, as described in Section 3.2.1
- The three components of each vector of the Local Frame of Reference, as described in Section 3.2.2
- The local curvature of each leaflet, as described in Section 3.2.2, Equation 3.42
- The membrane's local thickness as described in Section 3.3.1.2, Equation 3.60
- The lipid director tilt as described in Section 3.3.6, Equation 3.79
- The three components of each vector defining the lipid director, as described in Section 3.3.6

Taking into account both leaflets, these properties would total 31. However, because all the simulations were conducted with symmetrical bilayers, a complete analysis can be performed by considering only one leaflet, as the results for the other monolayer would be completely equivalent. Thus, the full analysis comprises only 16 properties. Furthermore, this grid search can be performed on each frame of the trajectory. However, to ensure the statistical independence of each grid, only frames separated by 20 ns of simulation were selected.

3.5.1.1 Data Standardisation

It should be noted that neither the units nor the order of magnitude of the selected properties necessarily match one another. To render them comparable, a Z-score normalisation was applied to each property:

$$Z_X = \frac{X - \mu_X}{\sigma_X} \tag{3.96}$$

In this equation, the average μ_X is subtracted from the property X, and the result is divided by the standard deviation σ_X. This yields a normalised, dimensionless metric, making the properties comparable.

3.5.1.2 Singular Value Decomposition

Singular Value Decomposition (SVD), in this present case implemented through the NumPy library[439], allows the factorisation of a $\mathrm{D}(m \times n)$ rectangular matrix into two square orthonormal matrices ($\mathrm{U}(m \times m)$ and $\mathrm{V}^{\mathrm{T}}(n \times n)$) plus a $\Sigma(m \times n)$ rectangular matrix:

$$\mathrm{D} = \mathrm{U} \cdot \Sigma \cdot \mathrm{V}^{\mathrm{T}} \tag{3.97}$$

From the previous equation, it follows that:

$$\mathrm{D} \cdot \mathrm{D}^{\mathrm{T}} = \mathrm{U} \cdot \left(\Sigma \cdot \Sigma^{\mathrm{T}}\right) \cdot \mathrm{U}^{\mathrm{T}} \tag{3.98}$$

$$\mathrm{D}^{\mathrm{T}} \cdot \mathrm{D} = \mathrm{V} \cdot \left(\Sigma^{\mathrm{T}} \cdot \Sigma\right) \cdot \mathrm{V}^{\mathrm{T}} \tag{3.99}$$

Thus, U contains the eigenvectors of $\mathrm{D} \cdot \mathrm{D}^{\mathrm{T}}$ and $(\Sigma \cdot \Sigma^{\mathrm{T}})$ its eigenvalues, while V is equivalent to U after replacing $\mathrm{D} \cdot \mathrm{D}^{\mathrm{T}}$ with $\mathrm{D}^{\mathrm{T}} \cdot \mathrm{D}$ and $(\Sigma \cdot \Sigma^{\mathrm{T}})$ with $(\Sigma^{\mathrm{T}} \cdot \Sigma)$. If the data matrix D is constructed such that each column represents a measured property, and each row represents a given grid cell at a given time, the eigenvectors of interest will be given by V^{T} and their eigenvalues $\Lambda = \Sigma^{\mathrm{T}} \cdot \Sigma$. From each $\lambda_i \in \Lambda$, the explained and cumulative variance can be calculated as:

$$\sigma_i^2(\%) = 100 \cdot \frac{\lambda_i}{\sum_i \lambda_i} \tag{3.100}$$

$$C\sigma_i^2(\%) = \sum_i \sigma_i^2(\%) \tag{3.101}$$

Using the cumulative and explained variances, initial indications of redundancies in the data can be obtained. If some eigenvalues are degenerate (they have roughly the same magnitude), this suggests that the corresponding eigenvectors encode the same amount of information. Furthermore, if some eigenvectors present a very low explained variance, this indicates that these eigenvectors may only encode noise and that a minimal, lower-dimensional set of variables can represent the full dataset in a complete manner.

3.5.1.3 Coupling of Properties

Two magnitudes are introduced to determine which measured properties are coupled to each other, *i.e.*, provide redundant information. Advantage is taken of the fact that V^{T} is an orthonormal matrix, so the sum of its squared coefficients $v_{ij} \in \mathrm{V}^{\mathrm{T}}$, along rows / eigenvectors i and columns / properties j equals 1. The Relevance of an eigenvector is thus defined:

$$R_{ji} = R_{EigVec=i}^{Prop=j} = \frac{v_{ij}^2 \cdot \sigma_i^2}{\sum_i \left(v_{ij}^2 \cdot \sigma_i^2\right)} \tag{3.102}$$

The variance values are employed to weigh the components of the relevance matrix R by a measure of the information carried by each eigenvector i used to construct it. The columns of the relevance matrix are then normalised, producing n-dimensional unitary vectors $\hat{R}_{ri}$, and the coupling matrix K is constructed as:

$$\kappa_{rs} = (1 - \delta_{rs}) \cdot \sum_i \hat{R}_{ri} \cdot \hat{R}_{si} \tag{3.103}$$

where δ is a Kronecker delta introduced to cancel the self-coupling, and this coupling is measured for the properties r and s summed over all the relevance vectors of R.

With these tools, a method to prune properties from the original data matrix D can be developed. The maximum number of properties to remove is first determined by counting the number of eigenvectors whose cumulative variance is greater than 95%. Then, properties that display identical (or quasi-identical) relevance vectors in the relevance matrix are identified, indicating that they produce the same latent information as they contribute equally to the eigenvectors V^T, and one of the two is then filtered out. After pruning, the SVD analysis is repeated with the minimal set of properties.

3.5.2 Clustering Analysis

One of the main objectives of this Thesis, introduced in Section 2.3, was to test the influence of an ultrasound wave on several lipid membranes of different compositions. Furthermore, an investigation was conducted to determine whether there were membrane compositions that behaved similarly and if they could be grouped by some criteria. Thus, a clustering analysis was proposed. The algorithm used was the k-prototypes[464], which is a variation of the well-known k-means, but allowing the mixing of numerical and categorical data. The implementation of the method was performed with the KModes library[465] built by Nelis J. de Vos. The implementation of the following methods was done in Python 3.x scripts, available on Github[441]. The dataset for the clustering was constructed with the following properties:

Numerical data:

- Area per Lipid, as described in Section 3.3.5.5
- The Variance of the Curvature as computed with Equation 3.42 described in Section 3.2.2
- Tail Tilt, as described in Section 3.3.6
- Membrane Thickness, as described in Section 3.3.1.2
- Order Parameters (each bead separately), as described in Section 3.3.7 with Equation 3.83

Categorical data:

- Area per Lipid upper outlier (Y/N)
- Area per Lipid lower outlier (Y/N)
- Variance of Curvature upper outlier (Y/N)
- Variance of Curvature lower outlier (Y/N)

- Tail Tilt upper outlier (Y/N)
- Tail Tilt lower outlier (Y/N)
- Order Parameter upper outlier (Y/N)
- Order Parameter lower outlier (Y/N)
- Presence of NaCl (Y/N)

Most categorical variables indicate whether a specific point in the dataset represents an outlier in any of the measured properties. The outliers were determined based on the Interquartile Range IQR = Q3 - Q1. Points 1.5 times smaller than Q1-IQR or 1.5 times larger than Q3+IQR for a given property are considered outliers. These are included to explicitly indicate abnormal instances where the properties oscillate either too much (with respect to their nominal behaviour) or too little, usually indicating the breaking of the membrane; and to test if these unusual points would form a cluster of their own.

Before the clustering was applied, the numerical data was spread out via a SVD to ensure the points are embedded in a space that holds them as spread out as possible. Refer to the previous Section 3.5.1.2 for an explanation of the technique. Therefore, the clustering algorithm was performed on the eigenvectors obtained from the SVD (U matrix in Equation 3.97), and not on the properties per se. The optimal number of clusters was determined by the knee estimator[466], where the algorithm is iteratively applied, increasing the number of clusters up to an arbitrary value and calculating the cost function at each clustering step. The optimal number of clusters is that corresponding to a change in trend - or knee - in the cost function against the number of clusters.

3.6 Technical Aspects of System Construction and Simulation

This section details the technical aspects of system construction and simulation for the studies conducted in this Thesis. Each subsection corresponds to a specific work that highlights the membrane compositions, system sizes, ionic concentrations, and simulation parameters employed.

3.6.1 Evaluation and Comparison of MD Forcefields

The study comparing MD forcefields for bacterial membrane models employed six distinct lipid compositions: pure 1-palmitoyl-2-oleoyl-*sn*-glycero-3-phosphocholine (POPC), 1-palmitoyl-2-oleoyl-*sn*-glycero-3-phosphatidylethanolamine (POPE), and 1-palmitoyl-2-oleoyl-*sn*-glycero-3-phosphatidylglycerol (POPG) membranes, as well as three mixtures - POPC:POPG (7:3), POPE:POPG (1:3), and POPE:POPG (3:1). These ratios were chosen to represent various bacterial membrane models, with the POPC:POPG mixture mimicking the bacterial inner membrane[120, 467] and the POPE:POPG mixtures representing Gram-negative and Gram-positive bacterial membranes[468], respectively.

All systems were built with the CHARMM-GUI Input Generator online tool[469, 470]. Each membrane system consisted of 500 lipids (250 per leaflet) and was solvated with 25,000 TIP3P[471] water molecules in a box of approximately 125 × 125 × 96 $Å^3$. For systems containing charged lipids, Na^+ ions were added to achieve charge neutrality. The systems were simulated using three different force fields: CHARMM-36M[421], Slipids[269, 472] and GROMOS-CKP[319]. Furthermore, the hydrogen isotope exchange (HIE) method was tested with GROMOS-CKP[422, 423].

The simulations were performed using the GROMACS 2018.3 package[473–475]. Before production runs, systems were minimised using the steepest descent method for 1,000 steps. An NPT ensemble was employed at 1 bar and 310 K, using a semiisotropic Parrinello-Rahman[434] barostat with a coupling constant of 1 ps and a v-rescale[431] thermostat with a coupling constant of 0.1 ps. The LINCS algorithm[476] was used to constrain bond vibrations. Electrostatic interactions were calculated using the PME method[419, 420] with a cutoff of 1.0 nm and a grid spacing of 0.12 nm. Van der Waals interactions were calculated using a 1.0 nm radius cut-off. Production MD simulations were run for 500 ns, with analyses performed on the last 100 ns of the trajectories. The time step for integration was set to 2 fs.

3.6.2 Equilibrium Properties and Hierarchical Organisation

The investigation of hierarchical organisation in lipid membranes focused on large membrane patches to observe natural undulations and deformations. Three membrane compositions were studied: pure POPC, POPE:POPG (1:1), and 1,2-dimyristoyl-*sn*-glycero-3-phosphocholine (DMPC). Each system consisted of 10,000 Martini 2.2[321] lipids (5,000 per leaflet), spanning approximately 57 nm in the X and Y dimensions.

The membranes were solvated using a ratio of 23 non-polarisable Martini water particles per lipid molecule, resulting in a $57 \times 57 \times 8$ nm^3 box. Monovalent ions were added to neutralise the total charge when necessary. Simulations were performed using the GROMACS 2020.4[473, 474, 477] molecular dynamics engine.

The systems were energy-minimised using the steepest descent algorithm for 5,000 steps, with a tolerance of 10 kJ mol^{-1} nm^{-1} and a step size of 0.01 nm. Equilibration was conducted in five consecutive stages, incrementally increasing the time step from 2 to 25 fs using the leap-frog integrator. The temperature was maintained at 310 K using a v-rescale[431] algorithm with a coupling constant of 1 ps, while the pressure was maintained at 1 atm using a Berendsen[432] semi-isotropic barostat with a coupling constant of 5 ps and a compressibility of 3×10^{-4} bar^{-1}.

Production runs were 10 µs long, using a leap-frog integrator with a 25 fs time step. Neighbour lists were updated every 20 steps using the Verlet method. Temperature and pressure were maintained using the same algorithms as in equilibration, with the barostat switched to Parrinello-Rahman[434] for production. Electrostatic interactions were calculated using the reaction-field method with a cutoff radius of 1.1 nm and a dielectric constant of 15 beyond this radius.

3.6.3 Influence of Lipid Composition on Ultrasound Effects

To study the effects of focused ultrasound (US) on lipid membranes of varying compositions, ten different membrane systems were constructed: pure POPC, POPE, POPG, and 1-palmitoyl-2-oleoyl-*sn*-glycero-3-phospho-L-serine (POPS) bilayers, and their binary mixtures in a 1:1 ratio. Each system consisted of 500 lipids (250 per leaflet) and was solvated in a 50 water molecules per lipid ratio. Na^+ ions were added to neutralise the charge when necessary.

Simulations were performed using AA CHARMM-36M[478] and CG Martini3.0[322, 323] forcefields. CG simulations included two sets: one without additional salt and the other with 0.15 M NaCl to evaluate the impact of ionic strength.

The GROMACS 2021.5[473, 474, 479] engine was used for all simulations. The systems were minimised and equilibrated following the same protocol described in the previous section. To simulate ultrasound waves, a modification of the Berendsen barostat was implemented, applying a sinusoidal pressure wave along the normal to the membrane plane. The ultrasound parameters were set to a maximum pressure of 35 bar and a frequency of 12 MHz.

For CG simulations, a time correction factor of 4 was applied to account for the accelerated dynamics, resulting in an effective frequency of 48 MHz. The simulations were run for 500 ns in the AA case and extended to 16.66 μs (effective time) for CG systems, comprising 200 compression-decompression cycles.

The temperature was maintained at 310 K using a v-rescale[431] thermostat. The modified Berendsen barostat[480] was used to apply the ultrasound waves along the Z dimension.

3.6.4 Influence of Ultrasound Parameters on Membrane Response

The investigation of ultrasound parameter effects on membrane response utilised four distinct lipid compositions: pure POPC, POPE, POPG, and POPS bilayers. Each system contained 500 lipids in total, with 250 lipids per leaflet. The membranes were parameterised using the Martini 3.0[322, 323] force field and solvated with a ratio of 50 water molecules per lipid. For charged lipids (POPG and POPS), Na^+ ions were added to achieve charge neutrality.

Simulations were performed using a modified version of GROMACS 2021.5[473, 474, 479], which incorporates a custom implementation of the Berendsen barostat to simulate ultrasound waves[480]. The ultrasound parameters were systematically varied, with frequencies ranging from 5 to 50 MHz in increments of 5 MHz, and amplitudes (overpressures) ranging from 5 to 50 bar in increments of 5 bars. This resulted in 100 distinct simulations for each membrane composition.

Each simulation encompassed 100 full oscillator cycles, with the duration adjusted according to the specific frequency. The temperature was maintained at 298 K using a v-rescale thermostat[431]. The modified Berendsen barostat was used to apply the ultrasound waves along the Z dimension, perpendicular to the membrane plane.

This set of simulations allowed for a systematic exploration of the effects of varying ultrasound parameters on different lipid membrane compositions, providing insight into the complex interplay between mechanical perturbations and membrane structure.

4 RESULTS

Mention this to me
mention something, mention anything.
Mention this to me...
Watch the weather change.

–Disposition,
TOOL.

Through this section we will review and discuss the most relevant findings for the present Thesis. The data shown here are divided into four main blocks, following what was introduced in the Objectives Chapter. Namely, the block of work comparing different forcefields for bacterial membrane simulation (introduced in Section 2.1), the block discussing membranes at equilibrium and postulating a Hierarchical organisation for lipid membranes (Section 2.2), the block discussing the implementation of a simulation protocol for ultrasounds in MD and the effect of lipid composition on the membranes' reaction to such deformation; and finally the block testing how different ultrasound parameters affect several lipid bilayers (Section 2.3).

4.1 Block 1: Comparative Assessment of Forcefields in Simulations of Bacterial Membrane Models

As we mentioned in the Introduction chapter of this work, as well as in the Objectives, one of the main challenges of MD in general, and simulations of lipid membranes in particular; is deciding which sets of parameters fit best the researcher's requirements. Thus, studies that perform systematic evaluations and comparisons of forcefields provide valuable data to correctly tailor simulations, as they help the rationalisation of some of the most routine decisions that need to be made to tackle any given problem from the computational point of view.

In recent years, many efforts have been made to develop and optimise forcefields for the simulation of lipid membranes[314, 319, 481–486]. However, most of these works have been focused on bilayers composed of a single lipid type, which opens the question if the developed sets of parameters still remain true to reality when employed to simulate more complex systems, such as inhomogeneous membranes containing several types of phospholipids; or even more realistic cases with membranes in contact with other kinds of macromolecules. To the best of our knowledge, no comparative studies of forcefields with models used to simulate bacterial membranes have been published to date, although hybrid membranes with several different lipids have been studied by theoretical and experimental methods[487–490].

Therefore, this study aimed to provide a comprehensive evaluation of several forcefields commonly used in MD simulations of lipid membranes. The selected forcefields were CHARMM 36M, Slipids, GROMOS-CKP, and GROMOS-H2Q. Furthermore, the influence of simulation meta-parameters was tested for CHARMM-36M and Slipids, labelled CHARMM-O and Slipids-O, respectively. The objective was to assess their strengths, weaknesses, similarities, and differences, enabling researchers to make informed decisions when selecting a forcefield for their specific needs. These forcefields were tested for six different membrane compositions, three representing simple bacterial membrane models, and three single-component membranes as comparative blanks, as introduced in the Objectives chapter, section 2.1. The specific compositions

were selected as to serve as simplified two-component models of bacterial membranes, as well as three single-component compositions as blanks for comparison. The technical aspects of the system construction and simulation parameters can be consulted in the Methods chapter, section 3.6.1.

The results of this study were published in the Journal of Chemical Theory and Computation[491] (doi: 10.1021/acs.jctc.4c00204) reproduced under Licence L7, copyright 2024 American Chemical Society. Besides the author of this Thesis, the article was co-authored by Anika Wurl, from the Martin-Luther-Universität Halle-Wittenberg; Tiago Mendes Ferreira, from the Martin-Luther-Universität Halle-Wittenberg; Ángel Piñeiro Guillén, from the Universidade de Santiago de Compostela; and Rebeca García Fandiño, from the Universidade de Santiago de Compostela. For this work, the author of this Thesis performed the simulations, analysed them, and contributed to the writing of the final manuscript.

The equilibration of the lipid bilayers was evaluated following the time profiles of the area per lipid (APL) and the thickness of all the bilayers (see Appendix A.1, Figure S7). These two properties were chosen because they are complementary, the former modulating the expansion and compression of the membranes in the XY plane and the latter modulating that same behaviour, but along the normal direction to their surface. These properties minimally characterise the mechanical state of the bilayer. We note that after the first 400 ns no drift in these properties is observed and interpret this as the bilayers having reached an equilibrium state, within the timescales of this work. In Figure 4.1 and Figures S1 to S6 we represent the molecular 3D representations of the bilayers at the final time of the simulations.

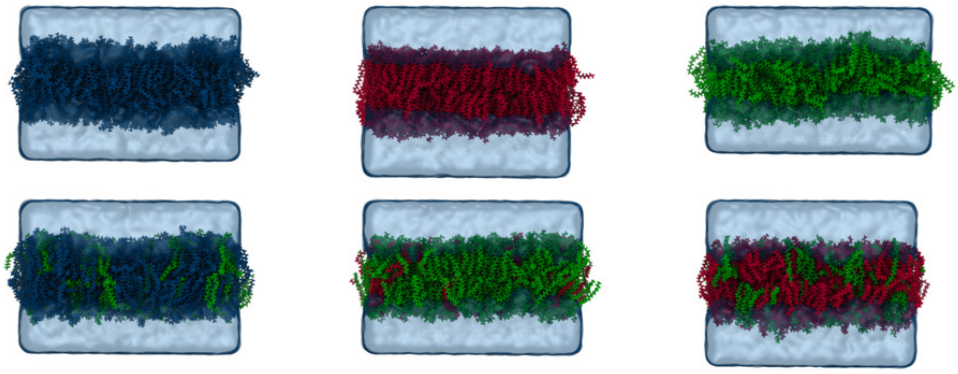

Figure 4.1: Molecular visualisation of six membrane compositions at t=500 ns, using the CHARMM 36M forcefield: Pure POPC (blue), POPE (red) and POPG (green) membranes, and bacteria model membranes: 7:3 POPC:POPG (bacterial inner membrane model), 1:3 POPG:POPE (Gram-negative bacteria model), and 3:1 POPG:POPE (Gram-positive bacteria model).

In addition, lateral density profiles, hydration levels within the inner region of the bilayer, H-bonding patterns, and radial distribution functions are calculated. CH order parameters were obtained from the simulations and compared to experimentally determined NMR measurements, in order to assess the reliability of the different forcefields and parameterisations used in this study.

4.1.1 Area per Lipid

The Area Per Lipid (APL) is a property that is frequently used when validating forcefields. Despite this, discrepancies can arise when simulation results are compared with those obtained in wet-lab experiments. This may be due to the fact that APL cannot be measured directly in an experiment, but instead is inferred through indirect means[492, 493]. Early MD studies using small systems suggested that the APL is very sensitive to methodological differences in the treatment of long-range electrostatic and van der Waals interactions (e.g., the use of shift functions and/or straight cutoffs *vs.* Ewald summations). However, recent studies using larger systems suggest otherwise, indicating that APL is relatively insensitive to methodological aspects[485].

Hence, due to the discrepancies between the experimental and simulation data, as well as the still unclear nature of its behaviour when adjusting the simulation parameters, the APL is a relatively poor estimator of the quality of the forcefield. Despite this, it has historically been considered a mandatory parameter to reproduce and is straightforward to measure when deformations of the bilayer are not significant (see Equation 3.69). Thus, it remains worthwhile to include it in a study.

Examining the average APL (Figure 4.2 & Table A.1) for the pure membranes (POPC, POPE, and POPG) over the last 100 ns of the simulations reveals interesting patterns. For the POPC membrane, the APL values are consistent between the different forcefields. The highest area is observed for the Slipids simulation, whereas the lowest value is observed for GROMOS-H2Q. This variation, despite being not too drastic, points to subtle differences in lipid-lipid interactions and packing for the different forcefields. The simulation-obtained values agree reasonably well with available experimental results (66.0 Å^2[494]), especially for Slipids and Slipids-O. POPE presents the lowest APL value for all tested forcefields, in good agreement with experimentally reported values, a tendency that is more pronounced for the CHARMM parameterisation, underscoring the significant role forcefield choice can have when testing properties like APL. For POPG, Slipids tops the charts, and GROMOS-H2Q occupies the lower end. The differences between the choice of simulation parameters (CHARMM vs CHARMM-O & Slipids vs Slipids-O) are less important for these lipids when compared to the differences with both GROMOS variants.

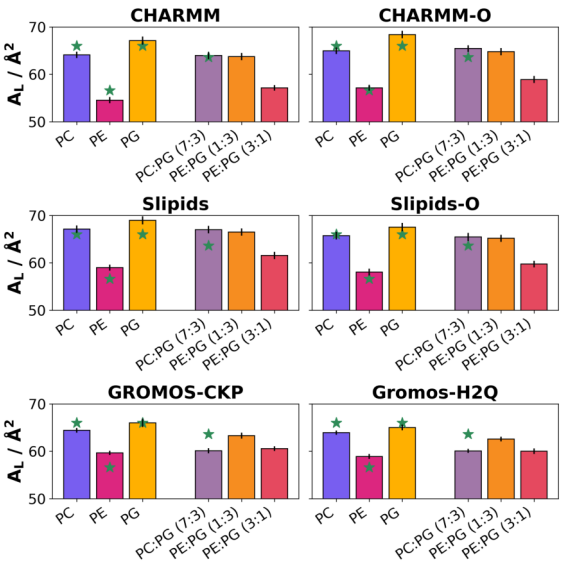

Figure 4.2: Area per lipid. The bars show the average values, and error bars indicate the standard deviation. The green stars represent experimental values, where available.

The simulations also revealed that, as a general trend, the APL values of a lipid mixture align reasonably well with the average of the APL values of the corresponding monocomponent membrane, weighted by their proportions. This points to additive effects where the interaction between the lipid types does not greatly affect the individual APL. However, an exception to this trend arises in the case of the POPC:POPG (7:3) membrane, clearly seen for the two GROMOS variants, where values much lower than the average of the individual components are observed.

This effect is also observed for the rest of the tested forcefields, although to a lesser extent. This suggests synergistic effects between POPC and POPG, which exhibit enhanced packing when combined. This finding also points out marked differences between the CHARMM & Slipids parameterisations against the GROMOS ones.

The POPE:POPG (1:3) simulation presents APL values closely clustered among the different forcefields, a characteristic shared by its reciprocal mixture POPE:POPG (3:1). This suggests that for these lipid types, the different forcefields tested in this work capture the interactions between POPE and POPG similarly. However, it should be noted that for lipid mixtures there is a substantial lack of experimentally-determined properties available, so deciding which is the best forcefield can be a highly interpretative task.

4.1.2 Bilayer Thickness

The average thickness of the bilayers and their standard deviations were calculated following Equations 3.56 & 3.58. The resulting data can be consulted in Figure 4.3 and Table A.2 in the supplementary annex. This property is reciprocal to the APL, as it measures the membrane size perpendicular to its surface plane.

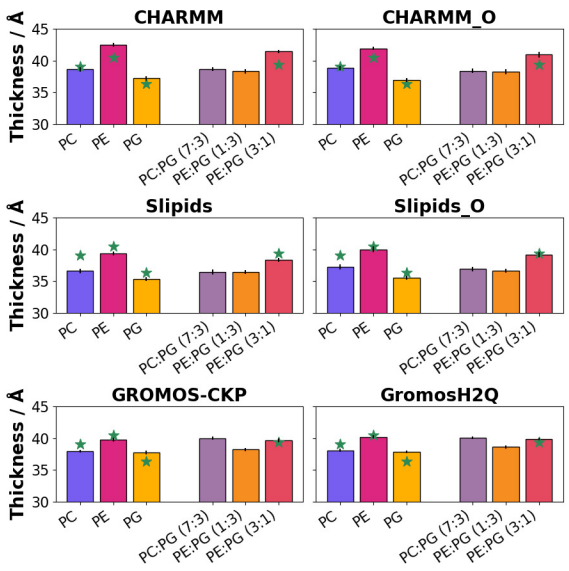

Figure 4.3: Bilayer thickness. The bars show the average values, and error bars indicate the standard deviation. The green stars represent experimental values, where available.

The values obtained from the simulations align reasonably well with the values reported experimentally, where available. This is expected as forcefields are usually designed to reproduce this parameter, among others, with good accuracy. Different membrane compositions display varying thickness values, as expected following the results of the APL. The mixed compositions tend to show discrepancies compared to pure lipid bilayers. Once again, the POPC:POPG (7:3) membrane is the one that shows the biggest deviations in this sense, especially for the GROMOS parameterisations, leading to a thickness higher than that of the pure components. Interestingly, both GROMOS variants produce values very close to those experimentally reported, and the similarity between the said variants is exceptional, hinting at the reliability of the isotope exchange method for simulations of lipid membranes.

On the side of discrepancies, it is observed that the POPC simulations using Slipids and Slipids-O deviate a considerable amount from the experimental values. This also happens for the POPE simulation using CHARMM. Unfortunately, no experimental thickness values are available for POPC:POPG (7:3) and for POPE:POPG (1:3). Significant differences exist between CHARMM and CHARMM-O for pure POPE, with the original parameterisation of this forcefield yielding values closer to experimental results. For other systems, the variations between these two CHARMM variants are less pronounced. The differences between Slipids and Slipids-O remain minimal across all cases.

4.1.3 Lateral Density and Membrane Hydration

The density distributions along the bilayer normal, as described in Section 3.3.1.1, were calculated for various components of all membrane compositions (see Figure S8), along the last 100 ns of simulation. The density profiles were consistent with those for well-equilibrated bilayer systems. The distributions further indicate that water penetrates the bilayer up to the glycerol ester region, while the methyl groups of the lipid tails are fully dehydrated, in agreement with experiments.

To gain a deeper understanding of the penetration of water in membranes and its variation across forcefields, the hydration levels of various lipid compositions were analysed (see Figure 4.4 and Table A.3), using the method described in Section 3.3.8, Equation 3.85. The findings show a general trend where the bilayers simulated with the CHARMM and Slipids forcefields exhibit higher levels of hydration compared to those using GROMOS-CKP and GROMOS-H2Q. This observation is consistent across multiple lipid compositions and has critical implications for other properties that affect membrane structure and behaviour.

Specifically, both CHARMM parameterisations predict a notably higher number of waters within the inner region of the bilayer, with minimal differences between them. The Slipids forcefields follow the trend of CHARMM, with slightly lower hydration values, and also with minimal differences between the two tested sets of simulation parameters. In contrast, GROMOS-CKP and GROMOS-H2Q predict a substantially lower number of waters within the core of the membranes, a fact that holds for all the compositions studied. The close agreement between GROMOS-CKP and GROMOS-H2Q across different lipid types and their mixtures reinforces the confidence in these simulations to faithfully reproduce similar conditions and supports the use of acceleration strategies such as the isotope exchange method proposed here.

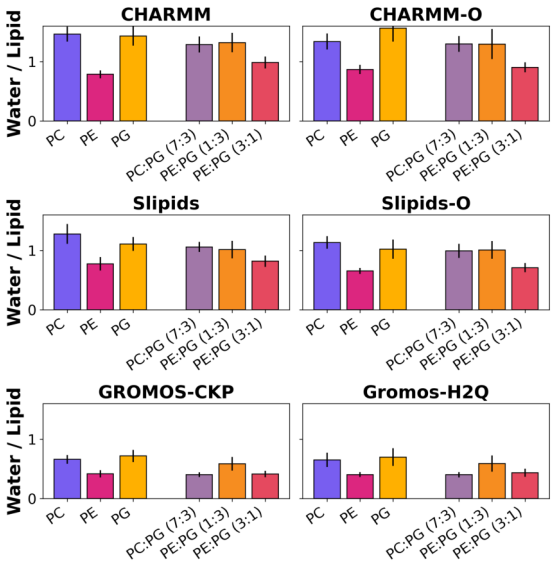

Figure 4.4: Number of water molecules per lipid. The bars show the average values, and error bars indicate the standard deviation.

The differences observed in hydration between forcefields are a remarkable example of how the choice of parameterisation can profoundly affect the results obtained for a given membrane. Hydration level can play a role in properties such as fluidity, thermodynamic phase behaviour, and permeability, because the proportions of the molecules that make up the biological material are altered. The enhanced hydration predicted by CHARMM and Slipids could translate to a more fluid and potentially more permeable bilayer state, while the lower hydration levels estimated by GROMOS-CKP and GROMOS-H2Q could suggest a tighter, less permeable bilayer.

Finally, the differences observed between the membranes are in good agreement with the results shown for the APL and thickness. In general, membranes with lower APLs, as exemplified by POPE, show lower hydration values. This is reasonable, as a lower APL means a more tightly packed membrane, thus leaving less space for water molecules to permeate. The opposite occurs for membranes with high APL, such as POPG, where high hydration numbers are observed.

4.1.4 Radial Distribution Functions

The RDF for the phosphates was calculated as explained in Section 3.3.2. Analysis of the probability of finding a lipid phosphate at a given distance from another reference phosphate provides insights into the ordering and structural properties of a bilayer. As observed for the previous properties, the pairs of flavours for the three tested forcefields yielded very similar results. However, significant differences were observed when comparing the forcefield families amongst each other.

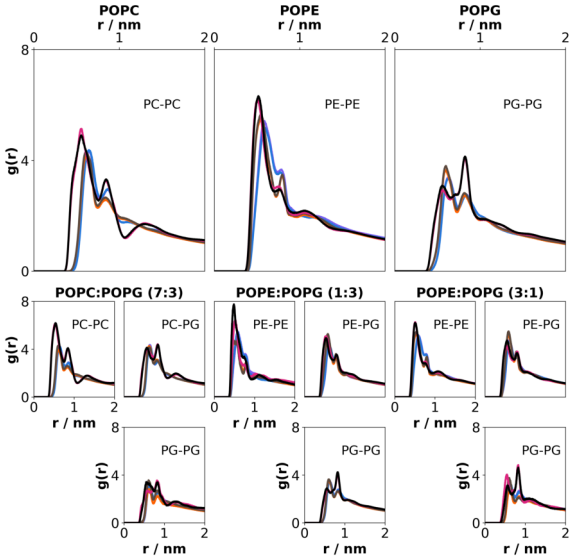

Figure 4.5: RDFs across different lipid compositions and forcefields. The specific RDF can be consulted in the text within each graph. The colour indicates the forcefield (violet for CHARMM, navy blue for CHARMM-O, orange for Slipids, brown for Slipids-O, magenta for GROMOS-CKP and black for GROMOS-H2Q).

GROMOS-CKP and GROMOS-H2Q consistently provide higher peaks for the initial coordination shell across all membranes studied and pairs of lipid types, with the exception of the POPG-POPG peaks. This first coordination shell also appears at lower r values than for CHARMM and Slipids, indicating a more compact and ordered arrangement of lipids when using the GROMOS family of forcefields. This suggests reduced fluidity, potentially impacting membrane dynamics and function. This finding aligns well with the significantly lower hydration values measured for the membranes simulated using GROMOS-CKP and GROMOS-H2Q, compared to those using CHARMM and Slipids. On the other hand, the reduced intensity of the first coordination shell for the POPG-POPG peaks can be attributed to the anionic nature of this lipid, with electrostatic repulsion having a greater effect in the GROMOS family, possibly due to different ion-binding characteristics that affect local structure.

In simulations of lipid mixtures, the trends become more nuanced but follow a similar pattern. The GROMOS family displays a more structured intermediate-range order, as evidenced by sharper peaks beyond the first coordination shell. This could imply that GROMOS predicts more defined domains or lipid phase segregation. It is noteworthy that, generally, the RDF curves of the mixtures do not show a significant deviation from those observed for single-component membranes.

The wider peaks observed in certain forcefields might signify a less compact distribution of lipid headgroups, affecting membrane fluidity and, potentially, lipid domains. These disparities are crucial for the interpretation of the lipid raft theory, as local environments and lipid packing can vary. These forcefield-specific variations might lead to unique biophysical properties in simulations, influencing lipid dynamics, membrane domain formation, and protein interactions.

4.1.5 Hydrogen Bonds

Hydrogen bonding patterns are an integral part of lipid membrane structure and integrity. This magnitude was computed following the method described in Section 3.3.3, applying a normalisation correction to facilitate comparison among the different systems. The data for Hydro-

gen bonds can be consulted in the Supplementary Annex A, in Figures S9 to S11 and Tables A.4 to A.9.

For the pure POPC bilayers, the GROMOS family exhibits a reduced Hydrogen bonding tendency compared to CHARMM and Slipids. The monocomponent POPE membranes simulated under the CHARMM and Slipids parameters show a predominant interaction between the headgroups, whereas for GROMOS this shifts to a headgroup-glycerol interaction. This type of change is the most significant difference that occurs depending on the choice of forcefield. Conversely, the Hydrogen bonds for the pure POPG bilayer were revealed to be relatively uniform among the six parameterisations studied, although slightly lower values were observed between the headgroup and the solvent for the GROMOS cases.

Once more, the POPC:POPG (7:3) bilayer was strikingly different from its peers across the various forcefields. The results for the CHARMM family indicate that the Hydrogen bonds between the headgroups of POPG lipids represent the dominant interactions, followed by those between the solvent and the headgroups of POPC and, to a lesser extent, that of POPG. The Slipids parameterisations show a lower number of Hydrogen bonds than CHARMM, particularly in the case of the POPG headgroups' interaction with themselves. This difference is even larger for the GROMOS forcefields, which display the lowest Hydrogen bonding pattern for this membrane.

For mixtures containing POPE and POPG, the observed trends depend on the specific ratio of lipids. The differences between the forcefields are also significant, and the GROMOS family is the most distinct. For the (1:3) ratio, the largest contribution of Hydrogen bonding in the CHARMM forcefields was observed between the POPG headgroups and themselves, or with the solvent, followed at a distance by the equivalent interactions of the POPE headgroups. A similar trend is observed for the Slipids family but, in contrast to CHARMM, the proportion of Hydrogen bonds between each headgroup and the solvent is much larger than between headgroups of the same lipid. For the GROMOS parameterisations, the Hydrogen bonds of the POPG headgroups are similar to those observed for the CHARMM forcefields but, again, the interactions between the POPE headgroups and the glycerols of both lipids are substantially increased, becoming the dominant contribution. The (3:1) mixture of POPE and POPG maintains fairly similar trends. The differences between the CHARMM and Slipids families become slightly less pronounced, and the interactions involving the POPE headgroups with the headgroups of both lipids, as well as with the solvent, dominate the Hydrogen bond interactions. However, the Hydrogen bonds between the headgroups of different lipids are larger in Slipids than in CHARMM. The GROMOS forcefields display again the previously observed trend in which the Hydrogen bonds between the POPE headgroups and the glycerols clearly dominate these interactions.

In general, the choice of an original-versus-common set of simulation parameters does not seem to significantly affect the Hydrogen bonds, nor does the isotope exchange acceleration method. However, the choice of forcefield does have a clear effect on them, showing numerous and nuanced differences in the simulation. It is particularly striking how some strong interactions switch from one forcefield to another, such as the case of the POPE headgroups interactions in CHARMM or Slipids compared to GROMOS. This points once more to differences in forcefields that, even subtle, can have substantial implications in the results and interpretation of MD simulations of lipid bilayers.

4.1.6 Order Parameters

Replicating NMR data with MD simulations has become a gold standard for gauging the quality of a forcefield. Among the various parameters accessible for NMR spectroscopy, the CH bond order parameters (S_{CH}) are of particular interest, as they provide a direct measure of the conformation of the lipid chains combined with the overall motion of the molecule. The method described in Section 3.3.7 was applied to calculate the S_{CH} of individual lipid types in each simulation and forcefield, for the last 100 ns of simulation. These results were then compared with experimental results, kindly provided by collaborators Anika Wurl and Tiago Mendes-Ferreira. One must note that accurate replication of order parameters by simulation is but a necessary condition for validation, and not a definitive proof of accuracy, since multiple distinct structures can yield the same values for this property[495].

For the *sn-2* aliphatic tails (Figure 4.6, right column), the order parameters decrease as one moves toward the terminal end of the chain. A prominent kink can be observed at Carbon C10, due to the double bond of the tail. This feature is captured by every parameterisation, membrane, and lipid type. However, clear forcefield-dependent differences are also evident. The order parameters for the *sn-1* aliphatic tails again show a continuous decrease from the glycerol link to the end of the tail. This behaviour is seen for all forcefields, membranes, and lipid types, as for the unsaturated tail. Once more, forcefield-dependent differences can be observed.

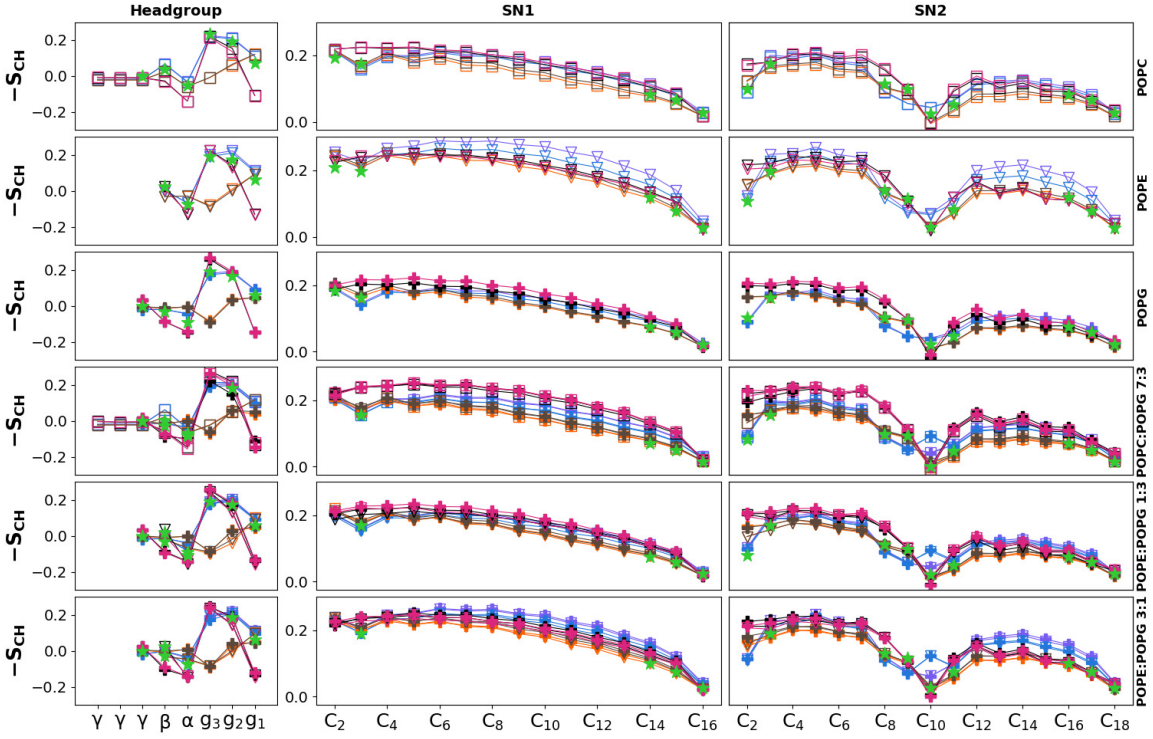

Figure 4.6: Order Parameters for the headgroups and aliphatic chains for the different studied membranes. Headgroups appear in the small subplots on the left. Marker types differentiate specific lipids (square for POPC, triangle for POPE, and plus sign for POPG). The colour indicates the forcefield (violet for CHARMM, navy blue for CHARMM-O, orange for Slipids, brown for Slipids-O, magenta for GROMOS-CKP and black for GROMOS-H2Q). The experimental values are plotted over the simulation results as green stars.

The POPE membrane exhibits the highest order parameters for both acyl chains. Interest-

ingly, in the POPE:POPG (3:1) membrane model, the high concentration of POPE causes an increase in the order parameters of POPG too. This elevated ordering can explain the increased melting point of -PE type lipids compared to the -PC and -PG types[478, 496]. This remains true for all studied forcefields, although to different extents, suggesting that promoting more tightly packed and ordered structures is a fundamental characteristic of POPE lipids. This observation is also consistent with the low APL, high thickness, and low hydration reported for POPE.

When comparing the results for the original sets of simulation parameters against the communal ones, it is observed that CHARMM-O (navy blue lines) tends to produce lower order parameters than CHARMM (violet lines). In contrast, both Slipids (orange lines) and Slipids-O (brown lines) produce virtually identical results. Thus, special care should be taken when using the CHARMM forcefield, as the results indicate that the choice of simulation meta-parameters can have a non-negligible impact on the results obtained. These changes in lipid tail order parameters can have profound effects on membrane fluidity and rigidity, which in turn could impact protein dynamics and membrane organisation.

Further analysis reveals that the GROMOS family of forcefields (magenta and black lines, for CKP and H2Q flavours, respectively) provides remarkably similar values for both the sn-1 and sn-2 tails across different lipid types, with their curves being nearly superimposable. This indicates, as for the previous properties, that using the isotope exchange method will not affect the prediction of the forcefield for this property, while greatly accelerating the computation.

When comparing the performance of the different forcefields among them, the Slipids family predicts the lowest order parameters. This suggests more fluid and dynamical membranes. This is in good agreement with previous studies, where the lower order parameters compared to CHARMM, which presents more ordered chains, is explained by the fact that the Slipids parameterisation has reduced 1-4 electrostatic interactions, since it is absent of partial charges for acyl chain methylenes[497].

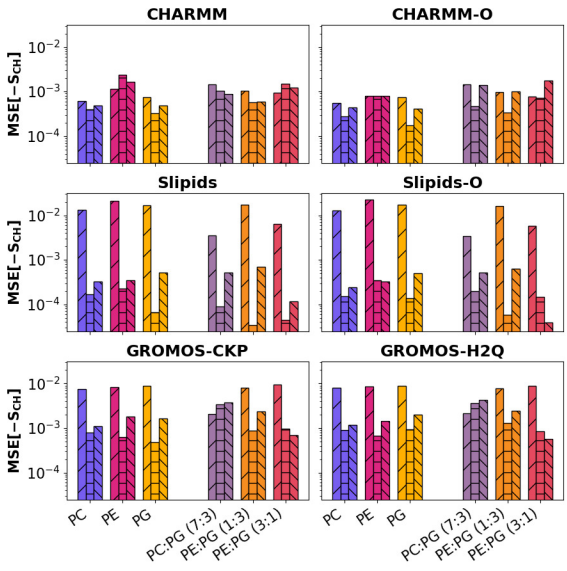

Figure 4.7: Mean Squared Errors for the Order parameters, in logarithmic scale, of the headgroups (forward slash hatching), sn-2 (horizontal hatching) and sn-1 (backward slash hatching) tails, calculated against the experimental values, when available. The bar colours represent lipid compositions.

Both GROMOS-CKP and GROMOS-H2Q predict, in general, the highest order parameters, except for the case of membranes containing a high amount of POPE where the highest values are observed for the CHARMM family. This is indicative of a more ordered membrane and less dynamic lipid environment. All of this paints a quite convoluted picture, where the choice of forcefield or simulation parameters can have a significant effect on the organisation of the acyl chains of a lipid bilayer, which can then lead to different mechanical, physical, and biological interpretations.

To further assess the results, experimental NMR data provided by collaborators were included. The Slipids family exhibits the best agreement with the experimental results, particularly for the *sn-2* tails, capturing the unsaturation with great precision, in support of previous

studies[498, 499]. This family also performs excellently for multicomponent membranes. However, for the headgroups, CHARMM and CHARMM-O are the best performing forcefields in the glycerol region, accurately capturing the NMR data, whereas Slipids does a much poorer job than for the aliphatic tails. On the other hand, the NMR data for the polar head is not completely captured by any specific forcefield, being dependent on the studied membrane and, in general, the experimental data falling within an average of the three forcefield families studied.

The performance of each parameterisation against the experimental results was evaluated by computing the Mean Squared Error (MSE) between the simulation results and the NMR data. The MSE is shown in Figure 4.7, and separates the contribution for the headgroup, *sn-1* and *sn-2* tails. For all forcefields, the results that most closely resembled the NMR data were those for the *sn-2* tails. There are, however, some exceptions to the trend. The GROMOS family captures the headgroups slightly better than the aliphatic tails for the POPC:POPG (7:3) membrane, and the *sn-1* tail than the other groups for the POPE:POPG mixtures. This effect is shared by Slipids-O for the POPE:POPG (3:1) mixture. For this last forcefield, Slipids, and the GROMOS parameterisations too (although to a lesser extent), there was a poor agreement between the results for the headgroups and experimental data, if compared to the results for the tails. However, for CHARMM and CHARMM-O, there is a comparable agreement for the aliphatic chains and headgroups, as in the case of the POPE and POPE:POPG (3:1) membranes. This is not surprising since CHARMM36 was developed to better reproduce the headgroup order parameters[497].

4.1.7 Lipid Lateral Displacement

The lateral displacement of lipid molecules and therefore their diffusion coefficients, is a fundamental magnitude characterising the physical state of a lipid membrane. The movement of lipids is closely linked to the fluidity of the membrane, which, in turn, affects many biological functions such as protein diffusion or membrane fusion. In this work, the lateral displacement and diffusion coefficients were calculated as detailed in Section 3.3.4. By comparing these movements across different forcefields and simulation parameters, and across all types of lipids and membrane compositions, it was observed that the displacement profiles generally show a single peak, indicating that the majority of lipids undergo a similar degree of lateral movement

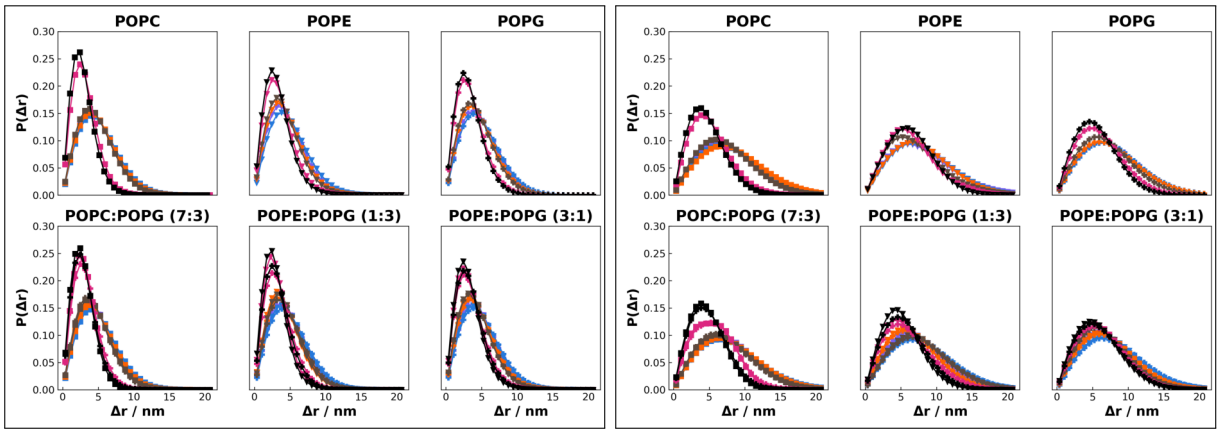

Figure 4.8: Lateral displacement probability density function. The left graph shows the data Δt = 2 ns, the right graph shows the data for Δt = 10 ns. The colour indicates the forcefield (violet for CHARMM, navy blue for CHARMM-O, orange for Slipids, brown for Slipids-O, magenta for GROMOS-CKP and black for GROMOS-H2Q), marker shape encodes lipid type (square for POPC, triangle for POPE and plus for POPG).

within a given time window (Figure 4.8 and Figures S12 to S14). The appearance of two or more peaks would indicate the coexistence of two different diffusion regimes for the lipids in the bilayer. This would be possible, for instance, in the presence of a macromolecule embedded in the membrane, which slows the movement of the neighbouring lipid units.

The lateral displacement provides information about the dynamics that arise from each forcefield. For the smallest tested time window (Figure 4.8, top graph), reasonably good agreement is observed within each tested forcefield family, as the curves almost overlap. This, however, does not hold for larger time windows. In a time window Δt = 10 ns (Figure 4.8, bottom graph), the curves for GROMOS-CKP and GROMOS-H2Q start to noticeably diverge from each other, as is clearly seen for the POPC:POPG (7:3) membrane. This is to be expected, as the isotope exchange method modifies the mass of the polar Hydrogens in the lipids, so it is reasonable for diffusion to be affected. Moreover, at long time windows some differences can be appreciated within the families of CHARMM and Slipids, especially for the latter. This demonstrates how changes in the simulation metaparameters can affect simulation results, making their proper interpretation an arduous task.

With regard to the comparison of different forcefield families, it is evident that GROMOS produces narrower distributions, centred at lower displacements than CHARMM and Slipids, which in turn yield similar results. These results follow the line discussed for previous properties, where GROMOS produce more tightly packed membranes, less hydrated, and with higher order parameters for the acyl chains. These differences remain true for all the studied time windows.

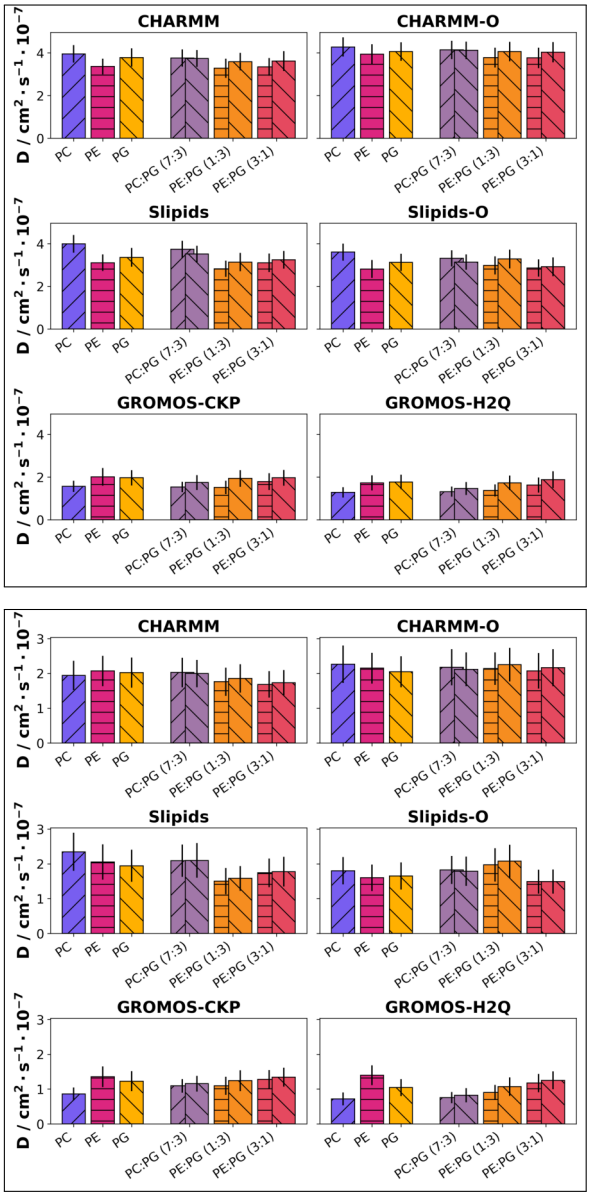

Figure 4.9: Bar plots from Figure 4.8, for Δt = 2 ns (top graph) and Δt = 10 ns (bottom graph). The hatching represents the specific lipid type: forward slash - POPC, horizontal slash - POPE, backward slash - POPG. The errorbar represents the standard deviation.

Furthermore, it is notable that in mixed lipid membranes, the lateral displacement appears to be independent of the type of lipid. Different lipids exhibit nearly identical displacement behaviours across all forcefields examined. This finding underscores a level of consistency in the physical movement of diverse lipid species within the bilayer, suggesting that, despite the chemical diversity, the forcefields predict a similar mobility pattern within the complex membrane environment.

This serves as a precursor for the calculation of the diffusion coefficients (Figures 4.9, S15

to S17 and Tables A.10 to A.12). The coefficients reaffirm the trends previously shown for the lateral displacement distributions. For a given time window, broader distributions correlate with higher diffusion coefficients, as is the case for the CHARMM and Slipids families, indicating a more fluid-like membrane. In contrast, the narrow distributions of GROMOS correlate with lower diffusion coefficients. Increasing the time window has the effect of producing lower diffusion coefficients. This is because with larger time windows the high frequency and fast movements of the lipids are no longer captured, and hence slower dynamics become the main observable contribution.

The calculated diffusion coefficients within each family of forcefields are slightly different, and although these differences are never substantial, they are non-negligible. This is as expected, as per the results shown for the lateral displacement curves, and follows the same reasoning: the influence of the quadrupling of Hydrogen mass for the GROMOS family, and the nuanced influence of simulation meta-parameters for CHARMM and Slipids.

These diffusion coefficients are reasonably well aligned with certain values reported in the literature for some lipids[500, 501]. This agreement provides further validation for the approach used to calculate these values. However, it must be noted that direct comparison of simulation-derived diffusion data with experimental results is a complex task. It is known that the use of periodic boundary conditions in a simulation can affect lipid mobility by influencing the time scales at which diffusive processes take place[502–504]. Moreover, it has been shown that other factors like the specific level of hydration or order parameters produced by a given parameterisation may also affect the diffusion processes of the lipids within a membrane. Higher hydrations, correlated with looser lipids, produce more fluid membranes, as in the case of CHARMM and Slipids. Similarly, the time window over which the lateral displacement is calculated can dramatically affect the resultant diffusion coefficient, with longer windows potentially capturing more complex and slower-moving dynamics. Even within computational studies, varying these parameters can yield divergent results, highlighting the challenge in achieving a direct comparison with experimental data. These differences in the estimated diffusion coefficients using different meta-parameters are significantly lower than those between forcefields. This agrees with the conclusions of the previous analyses, indicating that the membranes simulated using GROMOS are tighter, thicker, and have fewer water molecules penetrating the bilayer region. In contrast with the quantitative parameters obtained from other analyses, no special behaviour is observed for the POPC:POPG (7:3) membrane composition.

4.1.8 Conclusions

This comparison of forcefields for MD simulations of lipid membranes revealed several key findings. The GROMOS family of forcefields consistently produced more tightly packed membranes with lower hydration levels and higher order parameters for acyl chains compared to those of CHARMM and Slipids. This behaviour suggests that GROMOS may be particularly suitable for simulating highly ordered membrane phases or studying membrane permeability.

Slipids demonstrated exceptional performance in reproducing the experimental order parameters, particularly for the sn-2 tails and in multicomponent membranes. This makes Slipids a strong candidate for studies focusing on lipid tail dynamics or membrane fluidity. In contrast, CHARMM exhibited the best performance in capturing headgroup order parameters, especially in the glycerol region, indicating its strength in simulating lipid-water interfaces and potentially lipid-protein interactions.

The choice of simulation meta-parameters was found to have a noticeable impact on results,

particularly for the CHARMM forcefield. This underscores the importance of careful consideration and reporting of simulation parameters in MD studies. The isotope exchange method (GROMOS-H2Q) proved to be a viable acceleration strategy, producing results consistent with GROMOS-CKP while significantly reducing computational time. This finding supports the use of such acceleration techniques in large-scale or long-timescale simulations.

The lipid composition significantly influenced the properties of the membranes across all forcefields, with POPE-rich membranes showing distinct behaviour. This highlights the importance of using appropriate lipid mixtures when modelling specific biological membranes. Mixed lipid systems generally exhibited properties that were a weighted average of their components, with some exceptions like the POPC:POPG (7:3) mixture, which showed unique behaviour across multiple analyses.

These findings highlight the importance of carefully selecting a forcefield based on the specific properties of interest and the lipid composition being studied. They also underscore the need for the continued development and refinement of forcefields to better capture the complex behaviour of lipid membranes. Researchers should consider these comparative results when designing MD studies of lipid systems, ensuring that the chosen forcefield aligns with their specific research questions and target membrane compositions.

4.2 Block 2: Hierarchical Structural Organization of Lipid Membranes: Multi-Level Analysis and Mechanical Properties

Typically, when researchers reason about biological molecules such as nucleic acids and proteins, they not only do it in terms of the chemical species conforming them, but in terms of their spatial arrangement. That is, the activity of these biological systems is understood on the basis of hierarchical levels of structure, in which a linear sequence of covalently bound monomers produce specific topologies for the higher-order macromolecules they give rise to; which are ultimately responsible for their correct functioning. However, this kind of description is not commonly applied to lipid membranes, and thus, in this study we aimed to bridge that gap with the following proposal.

The different hierarchical levels of structure introduced to reinterpret membrane models are described in detail in this section. As explained in the Objectives chapter (Section 2.2), MD simulations of large-scale POPC, POPE:POPG (1:1) and DLPC membranes at the CG resolution, as well as different AA simulations from previous work in the group[505] are used to illustrate these concepts. The large membranes were chosen to demonstrate the impact of system size on analysed properties, to prove that even a membrane with a single component exhibits the proposed levels of structure, and to test the effect lipid headgroups, tail unsaturation, and tail length have on such structural descriptions. Atomistic simulations of more complex systems were employed to show the highest level of structure, as explained later. Specific information about the construction of the simulated systems, as well as simulation parameters can be consulted in the Methods chapter, section 3.6.2.

The contents reproduced in the subsequent section were published in the Computational and Structural Biotechnology Journal[506], **2022**, *20*, 2798-2806 (doi: 10.1016/j.csbj.2022.05.042), reproduced under a Creative Commons Licence. In addition to the author of this present Thesis, the article was co-authored by Ángel Piñeiro Guillén, from the Universidade de Santiago de Compostela; and Rebeca García Fandiño, from the Universidade de Santiago de Compostela. For this work, the first author performed the simulations, analysed them, and contributed to the writing of the final manuscript.

4.2.1 The Primary Structure of the Lipid Bilayer

This approach is analogous to the representations on four layers commonly used to reason about proteins and nucleic acids, modelling them in primary, secondary, tertiary and quaternary structure. Thus, the proposal for the primary structure of a lipid bilayer is the composition of each leaflet. Variations in headgroups and aliphatic chains allow the existence of more than 1000 different lipid types in a single eukaryotic cell[507]. Therefore, the different lipids that form a lipid bilayer constitute the lowest hierarchical level, akin to the sequence of amino acids that distinguishes one protein from another. However, there are differences in this analogy with respect to nucleic acids and proteins. The most obvious is that lipids are not covalently bound to each other, in contrast with nucleotides or amino acids. Furthermore, single lipids are not spatially localised within a bilayer, as amino acids occupy their specific place in the protein sequence but can diffuse through them. Lipid bilayers can also incorporate other molecules within them, fuse with other membranes, and show a remarkable ability to adapt to environmental changes by altering their composition. This high plasticity (not only in the mechanical sense) of lipid membranes allows them to maintain their bioactivity even in the presence of external perturbations, similarly to an organism expressing mutations in a protein to counteract some external stimulus. Thus, within this proposal, the primary sequence of a membrane is simply the proportions of

different lipids in each leaflet.

4.2.2 The Secondary Structure of the Lipid Bilayer

In DNA and RNA, the secondary structure arises from the interaction between two polynucleotide chains, or fragments of the same chain for RNA, forming a non-covalently bound structure. For proteins, this level of organisation appears by local and specific interactions, also non-covalent in nature, between amino acids leading to canonical structures like α-helices or β-sheets, among many others. The proposal of secondary structure in lipid bilayers reasonably follows and extends this, being similar to the case of the double helix in DNA: it consists of two monolayers facing each other, like a velcro strap, pointing the hydrophobic chains against each other and leaving the polar headgroups exposed to the solvating media. This analogy is not only structural, but extends to the type of interactions at play. The local interactions between polynucleotide chains are mediated by Hydrogen bonds, which are significantly stronger than the hydrophobic forces arising between two lipids in different leaflets. However, these latter interactions are cooperative, again, like in a velcro strap, which makes the overall interaction between the two monolayers very strong. This secondary structure is vital for the integrity of lipid bilayers, as monolayers do not exist in solution except in the presence of a hydrophobic/hydrophilic interphase. Some differences can still be found with the secondary structure of nucleic acids and proteins. First, the interactions that govern the secondary structure of the lipid bilayers occur in two dimensions, contrary to the quasi-1D nature of the interaction between two polynucleotide chains. Moreover, the inherent fluidity of lipids in a membrane makes the forces governing the appearance of their secondary structure non-local in nature, contrary to the highly specific interactions between pairs of nucleotides in DNA/RNA or the interactions between specific amino acids in a protein. As a result of this secondary structure in the lipid bilayers, the two leaflets that form them are highly correlated. This is clearly illustrated when observing the topography maps of the leaflets, their curvature, the vector fields arising from their Local Frames of Reference, or even the vector fields of the lipid directors.

4.2.3 The Tertiary Structure of the Lipid Bilayer

Higher levels of structure in a lipid bilayer can be inferred from the coordinate behaviour of lipids within them. This leads to local domains that interact with each other and modulate the spatiotemporal demeanour of the bilayer. However, these domains do not necessarily correspond to different thermodynamic phases within the membrane but are regions with a defined strong correlation in a given property or set of properties of the bilayer. Therefore, the definition and potential localisation of these domains depend on the specific property that is being measured. For example, the topography of a membrane patch may exhibit protuberances and valleys, display regions of different thicknesses, and the lipid tails could be orientated in a coordinate manner, forming recognisable patterns. Each of these properties could establish a basis upon which a domain can be defined. The analyses proposed in the Methods chapter, Section 3.5.1 identifies these lipid domains, as well as the interactions and couplings between them. The results corresponding to the large bilayers simulated at the CG level are discussed in what follows.

4.2.3.1 Identification of Domains

As shown in Figure 4.10 and Figures S18 to S20, the diameter and amplitude of the membrane protuberances in their topography maps clearly condition the vector fields arising from the LFR. Moreover, and because of this, both the topography and the LFR form well-

defined domains. The probability density functions for membrane curvature (Figures S21 to S23) exhibit their maximum at 0 $Å^{-1}$, as expected, since the membranes are overall flat; and their associated heatmaps show that the larger deviations from planarity correspond roughly to the highest hills or lowest valleys in the topography maps.

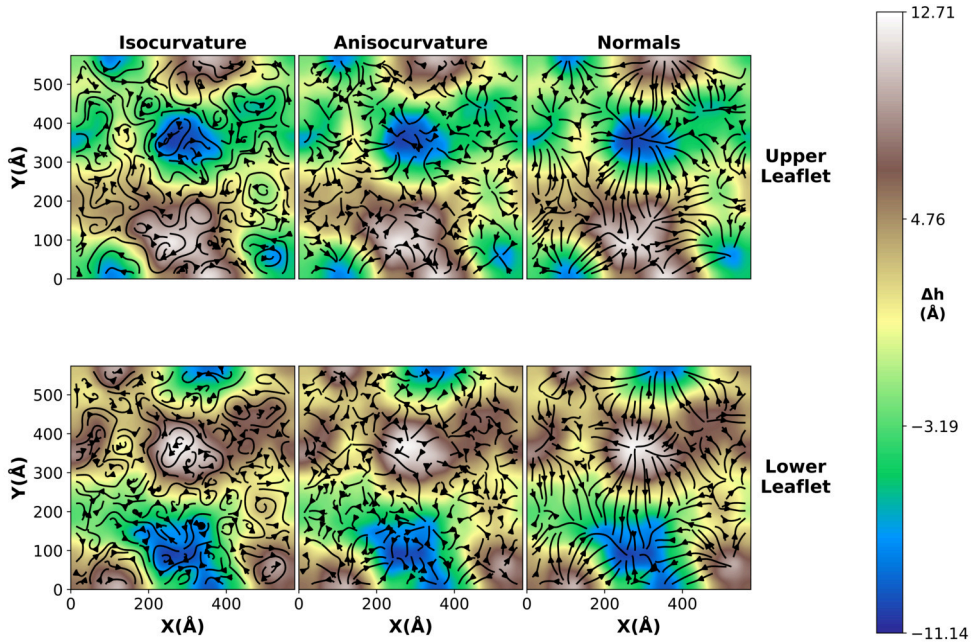

Figure 4.10: Topographic map and LFR vector fields for both leaflets (see labels on plots) of the POPC membrane. The connection between different regions and the anti-complementarity between the two leaflets are clearly seen in these vector field maps.

The vector fields arising from the lipid director were determined as explained in the Methods chapter, Section 3.3.6. The field lines emanate from the lowest topographic points and converge in the highest membrane regions (see Figures S24 to S26). Interestingly, the lipid director vector field is antiparallel to the field obtained for the membrane normal vectors. The angle between these two fields was measured, (*i.e.*, the tail tilt, see Section 3.3.6), and the results are shown in Figures S27 to S29. The corresponding heatmaps do not present domains as well defined as, for instance, the curvature, probably due to the fact that the membranes are in the fluid phase at the temperature at which the simulations were carried out. However, slightly lower tilt angles can be observed for the regions where the topographic slope is maximum.

The membrane thickness calculated accounting for the membrane shape, as described in the Methods chapter, section 3.3.1, exhibits a narrow normal-like distribution, centred at different values depending on the membrane composition, as expected (Figures S30 to S32). The associated heatmaps show spatial domains of different thicknesses in a more or less obvious manner, depending on the case. The correlation between the thickness and the rest of the properties is not directly evident, although the order of the tail is expected to simultaneously depend on membrane topography, curvature, and thickness and hence some connection is expected to appear between them.

4.2.3.2 Filtering Non-Redundant Properties

It is now clear that, in general, the structural domains observed so far arise from the interaction between groups of lipids behaving in a coordinate manner, spanning zones a few nanometres in size. These domains and the interactions between them will be identified with the tertiary structure of the lipid bilayer, in analogy to the tertiary structure of proteins or nucleic acids arising from the relative spatial orientation of different supramolecular motifs. However, and as stated above, a single definition of a domain is not self-evident, as they depend on the property one is discussing: a domain of topography may not necessarily have a complete spatio-temporal overlap with a domain of curvature, for example. It is thus convenient to identify which properties are coupled to one another and provide identical or quasi-identical domains; and which properties are independent of the rest and provide non-redundant information about the mechanical state of the lipid bilayer. Therefore, a minimal set of quantitative descriptors obtained from the calculated properties introduced in previous sections will be obtained. This set of variables strives to characterise the structural state of the lipid bilayer without redundancies. A Singular Value Decomposition analysis, as described in the Methods chapter, Section 3.5.1, will be used to this aim. The complete results for the three membranes studied can be checked in Figures S33 to S38.

The explained variance per eigenvector (Figure 4.11 and Figures S33 to S38, top left panel) is a step function where several groups of properties contribute equally to the total variance. This degeneracy in the explained information is a consequence of the close connection between the

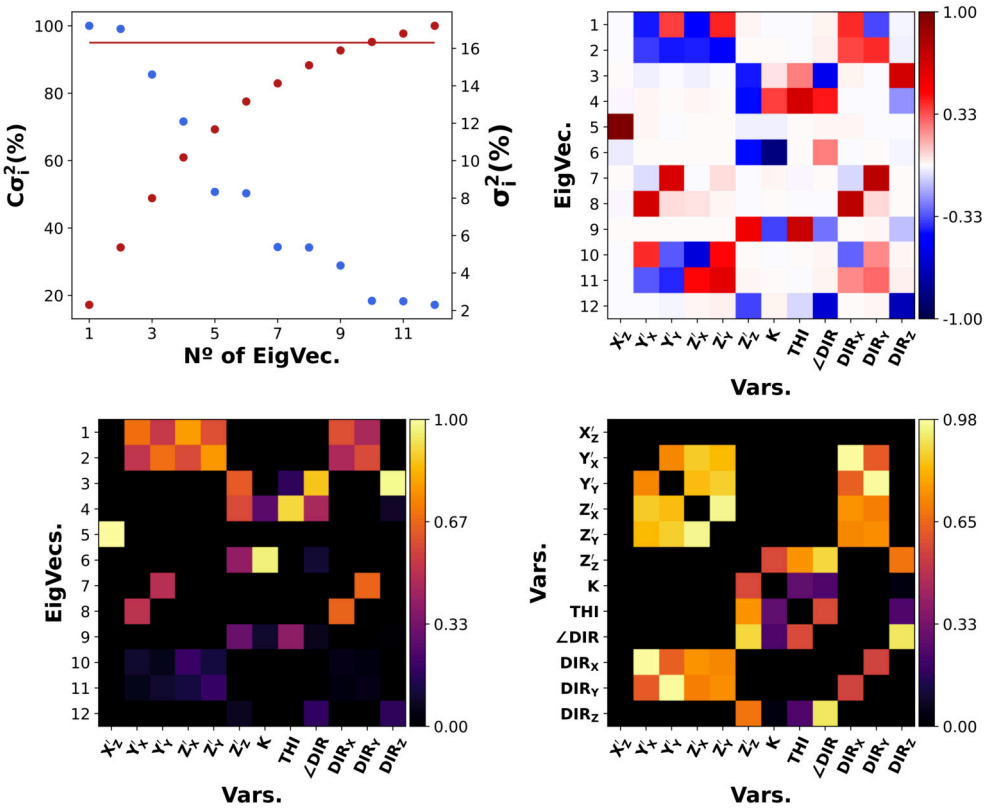

Figure 4.11: Results for the SVD analysis performed on the non-redundant set of variables for the POPC membrane. Starting from top left and going clockwise: Cumulative (red, red line 95% variance) and explained (blue) variance per eigenvector, V^T Matrix, Coupling Matrix and Relevance Matrix.

variables and their cooperative behaviour when forming the membrane domains, which would instead be defined as zones of cooperation between several properties. Complementarily, only 11 variables are required to explain 95% of the total variance for all studied membranes, and the last 3-4 eigenvectors are almost completely redundant, hinting that they are just encoding noise. The V^T matrices that contain the eigenvector components indicate that several variables are coupled to each other, as some eigenvectors show very similar loads for the same variables.

The property-property coupling was quantified in a coupling matrix (Figure 4.11 and Figures S33 to S38, bottom right panel), introduced in the Methods chapter Section 3.5.1.3. In these matrices it can be clearly observed that several components of each vector of the LFR are strongly coupled to each other. Moreover, the X and Y components of the surface normals are strongly coupled to the X and Y components of the lipid director vectors. These correlations were already an expected result after what was discussed in the previous Section 4.2.3.1, where the LFR vector fields were discussed, as well as the antiparallel disposition of the lipid director field with respect to the normal vector field; both are evident to the naked eye. This information points to the existence of a minimal set of properties that characterise the internal state of the bilayer. It is also interesting to observe the total lack of correlation between some variables, indicating that they are independent and complementary to each other. For instance, the topography of the membrane does not couple to either the X or Y component of the Iso or Anisocurvature, but it does show it, albeit faintly, with the Z component of the latter vector field; and quite more clearly with the membranes' curvature.

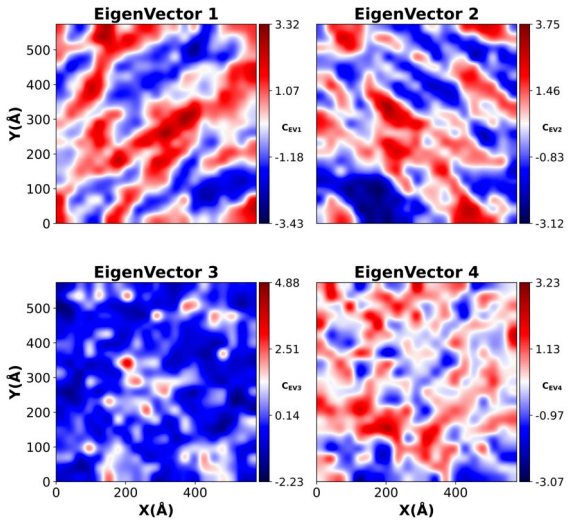

Figure 4.12: Projection of the first four eigenvectors resultant of the reduced SVD analysis on the surface of the POPC membrane in the last frame of the trajectory.

The redundant properties observed in previous analyses were detected and pruned from the data matrix with the method described at the end of Section 3.5.1.3, that is, by eliminating one of the instances of pairs of variables that display identical relevance vectors in the relevance matrix. After this pruning step, we are left with a minimal set of properties which was exactly the same for all membrane compositions studied, indicating that the mechanism giving rise to the phenomena we propose as the tertiary structure is independent, at least at this level, from membrane composition. The four discarded variables were the height function, the X and Y components of the isocurvature, and the Z component of the anisocurvature, in good agreement with the four redundant low-variance eigenvalues observed in the full SVD analyses. One should note that these properties are not actually being removed from our reasoning, but it is assumed that the information they carry is already encoded by some other property. Therefore, a redux version of the SVD analyses was performed with the following magnitudes: the Z component of the isocurvature, the X and Y component of the anisocurvature, the complete normals vector field, the curvature scalar field, the thickness of the membranes, the lipid director tilt, and the full lipid director vector field.

No redundant eigenvectors were observed in the cumulative variance plots (Figures 4.11,

S36 & S38, top left panel), indicating that all the properties considered for the redux SVD analyses are independent of each other, as expected. The final V^T, relevance and coupling matrices (Figures 4.11, S36 & S38, top right, bottom left and bottom right panels) show that there are still strong couplings between the variables, hinting at cooperative behaviour when defining membrane domains. Thus, from the initial set of 16 properties (31 if we consider both leaflets), only 12 were found to be not superfluous. In analogy to proteins, the different domains interacting with each other in a lipid membrane, which we propose to describe by the couplings of non-redundant properties, are postulated to be the tertiary structure. The coupling between the investigated properties is comparable for the three membrane compositions considered in this work, suggesting that the observed relationships are an underlying fundamental mechanism of how lipid membranes self-organise in equilibrium, independent of their composition. It is important to emphasise that this observation may not hold if other properties are taken into account. Finally, if we want to spatially resolve the domains created by the linear combination of coupled properties, we can project the eigenvectors over the MD trajectory (Figure 4.12 and S39 to S41), obtaining a complementary description to that provided by the pure properties.

4.2.4 The Quaternary Structure of the Lipid Bilayer

The levels of structure described above are expected to exist for all lipid membranes, regard-

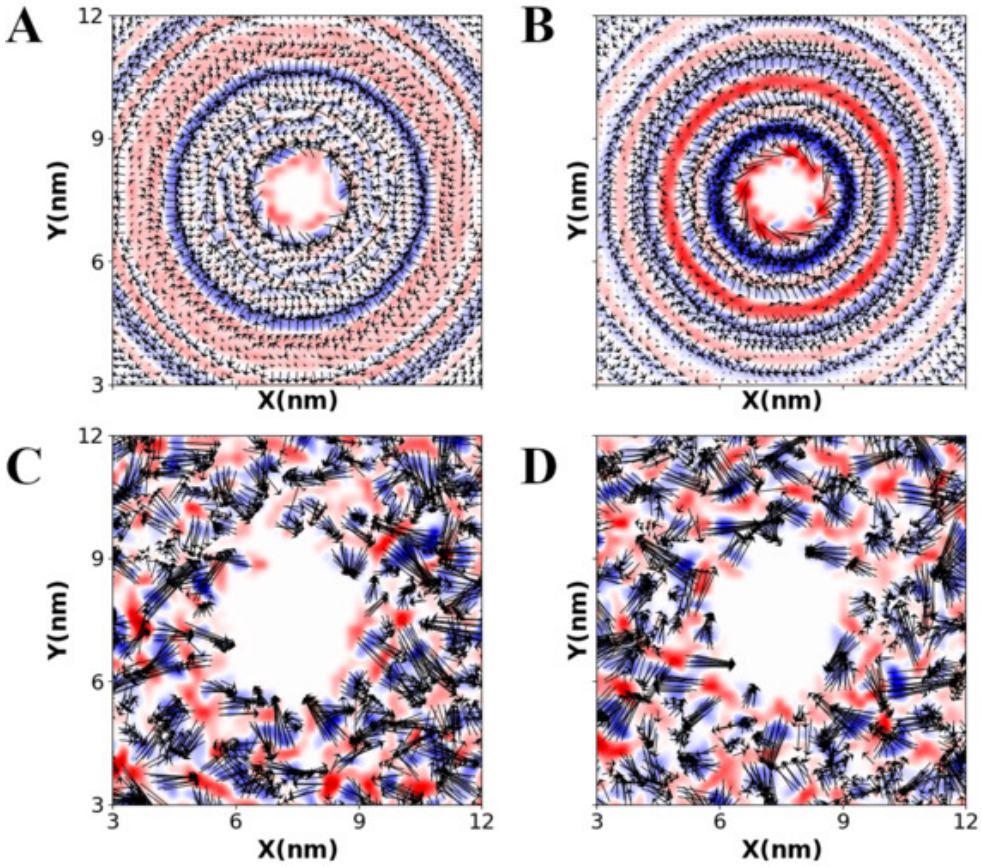

Figure 4.13: Schematic representation of the quaternary structure in a DOPC lipid bilayer containing a carbon nanotube (A,B) and a β-barrel protein model (C,D). The vector fields obtained from the orientation of the lipid SN1 tail (A,C) and SN2 tail (B,D) in the upper leaflet are plotted together with the corresponding divergence represented in red-blue colour gradient for divergence-convergence, respectively.

less of their composition. However, the highest-order hierarchy remains to be established. In the case of nucleotides, the quaternary structure is defined as the interaction between biomolecules and nucleic acid strands, forming other canonical structures like DNA around histones.

Taking advantage of previous work[505], the behaviour of an atomistic DOPC membrane model was tested and compared in the presence of a carbon nanotube (CNT) and a simple β-barrel model (Figure 4.13). By visual inspection, the influence of the macromolecules on the lipid organisation is remarkable and is clearly distinguishable depending on the system. The CNT creates a series of concentric circular ripples around itself and generates a discernible pattern in the lipid tails. On the other hand, the β-barrel generates localised clumps of lipids with the same orientation of the lipid directors but without an overall cohesion as in the previous case. Thus, the case of the quaternary structure is defined straightforwardly from that of proteins or nucleic acids: it is the response and interaction of lipid membranes with other macromolecules, which are distinctive depending on the case.

4.2.5 Conclusions

The analysis of lipid membrane structures presented in this chapter has revealed a hierarchical organisation that offers new insights into the complex nature of lipid bilayers. This perspective provides a novel framework for understanding the structure and function of the membrane.

The primary structure, defined as the proportions of different lipids in each leaflet, establishes the foundation for membrane diversity. This concept highlights the dynamic nature of membranes, capable of altering their composition in response to environmental changes, a feature distinct from the fixed primary structures of proteins and nucleic acids.

The secondary structure, which is characterised by the interaction between two monolayers facing each other like a Velcro strap, emphasises the cooperative nature of hydrophobic interactions in maintaining membrane integrity. This structure exhibits unique two-dimensional interactions that contribute to the membrane's fluidity and adaptability.

The tertiary structure, represented by the formation and interaction of various domains within the membrane, has been thoroughly examined using advanced analytical techniques. The identification of a minimal set of non-redundant properties through an SVD analysis revealed intricate couplings between different membrane characteristics. Notably, these couplings appeared to be largely independent of membrane composition for the POPC, POPE:POPG, and DMPC systems studied, suggesting fundamental organisational principles common to diverse lipid bilayers.

The analysis demonstrated that from an initial set of 16 properties (31 when considering both leaflets), only 12 were non-redundant. The coupling between these properties was comparable across the three membrane compositions studied, indicating that the observed relationships may represent the underlying mechanisms of lipid membrane self-organisation in equilibrium.

The quaternary structure, defined by the interaction of the membrane with other macromolecules, demonstrated the profound impact of embedded proteins or nanostructures on lipid organisation. The distinct patterns observed around carbon nanotubes and β-barrel proteins in DOPC membranes illustrated the membrane's ability to adapt its local structure in response to different inclusions.

This hierarchical framework provides a more nuanced view of membrane structure beyond the traditional fluid mosaic model, describing the complex interaction between lipid composition, domain formation, and interactions with other cellular components. The consistent patterns observed across different membrane compositions suggest that these structural principles may

be fundamental to the organisation of the lipid bilayer.

Further research could explore how this hierarchical structure is affected by various physiological conditions, membrane-protein interactions, and a wider range of lipid compositions. In addition, this framework may provide new avenues for investigating membrane-related phenomena and developing more accurate computational models of biological membranes.

4.3 Block 3: Influence of Lipid Composition on Membrane Response to Ultrasound: Structural and Dynamic Insights

As it was discussed in the Introduction chapter of this Thesis, lipid membranes can be used as therapeutic targets to treat a wide range of maladies. In general, these strategies are based on chemical attacks, taking advantage of the different chemical environments that said membranes create around specific cells. However, as introduced in section 1.2.3.4, the ability of cells to sense mechanical forces can also be exploited for therapeutic purposes, and the cellular membranes are intimately related to this. Therefore, a proper understanding of the factors involved at the molecular level is of paramount importance in designing better and more effective strategies.

Thus, another aspect of this Thesis was studying the effect of mechanical perturbations acting on lipid bilayers. The hypothesis was that, in principle, different membrane compositions would react differently to said perturbations. If differentiation were to be sufficient, this would open up possibilities for targeted therapies based on mechanical principles, as there would be a way to rationalise them. The family of mechanical perturbations is broad, so the focus was placed on ultrasounds (US), and more specifically, on High Intensity Focused Ultrasounds (HIFU), discussed in the Introduction chapter, section 1.2.3.4. As introduced in the Objectives chapter, Section 2.3, this work is divided into two differentiated blocks. The first one, reproduced in the following section, studies the feasibility of modelling US waves within a MD pipeline and, once implemented, examines the influence of one type of US wave on 10 different membrane compositions. The implementation of the method to simulate an US wave is explained in detail in the Methods chapter, Section 3.4.1, and information about the construction of the studied systems as well as simulation parameters can be consulted in section 3.6.3. A schematic representation of how the applied deformation can be interpreted is seen in Figure 4.14. The method proved to be easy to patch into the GROMACS legacy code and robust since, in principle, it can be used in any MD simulation that can be set up and run with the chosen engine.

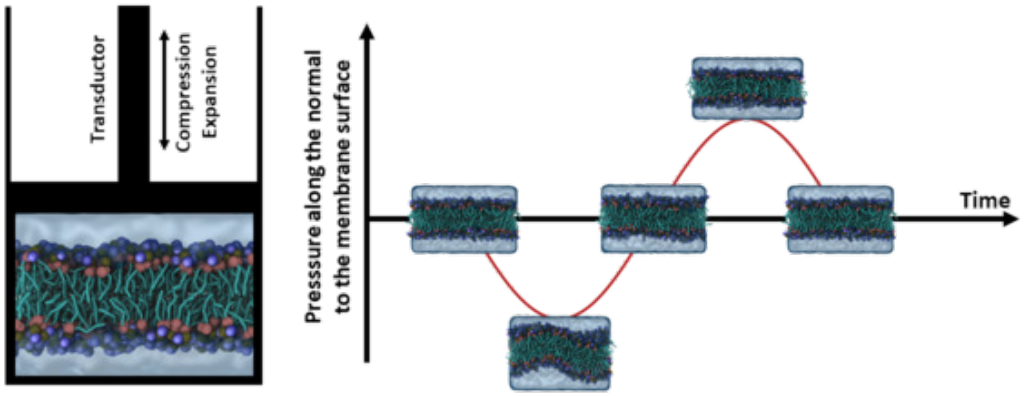

Figure 4.14: Illustration of the practical effect of a transducer applying a periodic pressure change along the normal to the membrane, together with a representation of the amplitude change as a function of time. The snapshots correspond to a POPC lipid bilayer at the pressure where they are located in the schematic plot. The NC3 group is coloured in blue, the PO_4 group in brown, Glycerols in salmon red, and water is shown as a blue, transparent volume.

Despite a detailed explanation of the most relevant results when testing the effects of the HIFU model on lipid membranes being provided in the following section, the reader is referred to an original publication in the Journal of Colloids and Interface Science[480], **2023**, *650*, 1201-

1210 (doi: j.jcis.2023.07.077) distributed under a Creative Commons 4.0 Licence. Of particular interest is a lengthy and detailed supplementary information (SM2 in the article), where the pertinent figures for all systems studied can be consulted. In addition to the author of this Thesis, the article was co-authored by Siewert-Jan Marrink, from the Rijksuniversiteit Groningen; Ángel Piñeiro Guillén, from the Universidade de Santiago de Compostela; and Rebeca García Fandiño, from the Universidade de Santiago de Compostela. For this study, the first author patched the MD engine source code in order to allow simulation of an US wave, performed the simulations, analysed them, and contributed to the writing of the final manuscript.

4.3.1 Response of the Membranes to a US wave

A molecular depiction of how the HIFU model impacted an atomistic and coarse-grained POPC membrane can be seen in Figure 4.15. The amplitude and frequency of the pressure wave were taken following typical values of a real HIFU treatment. The AA models were used to test whether the CG simulations reproduce the same behaviour which, under the studied conditions, produced the same results within a reasonable and expected discrepancy. Under these conditions, all the tested membranes were affected to a great extent by the mechanical perturbation induced by the US wave. However, the self-assembled bilayer state was never lost. The structural transformations in the properties measured were periodic in nature, closely following the pressure wave.

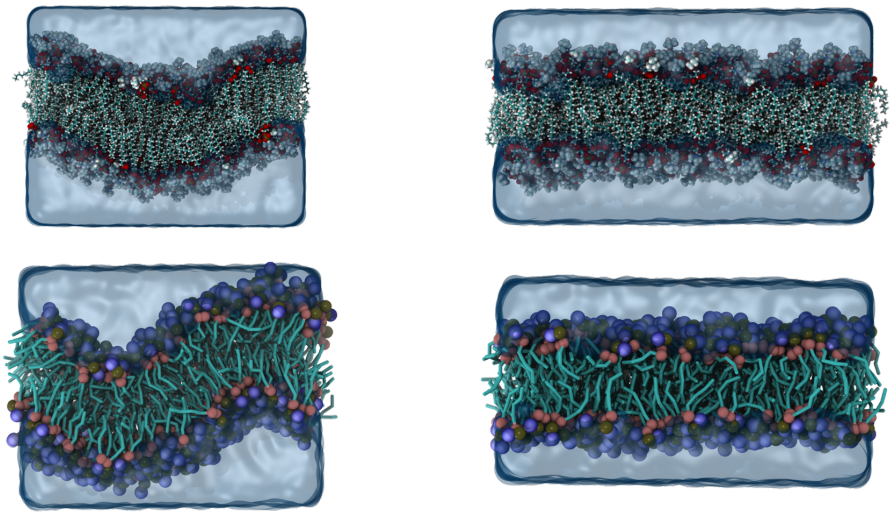

Figure 4.15: Snapshots of POPC membranes at All Atoms (top) and Coarse Grained (bottom) resolution. The images correspond to frames of MD trajectories at the minimum (-35 bar, left) and maximum (+35 bar, right) pressures. In the AA representation, oxygen atoms are coloured red, nitrogen atoms are coloured blue, phosphorus atoms brown, carbon atoms turquoise, and hydrogen atoms white. In the CG representation, the $N(CH_3)_3$ group is coloured blue, the PO_4 group is coloured brown, the glycerols are coloured salmon red, and the aliphatic chains are coloured turquoise. For both cases water is shown as a blue, transparent volume.

4.3.2 Comparison of AA and CG Simulations

The results obtained from MD simulations using the atomistic and CG resolution under the same oscillator parameters and number of US cycles are compared in this section. The

RDF (see Section 3.3.2 for its definition) of the phosphate groups provides information on how the lipids are distributed within a bilayer of the lipid membrane (Figure 4.16). This property shows a marked dependence on the pressure wave felt in the simulation box. The impact of this perturbation is felt to its greatest extent in the intensity of the RDF peaks, and much more subtly on their positions. The RDF clearly decreases for the highest pressures, showing an elastic response for all membranes, and the RDF peaks increase for the lowest pressures. There is no discernible delay between the applied deformation and the RDF response.

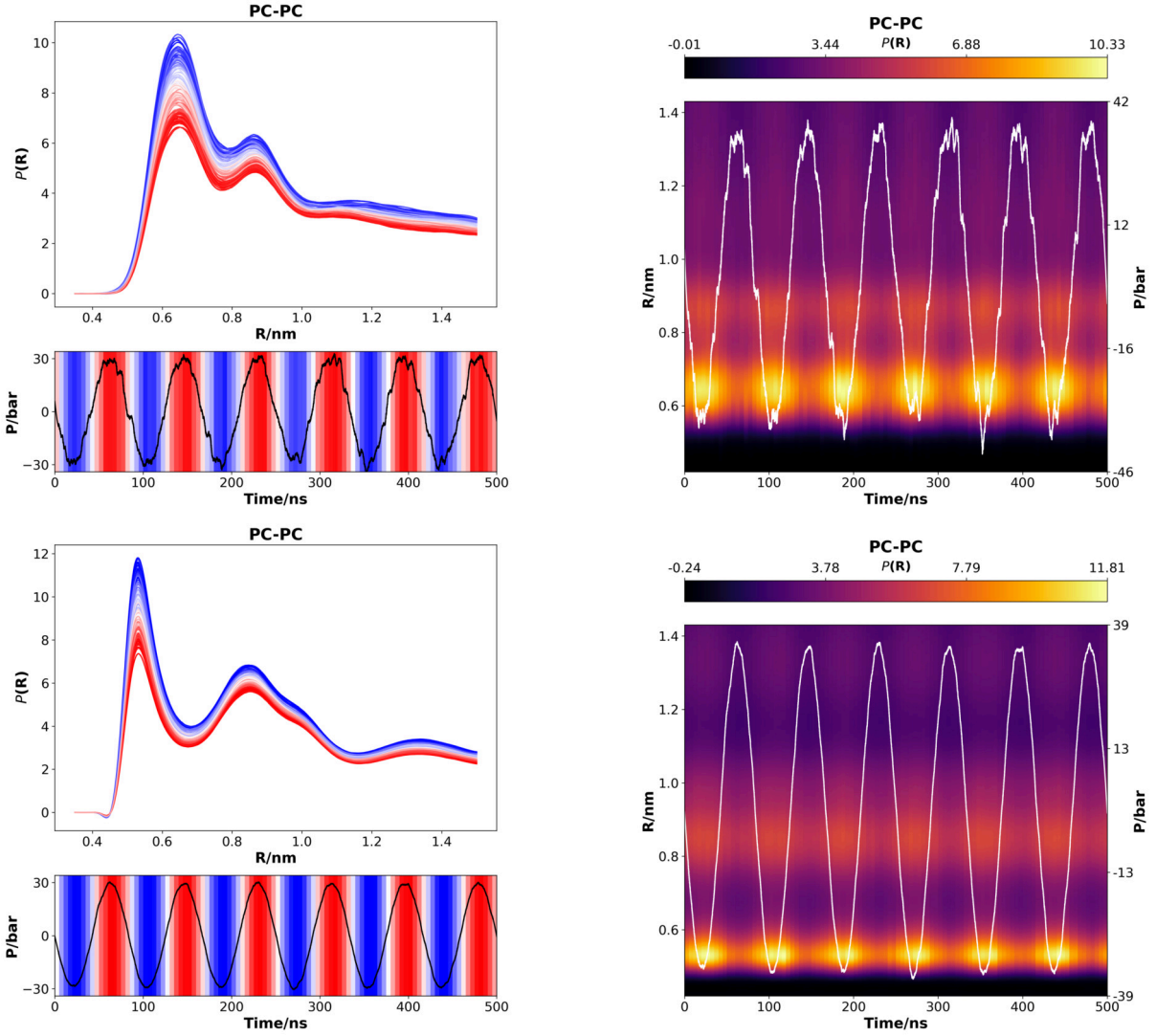

Figure 4.16: RDF profiles for the All Atoms (top) and Coarse Grained (bottom) simulations of the POPC membranes. The left graphs display the RDF as a function of the pressure with a blue-white-red gradient from low to high pressure. The right panels display the RDF as a function of time (left Y axis with the colour bar on top of the plot) and the instantaneous pressure as a white line (right Y axis).

In general, the RDF profile shows similarities at a qualitative level between atomistic and CG resolutions (Figures 4.16 & S42), regardless of the composition of the membrane. However, the RDF profiles for the CG simulations consistently show the appearance of the first maximum at shorter distances. The intensity of this first peak is also influenced by both the forcefield and

the salt concentration. It is also worth noting that the biggest peak of the RDF increases in intensity for some of the bilayers composed of two lipid types, hinting at more ordered membranes. While the main structural differences of the RDFs between atomistic and CG simulations can be attributed to the inherent differences in parameterisations of the forcefields, the dynamical response to the US wave-induced perturbations remains equivalent across all the simulations.

To analyse the possible enhanced permeability to water when membranes are subjected to ultrasounds, the density profiles of PO_4 groups as well as those of the solvent were calculated (Figures 4.17, and Figures Figs. S.31-S.60 in SM2 of the published article). A clear relationship between density and pressure can be observed as, in general, the PO_4 groups of opposite leaflets are pulled apart from each other during oscillator decompression cycles, while the waters seem to penetrate the membrane more deeply. However, in either case, water diffusion through the bilayer was not observed. The number of contacts between water molecules and lipid tails (Figure 4.18) decreased towards the end of the acyl chains, with the highest contacts occurring at high pressure moments. This is more evident for the CG simulations than for their atomistic counterparts, in which a small temporal lag with respect to the pressure wave can be appreciated. It should be noted that, despite contacts between the solvent and the last carbon of the acyl chains being appreciated in some instances, these are due to highly bent tails that get close to the membrane surface because of the substantial deformation induced by the US wave.

CG simulations are more sensitive to pressure changes than their AA counterparts, with the exception of systems containing POPG. In these cases, AA resolution simulations are more vulnerable to pressure perturbations. For systems that do not contain this lipid, atoms are more dispersed along the normal to the membrane plane, and PO_4 positions are significantly perturbed by pressure changes. In contrast, PO_4 group positions in AA systems are much more stable. This analysis was not sensitive to salt concentration, as CG simulations with the same lipid composition

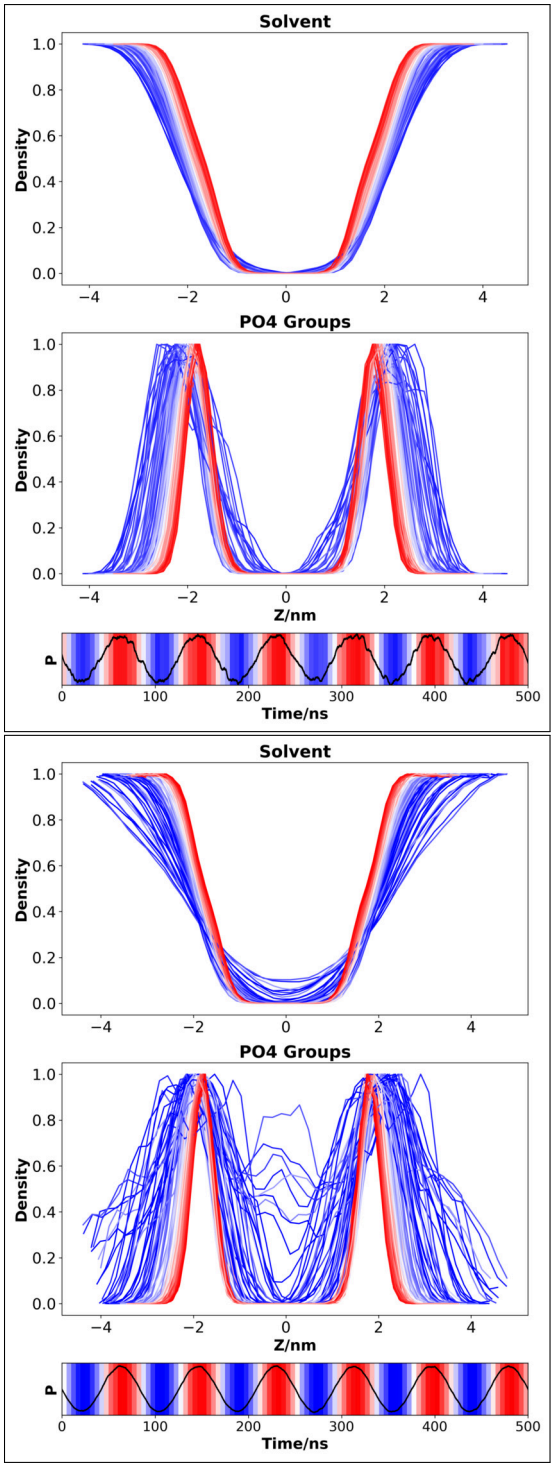

Figure 4.17: Lateral density profiles as a function of pressure. Top graph, AA POPC; bottom graph, CG POPC.

yielded equivalent results. For the atomistic systems, no water could be found in the innermost part of the hydrophobic core of the membrane, unlike that found in the case of their CG simulation counterparts. Overall, these findings indicate that focused US can significantly distort the membranes' structure, even in the absence of shockwaves from microbubble collapse or thermal effects. Depending on lipid composition, some significant and non-systematic differences can be observed between AA and CG simulations.

Further analyses were performed on the membranes, including the Area per Lipid (APL) as described in Section 3.3.5, membrane curvature as described in Section 3.2.2, tail tilt as described in Section 3.3.6 and the thickness of the membrane as described in Section 3.3.1.2. Their corresponding figures can be consulted in SM2 of the published paper: Figs. S.61-S.110, S.111-S.160, S.161-S.210, and S.211-S.260. All of these properties were found to be sensitive to the US wave. The APL and tail tilt are directly proportional to the applied deformation, that is, the highest deformations produced higher values for the subsequent properties in these magnitudes; and the thickness was inversely proportional. The average curvature remained zero for all cases, and the membrane models remained flat overall as the regions of local positive curvature countered the regions of local negative curvature. However, the dispersion of the curvature was clearly impacted by the US wave. Time-resolved histograms and spectrograms using the Short-Time Fourier Transform (STFT), as detailed in Section 3.4.2, for these properties. Deviations from the first-harmonic frequency of the mechanical perturbation indicate non-elastic behaviour, probably arising from specific lipid-lipid interactions within the membrane. Thus, the membrane acts as a mathematical kernel that transforms the single-component oscillating wave into a complex, property-dependent signal which carries information about the simulated system.

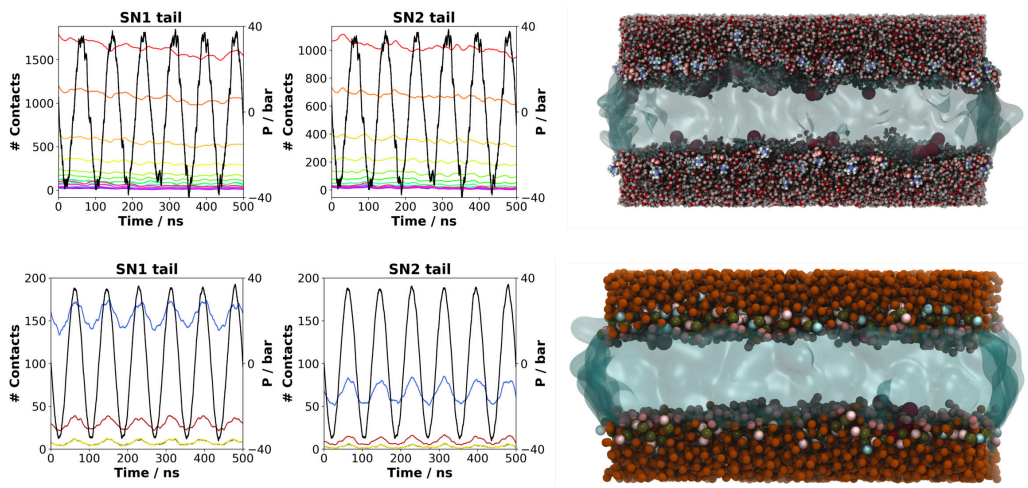

Figure 4.18: Number of contacts between water molecules and the lipid tail particles -carbon atoms or CG-beads, depending on the employed forcefield as represented by different coloured curves in the left-hand plots. Each curve corresponds to a specific particle within the lipid tail, with varying colours to distinguish the contacts with water molecules for each particle. The snapshots on the right correspond to the moment when the number of contacts with the last particle of some lipid tail is at its maximum. The plots depict the simulations of pure POPC in AA (top row) and CG (bottom row) resolutions. Lipid tails are shown as a transparent volume, and water molecules in contact with the last particle of some lipid tail are represented as large red spheres.

The APL response to perturbation shows, mainly, a single harmonic, with some lipid compositions displaying an evident second harmonic. Curvature, tail tilt, and thickness all exhibited harmonics beyond the fundamental frequency, evidencing a non-elastic behaviour. The pure POPG membrane shows a different demeanour, with only the fundamental frequency showing up in the STFT spectrogram. The thickness of the bilayers shows a higher correlation with the pressure wave than the rest of the properties. The results are consistent among forcefields, and the thickness is eloquent in highlighting differences between lipid compositions. The Order Parameters (OPs), as described in Section 3.3.7, were calculated and the STFT spectrogram was obtained for them (refer to Figures S.262-S.291 in SM2 in the published article). OPs exhibit a marked correlation with the US wave, agreeing with the observations for the tail tilt. Although the oscillatory nature is common for the AA and CG forcefields, the results are not directly comparable for the OPs, because of differing particle representations for the same molecules.

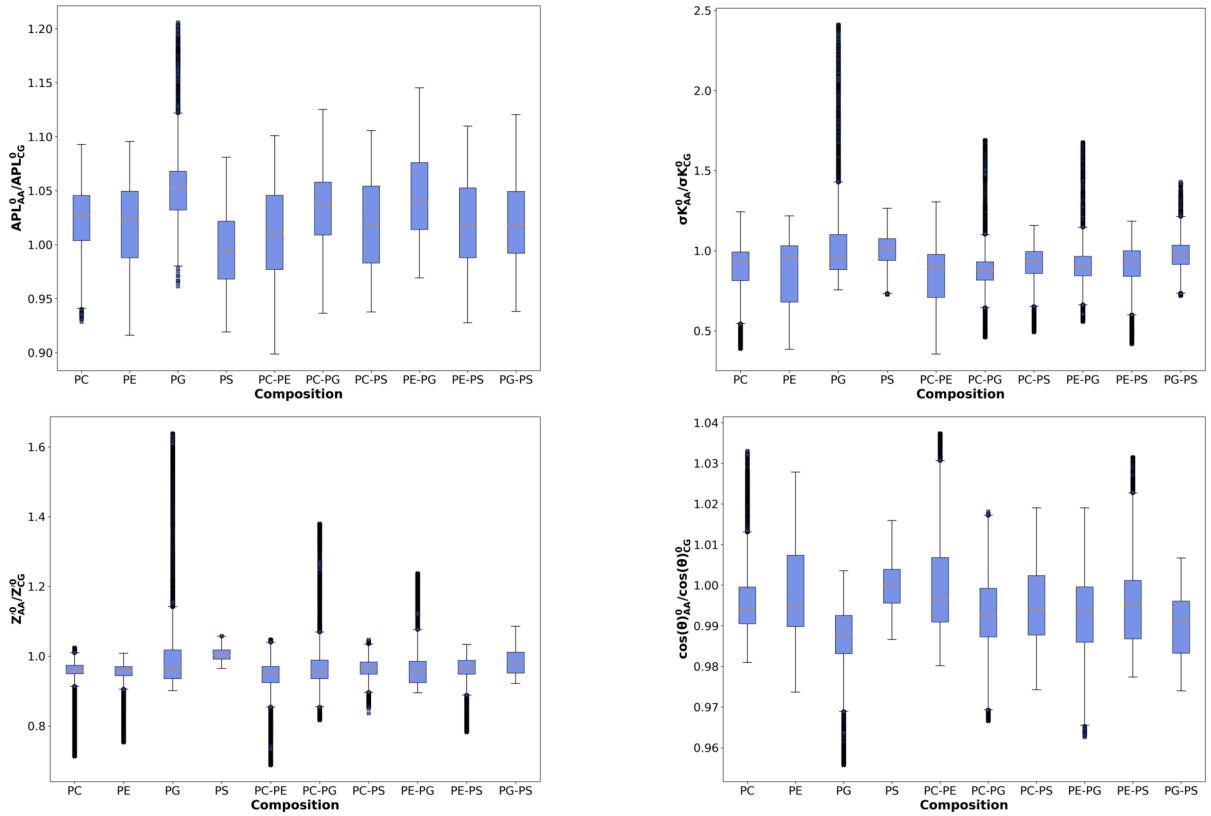

Figure 4.19: Ratios of the normalised time series of the calculated properties between the AA and the CG forcefields along the first 500 ns of each trajectory ($R_x = \langle X^0_{AA}/X^0_{CG} \rangle$). The different lipid compositions are indicated in the abscissa, without the 'PO' prefix for the name of each molecule. Starting from upper left and going clockwise, the APL, curvature dispersion, thickness, and tail tilt. The blue box areas represent the interquartile rank (iqr = Q3 - Q1), the yellow horizontal line represents the mean, and the whiskers are calculated as Q1-1.5·iqr and Q3+1.5·iqr, respectively. Outliers are represented by a 'x' marker.

In light of the results, four properties were chosen for the comparison between the CHARMM and Martini forcefields, because they do not depend on the level of resolution at which the molecules are represented; APL, curvature dispersion, tail tilt, and thickness. The properties

were normalised following the method introduced in Section 3.4.2.1, and the ratios of the normalised properties between the AA and CG simulations were obtained. The average values of these ratios were used to estimate the similarity between the CHARMM and Martini parameterisations. Figure 4.19 shows the results of the calculation of the ratio for such properties. These are always centred around 1, within an expected margin of error, for all membrane compositions. This indicates that both forcefields give equivalent results at the quantitative level within a reasonable margin for discrepancies, after normalisation against an equilibrium MD simulation. Some of the compositions display a considerable number of outliers, though, which arise from distinct events in the trajectories where their behaviour deviates significantly from one another.

4.3.3 The Influence of Lipid Composition

The simulations using the CG forcefield were extended until they reached 16.66 µs, comprising a total of 200 compression-decompression US cycles within each trajectory. This allows a significant increase in sampling, thus reducing the ratio of noise in subsequent comparisons. The area of the fundamental frequency of the oscillations plus its first two harmonics along the different trajectories, and for each selected property, was obtained and compared between different lipid compositions (see details and explanation in Section 3.4.2). The results (see Figure 4.20 & Figures S43 to S52) clearly show that different membranes have different sensitivities to ultrasound waves, as expected from the discussion in the previous section. The presence of ions did not seem to be a relevant factor, as the simulations in the presence of 0.15 M NaCl gave the same predictions as those in the absence of the salt. Despite this, there seems to be a systematic effect of lowering the intensity of the oscillation, although this effect is always well within the error of the measurement and thus not statistically relevant.

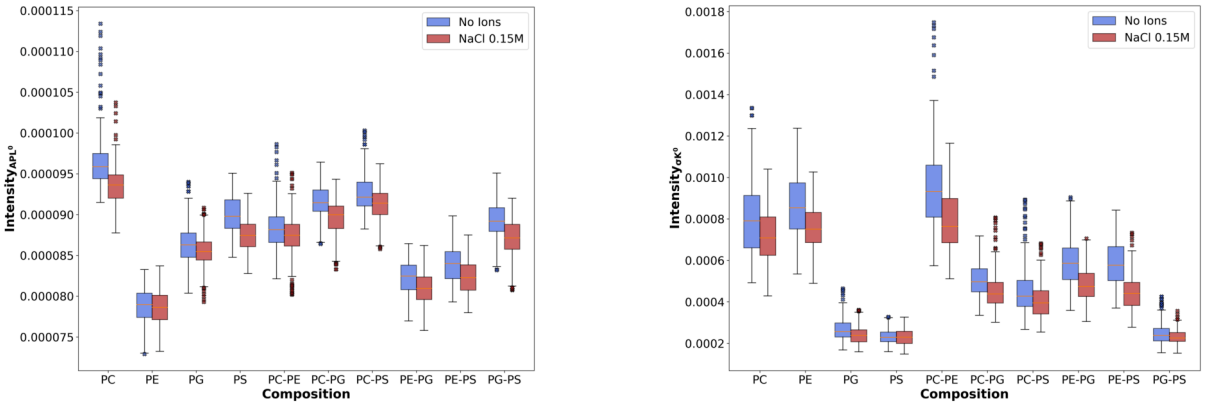

Figure 4.20: Box plot showing the APL (left) and curvature dispersion (right) response of all the simulated systems to the ultrasonic wave. The different lipid compositions are indicated in the abscissa, without the 'PO' prefix for the name of each molecule. The boxes represent the interquartile range (iqr = Q3 Q1) for simulations without additional ions (blue) and with added salt (red), the yellow horizontal line represents the mean, and the whiskers are calculated as Q1 1.5·iqr and Q3+1.5·iqr, respectively. Outliers are represented by an 'x' marker.

An important result is that the response to mechanical perturbations induced by the US wave is highly dependent on the property that is measured (see Figure 4.20 & Figures S43 to S52). The POPE membrane is the most insensitive to the deformations in the APL, whereas the POPG, POPS, and POPG:POPS membranes are the ones that provide the most unresponsive

signals for the curvature. These results also show that mixing different lipids in a membrane leads to additive behaviour in the response of their properties to the US wave, as the reported values for the non-homogeneous membranes fall roughly in the average of the equivalent values for the pure bilayers. For instance, the pure POPC and POPE membranes report the highest and lowest sensitivities in their APL, respectively. Then, the POPC:POPE mixture shows an intermediate behaviour. This is observed for all lipids and all properties.

These differences in behaviour can be related to the inherent mechanical properties of the lipid bilayers. For example, if the bending moduli for POPC (30.3 kBT), POPE (28.9 kBT), POPG (22.5 kBT) and POPS (23.7 kBT) membranes, available in the literature[508], are compared; it is observed that their values align well with which membranes will have the highest and lowest responses in their curvature to US-induced deformations. In essence, a larger bending modulus represents a higher energetic penalty for a bending (*i.e.*, curving) deformation. These relationships underscore how intrinsic membrane properties shape their reactions to an external mechanical perturbation.

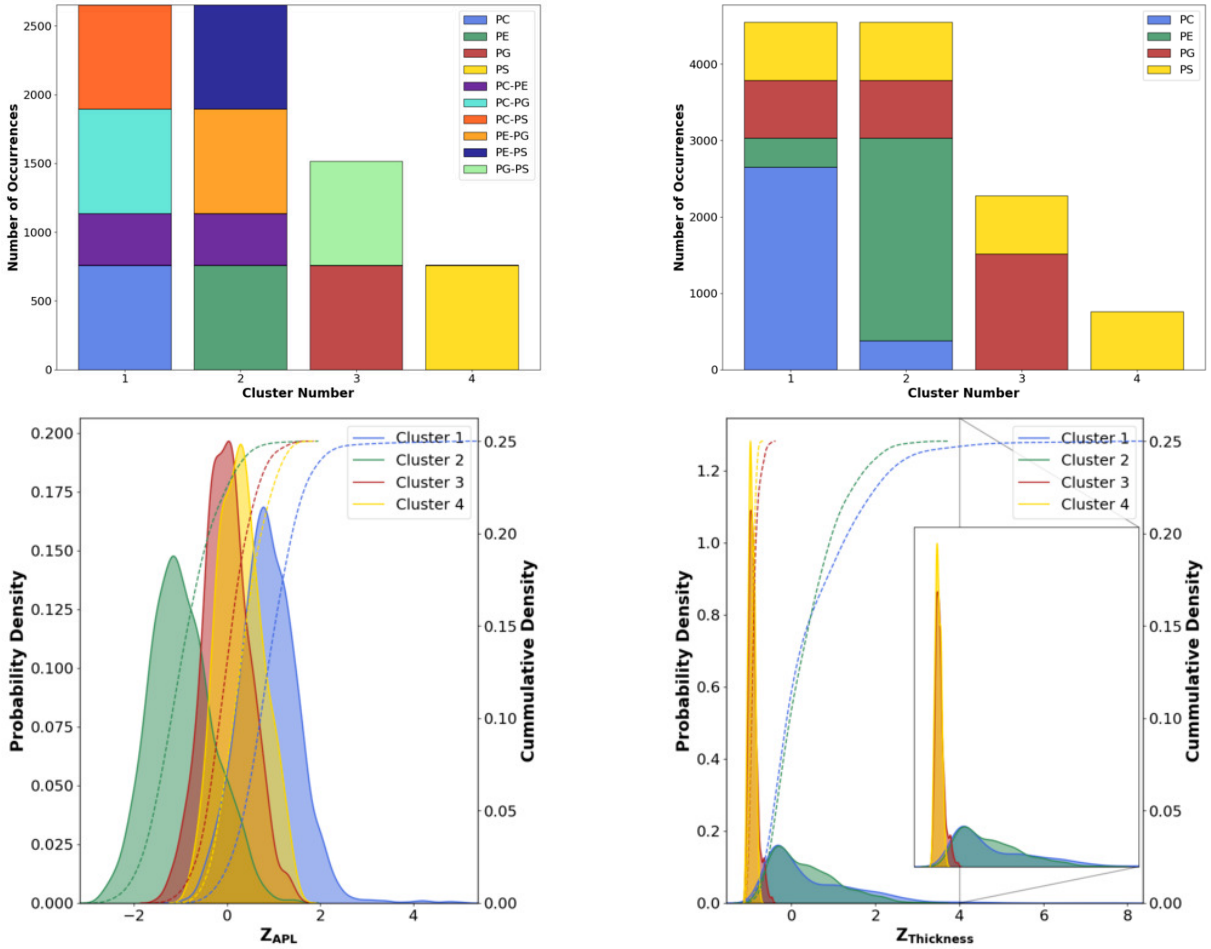

Figure 4.21: Relevant results for the clustering analysis performed over the CG simulations dataset. Starting from top left and going clockwise: composition per cluster, lipid type per cluster, thickness distribution per cluster and APL distribution per cluster.

To investigate whether different membranes exhibit equivalent behaviour, a cluster analysis was performed (see the Methods chapter, Section 3.5.2 for an explanation). A dataset was built

using the results from the intensity of the oscillations for each property measured via the STFT, and then a k-prototypes algorithm was applied to find clusters in the data. The relevant results can be consulted in Figure 4.21 and Figures S53 to S63.

The optimal number of clusters was determined to be four (Figure S53), and the results show clusters that group membrane compositions in a remarkable way (top left panel of Figure 4.21). All but one of the membranes belong to a single cluster, and the composition which is split (POPE:POPG) is so in a 50/50 way in just two clusters. These results point to the groupings that were found to be meaningful and not just an artefact of the algorithm.

The top right panel of Figure 4.21 shows that clusters 1 and 2 are the most abundant and, interestingly, cluster 1 contains all the membranes with POPC, cluster 2 all the membranes with POPE, and the POPC:POPE membrane is evenly distributed between those two clusters. Cluster 3 is comprised of the pure POPG membrane plus the POPG:POPS one; and finally cluster 4 is populated by the pure POPS membrane alone. These results are interpreted as POPC and POPE being lipids with a remarkable ability to modulate and tune the membrane reaction to the US wave as they are able to 'drag' the rest of the systems into their cluster. From that interpretation follows that POPG is able to have an effect over POPS and this last lipid is either on its own, or will be accommodated into the behaviour dictated by a more dominant lipid.

The probability density functions for the different properties, calculated for each cluster (bottom panels in Figure 4.21), provide useful information about their specific sensitivity to the HIFU model. It is observed that the distributions for the APL and the thickness clearly display two different trends. The case for APL shows that the membranes with the lowest response to the US wave are those belonging to cluster 2, while the systems in cluster 1 sit on the other end of the spectrum, and clusters 3 and 4 share the midrange, being cluster 3 slightly biased to higher response values. On the other hand, the probability density functions for the thickness display markedly different behaviours. Clusters 3 and 4 form extremely narrow and down-shifted distributions, indicating that the membranes belonging there have an unresponsive behaviour in this property to the US wave. Clusters 1 and 2 are mostly overlapped at the upper end of the scale and display much broader distributions, indicating that the systems in those clusters will experience a significant amount of deformation to their thickness when the HIFU model is applied.

The results also show that the two trends described in the previous paragraph are the only ones that were found for all the studied properties: the segmental order parameters follow the APL trend, while the curvature follows the thickness trend. Thus, a case-by-case reasoning must be built, as the lipid composition affects not only how much a membrane will be affected by a US wave but also the specific properties of the membranes will react differently to the same type of deformation.

4.3.4 Conclusions

The present study provides a comprehensive analysis of the effects of focused ultrasound (US) waves on lipid membranes of varying compositions. By employing Molecular Dynamics simulations at both atomistic and coarse-grained levels, coupled with machine learning classification tools, this work offers valuable insights into the dynamic-structural responses of membrane models to mechanical perturbations induced by sound waves.

A key finding of this study is the development and validation of a robust method to simulate US waves within the MD pipeline. The implemented protocol proved to be easily integrated into the legacy GROMACS code and demonstrated versatility in various MD simulations. This

methodological advancement paves the way for future investigations into the effects of mechanical perturbations on biological membranes.

Comparison between atomistic and CG simulations revealed that both resolutions produce qualitatively similar results under the studied conditions. This consistency across different levels of detail reinforces the reliability of the findings and supports the use of computationally efficient CG models for extended simulations of the effects of the US on membranes.

A central outcome of this research is the clear demonstration that the dynamic-structural response of membrane models to US-induced mechanical perturbations strongly depends on the lipid composition. This was evidenced across various structural properties, including area per lipid, bilayer curvature, tail tilt, and membrane thickness. The observed differences in membrane behaviour can be linked to intrinsic mechanical properties of the lipid bilayers, such as their bending moduli.

The study revealed that POPC and POPE lipids exhibit remarkable ability to modulate and tune the membrane's reaction to US waves. These lipids were found to dominate the response characteristics of mixed membranes, effectively 'dragging' other lipid types into their behavioural cluster. In contrast, POPG and POPS showed different behaviours, with POPS showing the most adaptable response to different membrane compositions.

Interestingly, the presence of ions at physiological concentrations did not significantly alter the membrane responses to US waves. This finding suggests that the primary determinants of the behaviour of the lipid membrane under US stimulation are the intrinsic properties of the lipids themselves, rather than the ionic environment.

A machine learning-based clustering analysis provided a novel perspective on membrane responses, identifying four distinct clusters of behaviour. This classification offers a potential framework for predicting membrane responses based on lipid composition, which could be invaluable for designing targeted US-based therapies.

Furthermore, the study highlighted that different structural properties of membranes react differently to the same type of deformation. For instance, the area per lipid and segmental order parameters showed one type of response trend, while curvature and thickness displayed another. This complexity underscores the need for a multifaceted approach when assessing membrane responses to US waves.

These findings have significant implications for the development of US-based therapeutic strategies. By understanding how specific lipid compositions respond to various US parameters, it may be possible to design treatments that selectively target pathological cells based on their membrane composition, while minimising effects on healthy tissues.

Future research directions emerging from this work include the exploration of more complex membrane models incorporating proteins and a wider variety of lipids, investigation of the temperature effects associated with US treatments, and experimental validation of computational predictions. Additionally, exploring the effects of different US frequencies and amplitudes on membrane behaviour could further refine our understanding of the mechanisms underlying US-membrane interactions.

In conclusion, this study provides a solid foundation for understanding the molecular-level effects of focused US on lipid membranes. By elucidating the relationship between membrane composition and US response, it opens new avenues for the rational design of US-based therapies and contributes to the broader field of membrane biophysics.

4.4 Block 4: Effects of Ultrasound Parameters on Membrane Properties: Frequency, Pressure, and Structural Responses

As it was discussed in the previous section, as well as in the Introduction chapter, section 1.2.3.4; understanding the molecular mechanisms through which lipid membranes react to mechanical deformations, and in particular to ultrasounds, allows us to rationalize the design of potential therapies that have them as a target. However, the previously presented study with this focus left a relevant gap; how the ultrasound parameters affect the responses of the different membrane compositions tested. Thus, this section of the thesis discusses just that: the effects of varying the parameters for the HIFU model (i.e. its overpressure and frequency) on lipid membranes at a molecular level. A detailed and systematic explanation of how the oscillator parameters affect the membrane structure and dynamics is provided, providing insight into the specific conditions that lead to membrane stability, deformation, or potential failure.

As described in the Objectives chapter, Section 2.3, the study was designed to systematically change the overpressure of the oscillator from 5 to 50 bar in increments of 5 bar and its frequency from 5 to 50 MHz in increments of 5 MHz, resulting in a total of 100 unique combinations of frequency and overpressure. Each combination was tested on four pure lipid compositions; POPC, POPE, POPG, and POPS, thus producing a set of 400 individual simulations. By exploring this parameter space, the aim is to construct a detailed response map that links ultrasound input with membrane behaviour across different lipid environments. The specific details of system construction as well as simulation parameters can be constructed in the Methods chapter, section 3.6.4.

The analyses include multiple structural properties: area per lipid (APL) as a quantitative measurement of membrane elasticity and packing, curvature to account for bending and undulation responses, thickness to assess compression and expansion dynamics, and order parameter to probe lipid tail conformations and membrane fluidity. The following sections present the findings, emphasising how the interplay between ultrasound parameters and lipid composition governs the membrane response.

4.4.1 Visual Trajectory Analysis

Figure 4.22 encapsulates the significant impact the choice of ultrasound parameters has on the integrity of a lipid membrane, illustrating different behaviours during the decompression

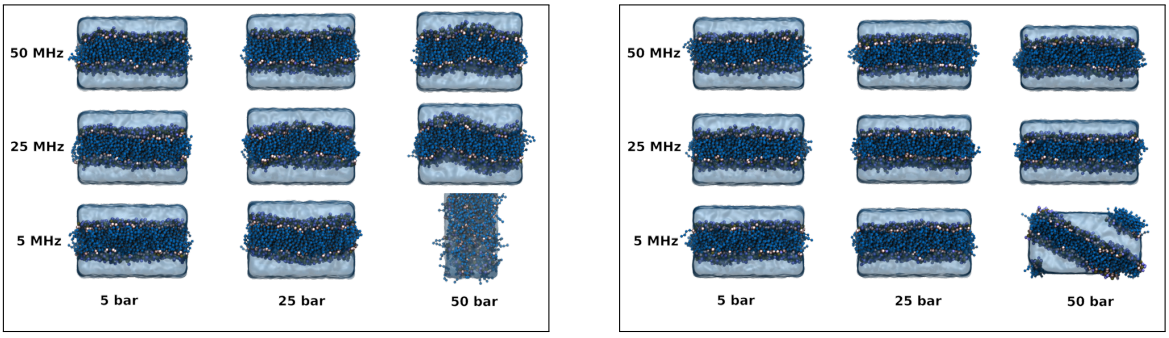

Figure 4.22: Snapshots of POPC membrane deformation under varying ultrasound parameters. The matrix shows membrane responses at different frequencies (5 MHz, 25 MHz, 50 MHz) and overpressures (5 bar, 25 bar, 50 bar). Left panel: membrane states during decompression. Right panel: membrane states during compression. All snapshots are taken at the 100th oscillator cycle, illustrating the cumulative effects of prolonged ultrasound exposure on membrane structure.

and compression phases of the oscillator cycle. For the low pressure phase (left panel), the most dramatic effects are observed at low frequencies and high overpressures. The membrane under the 5 MHz 50 bar ultrasound wave undergoes a complete transformation, losing its characteristic bilayer structure and elongating significantly in the direction of the applied force. This suggests the existence of a threshold in the parameter space beyond which membrane integrity becomes compromised. For the system under the 25 MHz 50 bar ultrasound wave, the observed response is not as dire, although a considerable amount of curvature in the membrane is observed. This already shows the differences in membrane sensitivity depending on specific combinations of frequency and overpressure.

The compression phase (right panel) presents a contrasting scenario. Notably, the system at 5 MHz 50 bar shows a complete recovery of the nominal bilayer shape, albeit with a marked tilt relative to the XY plane, most likely due to the continuous application of ultrasound cycles. This recovery, seen for all systems, indicates the resilient ability of the lipid membranes, which are capable of recovering even from extreme distortions.

The marked difference between the decompression and compression cycles highlights the dynamical nature of the response of membranes to ultrasound-induced deformation. This suggests a complex interplay between factors governing the mechanical properties of membranes, such as their elasticity and lipid packing, and the mechanical forces applied. The dependence on frequency can be attributed to the characteristic timescales of lipid reorganisation within a bilayer. Lower frequencies hold the applied deformation for longer time, allowing for lipid reorganisation, thus creating a large-scale effect that leads to the extreme deformations observed. On the other hand, higher frequencies may induce more localised perturbations, as lipids do not have time to reorient themselves, and thus lead to subtler effects.

Moreover, pressure-dependent responses provide clues about the mechanical limits of the lipid bilayers. The complete loss of the nominal shape observed for the membrane at 5 MHz 50 bar indicates a regime under which the applied force overcomes the membrane's intrinsic stability. In a realistic system, this can potentially lead to pore formation or even total membrane rupture, having significant implications for ultrasound-mediated drug delivery or sonoporation techniques. Recovery observed during the compression phase, particularly at lower pressures, demonstrates remarkable self-healing abilities for these bilayers. This resilience is crucial to maintaining cellular integrity in biological systems subjected to mechanical stress.

4.4.2 Area Per Lipid

Figure 4.23 reveals distinct patterns which depend on ultrasound parameters, with complex response surfaces for the APL in the four tested lipid compositions. Common to all of them is the existence of a critical parameter region at high overpressures and low frequencies. In this region, the membranes exhibit exceptionally large average responses (bright colours in the heat maps) as well as large relative deviations. This indicates both a significant influence of ultrasound upon the membranes and unstable behaviour, suggesting structural failure of the bilayers. The specific regions in which this occurs are dependent on the bilayer composition. For POPC and POPE, this demeanour is observed at overpressures over 30-35 bar and frequencies falling under 15-20 MHz. In contrast, POPG and POPS exhibit higher resistance, as the anomalous regions occur only at overpressures exceeding 40-45 bar and frequencies below 10 MHz. The transition between the stable to unstable regions is clearly gradual for POPC and POPG membranes, where a visible gradient of increasing values both in the average and relative deviations as the conditions become critical; but are more abrupt for the case of POPG and POPS, even when these membranes are, in

general, more stable than the previous two. These results show the influence of the headgroups on membrane stability when subjected to an ultrasound-induced deformation, since the negatively charged POPG and POPS exhibit distinct characteristics in their response maps when compared to those of the zwitterionic POPC and POPE.

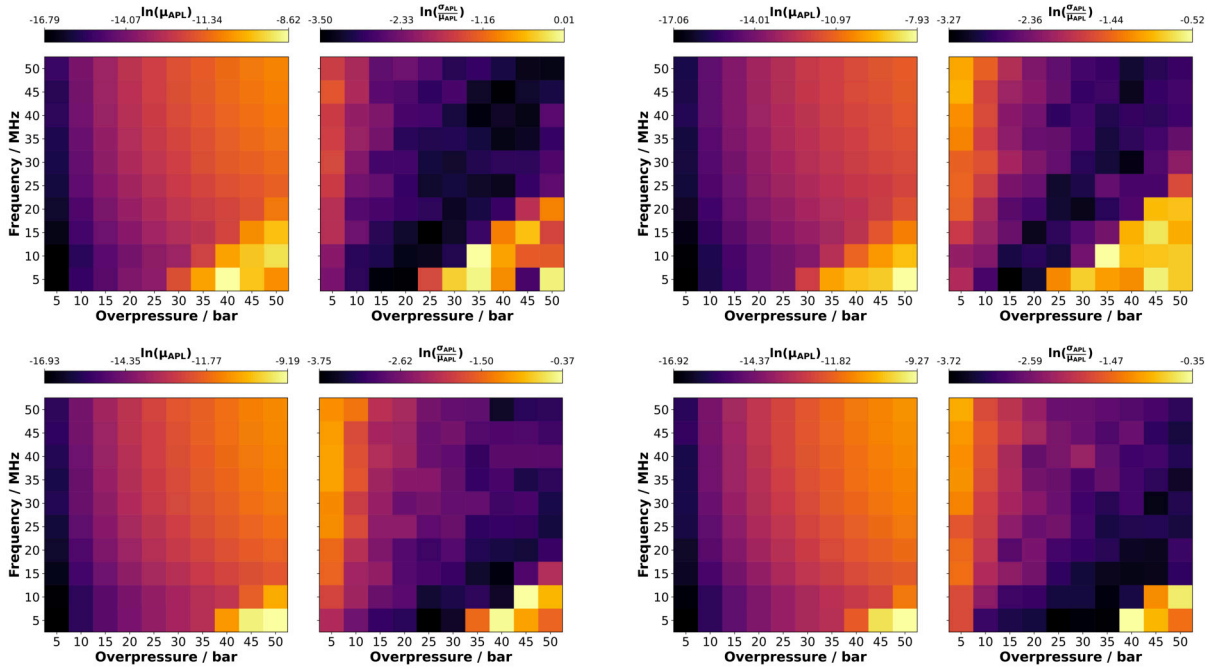

Figure 4.23: APL response for the studied systems (starting in top left and going clockwise: POPC, POPE, POPS and POPG). The average intensity of the oscillation($\ln(\mu_{APL})$ left insets) and its relative deviation ($\ln\left(\frac{\sigma_{APL}}{\mu_{APL}}\right)$ right insets) are shown.

A consistent trend is observed between frequency and overpressure causing membrane failure, for all the studied compositions; lower frequencies require lower overpressures to induce instability. This indicates that as the frequency decreases, the membranes become more susceptible to failure. This is in good agreement with what was discussed in the previous section. On the other hand, at higher frequencies the bilayers are able to withstand larger overpressures. It remains unknown if other thresholds of instability also exist for the high frquency end of the spectra, but the data seems to suggest so, as the response of the APL (outside the observed instability region) increases in the direction of increasing overpressures and frequencies.

The relative deviations in the APL show a distinct pattern. This magnitude shows its highest values in the instability regions, as expected, as when the nominal bilayer shape is lost, properties such as the APL are ill-defined, and noise becomes a very relevant factor in the measurements. High values of the relative deviations can also be observed for the lowest overpressures. This is attributed to the fact that, when such a small deformation is applied, the response of the membrane is minimal, thus rendering a very poor signal-to-noise ratio in the spectrogram. Beyond that, the relative deviations tend to create a tilted U-shaped profile along the overpressure dimension, marking a region where the oscillations of APL are stable.

Figure 4.24 shows a difference matrix for APL over the four lipid compositions used in this work. This matrix illustrates pairwise differences in the response surfaces that cover the whole parameter space. The matrix reveals that POPC consistently has the highest response for the

APL among all lipid types, as can be appreciated by the eminently positive (red-coloured) differences in its corresponding column. This is particularly pronounced in the highest overpressure and frequencies, as well as in most of its instability region. In contrast, POPE shows the opposite trend, with consistently negative (blue-coloured) values along its corresponding column, especially when compared to POPC. POPG and POPS display intermediate behaviours, both having lower responses than POPC but larger than POPE; and POPS shows a larger response than POPG, albeit not very pronounced.

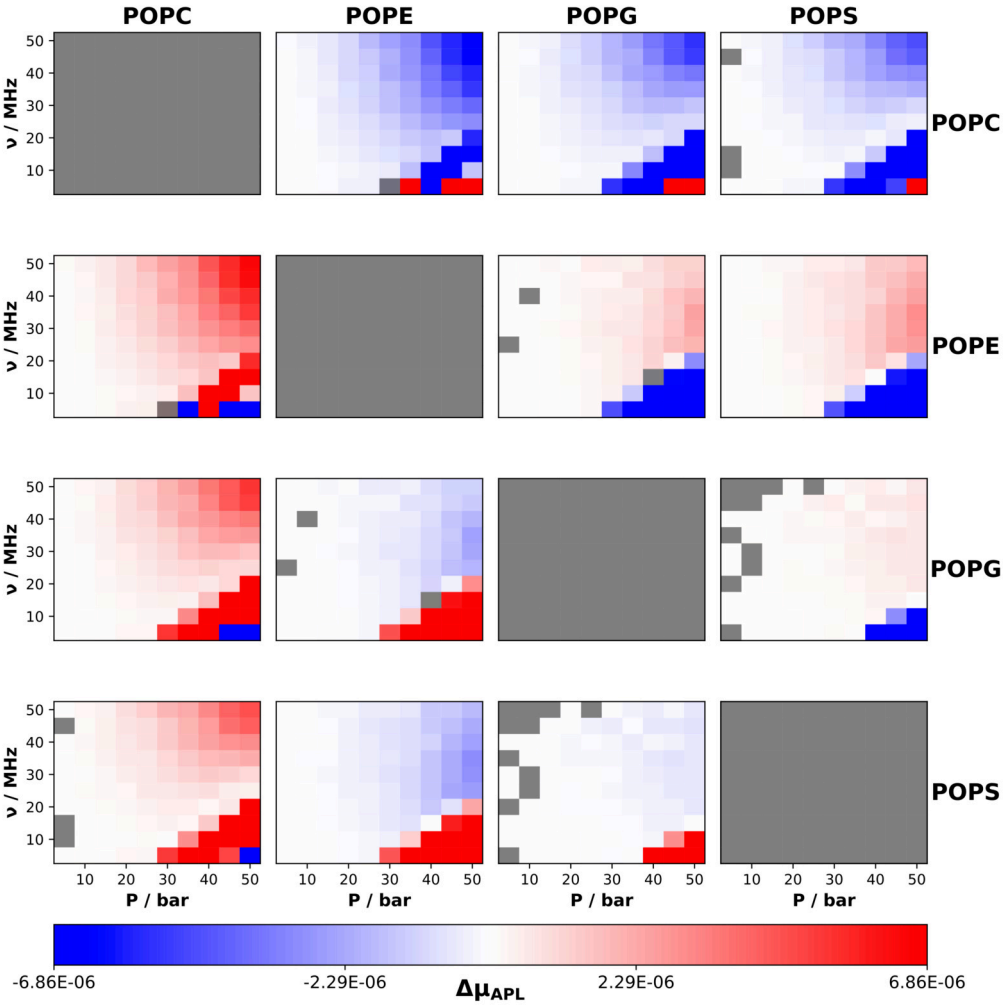

Figure 4.24: Difference matrix of APL response for the studied membranes. Each subplot shows ΔAPL (column lipid minus row lipid). Red indicates positive differences, blue negative. The grey areas represent differences that are not statistically significant at the 99.9% confidence level.

Across all types of lipids, the differences increase with overpressure and frequency, suggesting that composition-derived effects become more relevant for more extreme conditions. At low frequencies and overpressures these differences become minimal, as expected as no significant deformation is applied. The grey areas in the plots indicate that the differences are not statistically significant according to the Mann-Whitney U test. As can be observed, most of the difference matrix shows that the differences are relevant, with grayed areas only significantly present for the POPG-POPS comparison, at low overpressures and high frequencies, indicating

that these membranes have their APL affected equivalently under those conditions.

4.4.3 Curvature

Figure 4.25 shows the response surfaces for the membrane curvature to the variation of ultrasound parameters. It is evident that these response surfaces show trends different from those observed for the APL in the previous section. The lowest overpressures exerted a minimal effect on all lipid compositions, regardless of the frequency used; and these low responses were once again accompanied by a high relative deviation, which is likewise attributed to a poor signal-to-noise ratio. Similarly to what occurred for the APL, regions of membrane instability can also be found in the curvature response maps. These are characterised by, in general, abrupt changes in curvature response with small variations in ultrasound parameters, suggesting a special sensitivity of membranes under specific conditions. The U shape in the relative deviations is observed, too, for this property, as it was for the APL. Regions of high fluctuations are observed at low overpressures, followed by a strong decrease at intermediate values and another strong increase above 35-40 bar. This shows the complex relationship between ultrasound parameters and the structural properties of the membrane, which are, in turn, influenced by the composition of the membrane.

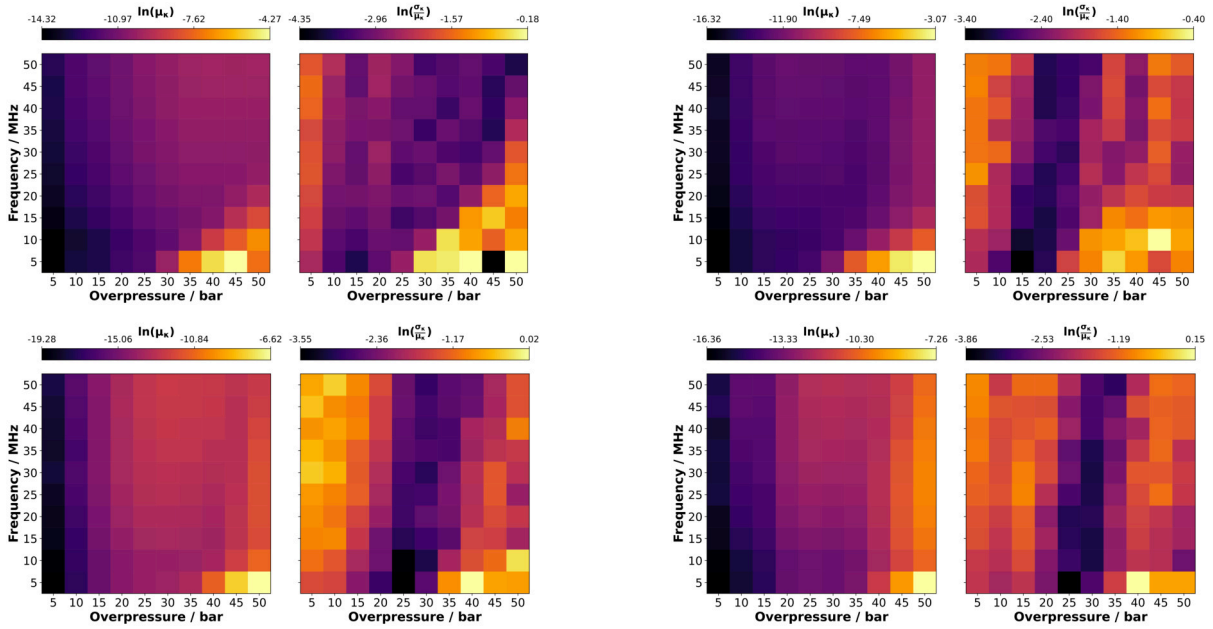

Figure 4.25: Curvature response for the studied systems (starting in top left and going clockwise: POPC, POPE, POPS and POPG). The average intensity of the oscillation($\ln(\mu_\kappa)$ left insets) and its relative deviation ($\ln\left(\frac{\sigma_\kappa}{\mu_\kappa}\right)$ right insets) are shown.

For this property, the response maps show a more complex topography with several local maxima and minima. In general, and not taking into consideration the regions of membrane instability, a maximum can be observed for medium overpressures and high frequencies. This is particularly noticeable for POPG and POPS membranes. The precise position and shape of these maxima are also influenced by membrane compositions, as POPE displays it at lower overpressures, while POPC displays a broader peak at higher overpressures. At each side of these maxima are valleys: at lower pressures leading to the global minima observed, and at higher

overpressure to zones of local minima, with responses increasing again as one keeps moving up the overpressure axis. It is worth noting that for the curvature, at the highest overpressures, some specific frequencies produce local maxima in the response, which are centred at about 30 MHz. This is clearly observed for POPS, to a lesser extent for POPE and POPG, and interestingly, not observed at all for POPC.

The difference matrix for curvature, seen in Figure 4.26, reveals significant variations for all membrane compositions investigated in all ultrasound parameters tested, further demonstrating the complex interaction between ultrasound parameters and the lipidic composition of the bilayers, with respect to their response to the applied deformation. POPC membranes consistently exhibit larger curvature responses than the rest of the tested compositions. The differences between the POPC and the rest of the membranes are nuanced. A small region where the response of the POPC membrane is very similar (white-ish) or even lower (blue colour) than that of the other membranes is observed at the highest overpressure and intermediate frequencies. Moreover, in its instability zone, the highest overpressures and lowest frequencies produced a smaller response, marked by its intense blue colour. However, these results have to be taken carefully

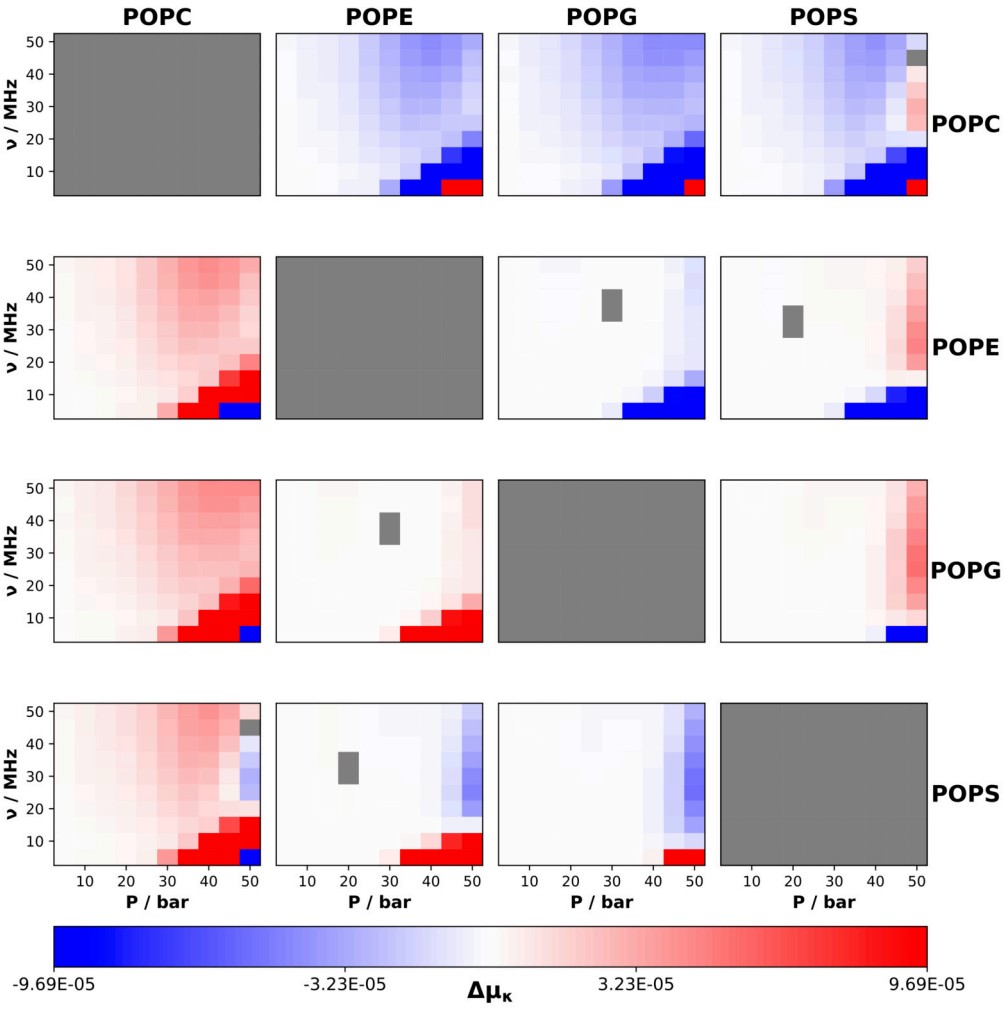

Figure 4.26: Difference matrix of curvature response for the studied membranes. Each subplot shows $\Delta\kappa$ (column lipid minus row lipid). Red indicates positive differences, blue negative. Grey areas represent differences not statistically significant at the 99.9% confidence level.

because, as was previously mentioned, when membranes lose their nominal bilayer shape, their structural properties can be ill-defined, thus producing extravagant outcomes.

The POPE membrane displays a more complex pattern of differences. Against POPG and POPS, this membrane shows an almost identical (despite statistically significant!) response over most of the ultrasound parameter space. It is at the highest overpressures that POPE shows a larger response than POPG, but a smaller response than POPS. These last two compositions, POPG and POPS, demonstrate a similar behaviour, as was observed for the APL. Significant deviations are only seen for the highest overpressures, where POPG shows a diminished response than POPS.

4.4.4 Thickness

The response maps for the thickness of the membranes (Figure 4.27) are similar to those observed in the previous section discussing the results for the curvature. The influence of frequency is minimal when the ultrasound has the lowest overpressures and has a high relative deviation associated. Instability regions are observed once more at high overpressures and low frequencies, in concordance with what was observed for the properties discussed above. The dependence on membrane composition is again evident, as per what is observed in the difference matrix of Figure 4.28.

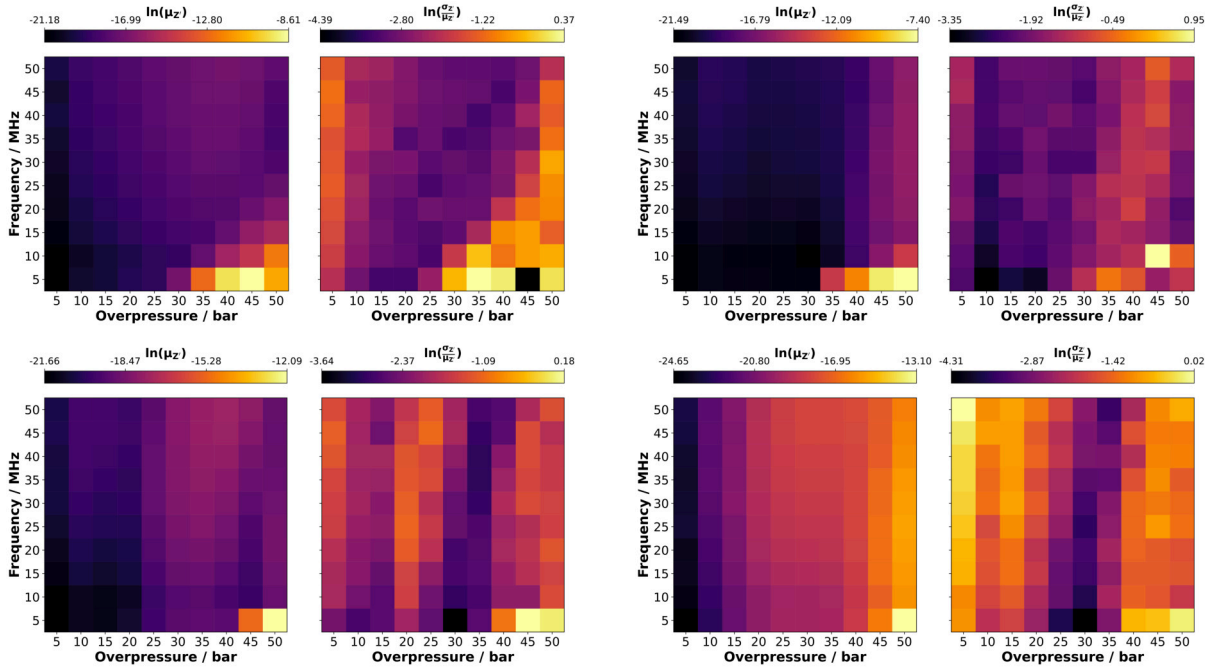

Figure 4.27: Thickness response for the studied systems (starting in top left and going clockwise: POPC, POPE, POPS and POPG). The average intensity of the oscillation($\ln(\mu_Z)$ left insets) and its relative deviation ($\ln\left(\frac{\sigma_Z}{\mu_Z}\right)$ right insets) are shown.

Similarly to the case of curvature, the response maps of the thickness show local maxima and minima outside the instability regions. The local maxima are evident this time for POPS, POPG, and POPC, while POPE shows a markedly different behaviour. POPC has the location of its local maximum at high frequencies and mid-to-high overpressures. Interestingly, at the highest overpressure and almost the highest frequency, a local minimum appears. POPG shows

a banded pattern, with two distinct local maxima: the first, smaller, centred at 10-15 bar and high frequencies; and the second at around 35 bar and mid to high frequencies. This membrane has local minima at 45 bar and low frequencies and, surprisingly, at 50 bar and high frequencies, painting a convoluted response map. POPS has a fairly homogeneous response surface, where overpressure generally has a much stronger influence on the intensity of the oscillation for this property. At the highest overpressures, the response of the oscillation increases even further, even more so for the mid-range frequency. Finally, POPE is discordant with these previous results as it shyly shows a local maximum at high frequencies and low overpressures, and then the intensity of the oscillation increases rapidly at the upper end of the overpressure axis, with a slight bias on the intermediate frequencies.

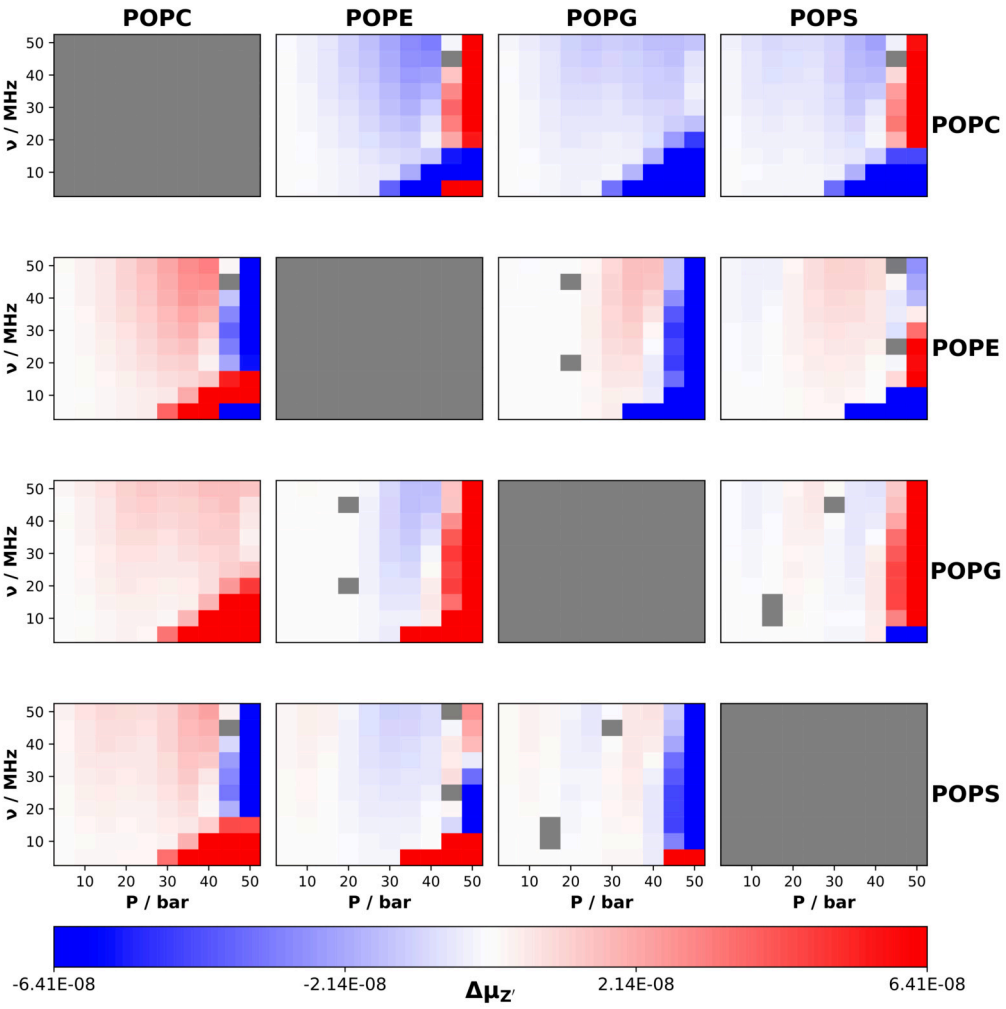

Figure 4.28: Difference matrix of thickness response for the studied membranes. Each subplot shows ΔZ (column lipid minus row lipid). Red indicates positive differences, blue negative. Grey areas represent differences not statistically significant at the 99.9% confidence level.

The difference matrix seen in Figure 4.28 presents us with a complex landscape, more so than those previously discussed for the APL and the curvature response to the ultrasound wave. No matter which two membranes are compared, multiple trends are always present. These differences are also statistically significant across the entire parametric space studied. This shows

again the relevance of the lipid composition in the reaction of the thickness of a bilayer to an ultrasound-induced deformation, even when the variations in the lipid types pertain only to the polar heads. The POPC membrane shows the most different demeanour, as evidenced by the intense red (positive) and blue (negative) colours in its corresponding column of the difference matrix. Comparison of POPC with POPE reveals a transition from positive to negative differences as the overpressure of the oscillator increases. Compared with POPG, the oscillation of thickness of the POPC membrane is always larger, although at the highest overpressure and mid-range frequencies this difference becomes smaller. The comparison with POPS paints a similar picture to that of POPE, but in this case, the instability region of POPC always shows higher values. However, it is important to remember once again that the results discussed for the instability regions should be taken with caution.

The POPE membrane displays a complex trend compared to the rest. When faced with POPG, at all but the highest overpressures the POPE membrane shows a slightly lower response in its thickness. However, after 45 bar, the POPE membrane oscillates much more than POPG. When compared with POPS the picture is even more convoluted, as for the lowest overpressures the thickness of POPE oscillates slightly more, then for the medium overpressures oscillates slightly less, and finally after the threshold of 45 bar there is a clear frequency dependency, oscillating much less at lower frequencies and more at higher frequencies.

The POPG membrane also shows mixed trends in the corresponding column of the difference matrix. Most of its results were already discussed when compared with POPC and POPE membranes in the previous paragraph. However, when facing POPS, a complex difference surface can be observed. The differences become more marked as the overpressure axis increases. Nonetheless, there are several transitions from positive differences at the lowest overpressures, then to negative, then to positive again, until reaching a threshold at 35 bar where POPG has markedly lower oscillations in its thickness than POPS. For all but the last mentioned trend, the differences become slightly bigger with larger frequencies; but in the case of the post 45 bar differences, mid-to-low frequencies seem to increase the thickness response of POPG when compared to POPS.

4.4.5 Order Parameters

Figure 4.29 and Figures S64 to S69 illustrate the complex response of the order parameters to the different ultrasound conditions studied tested in the study. A clear trend can be observed where an increasing response for the order parameters for high overpressures and mid-to-low frequencies. Even though the intensity of the oscillation on the order parameters is dependent on lipid type, the position of the local maxima and minima in the response surface is agnostic both to the lipid type (as expected, as they all share the same acyl tail motifs) and to the specific tail and bead for which the order parameter is calculated. There is an evident and remarkable region of unresponsiveness for this property found around 40 MHz, for all overpressures. Increasing this latter parameter of the ultrasound wave has the effect of also increasing the response of oscillation of the order parameters, but the aforementioned valley in the response surface remains clear for all the conditions studied.

The relative deviations for the order parameters are the highest at high frequencies and low overpressures, in the regions where the response surfaces reach their minimum values. This observation is attributed again to the poor signal-to-noise ratio, as the deformation applied to the membrane is minimal for the lowest overpressures. In general, moving to the low frequency, high overpressure region of the parametric space decreases the relative deviation of the response

of the order parameters. This is reproducible for all of the tested compositions, although the POPG seems to have relatively larger relative dispersion values.

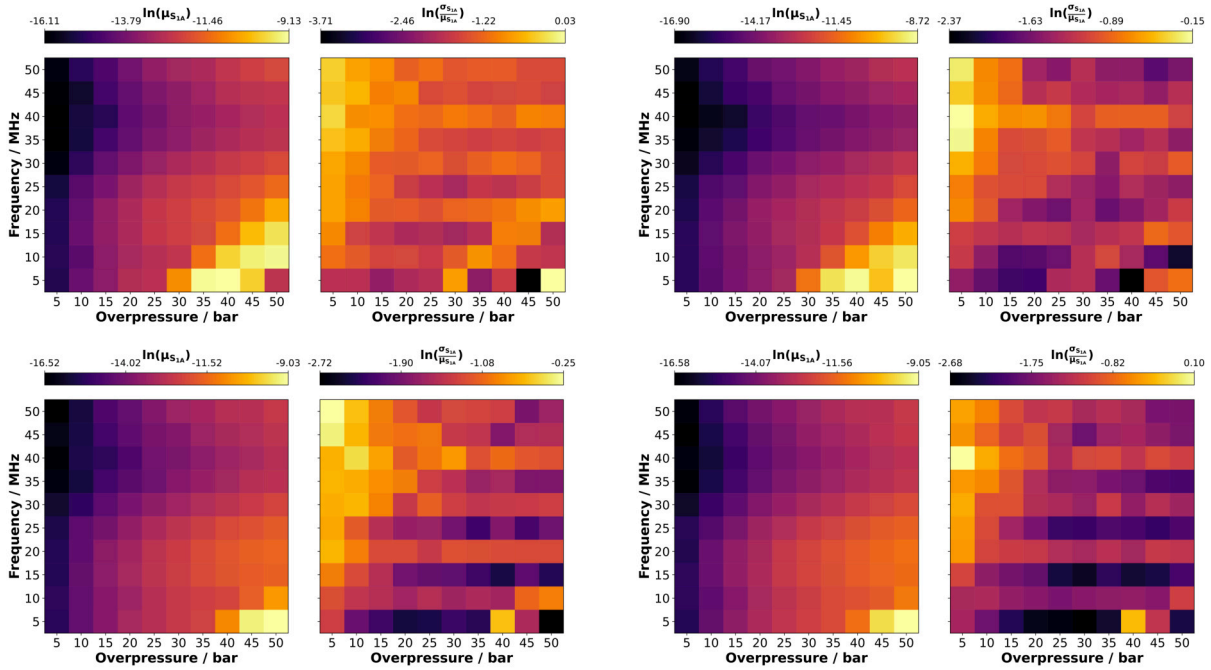

Figure 4.29: Order parameter response for first bead of the *sn-1* tail for the studied systems (starting in top left and going clockwise: POPC, POPE, POPS and POPG). The average intensity of the oscillation($\ln\left(\mu_{S_{1A}}\right)$ left insets) and its relative deviation ($\ln\left(\frac{\sigma_{S_{1A}}}{\mu_{S_{1A}}}\right)$ right insets) are shown.

All difference matrices (Figure 4.30 and Figures S70 to S75) show clearly different characteristics than those discussed in previous sections. This is rather expected, as the topographies of the response maps of the order parameters are also distinct from those of APL, curvature, or thickness. Despite all the compositions studied sharing the same type of aliphatic tails, there are clear differences between the different membranes within the confidence interval used for this work.

The POPC membrane consistently shows larger responses than the other lipid types for the S_{1A} order parameter, an observation that is particularly pronounced compared to POPE. The smallest difference of POPC with the rest of membranes is seen in the previously mentioned unresponsive region, centred around 40 MHz. This does not happen only for POPC, but holds true for all of the membranes studied. The maxima of these differences are located, in general, near the instability regions at high overpressure and low frequencies. Interestingly, the POPC membrane seems to have a lower response than the rest of the membranes in its instability region, but, again, the results of that region of parametric space cannot be too trusted because of already discussed reasons.

Contrary to POPC, the response to the ultrasound wave of the order parameters of the first bead of the *sn-1* tail for POPE is lower than that for POPG and POPS, beyond the instability region. In this region, the response of POPE is larger than that of POPG and POPS. These two membranes show very similar results, as evidenced by the predominantly white colour (values very close to 0) on their difference surfaces, being POPG slightly less responsive than POPS.

The comparison between these two membranes also shows a considerable amount of greyed-out areas, indicating instances where the difference was found to be not statistically significant.

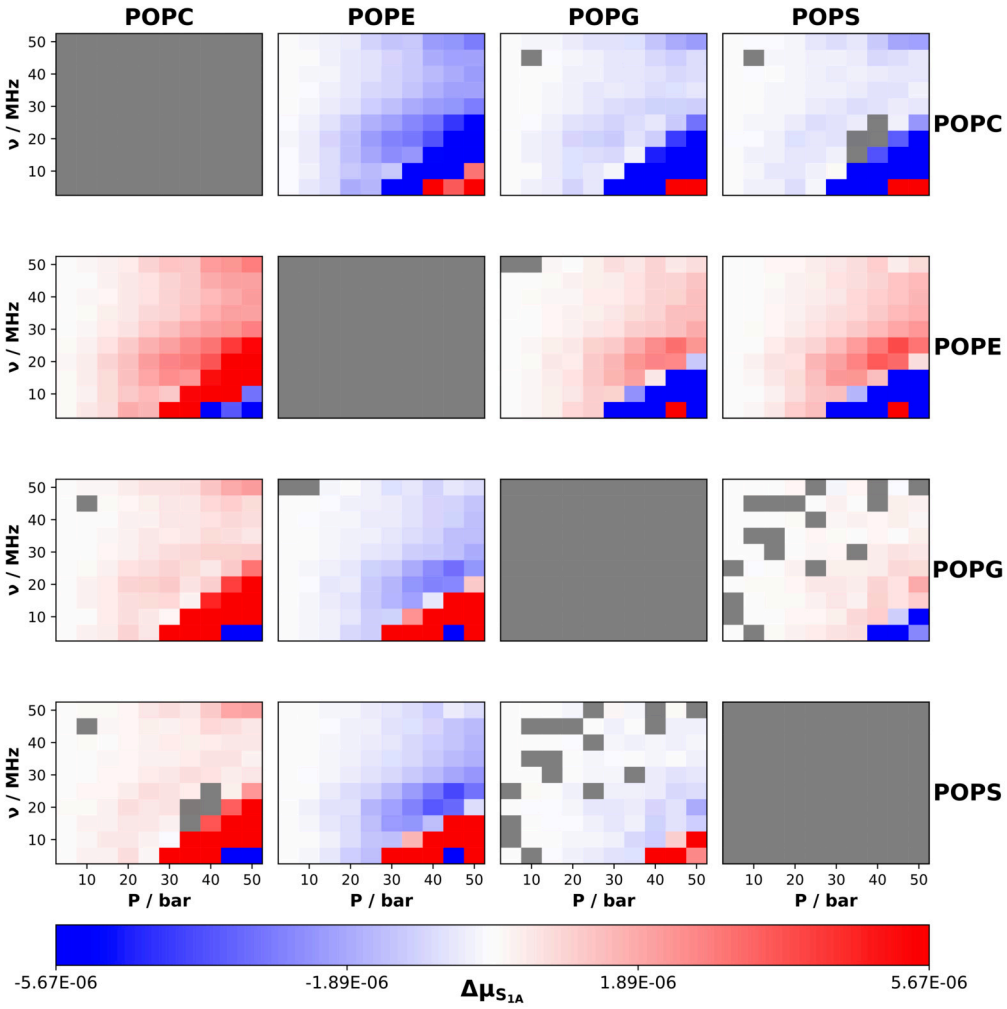

Figure 4.30: Difference matrix of thickness response for the studied membranes. Each subplot shows ΔS_{1A} (column lipid minus row lipid). Red indicates positive differences, blue negative. Grey areas represent differences not statistically significant at the 99.9% confidence level.

The remaining difference matrices (see Figures S71 to S75) generally mirror the behaviour discussed in the previous paragraphs. However, there is a notable exception for the cases relative to the POPC membrane, where differences are more nuanced, particularly around the instability regions. For this membrane, the response to the ultrasound wave becomes smaller against POPG and POPS, while it remains larger when faced with POPE. This trend holds for the two acyl tails and beads, with the exception of the S_{1A} bead, although to varying degrees.

Additionally, as one moves towards the end of the acyl chains of the lipid molecules, an increasing number of values not meeting the statistical significance threshold imposed in this work can be observed. This suggests a convergent behaviour in the order parameters, where the differences caused by the lipid composition of the bilayers become less pronounced, which can be indicative of a more homogeneous physical behaviour in the hydrophobic cores of the membranes.

4.4.6 Conclusions

The systematic investigation of the effects of varying ultrasound parameters on four distinct lipid bilayers (POPC, POPE, POPG, and POPS) has revealed complex and nuanced relationships between membrane composition, US frequency, and overpressure. These findings provide valuable insights into the mechanical responses of lipid membranes under US-induced stress, with potential implications for therapeutic applications and our understanding of membrane biophysics.

A key observation from this study is the composition-dependent stability of membranes under US stress. The stability thresholds of membranes vary significantly with lipid composition, with POPG and POPS membranes demonstrating higher resilience. These anionic lipids required greater overpressures and lower frequencies to induce instability compared to the zwitterionic POPC and POPE membranes. This variation in stability thresholds underscores the crucial role of lipid headgroup chemistry in determining the behaviour of the membrane under mechanical stress.

The responses of structural properties such as APL, curvature, and thickness to US parameters exhibited non-linear behaviour highly dependent on both frequency and overpressure. This non-linearity suggests complex underlying mechanisms governing membrane deformation under US stress. Generally, lower frequencies induced more pronounced deformations, particularly at high overpressures. This observation aligns with the hypothesis that lower frequencies allow more time for lipid reorganisation within each US cycle, leading to larger-scale deformations.

The order parameters displayed a consistent trend of an increased response for high overpressures and mid-to-low frequencies across all lipid types. In particular, a region of non-responsiveness was identified around 40 MHz, independent of lipid composition. This unexpected behaviour warrants further investigation and could potentially be used in applications that require minimal disruption of lipid tail orientations.

Despite sharing identical acyl tails, the four lipid types exhibited distinct responses to US, particularly evident in the difference matrices for various properties. This observation further emphasises the significant role of headgroup chemistry in determining membrane behaviour under mechanical stress, even when the hydrophobic core of the membrane remains constant.

These findings have significant implications for the development and optimisation of US-based therapies. The observed composition-dependent responses suggest that US parameters could potentially be tuned to target specific membrane compositions, offering a pathway to more selective treatments. For example, the higher resilience of POPG and POPS membranes could be exploited in therapies targeting bacterial or cancerous cells, respectively. Furthermore, the identification of specific frequency and overpressure combinations that induce instability or significant deformation in certain membrane types but not others opens avenues for precise control in applications such as drug delivery or sonoporation.

In conclusion, this study demonstrates that the interaction between US parameters and the composition of the lipid membrane is complex and multifaceted. It highlights the need to carefully consider both membrane composition and US characteristics in the design of ultrasound-based therapies. Future work should focus on extending these findings to more complex and biologically relevant membrane models and exploring the molecular mechanisms underlying the observed behaviours. Such efforts will be crucial in bridging the gap between these fundamental biophysical insights and practical therapeutic applications.

5 CONCLUSIONS

Yer fond of me lobster, ain't ye? I seen it - yer fond of me lobster! Say it! Say it. Say it!!

–Thomas Wake,
The Lighthouse by Robert Eggers

In this Thesis we have investigated the behavior of lipid membranes, specifically while in their bilayer nominal shape ubiquitously found in biological systems, under different circumstances. We have shown results of a comprehensive comparison of several widely used forcefields, using them to model several bilayer compositions, to test their performance when dealing with systems of moderate complexity and comparing their results with experimental data. We have also dealt with bilayer systems of great size, to test and propose a hierarchical organization scheme in the fashion of how proteins or nucleic acids are rationalized in other areas of biochemistry; and we have developed a set of tools that are able to accurately measure many relevant properties for lipid membranes when in the presence of geometrical deformations. Finally, we have studied the influence of Ultrasound-induced deformation on a series of different lipid bilayer compositions, probing both how this composition affects the reaction of the membranes to the ultrasounds, as well as which is the influence of tuning the ultrasound parameters.

In general, this body of work aimed to provide some insight into the vast ocean that is the topic of lipid membranes. By systematically studying them through computer simulations, we expect to shed some light into the structural and dynamical factors that govern these fascinating structures. This is a work of basic Science, but we hope it will help future research, applied or not, to rationalise and study these biological systems. Now, in this final Chapter, and in the light of the results previously presented, we will give a final discussion of the most relevant topics introduced along this work.

5.1 Comparative Evaluation of Force Fields: Performance Across Bacterial Membrane Models

This section of the work compared a total of 6 different membranes (POPC, POPE, POPG, POPC:POPG (7:3), POPE:POPG (1:3) & POPE:POPG (3:1)), comprising three simple mono-component bilayers as a blank, and three double component bilayers as possible models for bacterial membranes. These lipid membranes were then simulated under six different parametric conditions, taking into account the various forcefields used (CHARMM-36M, Slipids, GROMOS-CKP & GROMOS-H2Q) and the legacy *vs.* common set of simulation parameters. This led to a total of 36 unique simulated systems. In summary, our study showed that both the choice of forcefield and simulation meta-parameters can affect in a relevant manner the results that are measured from a simulation although, as one can expect, things are a bit more complex than that.

5.1.1 Common or Legacy? The Question about Meta-parameters

When researching MD simulation literature it is way too common to find studies lacking clear information on the specific simulation meta-parameters (choice of coupling constants, cut-off radii, corrections to energy, *etc.*) that were used. Thus, being able to use a common set of parameters that one could apply to all forcefields in general would be helpful. This is, of

course, if using a forcefield under simulation conditions it was not parameterised for can also give reasonable predictions.

In this part of the work we tested just that for the CHARMM-36M and Slipids forcefields. Unfortunately, for the common set of parameters, our results indicate that they can significantly affect the values of several properties in a typical, well-behaved, MD simulation of lipid bilayers, and one can expect these differences to become more stringent when the forcefields are pushed even further in more exotic simulations, outside thermodynamic equilibrium. These differences, although never aberrant, are in all the cases non-negligible. For example, legacy meta-parameters for CHARMM consistently produce larger APL values (consult table A.1), while for Slipids it is the common set of simulation parameters that produced the highest APL values. The magnitude of these differences also depends on the membrane one is studying (POPE seems to be more affected) and the property one is measuring (the thickness or hydrogen bonds are not as affected as the APL or the diffusion coefficients).

Therefore, at least caution is recommended when not using the simulation parameters provided with each forcefield to perform an MD simulation. The choice of a common set of parameters can be justifiable - or even necessary - in some cases, as it does facilitate the comparison between systems. Using the same meta-parameters for a study involving a great number of simulations and forcefields removes (or hides) several degrees of freedom, as one knows that the differences one observes would arise by the things that one did change. However, if we gauge these differences among themselves and against reliable data, and find deviations, it would be impossible to know if they appeared because one specific forcefield is bad at capturing one property, or just because the forcefield was not used as the creators intended.

We do believe that task for finding a common set of meta-parameters that can accurately capture the desired behavior, within a legitimate discrepancy, for several forcefields is an interesting one, although it is a question that remained unanswered in this Thesis. Despite this, it is reasonable to think that a study could be designed to systematically change several simulation parameters, monitor how these changes affect simulation results for several forcefields, and optimise them such that the average difference between the results produced by the common set of parameters and the legacy set of parameters for all simulations becomes minimal. Such a study would therefore rationally synthesise a 'master' set of parameters based on a known metric, and be supported by educated evidence.

5.1.2 The Quest for the Best Forcefield

The ever-lasting question of MD simulation: *which forcefield is the best forcefield?* And the ever-lasting answer: *it depends.* Of course, our study was no different from that. Defining 'the best' and 'the worst' is always an interpretative task and will depend on what we are interested in. Thus, we found that each forcefield we tested had its advantages and weaknesses.

The most obvious differences between the three families (CHARMM *vs.* Slipids *vs.* GROMOS) of forcefields that we tested is their time performance when running simulations. GROMOS being a United Atoms parameterisation greatly reduces the degrees of freedom for the same representation of a given system, reducing the number of operations that have to be performed for each integration step of the MD pipeline, effectively increasing the speed of computation. GROMOS-CKP already represents about a 40% increase in simulation speed compared to CHARMM and Slipids, which both produce very similar results in their performance. When using the GROMOS-H2Q acceleration strategy, this increase in performance jumps to around 300% compared to CHARMM and Slipids, which is obviously an incredible advantage, espe-

cially if one takes into account that the variants CKP and H2Q produced virtually the same results for each property calculated, except for some slight discrepancies in the diffusion coefficients which were already expected due to the different masses of the lipid molecules.

However, we have seen that the GROMOS family diverged quite significantly from the predictions of CHARMM and Slipids. This was particularly evident in the case for membrane hydration (see Figure 4.4 and Table A.3), where a significantly lower amount of water was observed from GROMOS than for the other parameterisations, and for the RDFs (see Figure 4.5) where the first solvation peaks for GROMOS appeared much earlier than for CHARMM and Slipids. These observations, implying stiffer and more compact membranes, were followed with indeed much slower diffusion coefficients for GROMOS and with generally larger order parameters in the acyl chains.

Interestingly, when the results are compared with values available in the literature for APL and thickness, the GROMOS family performs reasonably well, sometimes even better than the totally atomistic representations of CHARMM and Slipids. On the other hand, when comparing the order parameter results obtained in this Thesis with the experimental data provided by our collaborators, GROMOS consistently did the worst job at reproducing them. Moreover, while Slipids reproduced the experimental order parameters for the acyl chains extremely well, the other two families outperformed them when reproducing the data for the polar lipid head, to which CHARMM fitted the best.

All of this just proves what was said in the first paragraph of this section discussing the fitness of different forcefields. Which one is the best, or the worst, will depend on what we need. Slipids produced very accurate results for order parameters, and its predictions on experimental data in the literature are more than acceptable. CHARMM, despite producing slightly too disordered membranes, also gave finer predictions than GROMOS, in general. This last family, GROMOS, produced specially stiffer and slower diffusing membranes and did not align particularly well with experimentally determined order parameters, but it is very convenient to perform fast simulations. Hence, depending on the situation, one may choose between the different parametrizations. If fast simulations are paramount and extreme accuracy is not needed, GROMOS would be a reasonable choice. If, on the other hand, a high level of precision is required, then Slipids would be the ideal candidate.

5.2 Structural Equilibrium in Lipid Membranes: Defining Hierarchical Organization and Spatial Domains

On this section of the work, we focused our efforts into developing a rational scheme to understand how large patches of square lipid bilayers behave when they are in thermodynamic equilibrium. In order to simulate such big systems, we used a coarse-grained forcefield, allowing us to also achieve large simulation timescales, in the order of microseconds. We found that when some relevant properties for the membranes are carefully measured, there are correlations between them, and these can be used to define spatial domains that propagate through the bilayers. Moreover, we found that these correlations are independent of the three lipid compositions that we tested: a pure POPC membrane, a mixed POPE:POPG membrane to assess the effects of having more than one lipid type, and a DLPC membrane to evaluate how different acyl chains affect the aforementioned correlations. We also supported our proposal for hierarchical membrane organisation with previous all-atoms simulations of several macromolecules inserted into lipid bilayers.

5.2.1 The Minimal set of Descriptors

When measuring several properties for the membranes used in this study, it was found that cooperative, or at least correlated, behavior happened between some of them. One of the most evident cases was how the vector field arising from the orientation of the lipid tails (refer to Figures S24 to S26) is consistently arranged in an antiparallel way to the vector field arising from the normal vectors to the membrane's surface (refer to Figures S18 to S20). These correlations pushed us to investigate further, and through a systematic method, we were able to select a set of 12 non-redundant properties that fully characterise the mechanical state of the lipid bilayer.

Furthermore, we did not only find a minimal set of descriptors, but once all the redundancies were pruned, correlations between some of the descriptors could be observed, which is an indicator of cooperative behaviour. For instance, we observed that the direction in which the lipid tails orient along the surface defined by the membrane to which they conform is heavily correlated with the directions of maximum and minimum change of curvature of said surface. Some more evident correlations were also detected, for example, as to how the degree to which lipid tails are tilted is correlated to the membrane thickness. However, the causal correlations between these facts are not directly interpretable; that is, we cannot tell if the lipids are tilted because the membrane is not sufficiently thick or vice versa.

The analysis that allowed us to elucidate these correlations was, in its most fundamental form, a decomposition in eigenvectors of the measured properties of the membrane. Thus, since we found that the correlated properties were grouped in specific eigenvectors, we projected them onto the membrane surface. What we found is that these eigenvectors, representing linear combinations of properties, could form well-defined spatio-temporal domains over the bilayer.

5.2.2 The Hierarchical Structure

Following what we observed when obtaining the minimal set of descriptors, we proposed that the correlations observed between those properties could be understood as a fundamental way in which lipid bilayers self-organize, specially taking into account that for all the studied compositions the set of minimal descriptors and the correlations between them were always the same. Thus, in parallel to what is done for proteins and nucleic acids, we propose a way to organise lipid bilayers in a primary, secondary, tertiary, and quaternary structure.

- **Primary structure**: The specific lipid composition of a membrane. Akin to amino-acid sequence.
- **Secondary structure**: The nominal bilayer structure, driven by the interaction between leaflets. Akin to nominal protein structures such as an α-helix.
- **Tertiary structure**: Local domains form within the bilayer because of the coordinate behaviour of the lipids. Akin to the interaction between different domains within the same protein.
- **Quaternary structure**: Arises from the interaction of the lipid bilayer with other macromolecules, such as embedded proteins. Akin to the interaction between different protein subunits in a protein complex.

With this proposal, we aim to provide a comprehensive reinterpretation of the organisation of the lipid bilayers through a hierarchical framework. We acknowledge that this proposal can be enhanced and modified, as many magnitudes were not taken into account. Despite this, our

approach could serve as a proof-of-concept upon which more thorough analyses can be built. It is reasonable to think that if properties like the APL or the diffusion of the lipids was accounted for, as well as some of the purely geometrical quantities calculated for the membranes used in this work like the LFR or the curvature, other correlations could appear that would shed more light into the self-organization of these biological structures.

5.3 Ultrasound-Induced Deformation in Membranes: Influence of Lipid Composition and Simulation Models

After studying well-behaved systems, where membranes were in thermodynamic equilibrium and in the absence of any external mechanical perturbation, we decided to extend our work to the field of non-equilibrium MD. We hypothesised that, depending on their composition, lipid membranes would react differently to the same physical stimuli. The field of ultrasounds seemed like a good choice for this because, as has been already discussed, it has found applications in the medical field, and its effects are supposed to be mainly based on mechanical factors.

Thus, we devised a study where we first developed a method to simulate the effects of an ultrasound wave at the nanoscopic scale, at which MD simulations are done; and then tested our ultrasound model against several different membrane compositions. We aimed to test whether, in fact, the responses of the different membranes could be distinguished from each other based on their composition. Moreover, as this study was the first exhaustive work on the influence of an ultrasound wave on several membrane compositions, we tested if the results produced by a conveniently fast coarse-grained model align with those produced by a more realistic atomistic representation of the system.

Our results indicate that the implementation of ultrasound-induced mechanical deformations in the MD simulation pipeline is feasible and not too complex. Furthermore, we showed that the results from a coarse-grained and a fully atomistic simulation are equivalent, within an expected discrepancy. Finally, after testing the prolonged exposure of 10 different membranes to an ultrasound wave, we proved that their composition has a relevant effect on how they react to the applied mechanical deformation.

5.3.1 Development of the Ultrasound Model

We based the implementation of an ultrasound model based on the fact that these phenomena are, in essence, a pressure wave. Thus, as most commonly within the MD pipeline there is a pressure control algorithm, most of the framework needed to simulate an ultrasound was already in existence. We selected the Berendsen pressure control scheme for its simplicity and ease of modification.

We modified the barostat by just adding an oscillating term, a sine wave, to its scaling matrix term. This allows us to control the direction upon which the deformation is applied. However, we must note that our implementation could be improved. For starters, our method requires us to recompile the whole GROMACS source code if a modification is to be made to any of the oscillator parameters. This is due to the oscillator being hard coded into the specific barostat algorithm and not using, instead, GROMACS native message passing code to read simulation meta-parameters. Despite this not producing any physical errors in the implementation, it can be cumbersome on the user's end, especially when dealing with large amounts of individual simulations that require different ultrasound parameters.

Moreover, the Berendsen barostat is known to be a first-order coupling scheme that does not actually reproduce the isothermal-isobaric ensemble. Despite our simulations being out of

equilibrium, it is unknown to us if this fact about this concrete scheme affects how the ultrasound model behaves. The implementation of ultrasounds for other barostats like the Parrinello-Rahman second-order scheme, or the newly devised c-rescale first-order scheme, remains to be explored, and thus a systematic comparison on the effects of ultrasound-induced mechanical deformation on lipid membranes via different pressure coupling algorithms remains unknown. Furthermore, the effects of changing some pressure coupling meta-parameters, like the coupling time constant, also remain to be studied.

5.3.2 The All-Atoms *vs.* the Coarse-Grained View

The main objective of this piece of work was to study the influence of the lipid composition of several bilayers on their reaction to the same ultrasound wave. However, since no exhaustive studies had been previously done, we decided to first compare the results of simulations carried out in an all-atoms representation of our selected systems against one at the coarse-grained level. The latter, as has been persistently mentioned along this manuscript, have the advantage of running much faster due to their low-dimensional representation of a given system. However, this advantage comes at the cost of loss of precision.

Our results indicate that, within some discrepancies, atomistic and coarse-grained simulation can produce equivalent results. However, we were very surprised by the fact that without applying any kind of correction factor, coarse-grained simulations saw a total loss of the bilayer shape under the same ultrasound conditions as the atomistic equivalent simulation. We attributed this fact, once more, to the lower total degrees of freedom of the system. We hypothesise that this reduced number of available microstates for the system to occupy has an impact on the amount of configurations that the bilayer can adopt to oppose the deformation applied. Following this reasoning, and supported by studies showing that the diffusion of coarse-grained lipids is around four times faster than that of their atomistic counterparts, we applied a correction factor to the frequency of the coarse-grained systems, multiplying it by four. This can be understood as assuming that time flows four times faster in a coarse-grain simulation. Much to our relief, the simulations produced equivalent results when the correction was applied.

We acknowledge that our reasoning for the correction is based on untested hypotheses, some data about diffusion coefficients, and the fact that the correction just works. We do believe that a deeper study on this topic would be of great interest, although niche, to really understand what the fundamental implications of coarse-graining a system are.

5.3.3 The Influence of Lipid Composition

Once we were confident that the coarse-grained representation of our systems would produce results that could capture a traditional all-atoms behavior, we extended the simulations to span enough time to cover two hundred ultrasound pressure cycles. This, which would be unfeasible if we were to use an all-atoms forcefield, allowed us to study the effects of a relatively prolonged exposure to an ultrasound wave on lipid membranes.

We proposed a method based on Fourier analysis to quantify the extent to which the measured properties reacted to the ultrasound-induced deformation. Our results clearly indicate that lipid composition had a non-negligible effect on the extent to which the membranes deform when subjected to an ultrasound. Moreover, we found evidence that the effects of lipid composition are additive, that is, the deformation induced on a membrane composed of a mixture of two lipids is roughly the average of the effect on the membranes composed by the single lipid types. However, the results are more nuanced than that, as we also found that the specific prop-

erty one is measuring in a bilayer also has an impact on how much that membrane reacts to the ultrasound.

This painted a convoluted picture, although some trends could still be seen with the naked eye. Therefore, we decided to test if the ten different membranes simulated in this piece of work could be categorized based on their reaction to the ultrasound and assess if discernible patterns would appear. We thus performed a clustering analysis on our simulation data and, interestingly, we discovered that the data was indeed packed in a very compact way. All but one of the membranes appeared in just one cluster, and the membrane that was not was split into two chunks of the same size. In addition, we found that the clusters were dominated by just one type of lipid.

This was indicative of the fact that there were, indeed, discernible trends within the data arising from the reaction of the membranes to the ultrasound wave. Some lipid types were dominant over the others, namely POPC and POPE over POPG and POPS, because they could 'drag' the data to their own cluster; which demonstrates that some lipids have a stronger ability than others to modulate the behaviour of the lipid membranes they conform. Furthermore, by obtaining the probability density functions for the intensity of the response of each property to ultrasound within each cluster, we could determine the sensitivity of the membranes to the induced deformation. This showed again different trends, as how sensitive a membrane - or a cluster of membranes - is to the ultrasound depends on the property one measures.

Thus, this study showed that the lipid composition plays an important role in how different membranes react to a specific mechanical deformation, at least according to the predictions of molecular dynamics simulations. However, the response of the membranes is complex and is also dependent on the specific property one is measuring. Despite this, we propose that this complexity can be thought of as an advantage. By rationalising how different properties of different membranes react to an ultrasound wave, one could, in principle, design membranes that show very specific strengths (or weaknesses) to a concrete stimulus.

5.4 Impact of Ultrasound Parameters on Membrane Behaviour: Exploring Frequency and Pressure Effects

In the previous study we tested how different membrane compositions reacted to the exact same ultrasound model. Our results showed that in fact the composition of the membrane plays an important effect on how it reacts to the ultrasound. However, an important question remained to be studied: What are the effects of changing the ultrasound parameters, that is, its overpressure and frequency.

In the final piece of this Thesis, we aimed to answer exactly that question. In light of the additive effects seen for membrane composition, where mixed membranes displayed the averaged behaviour of the demeanor observed for the single-component bilayers, we chose our study to be conducted for the POPC, POPE, POPG, and POPS bilayers and then we systematically changed the ultrasound wave's overpressure and frequency. Our results provided response maps for different relevant properties and membrane compositions, further paving the way to a rational understanding of how these specific mechanical deformations affect, at a molecular level, the lipid membranes.

5.4.1 Systematic Changes on Pressure and Frequency

We designed our study to span a range of overpressures and frequency that could encompass several pairs of parameters that could be found already in use in actual, real life therapeutic

applications. Thus, we created a 10 by 10 grid in the parametric space of overpressure and frequency, upon which to test a total of 100 unique combination of parameters over our bilayers.

This systematic approach allowed us to obtain response maps for all membranes and measured properties. Moreover, as the response maps could be perfectly overlaid and subtracted from one another due to the grid disposition, direct comparison between different membranes was facilitated.

5.4.2 The Complex Parameter ↔ Composition ↔ Property Interplay

As it could be expected, after performing the simulations and analysing the data we found a rather convoluted picture. All of the membranes studied showed a region in their response maps for all of the properties in which abnormally large values could be seen. These regions were characterized for having large overpressures and low frequencies. They represent parametric coordinates where the membranes break and lose their bilayer shape, not being able to withstand the mechanical deformation imposed by the ultrasonic wave. However, the size of that region was clearly dependent on the lipid composition of the membrane.

Furthermore, when comparing the different measured properties, we could see that they did not produce the same topographies in their response surfaces. That is, the changes in the sensitivity of different properties were not equal for the same changes in ultrasound parameters. Although in general, and outside the region where the membranes broke up, the response of the properties was higher along the directon through which the ultrasound's overpressure and frequency increased, several local maxima could be observed depending on the property. In addition, the location and shape of the maxima also depended on what was being measured. In general, changes in overpressure seemed to have a greater effect on the reaction of the membranes to the ultrasound wave, but, for the case of order parameters, a clear region of insensitivity to a specific frequency (40 MHz) could be found. We are yet to determine the exact process that causes the damping of the oscillations in that region, but it must be related to the ability of the acyl chains to absorb energy through changes in their relative angle to the normal of the membrane.

The effect of lipid composition added yet another layer of complexity to our results. By computing the difference between the response surfaces for a given property of any two different membranes, we could assess which one reacted more (or less) than the other; and at which specific point in parametric space this happened. In general, we observed that the membranes produced statistically different results from each other. Only for the case of the order parameters of the last segment of the acyl chains could a considerable amount of non-significant differences be observed. We found that the POPC membrane was overall the most reactive to ultrasound deformation and the POPE membrane the last. The POPG and POPS membranes showed very similar behaviour and showed an intermediate response. However, there are several nuances to this trend, where specially resistant membranes go through a threshold and become those more affected by the mechanical deformation, or vice versa.

A SUPPLEMENTARY MATERIALS

A.1 Supplementary Figures for Section 4.1

A.1.1 System Snapshots

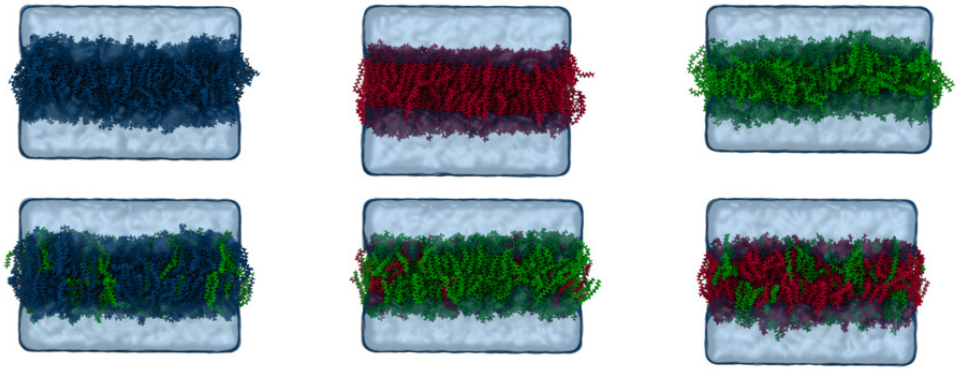

Figure S1: Molecular visualization of six membrane compositions at t=500 ns, using the CHARMM 36M forcefield: Pure POPC (blue), POPE (red) and POPG (green) membranes, and bacteria model membranes: 7:3 POPC:POPG (bacterial inner membrane model), 1:3 POPG:POPE (Gram-negative bacteria model), and 3:1 POPG:POPE (Gram-positive bacteria model).

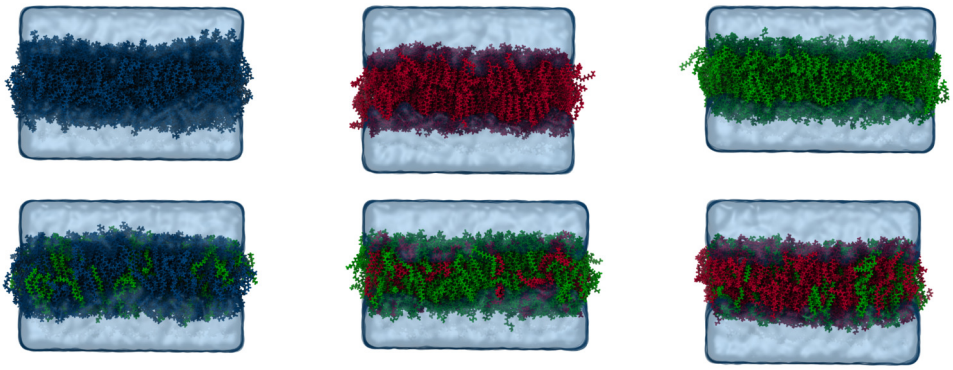

Figure S2: Molecular visualization of six membrane compositions at t=500 ns, using the CHARMM 36M forcefield, with original parameters: Pure POPC (blue), POPE (red) and POPG (green) membranes, and bacteria model membranes: 7:3 POPC:POPG (bacterial inner membrane model), 1:3 POPG:POPE (Gram-negative bacteria model), and 3:1 POPG:POPE (Gram-positive bacteria model).

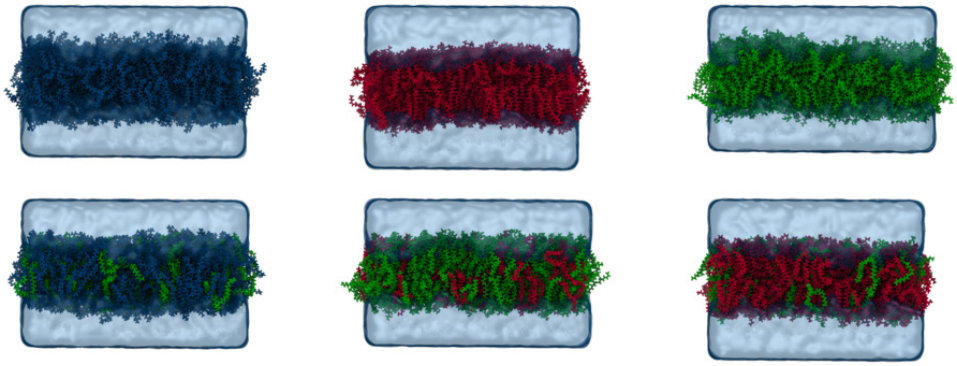

Figure S3: Molecular visualization of six membrane compositions at t=500 ns, using the Slipids forcefield: Pure POPC (blue), POPE (red) and POPG (green) membranes, and bacteria model membranes: 7:3 POPC:POPG (bacterial inner membrane model), 1:3 POPG:POPE (Gram-negative bacteria model), and 3:1 POPG:POPE (Gram-positive bacteria model).

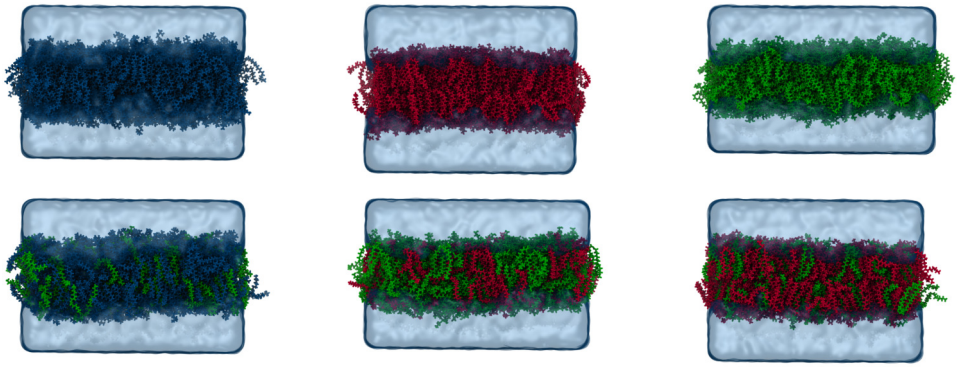

Figure S4: Molecular visualization of six membrane compositions at t=500 ns, using the Slipids forcefield, with original parameters: Pure POPC (blue), POPE (red) and POPG (green) membranes, and bacteria model membranes: 7:3 POPC:POPG (bacterial inner membrane model), 1:3 POPG:POPE (Gram-negative bacteria model), and 3:1 POPG:POPE (Gram-positive bacteria model).

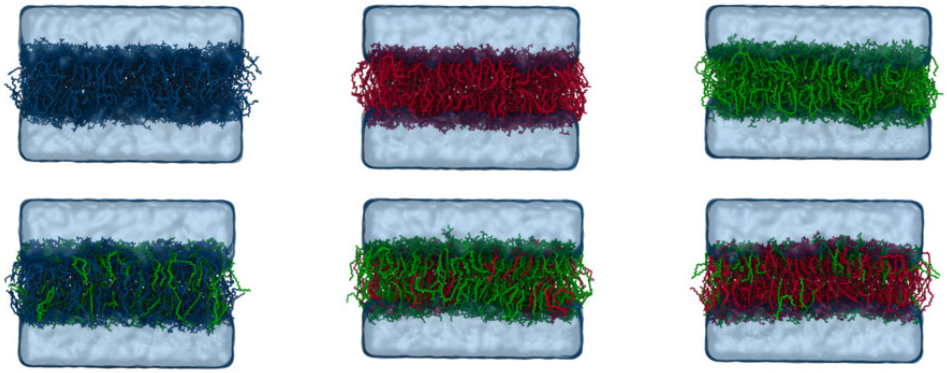

Figure S5: Molecular visualization of six membrane compositions at t=500 ns, using the GROMOS-CKP forcefield: Pure POPC (blue), POPE (red) and POPG (green) membranes, and bacteria model membranes: 7:3 POPC:POPG (bacterial inner membrane model), 1:3 POPG:POPE (Gram-negative bacteria model), and 3:1 POPG:POPE (Gram-positive bacteria model).

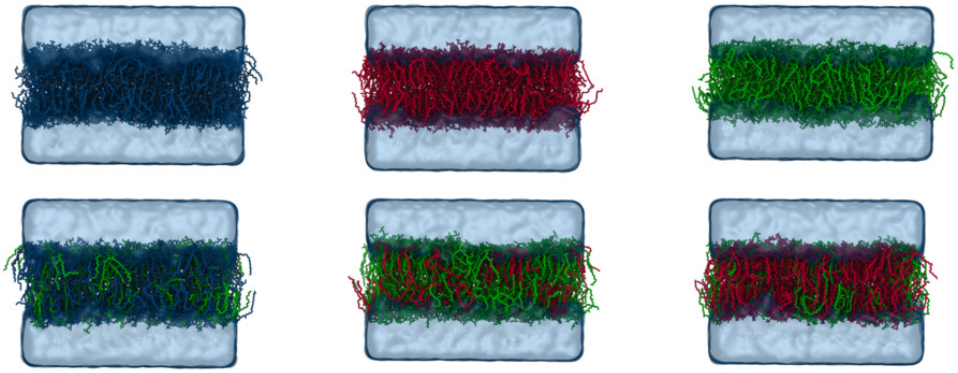

Figure S6: Molecular visualization of six membrane compositions at t=500 ns, using the GROMOS-H2Q forcefield: Pure POPC (blue), POPE (red) and POPG (green) membranes, and bacteria model membranes: 7:3 POPC:POPG (bacterial inner membrane model), 1:3 POPG:POPE (Gram-negative bacteria model), and 3:1 POPG:POPE (Gram-positive bacteria model).

A.1.2 Timeseries

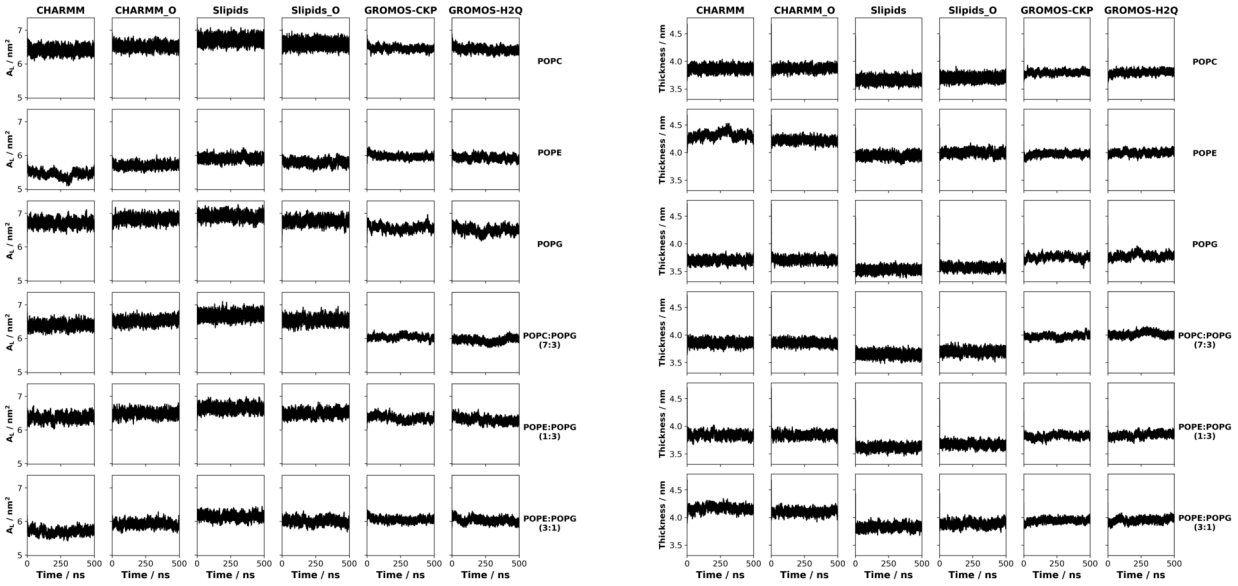

Figure S7: Time profiles for the Area per Lipid (left) and Thickness (right)

A.1.3 Lateral Density

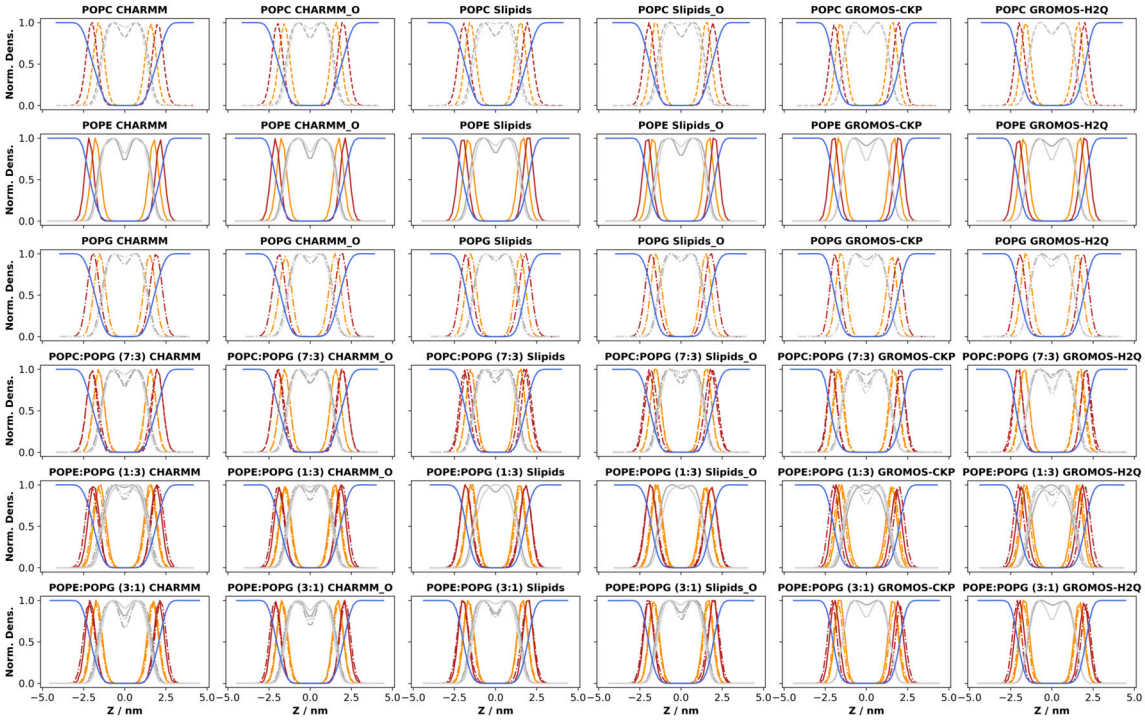

Figure S8: Lateral density distributions along the bilayer normal, calculated for various components of all the membrane along the last 100 ns of the simulation, for all the force-fields and all the lipid compositions. Water (blue), headgroups (red), glycerol (yellow), *sn1* tail (grey, solid line), *sn2* tail (grey, dotted line).

A.1.4 Hydrogen Bonds

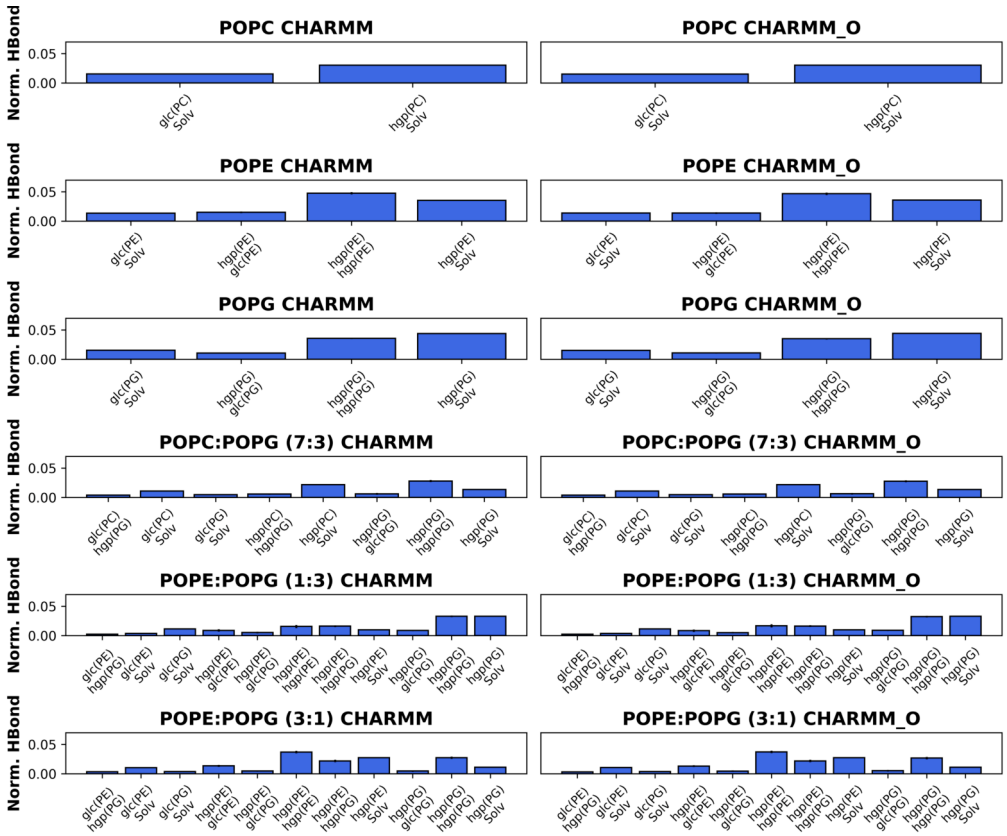

Figure S9: Normalized H-bonds between the different groups (solvent, headgroups and glycerol) of each lipid and the neighbors for CHARMM and CHARMM-O, along the last 100 ns of the trajectory.

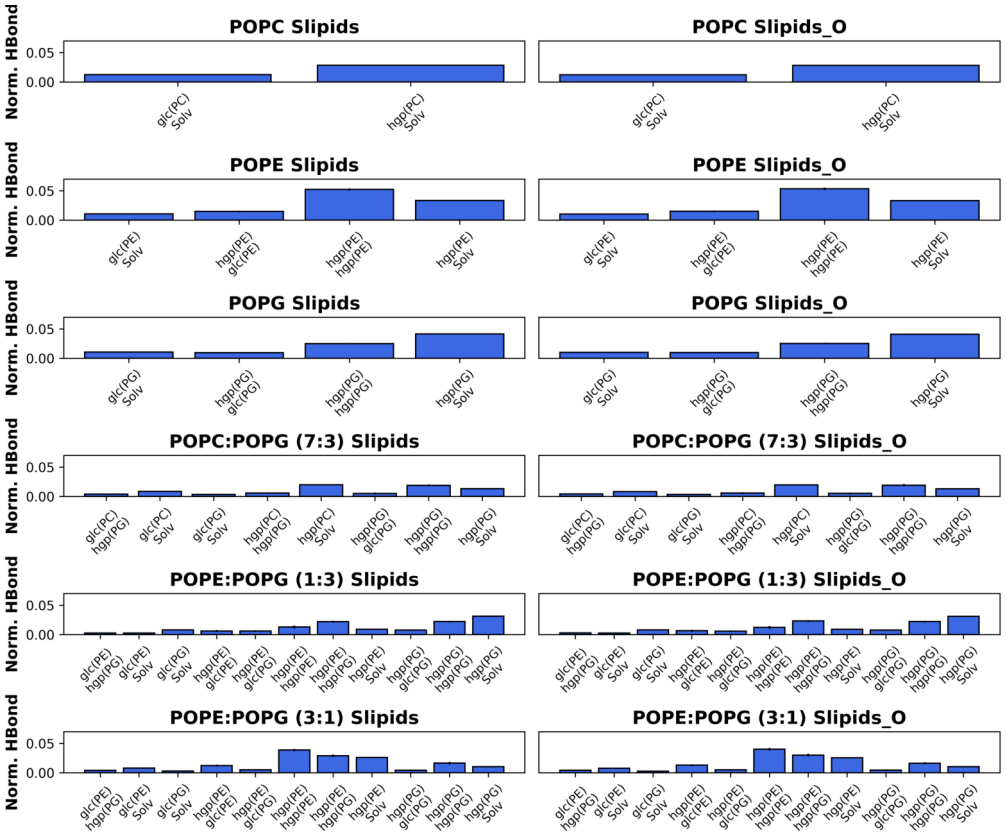

Figure S10: Normalized H-bonds between the different groups (solvent, headgroups and glycerol) of each lipid and the neighbors for Slipids and Slipids-O, along the last 100 ns of the trajectory.

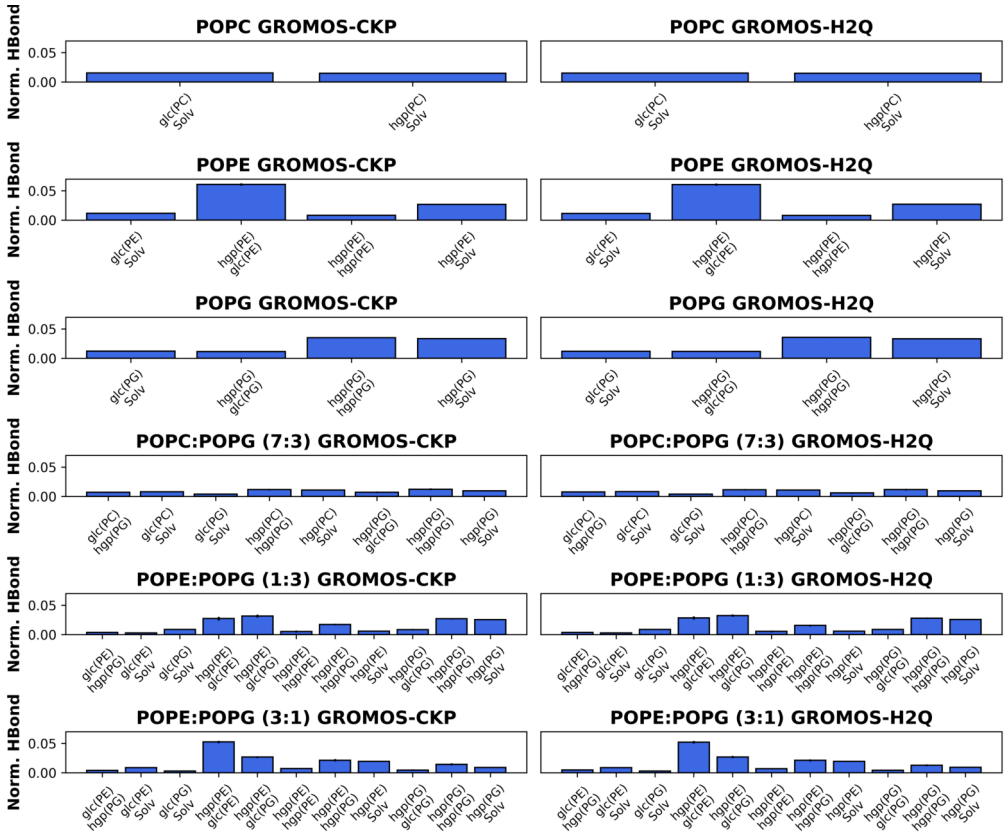

Figure S11: Normalized H-bonds between the different groups (solvent, headgroups and glycerol) of each lipid and the neighbors for GROMOS-CKP and GROMOS-H2Q, along the last 100 ns of the trajectory.

A.1.5 Lateral Displacement and Diffusion Coefficients

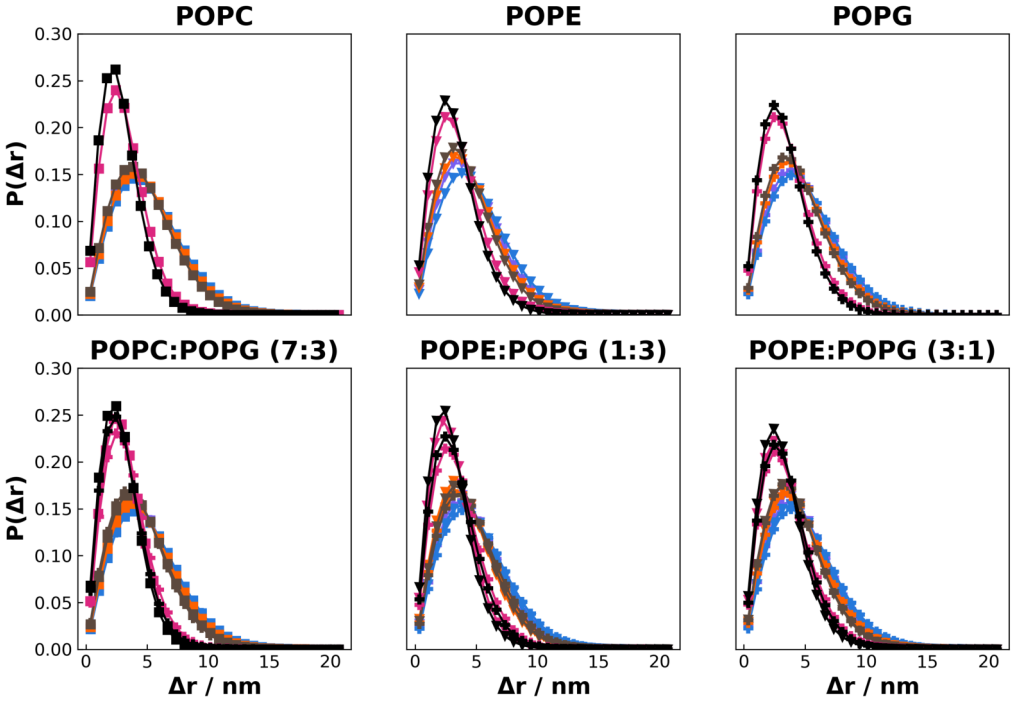

Figure S12: Probability density for the lateral displacement for each lipid type in a time window of Δt = 2 ns, calculated along the last 100 ns of the trajectory. Marker types differentiate specific lipids (square for POPC, triangle for POPE and plus for POPG), and color indicates force field (violet for CHARMM, orange for Slipids, magenta for GROMOS-CKP and black for GROMOS-H2Q).

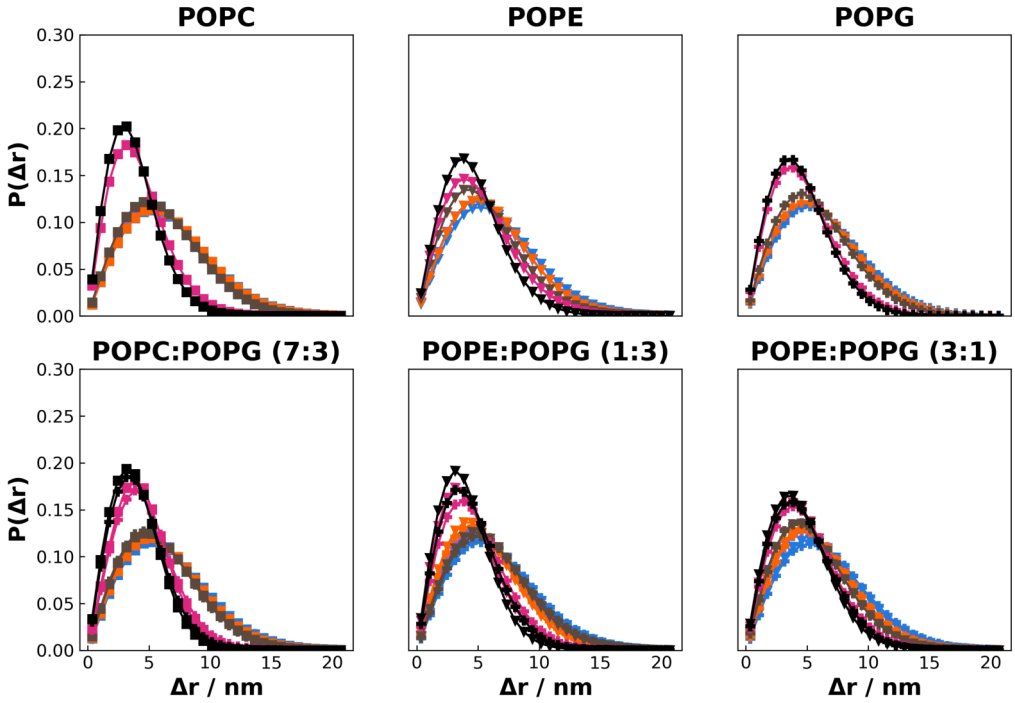

Figure S13: Probability density for the lateral displacement for each lipid type in a time window of Δt = 5 ns, calculated along the last 100 ns of the trajectory. Marker types differentiate specific lipids (square for POPC, triangle for POPE and plus for POPG), and color indicates force field (violet for CHARMM, orange for Slipids, magenta for GROMOS-CKP and black for GROMOS-H2Q).

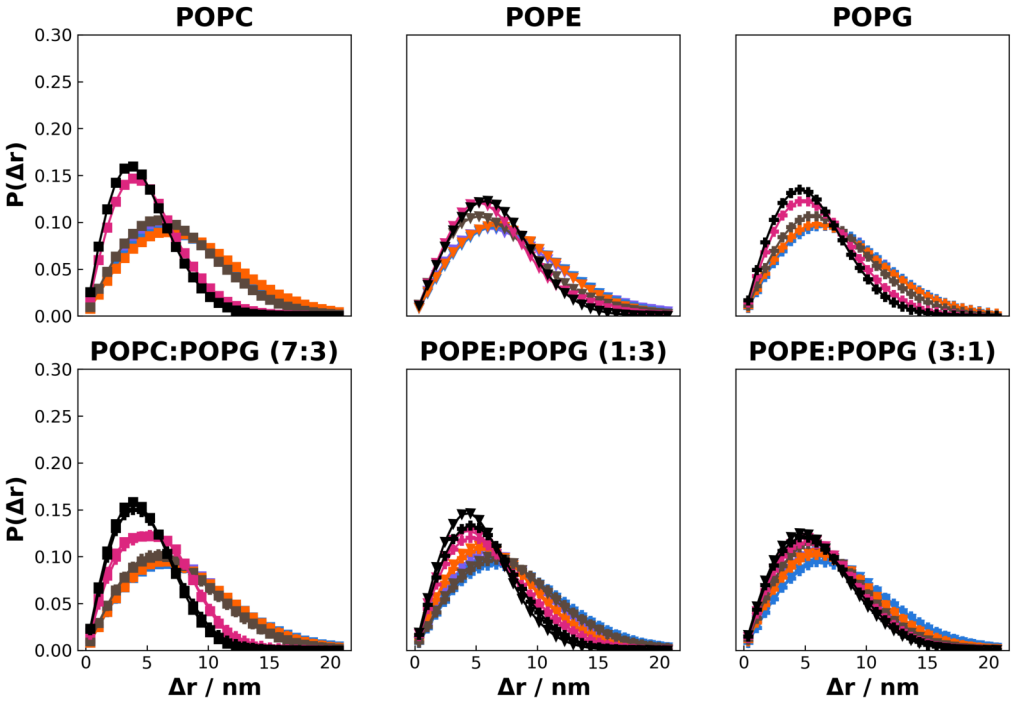

Figure S14: Probability density for the lateral displacement for each lipid type in a time window of Δt = 10 ns, calculated along the last 100 ns of the trajectory. Marker types differentiate specific lipids (square for POPC, triangle for POPE and plus for POPG), and color indicates force field (violet for CHARMM, orange for Slipids, magenta for GROMOS-CKP and black for GROMOS-H2Q).

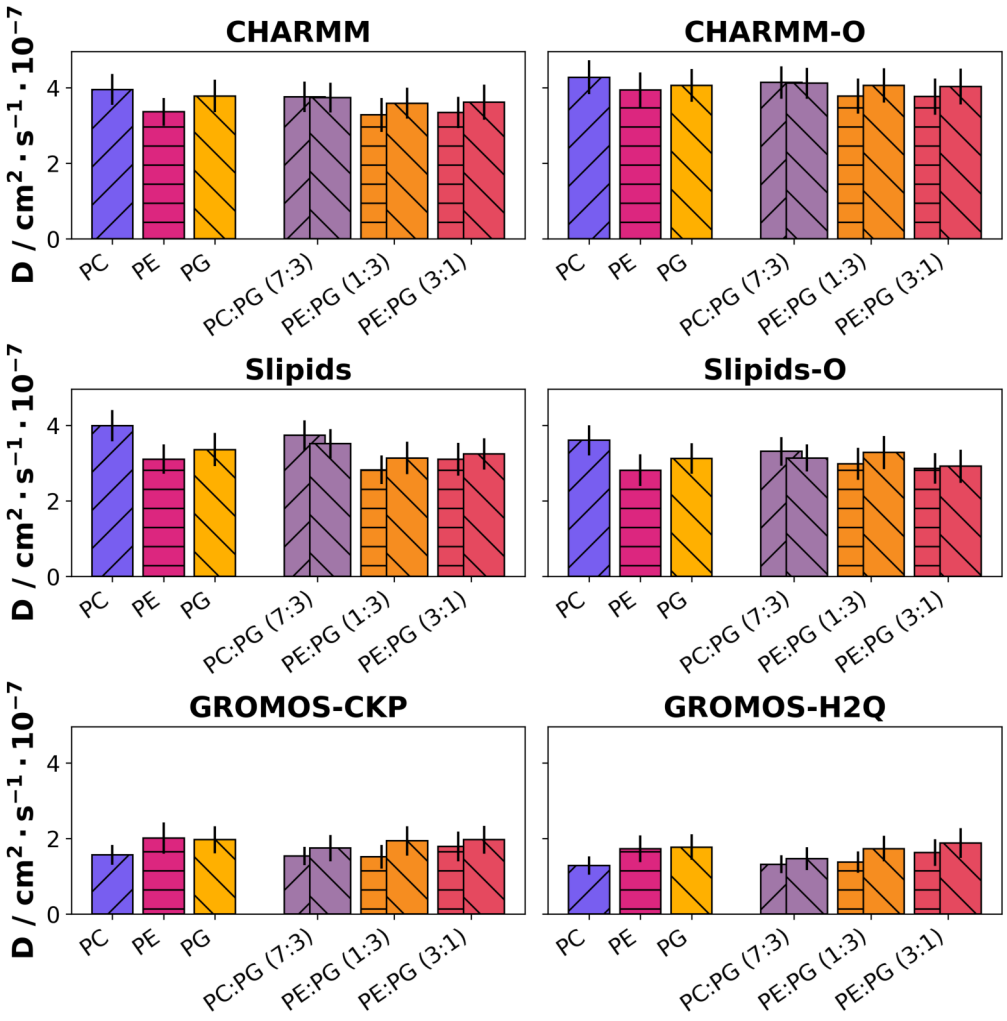

Figure S15: Bar plots from Figure S12, for a time window of Δt = 2 ns. The hatching represents the specific lipid type: forward slash - POPC, horizontal slash - POPE, backward slash - POPG. The errorbar represents the standard deviation.

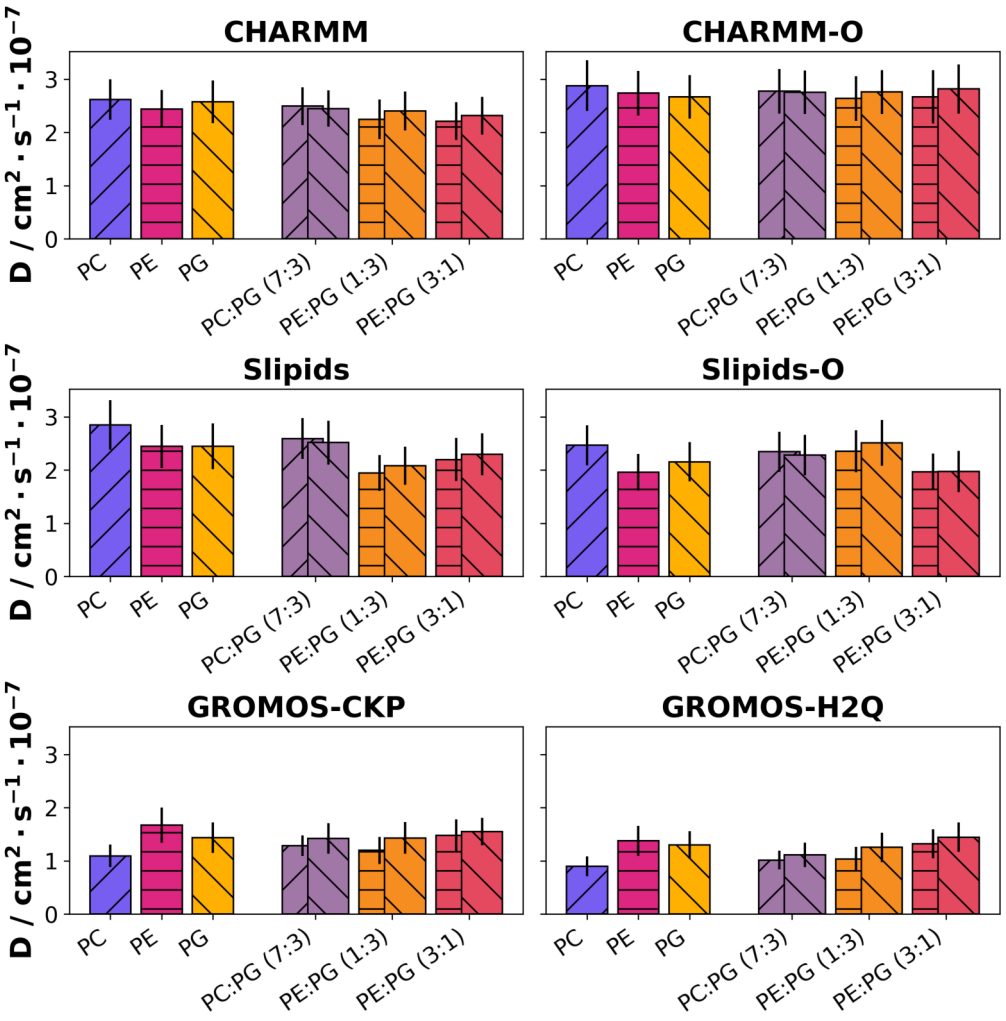

Figure S16: Bar plots from Figure S13, for a time window of Δt = 5 ns. The hatching represents the specific lipid type: forward slash - POPC, horizontal slash - POPE, backward slash - POPG. The errorbar represents the standard deviation.

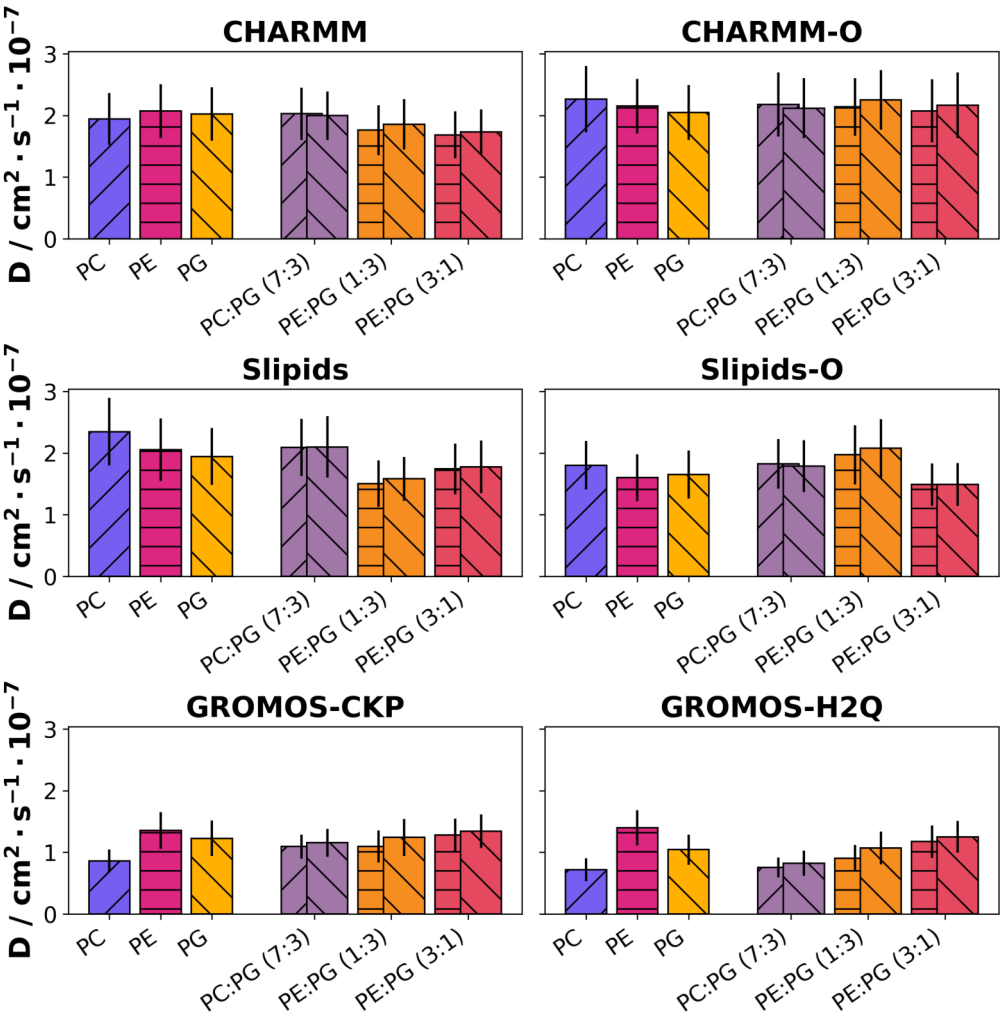

Figure S17: Bar plots from Figure S14, for a time window of Δt = 10 ns. The hatching represents the specific lipid type: forward slash - POPC, horizontal slash - POPE, backward slash - POPG. The errorbar represents the standard deviation.

A.2 Supplementary Tables for Section 4.1

A.2.1 Area per Lipid

Mem. / FF	CHARMM	CHARMM-O	Slipids	Slipids-O	GROMOS-CKP	GROMOS-H2Q	EXP.
POPC	64.11±0.69	64.99±0.69	67.10±0.78	65.72±0.80	64.41±0.49	63.94±0.46	54.0 (275K)[509] 62.7 (293K)[510] 63.0 (297K)[511] 68.3 (303K)[512] 64.3 (303K)[510] 66.0 (310K)[494] 62.0 (323K)[509]
POPE	54.56±0.64	57.16±0.59	58.97±0.63	58.03±0.73	59.65±0.45	58.92±0.51	58.0 (308K)[513]
POPG	67.13±0.84	68.40±0.79	68.98±0.85	67.54±0.88	65.99±0.90	65.03±0.61	66.3 (303K)[514] *
POPC:POPG (7:3)	63.96±0.72	65.44±0.71	67.00±0.78	65.48±0.86	60.11±0.55	60.08±0.44	63.6[515] *
POPE:POPG (1:3)	63.76±0.77	64.79±0.75	66.50±0.77	65.18±0.74	63.31±0.62	62.57±0.50	n.a
POPE:POPG (3:1)	57.14±0.57	58.92±0.72	61.55±0.77	59.74±0.70	60.56±0.50	60.02±0.58	n.a

Table A.1: Area per Lipid values, in Å^2, for all of the studied membranes and forcefields, calculated along the last 100 ns of the simulation (average and standard deviation). The last column corresponds to the experimental published values. n.a. (not available). (*) Non-very trustable value.

A.2.2 Thickness

Mem. / FF	CHARMM	CHARMM-O	Slipids	Slipids-O	GROMOS-CKP	GROMOS-H2Q	EXP.
POPC	38.81±4.22	38.66±4.05	37.14±4.17	37.29±3.94	37.49±3.85	37.84±3.86	39.1 (303K)[510]
POPE	42.19±3.60	41.50±3.68	39.12±3.84	39.96±3.60	38.99±3.61	39.84±3.78	40.5 (308K)[513]
POPG	37.23±4.55	36.94±4.75	35.77±4.41	35.80±4.39	37.21±4.15	37.51±4.21	36.3-38.5 (303K)[514]
POPC:POPG (7:3)	38.62±4.18	38.15±4.14	36.17±3.96	37.26±4.10	40.16±3.61	39.99±3.63	n. a.
POPE:POPG (1:3)	38.77±4.61	37.50±4.30	35.75±4.31	36.10±4.46	38.20±4.28	38.77±4.27	n. a.
POPE:POPG (3:1)	41.34±4.16	40.88±3.93	38.78±3.95	38.80±3.89	39.02±3.71	39.53±3.73	39.4 (309K)[516]

Table A.2: Bilayer thickness values, in Å, for all of the studied membranes and forcefields, calculated along the last 100 ns of the simulation (average and standard deviation). The last column corresponds to the experimental published values. n.a. (not available). (*) Non-trustable value.

A.2.3 Membrane Hydration.

Mem. / FF	CHARMM	CHARMM-O	Slipids	Slipids-O	GROMOS-CKP	GROMOS-H2Q
POPC	1.46±0.13	1.34±0.13	1.28±0.17	1.13±0.11	0.66±0.07	0.65±0.12
POPE	0.79±0.07	0.87±0.08	0.77±0.11	0.65±0.05	0.42±0.06	0.40±0.04
POPG	1.43±0.16	1.56±0.23	1.11±0.12	1.02±0.16	0.72±0.10	0.70±0.15
POPC:POPG (7:3)	1.29±0.13	1.30±0.13	1.06±0.08	0.99±0.12	0.40±0.04	0.40±0.04
POPE:POPG (1:3)	1.32±0.16	1.30±0.25	1.01±0.15	1.01±0.15	0.59±0.12	0.59±0.14
POPE:POPG (3:1)	0.99±0.10	0.90±0.08	0.82±0.10	0.71±0.08	0.41±0.05	0.43±0.07

Table A.3: Number of water molecules per lipid for all of the studied membranes and forcefields, calculated along the last 100 ns of the simulation (average and standard deviation).

A.2.4 Hydrogen Bonds

Groups / FF	CHARMM	CHARMM-O	Slipids	Slipids-O	GROMOS-CKP	GROMOS-H2Q
glc(PC)-Solv	1.530±0.031	1.515±0.031	1.249±0.029	1.221±0.027	1.534±0.026	1.514±0.027
hgp(PC)-Solv	3.014±0.029	3.015±0.029	2.828±0.025	2.811±0.025	1.487±0.024	1.488±0.025

Table A.4: Normalized number of H-Bonds between different groups (glycerol, headgroup and solvent) for the POPC membrane in all forcefields, calculated along the last 100 ns of the simulation (average and standard deviation)

Groups / FF	CHARMM	CHARMM-O	Slipids	Slipids-O	GROMOS-CKP	GROMOS-H2Q
glc(PE)-Solv	1.356±0.032	1.388±0.032	1.050±0.030	1.023±0.027	1.149±0.034	1.146±0.034
hgp(PE)-glc(PE)	1.50±0.14	1.38±0.13	1.47±0.14	1.51±0.13	6.08±0.21	6.07±0.19
hgp(PE)-hgp(PE)	4.76±0.18	4.67±0.20	5.25±0.18	5.36±0.21	0.80±0.10	0.80±0.10
hgp(PE)-Solv	3.532±0.051	3.591±0.055	3.361±0.048	3.327±0.051	2.687±0.041	2.707±0.039

Table A.5: Normalized number of H-Bonds between different groups (glycerol, headgroup and solvent) for the POPE membrane in all forcefields, calculated along the last 100 ns of the simulation (average and standard deviation)

Groups / FF	CHARMM	CHARMM-O	Slipids	Slipids-O	GROMOS-CKP	GROMOS-H2Q
glc(PG)-Solv	1.527±0.033	1.521±0.031	1.049±0.031	1.011±0.032	1.203±0.037	1.187±0.037
hgp(PG)-glc(PG)	1.056±0.092	1.080±0.099	0.940±0.090	0.965±0.094	1.10±0.10	1.152±0.088
hgp(PG)-hgp(PG)	3.56±0.11	3.50±0.11	2.50±0.13	2.53±0.11	3.51±0.11	3.56±0.12
hgp(PG)-Solv	4.390±0.050	4.413±0.050	4.146±0.052	4.103±0.055	3.335±0.049	3.316±0.048

Table A.6: Normalized number of H-Bonds between different groups (glycerol, headgroup and solvent) for the POPG membrane in all forcefields, calculated along the last 100 ns of the simulation (average and standard deviation)

Groups / FF	CHARMM	CHARMM-O	Slipids	Slipids-O	GROMOS-CKP	GROMOS-H2Q
glc(PC)-hgp(PG)	0.397±0.094	0.393±0.095	0.40±0.10	0.404±0.097	0.70±0.10	0.77±0.11
glc(PC)-Solv	1.073±0.026	1.076±0.027	0.832±0.025	0.805±0.024	0.799±0.023	0.803±0.022
glc(PG)-Solv	0.458±0.018	0.456±0.017	0.343±0.016	0.331±0.016	0.399±0.016	0.379±0.016
hgp(PC)-hgp(PG)	0.58±0.11	0.56±0.11	0.56±0.12	0.58±0.13	1.15±0.13	1.14±0.13
hgp(PC)-Solv	2.164±0.026	2.170±0.027	1.976±0.024	1.968±0.025	1.070±0.021	1.079±0.023
hgp(PG)-glc(PG)	0.60±0.15	0.64±0.13	0.51±0.14	0.52±0.13	0.71±0.13	0.59±0.12
hgp(PG)-hgp(PG)	2.80±0.18	2.77±0.17	1.89±0.19	1.92±0.19	1.22±0.15	1.16±0.14
hgp(PG)-Solv	1.346±0.028	1.358±0.026	1.314±0.029	1.307±0.026	0.951±0.024	0.938±0.026

Table A.7: Normalized number of H-Bonds between different groups (glycerol, headgroup and solvent) for the POPC:POPG (7:3) membrane in all forcefields, calculated along the last 100 ns of the simulation (average and standard deviation)

Groups / FF	CHARMM	CHARMM-O	Slipids	Slipids-O	GROMOS-CKP	GROMOS-H2Q
glc(PE)-hgp(PG)	0.226±0.062	0.221±0.061	0.242±0.063	0.269±0.065	0.365±0.081	0.351±0.071
glc(PE)-Solv	0.373±0.016	0.367±0.016	0.261±0.015	0.247±0.013	0.294±0.016	0.288±0.015
glc(PG)-Solv	1.133±0.027	1.125±0.029	0.798±0.026	0.777±0.028	0.865±0.034	0.864±0.031
hgp(PE)-glc(PE)	0.88±0.21	0.83±0.21	0.61±0.18	0.65±0.17	2.70±0.30	2.84±0.26
hgp(PE)-glc(PG)	0.52±0.13	0.51±0.12	0.60±0.13	0.58±0.13	3.16±0.25	3.23±0.19
hgp(PE)-hgp(PE)	1.56±0.25	1.67±0.28	1.31±0.22	1.22±0.23	0.51±0.15	0.54±0.15
hgp(PE)-hgp(PG)	1.60±0.14	1.62±0.15	2.21±0.14	2.33±0.15	1.72±0.14	1.55±0.14
hgp(PE)-Solv	0.987±0.026	0.982±0.025	0.895±0.025	0.890±0.024	0.579±0.021	0.580±0.019
hgp(PG)-glc(PG)	0.86±0.11	0.90±0.10	0.753±0.097	0.754±0.100	0.85±0.11	0.879±0.094
hgp(PG)-hgp(PG)	3.29±0.13	3.24±0.13	2.23±0.13	2.23±0.13	2.70±0.12	2.80±0.12
hgp(PG)-Solv	3.287±0.042	3.302±0.044	3.134±0.044	3.106±0.044	2.559±0.047	2.572±0.042

Table A.8: Normalized number of H-Bonds between different groups (glycerol, headgroup and solvent) for the POPE:POPG (1:3) membrane in all forcefields, calculated along the last 100 ns of the simulation (average and standard deviation)

Groups / FF	CHARMM	CHARMM-O	Slipids	Slipids-O	GROMOS-CKP	GROMOS-H2Q
glc(PE)-hgp(PG)	0.336±0.093	0.313±0.083	0.380±0.098	0.404±0.099	0.378±0.091	0.466±0.098
glc(PE)-Solv	1.040±0.029	1.043±0.028	0.784±0.026	0.751±0.023	0.871±0.028	0.870±0.027
glc(PG)-Solv	0.372±0.017	0.373±0.016	0.271±0.014	0.263±0.016	0.271±0.015	0.278±0.017
hgp(PE)-glc(PE)	1.34±0.16	1.30±0.15	1.23±0.15	1.28±0.15	5.30±0.20	5.21±0.21
hgp(PE)-glc(PG)	0.50±0.10	0.45±0.11	0.49±0.11	0.48±0.11	2.67±0.15	2.68±0.18
hgp(PE)-hgp(PE)	3.70±0.21	3.73±0.19	3.88±0.19	4.02±0.21	0.70±0.10	0.69±0.11
hgp(PE)-hgp(PG)	2.20±0.20	2.18±0.20	2.90±0.21	3.01±0.22	2.10±0.20	2.12±0.17
hgp(PE)-Solv	2.731±0.045	2.739±0.042	2.590±0.042	2.544±0.039	1.933±0.033	1.934±0.034
hgp(PG)-glc(PG)	0.46±0.13	0.53±0.14	0.43±0.13	0.45±0.14	0.45±0.12	0.41±0.11
hgp(PG)-hgp(PG)	2.70±0.20	2.67±0.19	1.65±0.21	1.61±0.19	1.44±0.17	1.27±0.15
hgp(PG)-Solv	1.103±0.028	1.111±0.027	1.040±0.027	1.017±0.029	0.893±0.027	0.915±0.024

Table A.9: Normalized number of H-Bonds between different groups (glycerol, headgroup and solvent) for the POPE:POPG (3:1) membrane in all forcefields, calculated along the last 100 ns of the simulation (average and standard deviation)

A.2.5 Diffusion Coefficients

Mem. / FF	CHARMM	CHARMM-O	Slipids	Slipids-O	GROMOS-CKP	GROMOS-H2Q
POPC	3.95±0.41	4.28±0.45	3.99±0.41	3.60±0.40	1.57±0.26	1.28±0.24
POPE	3.36±0.37	3.94±0.47	3.11±0.39	2.81±0.42	2.01±0.41	1.73±0.36
POPG	3.78±0.43	4.06±0.44	3.36±0.44	3.12±0.41	1.97±0.36	1.77±0.34
POPC:POPG	3.80±0.40	4.14±0.43	3.70±0.40	3.31±0.38	1.55±0.32	1.32±0.24
(7:3)	3.74±0.39	4.12±0.41	3.51±0.39	3.14±0.36	1.71±0.41	1.50±0.30
POPE:POPG	3.28±0.45	3.78±0.47	2.82±0.38	2.98±0.42	1.52±0.31	1.37±0.28
(1:3)	3.59±0.41	4.06±0.46	3.14±0.42	3.28±0.44	1.94±0.39	1.73±0.34
POPE:POPG	3.34±0.41	3.77±0.48	3.10±0.44	2.86±0.41	1.79±0.39	1.63±0.36
(3:1)	3.62±0.46	4.03±0.48	3.25±0.42	2.92±0.44	1.97±0.37	1.88±0.39

Table A.10: Diffusion coefficients, in 10^{-7} $cm^2 \cdot s^{-1}$ using a time window of 2 ns, for all of the studied membranes and forcefields, calculated along the last 100 ns of the simulation (average and standard deviation).

Mem. / FF	CHARMM	CHARMM-O	Slipids	Slipids-O	GROMOS-CKP	GROMOS-H2Q
POPC	2.62±0.38	2.88±0.48	2.85±0.47	2.46±0.38	1.09±0.21	0.90±0.18
POPE	2.44±0.36	2.74±0.42	2.44±0.41	1.96±0.34	1.67±0.33	1.38±0.28
POPG	2.60±0.40	2.67±0.41	2.45±0.43	2.15±0.37	1.43±0.29	1.30±0.26
POPC:POPG	2.49±0.35	2.77±0.42	2.59±0.38	2.34±0.38	1.20±0.25	1.01±0.18
(7:3)	2.45±0.34	2.75±0.41	2.51±0.40	2.28±0.38	1.31±0.29	1.11±0.23
POPE:POPG	2.25±0.37	2.64±0.42	1.94±0.34	2.35±0.39	1.19±0.25	1.03±0.23
(1:3)	2.40±0.37	2.76±0.41	2.08±0.3	2.51±0.4	1.40±0.30	1.25±0.27
POPE:POPG	2.21±0.35	2.67±0.50	2.20±0.41	1.96±0.35	1.50±0.30	1.32±0.27
(3:1)	2.31±0.36	2.81±0.46	2.29±0.39	1.97±0.39	1.55±0.26	1.44±0.27

Table A.11: Diffusion coefficients, in 10^{-7} $cm^2 \cdot s^{-1}$ using a time window of 5 ns, for all of the studied membranes and forcefields, calculated along the last 100 ns of the simulation (average and standard deviation).

Mem. / FF	CHARMM	CHARMM-O	Slipids	Slipids-O	GROMOS-CKP	GROMOS-H2Q
POPC	1.94±0.42	2.26±0.54	2.35±0.55	1.80±0.39	0.86±0.18	0.72±0.18
POPE	2.07±0.43	2.15±0.44	2.06±0.51	1.60±0.38	1.36±0.30	1.40±0.28
POPG	2.02±0.43	2.05±0.44	1.94±0.46	1.65±0.39	1.23±0.29	1.04±0.25
POPC:POPG	2.03±0.42	2.18±0.52	2.09±0.46	1.83±0.40	1.09±0.19	0.75±0.16
(7:3)	2.00±0.39	2.12±0.49	2.10±0.50	1.79±0.42	1.15±0.23	0.82±0.21
POPE:POPG	1.76±0.40	2.14±0.47	1.50±0.38	1.97±0.48	1.10±0.26	0.90±0.22
(1:3)	1.86±0.41	2.25±0.48	1.58±0.36	2.08±0.47	1.24±0.30	1.07±0.27
POPE:POPG	1.69±0.38	2.07±0.51	1.74±0.41	1.49±0.34	1.28±0.27	1.17±0.26
(3:1)	1.73±0.36	2.17±0.53	1.78±0.42	1.49±0.35	1.34±0.27	1.25±0.26

Table A.12: Diffusion coefficients, in 10^{-7} $cm^2 \cdot s^{-1}$ using a time window of 2 ns, for all of the studied membranes and forcefields, calculated along the last 100 ns of the simulation (average and standard deviation).

A.3 Supplementary Figures for Section 4.2

A.3.1 Local Frame of Reference

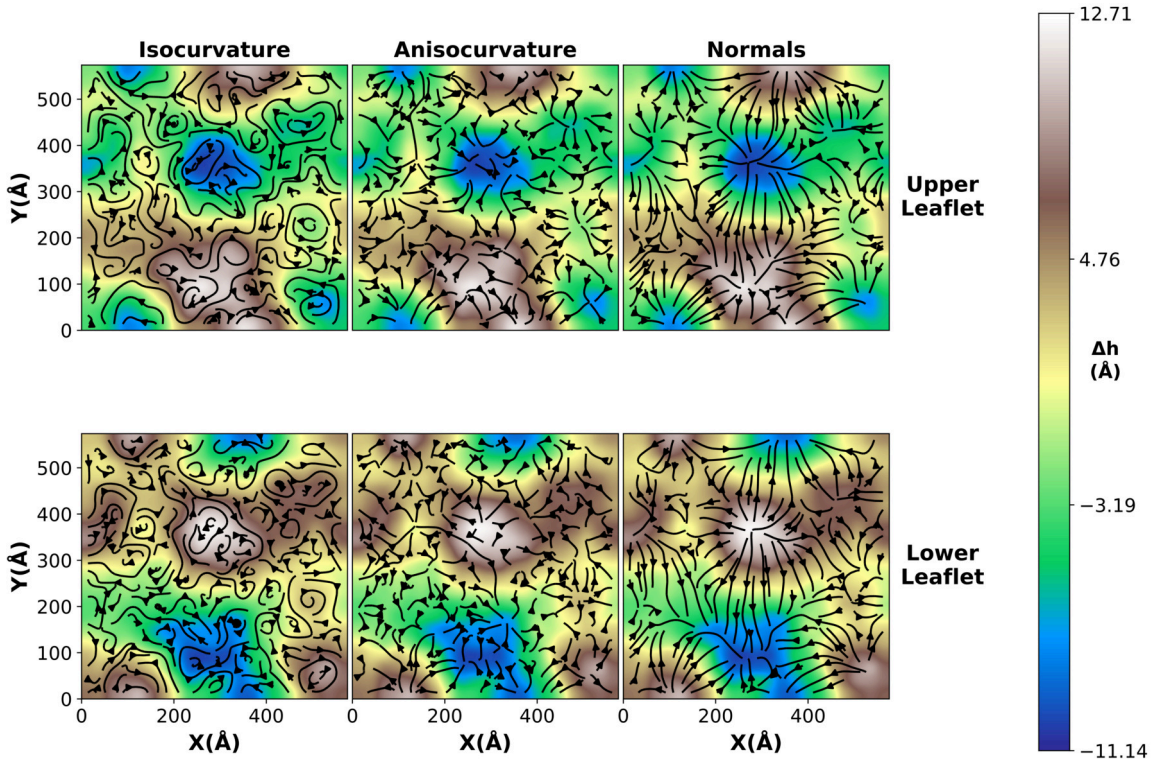

Figure S18: Topographic map and Local Frame of Reference vector fields for the POPC membrane. Image obtained by averaging over the last ns of trajectory.

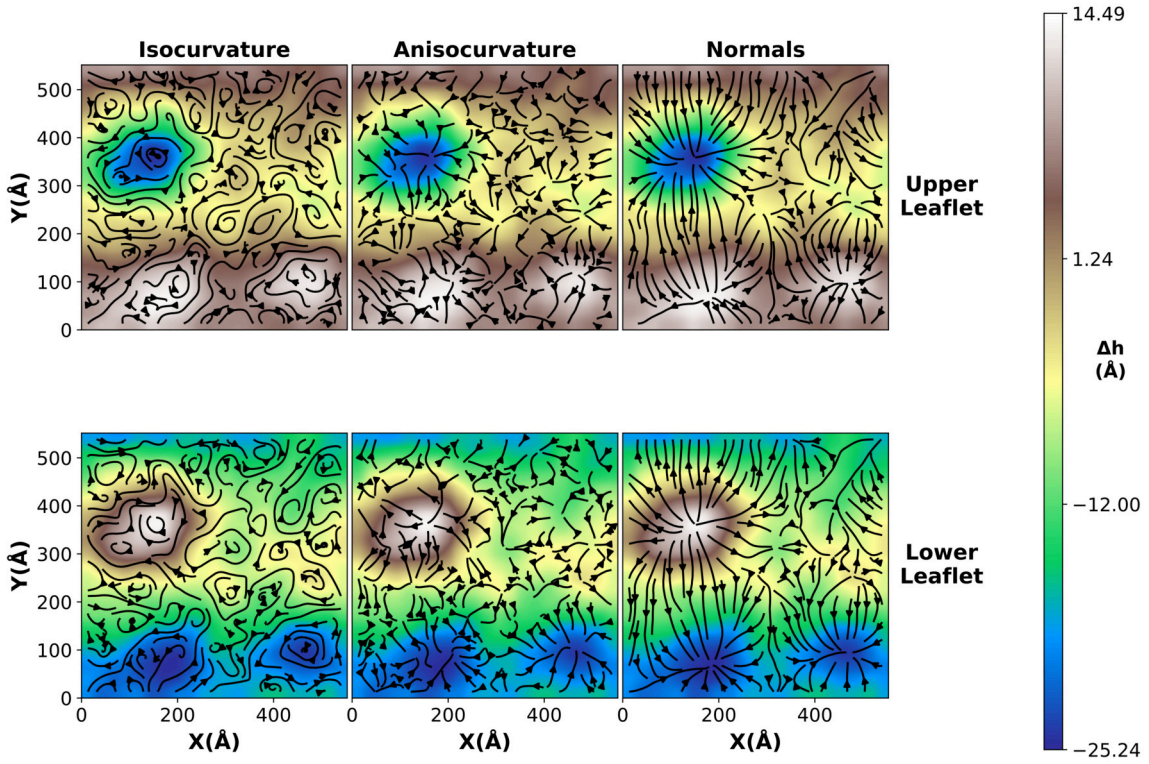

Figure S19: Topographic map and Local Frame of Reference vector fields for the DLPC membrane. Image obtained by averaging over the last ns of trajectory.

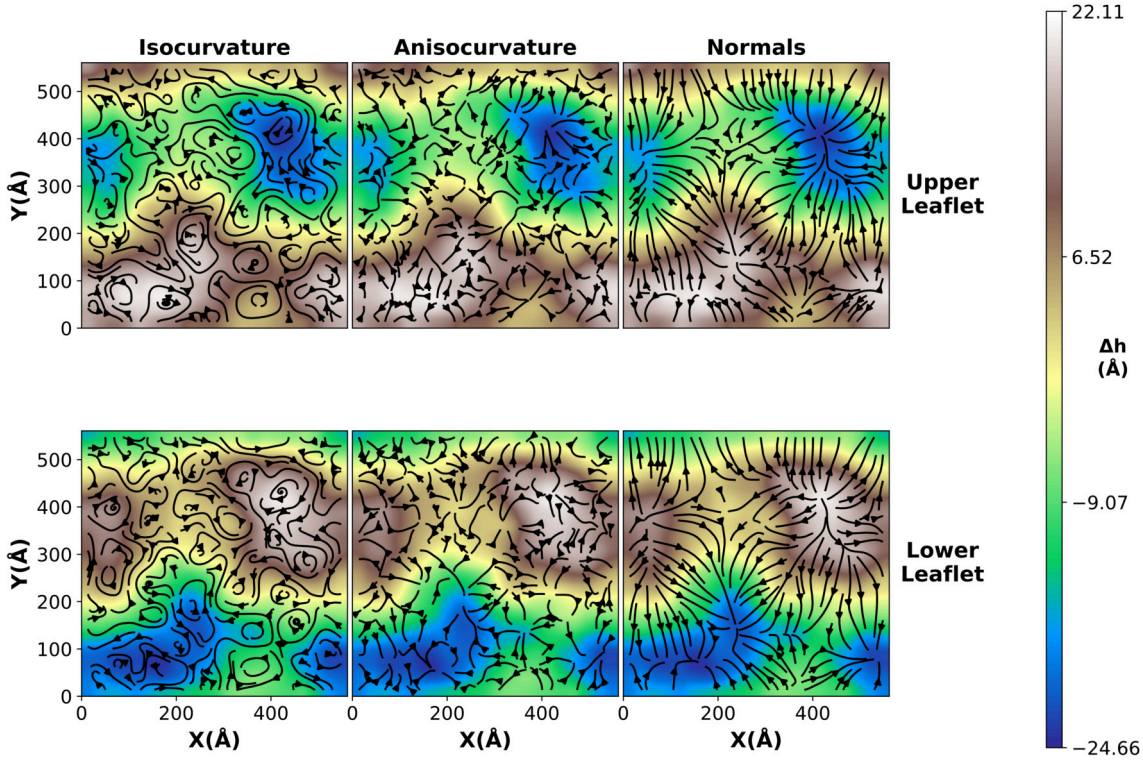

Figure S20: Topographic map and Local Frame of Reference vector fields for the POPE:POPG membrane. Image obtained by averaging over the last ns of trajectory.

A.3.2 Curvature

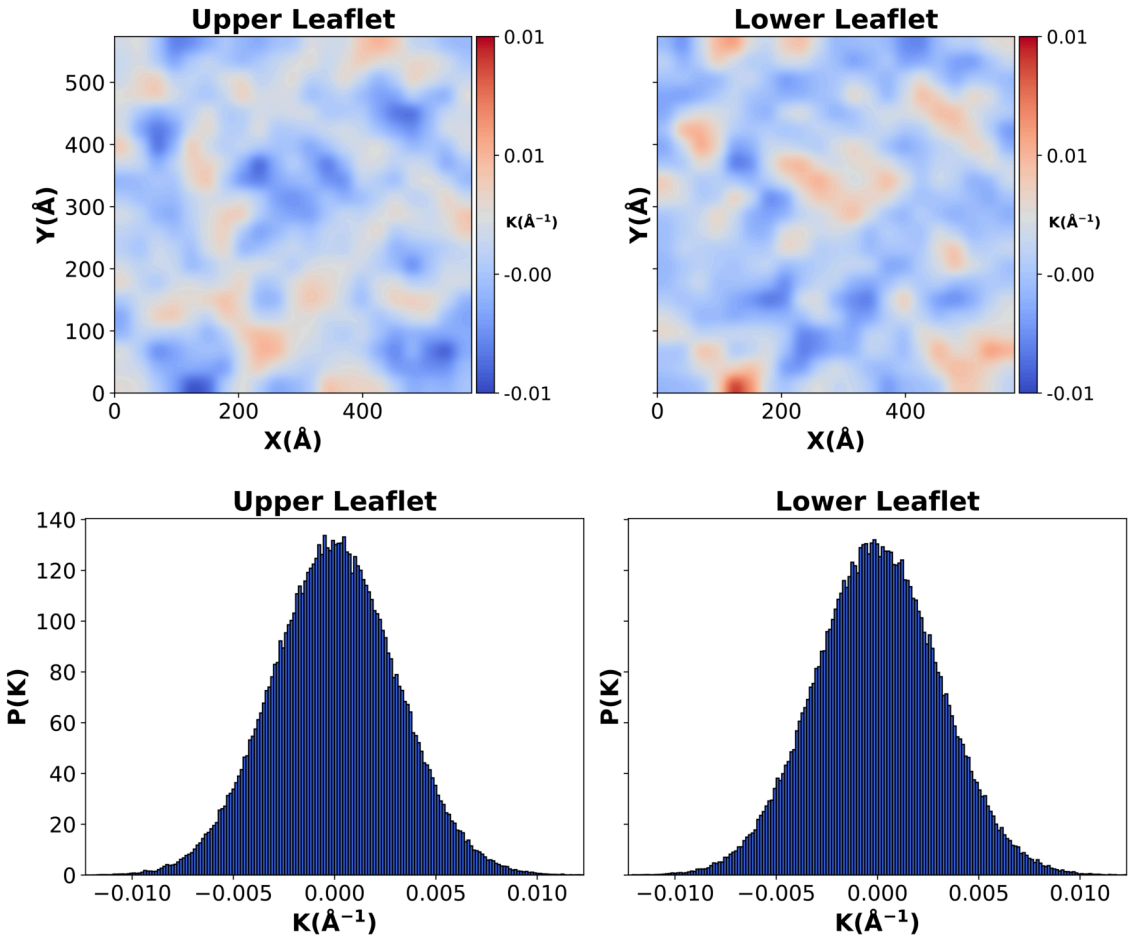

Figure S21: Curvature heatmap over the surface of the POPC membrane (top), obtained by averaging the last ns of trajectory and curvature probability density function for the POPC membrane (bottom). The distribution is obtained by just considering the statistically independent frames throughout all the trajectory.

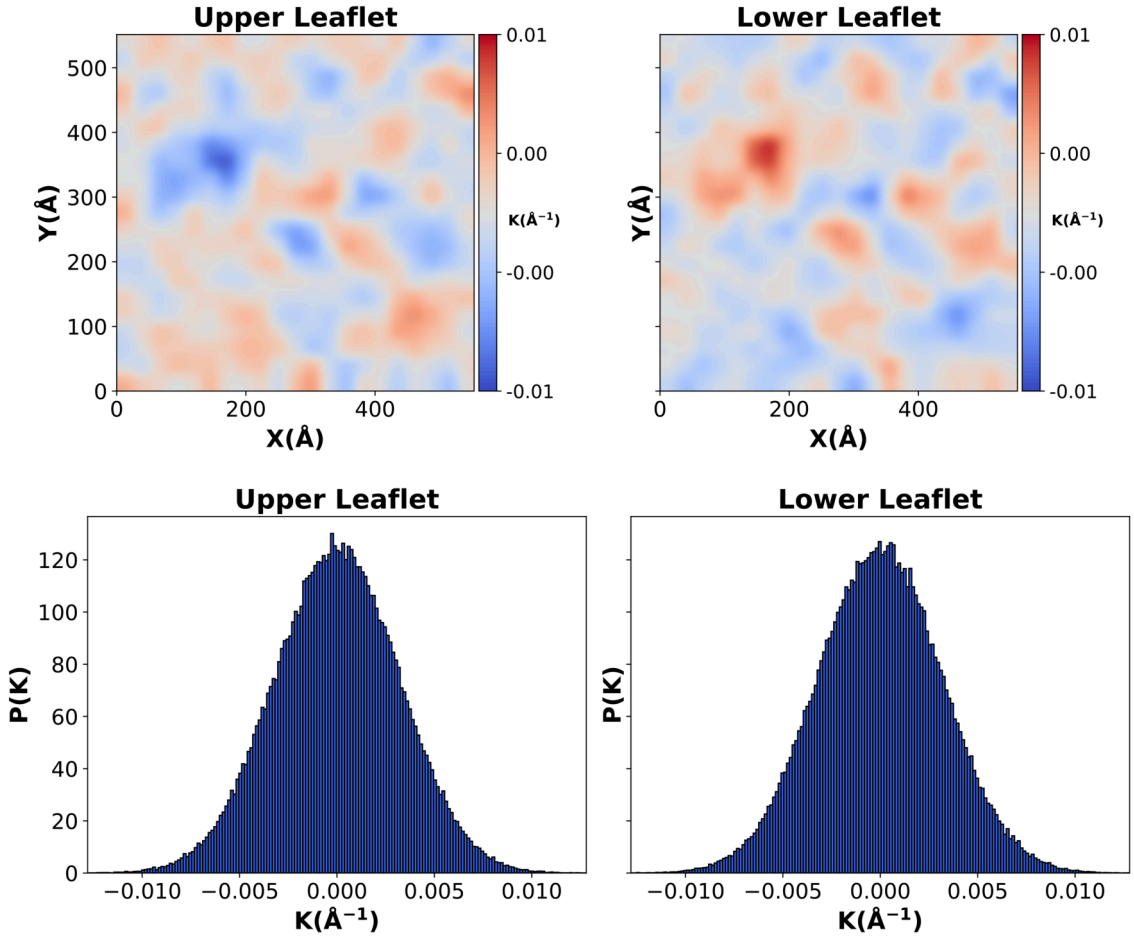

Figure S22: Curvature heatmap over the surface of the DLPC membrane (top), obtained by averaging the last ns of trajectory and curvature probability density function for the DLPC membrane (bottom). The distribution is obtained by just considering the statistically independent frames throughout all the trajectory.

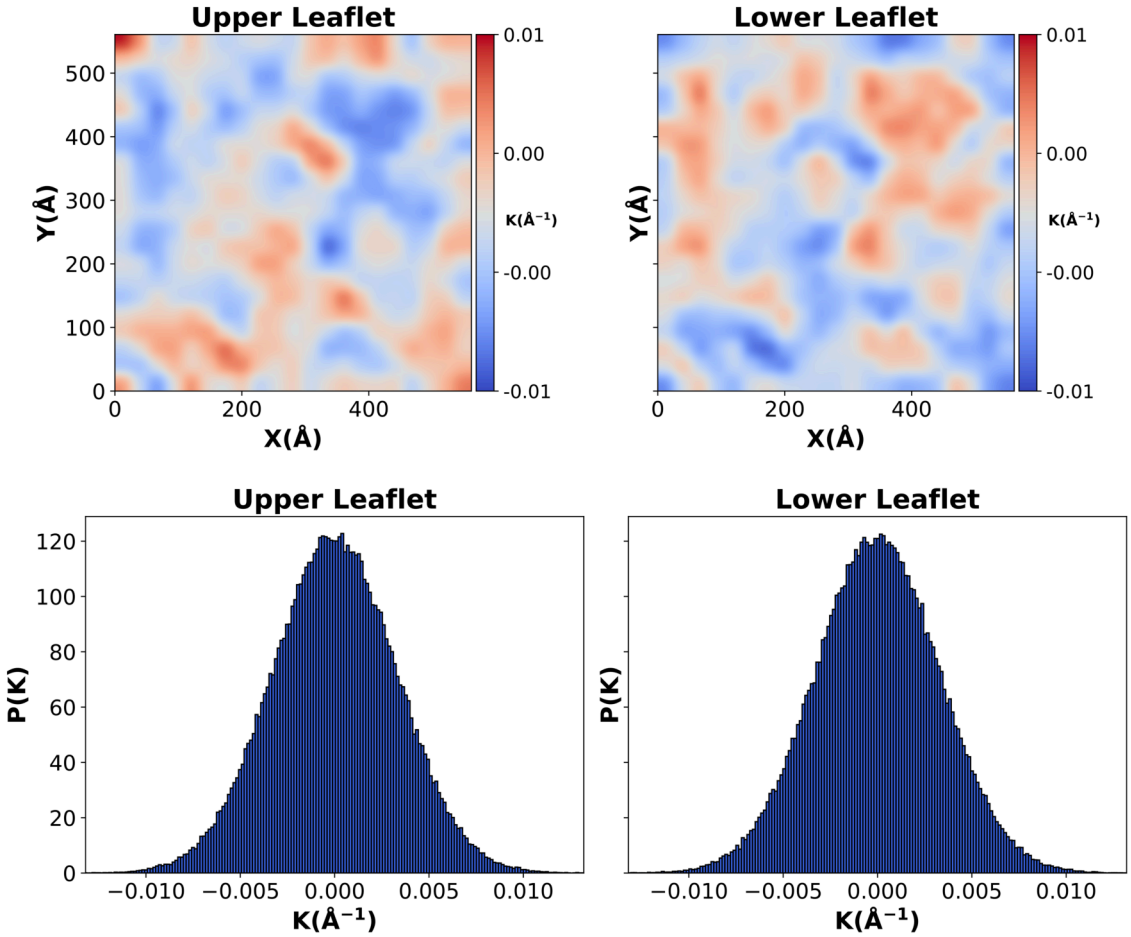

Figure S23: Curvature heatmap over the surface of the POPE:POPG membrane (top), obtained by averaging the last ns of trajectory and curvature probability density function for the POPE:POPG membrane (bottom). The distribution is obtained by just considering the statistically independent frames throughout all the trajectory.

A.3.3 Lipid Director

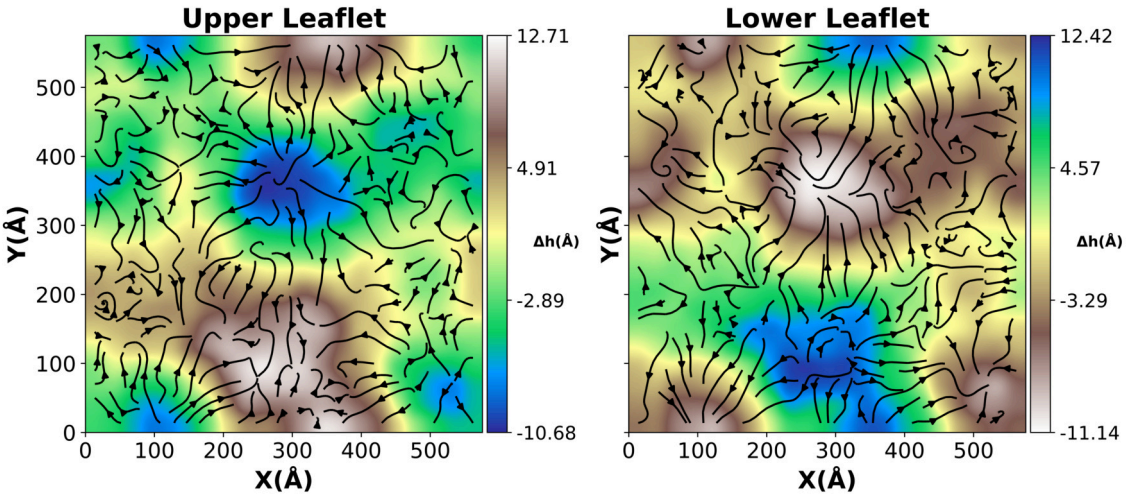

Figure S24: Topographic map and Lipid Director vector fields for the POPC membrane. Image obtained by averaging over the last ns of trajectory.

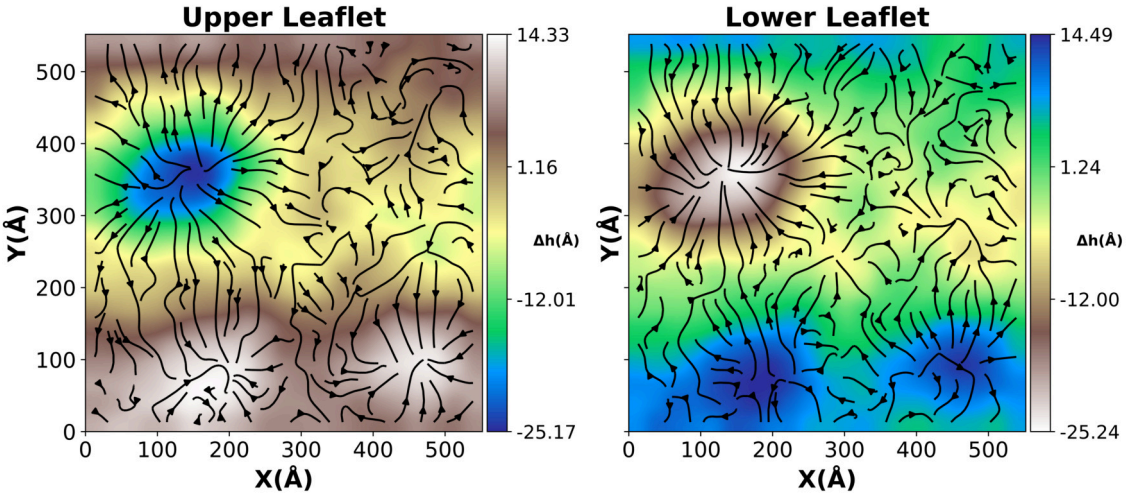

Figure S25: Topographic map and Lipid Director vector fields for the DLPC membrane. Image obtained by averaging over the last ns of trajectory.

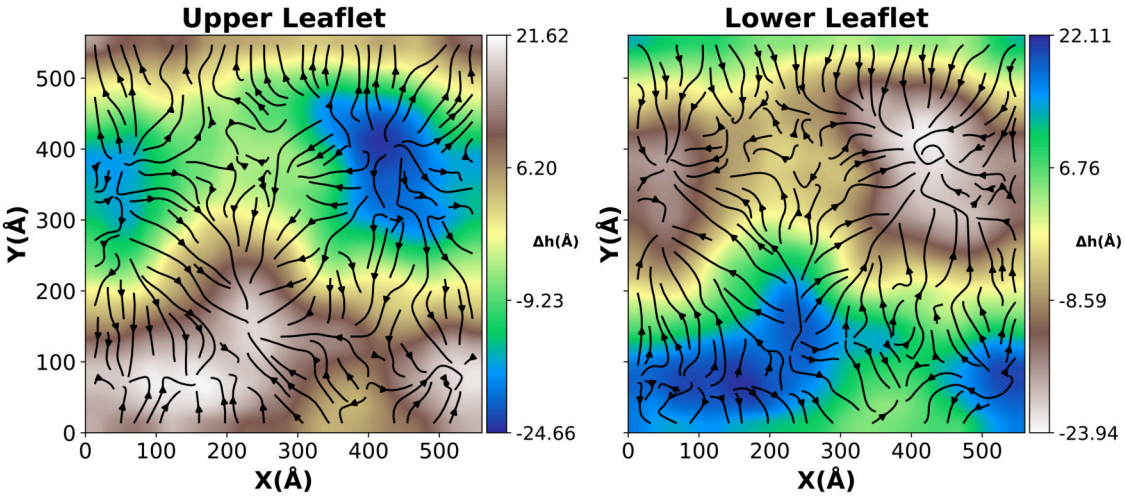

Figure S26: Topographic map and Lipid Director vector fields for the POPE:POPG membrane. Image obtained by averaging over the last ns of trajectory.

A.3.4 Tail Tilt

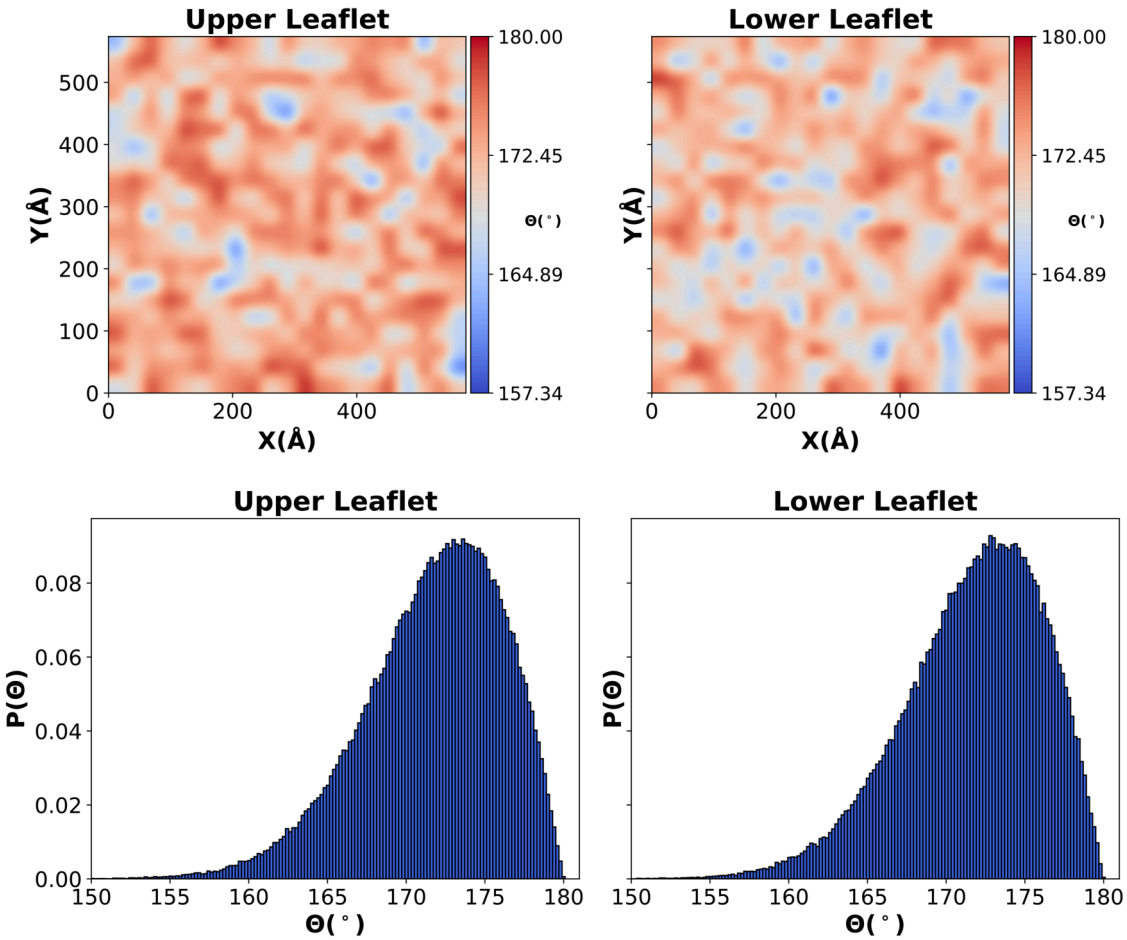

Figure S27: Tail tilt heatmap over the surface of the POPC membrane (top), obtained by averaging the last ns of trajectory and tail tilt probability density function for the POPC membrane (bottom). The distribution is obtained by just considering the statistically independent frames throughout all the trajectory.

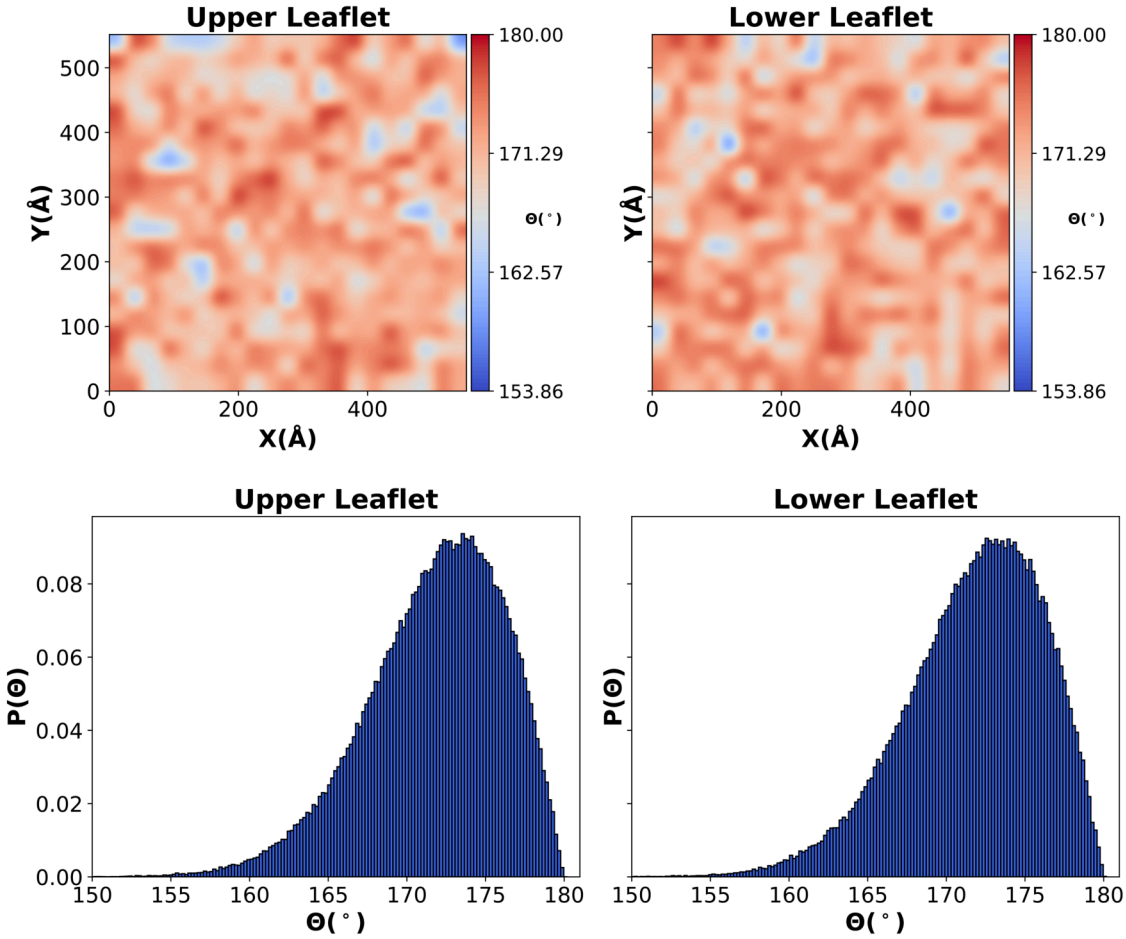

Figure S28: Tail tilt heatmap over the surface of the DLPC membrane (top), obtained by averaging the last ns of trajectory and tail tilt probability density function for the DLPC membrane (bottom). The distribution is obtained by just considering the statistically independent frames throughout all the trajectory.

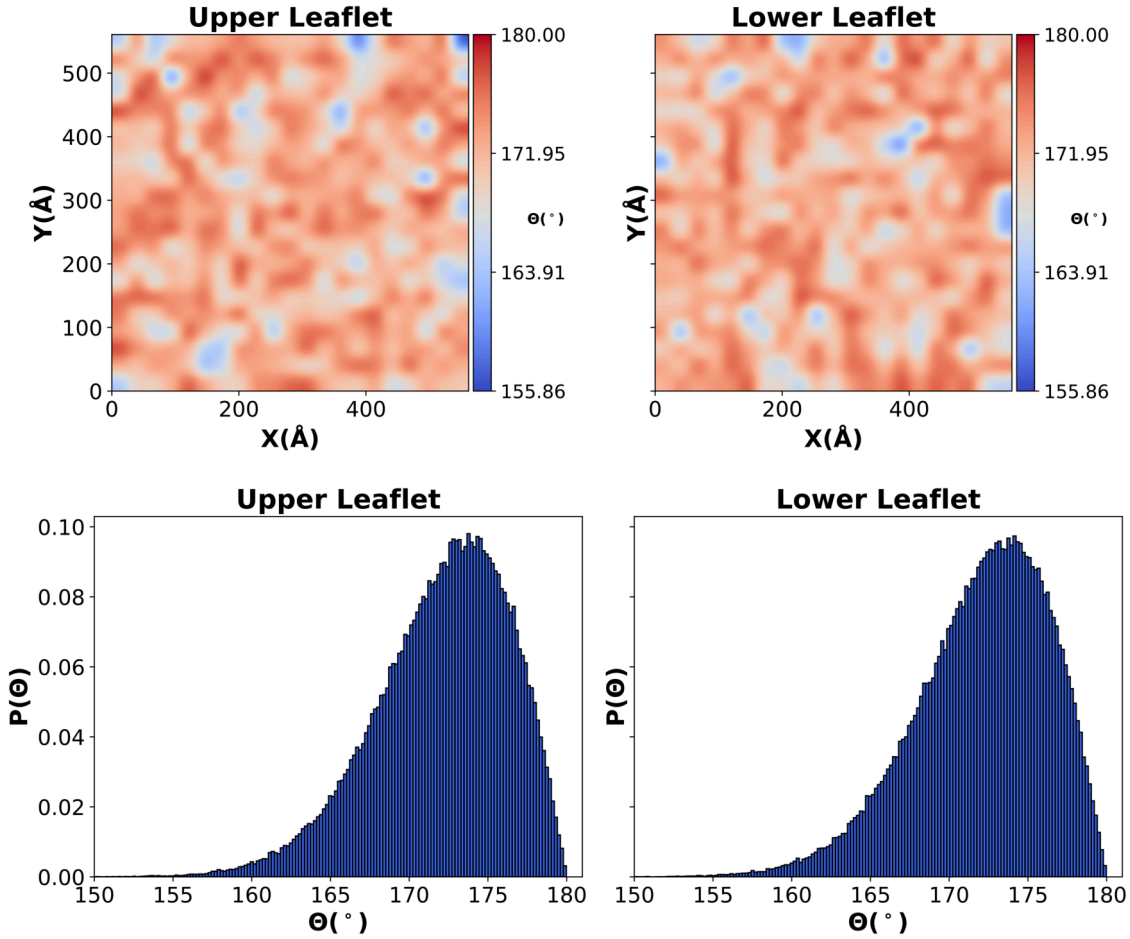

Figure S29: Tail tilt heatmap over the surface of the POPE:POPG membrane (top), obtained by averaging the last ns of trajectory and tail tilt probability density function for the POPE:POPG membrane (bottom). The distribution is obtained by just considering the statistically independent frames throughout all the trajectory.

A.3.5 Membrane Thickness

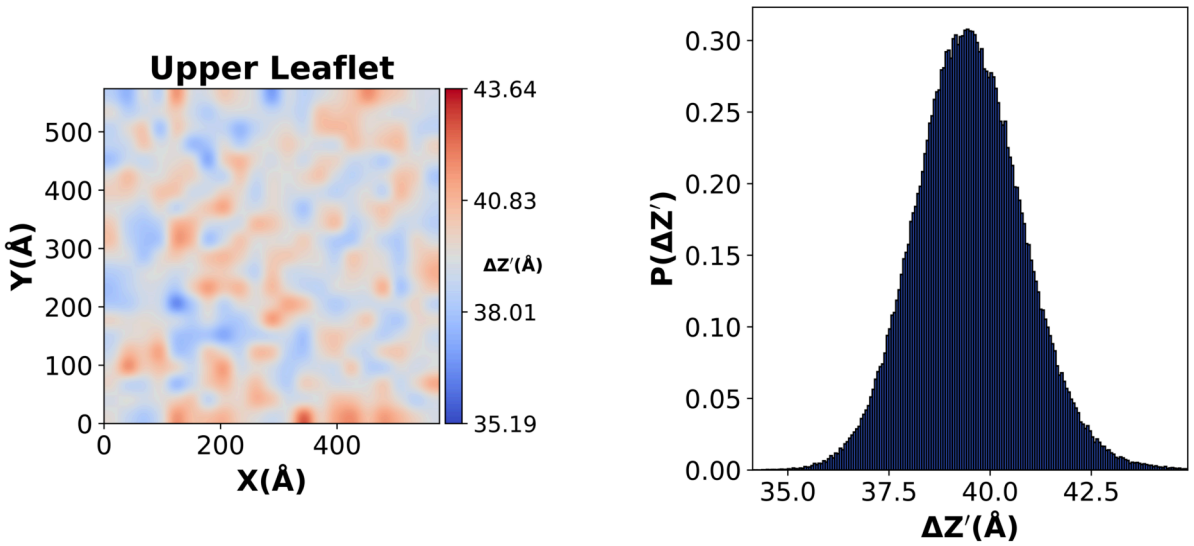

Figure S30: Thickness heatmap over the surface of the POPC membrane (left), obtained by averaging the last ns of trajectory and thickness probability density function for the POPC membrane (right). The distribution is obtained by just considering the statistically independent frames throughout all the trajectory.

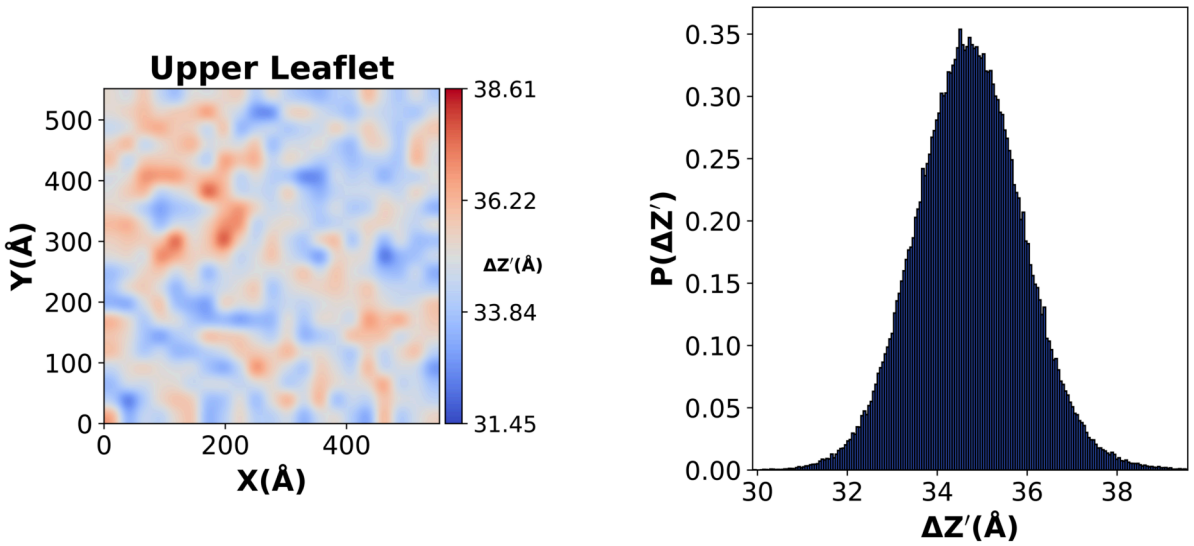

Figure S31: Thickness heatmap over the surface of the DLPC membrane (left), obtained by averaging the last ns of trajectory and thickness probability density function for the DLPC membrane (right). The distribution is obtained by just considering the statistically independent frames throughout all the trajectory.

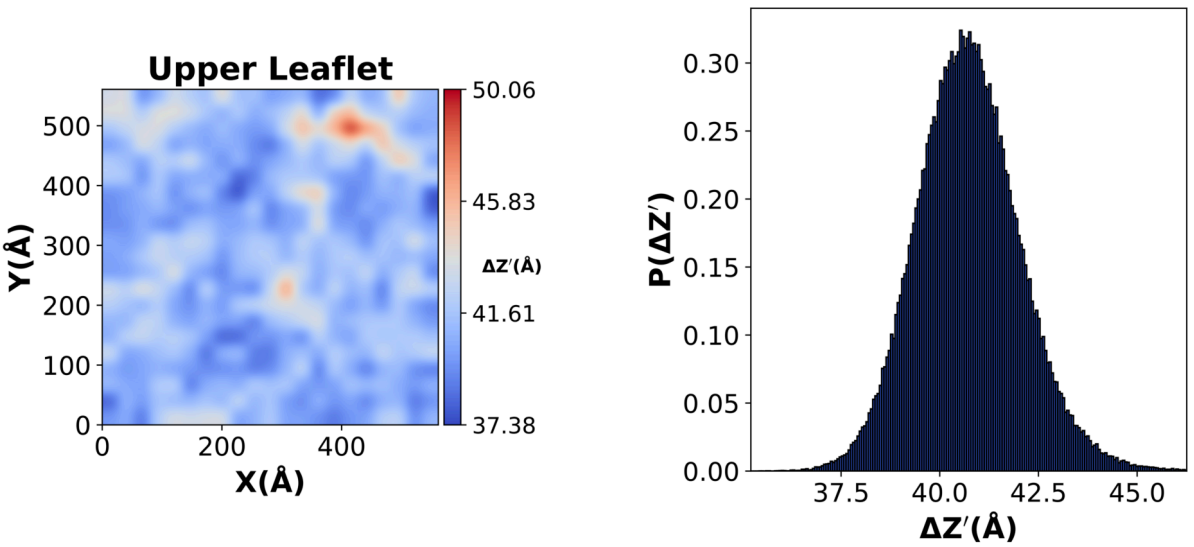

Figure S32: Thickness heatmap over the surface of the POPE:POPG membrane (left), obtained by averaging the last ns of trajectory and thickness probability density function for the POPE:POPG membrane (right). The distribution is obtained by just considering the statistically independent frames throughout all the trajectory.

A.3.6 Singular Value Decomposition Analyses

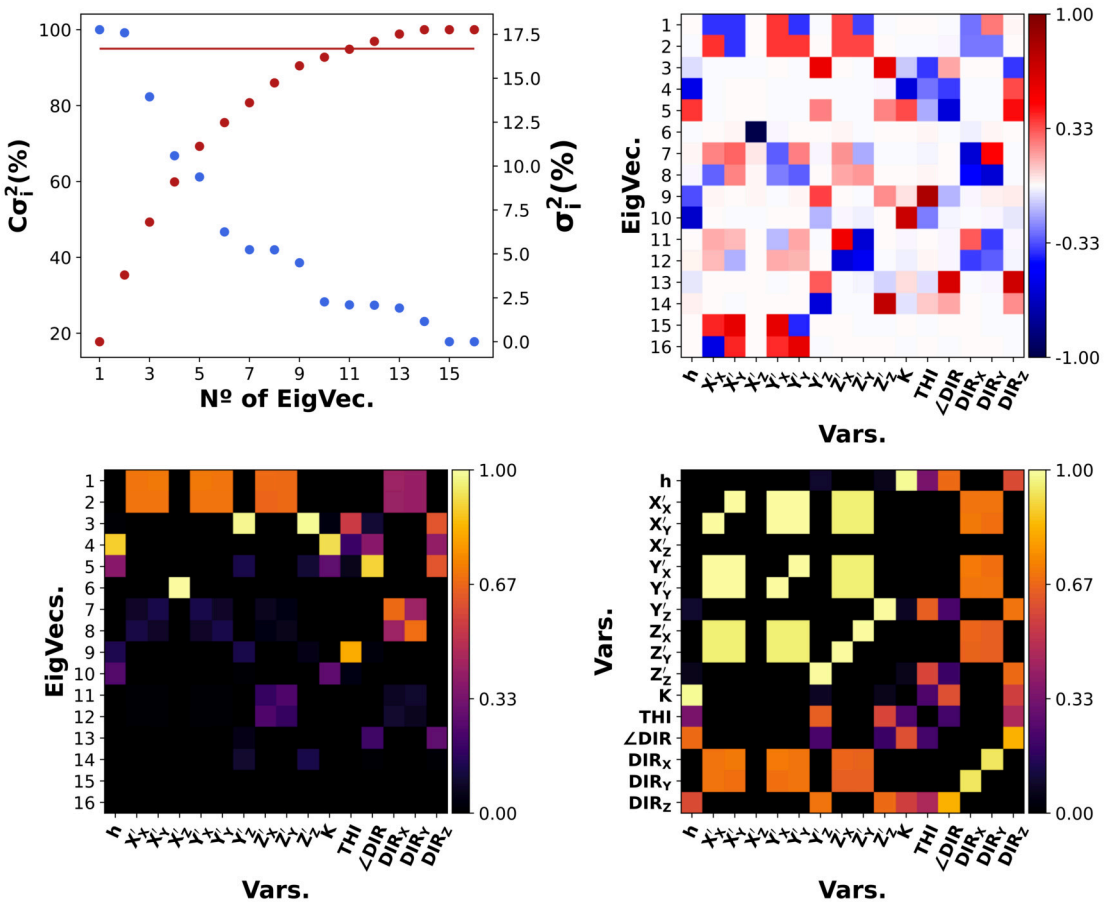

Figure S33: Results of the complete SVD analysis for the POPC membrane. Starting from top left and going clockwise: Cumulative (red, red line 95% variance) and explained (blue) variance per eigenvector, V^T Matrix, Coupling Matrix and Relevance Matrix.

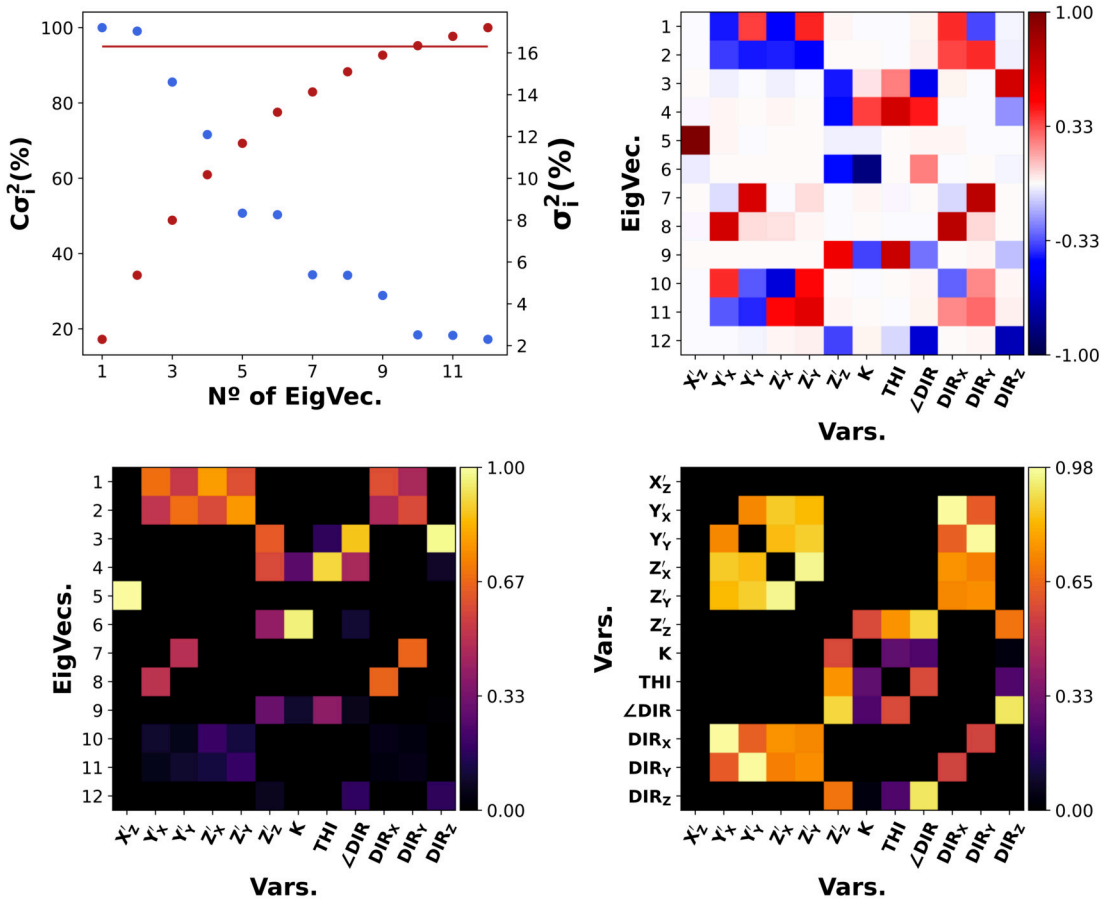

Figure S34: Results of the minimal SVD analysis for the POPC membrane. Starting from top left and going clockwise: Cumulative (red, red line 95% variance) and explained (blue) variance per eigenvector, V^T Matrix, Coupling Matrix and Relevance Matrix.

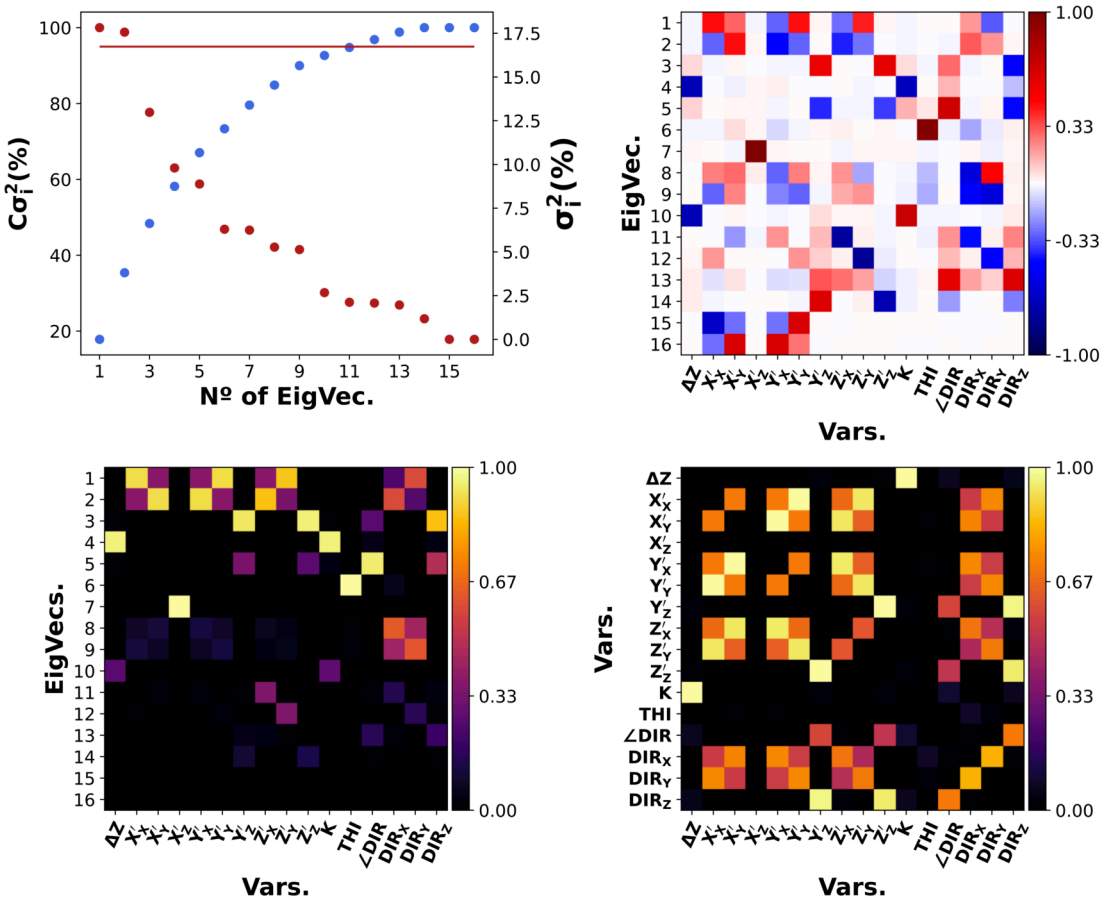

Figure S35: Results of the complete SVD analysis for the DLPC membrane. Starting from top left and going clockwise: Cumulative (red, red line 95% variance) and explained (blue) variance per eigenvector, V^T Matrix, Coupling Matrix and Relevance Matrix.

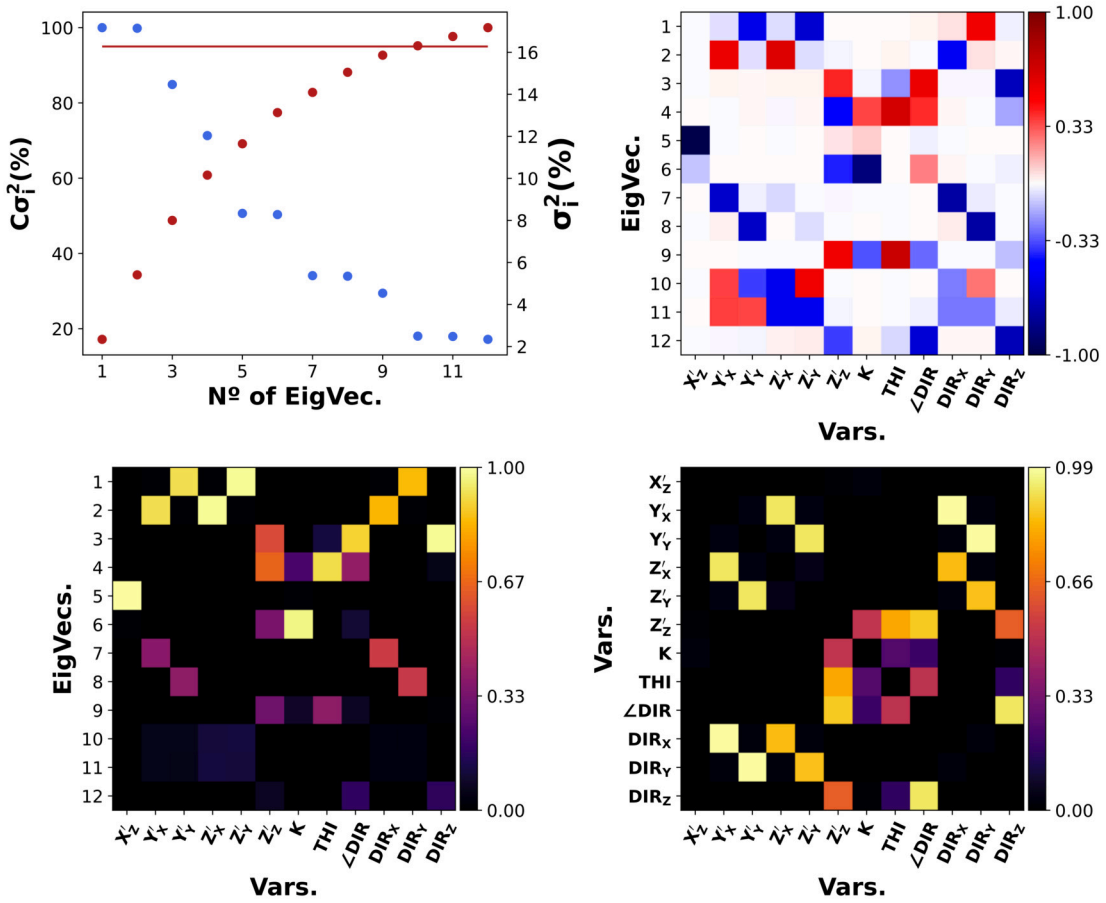

Figure S36: Results of the minimal SVD analysis for the DLPC membrane. Starting from top left and going clockwise: Cumulative (red, red line 95% variance) and explained (blue) variance per eigenvector, V^T Matrix, Coupling Matrix and Relevance Matrix.

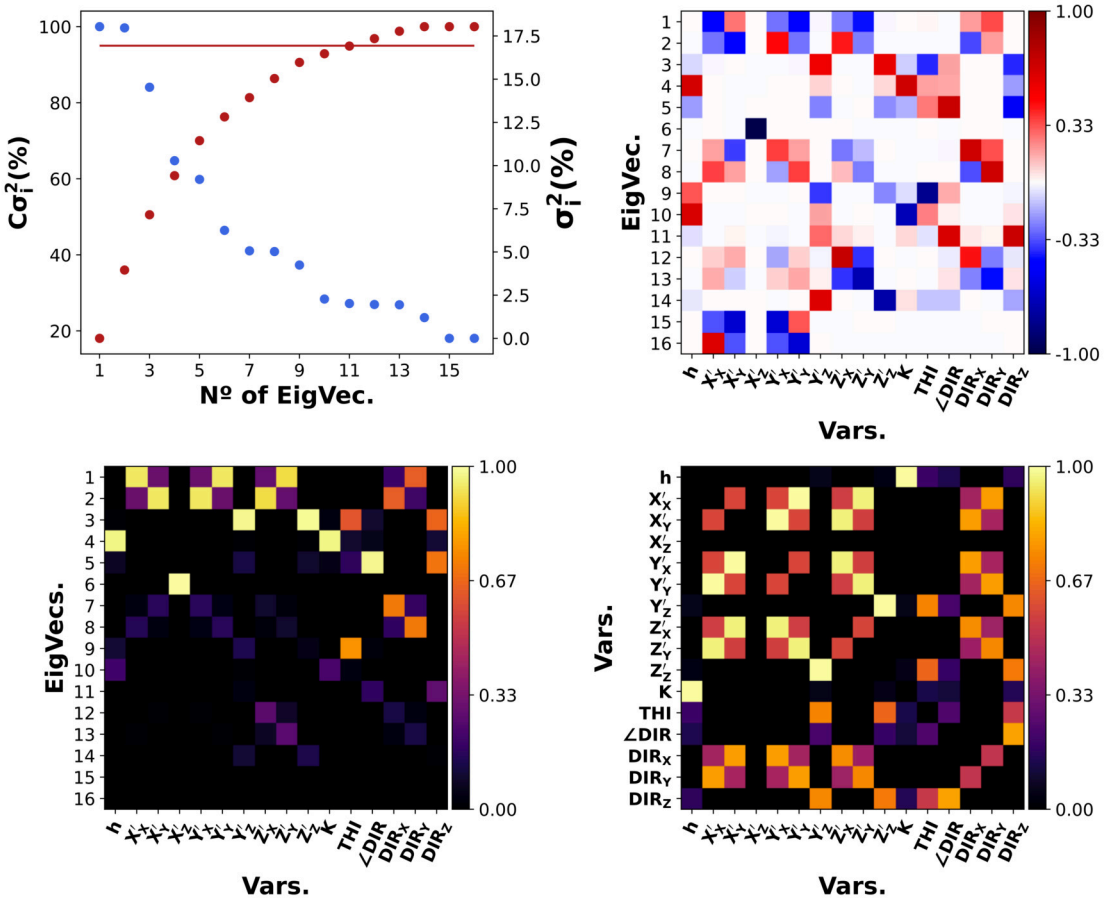

Figure S37: Results of the complete SVD analysis for the POPE:POPG membrane. Starting from top left and going clockwise: Cumulative (red, red line 95% variance) and explained (blue) variance per eigenvector, V^T Matrix, Coupling Matrix and Relevance Matrix.

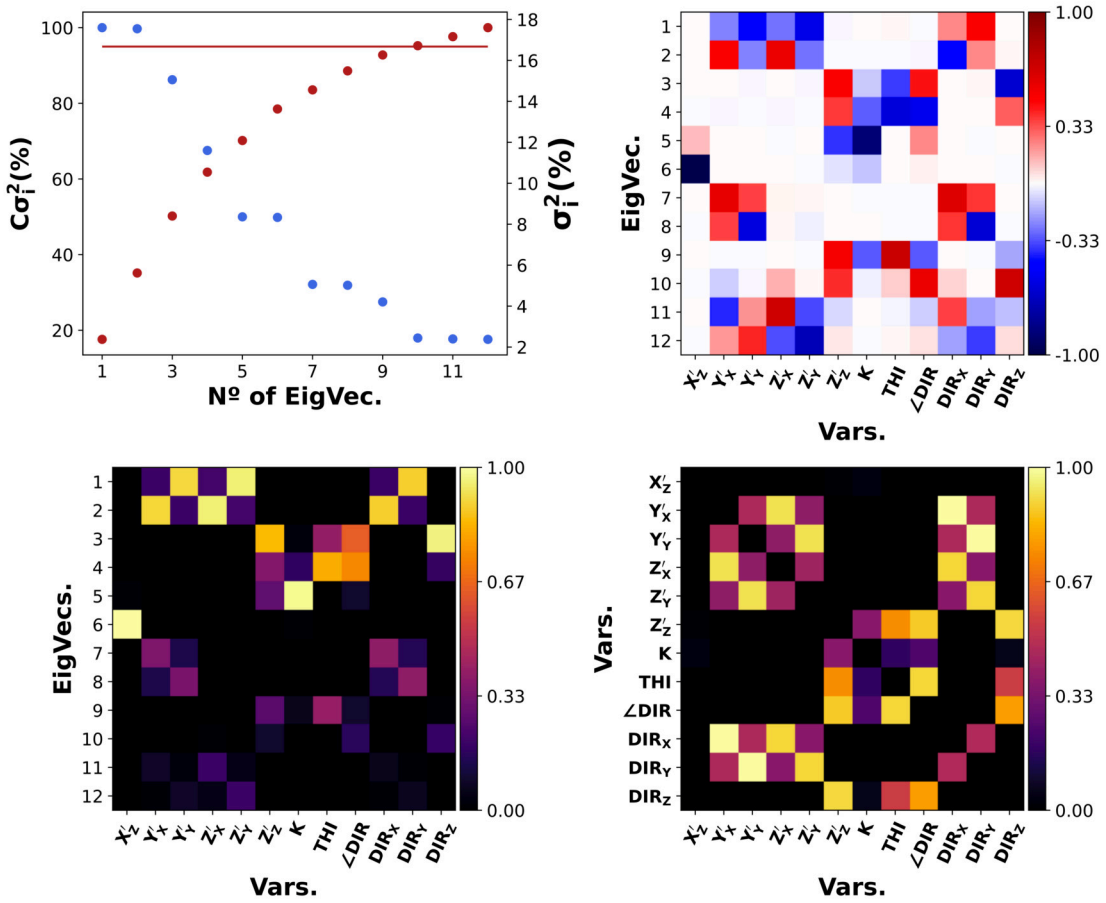

Figure S38: Results of the minimal SVD analysis for the POPE:POPG membrane. Starting from top left and going clockwise: Cumulative (red, red line 95% variance) and explained (blue) variance per eigenvector, V^T Matrix, Coupling Matrix and Relevance Matrix.

A.3.7 Projection of Eigenvector over Membrane

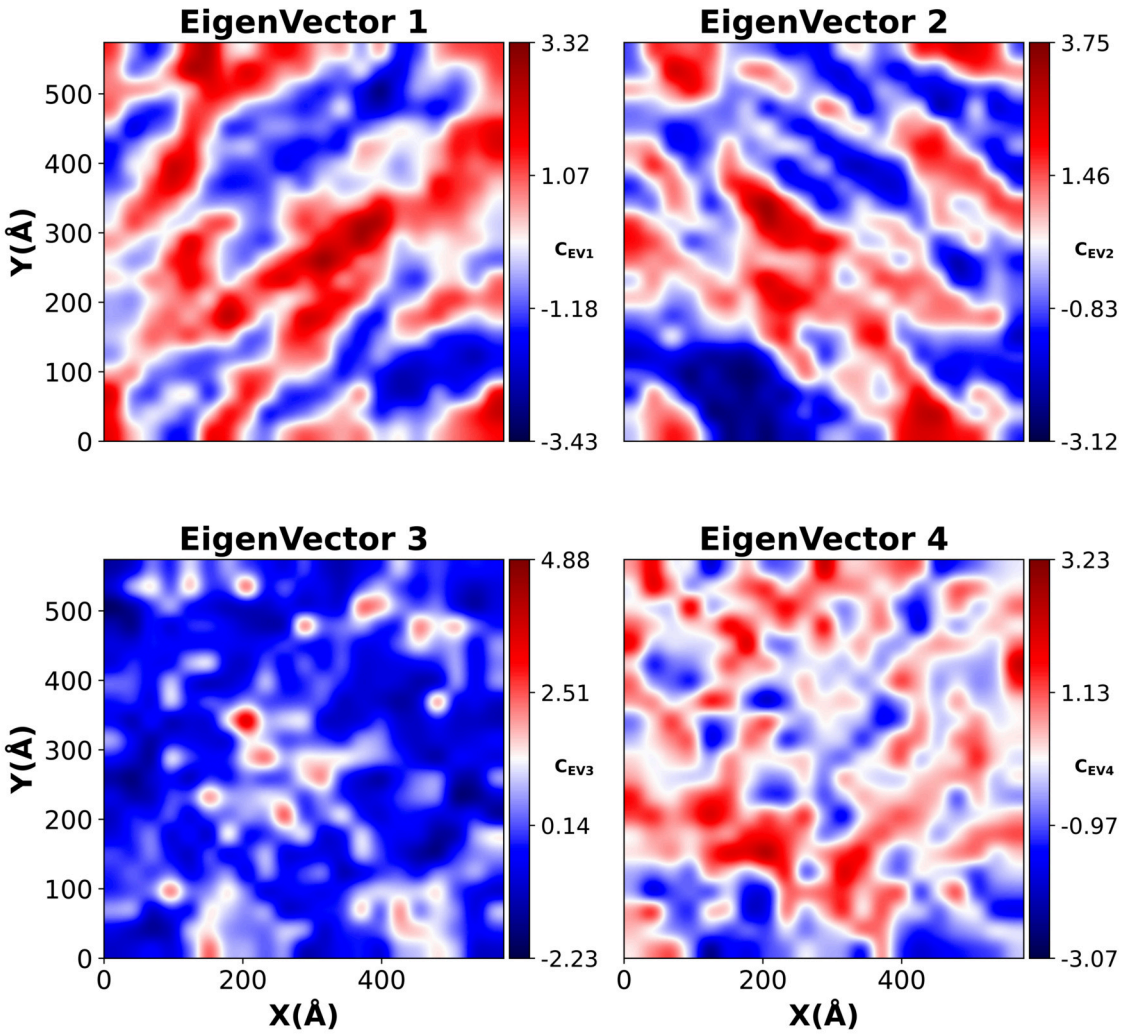

Figure S39: Projection of the first four eigenvectors resultant of the reduced SVD analysis on the surface of the POPC membrane in the last frame of the trajectory.

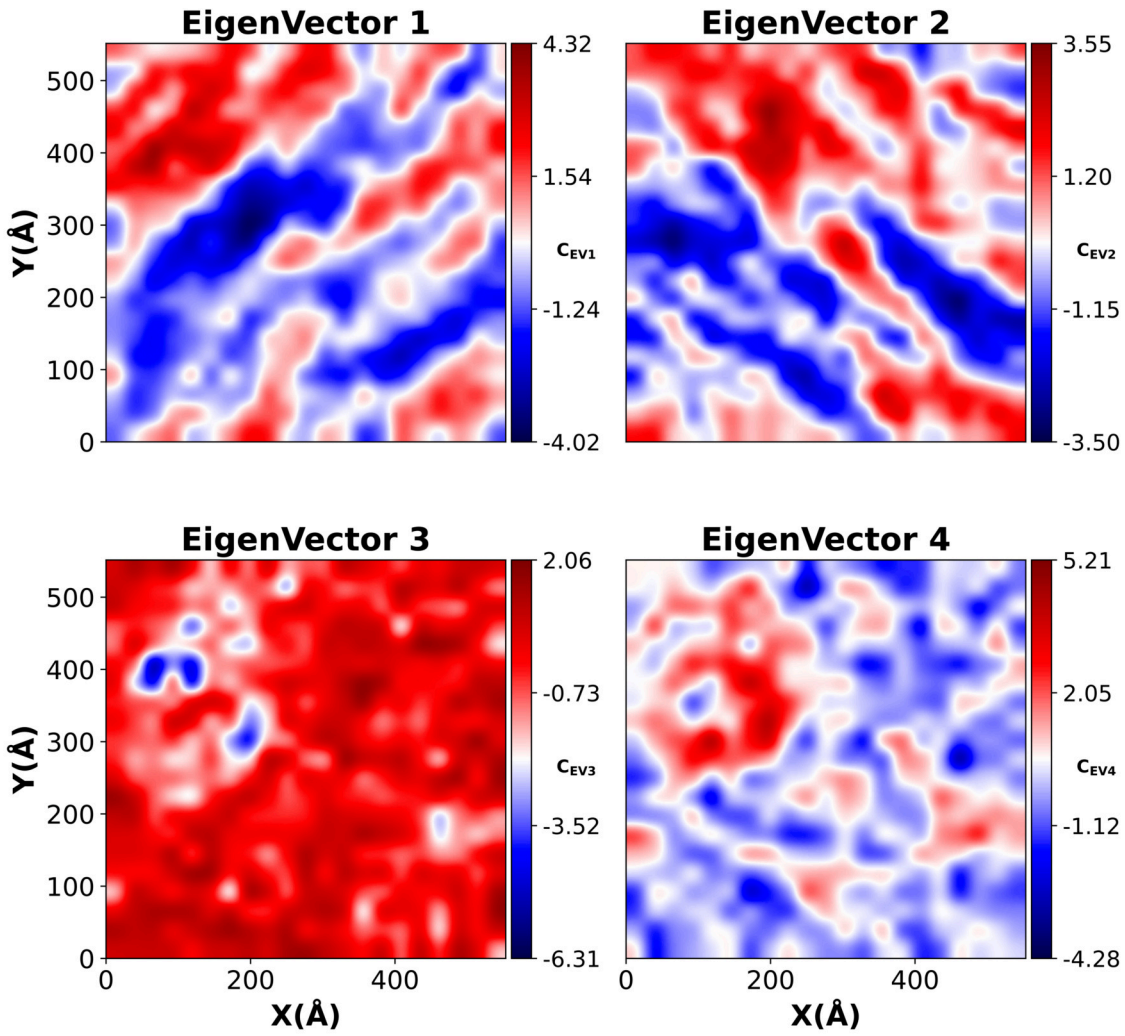

Figure S40: Projection of the first four eigenvectors resultant of the reduced SVD analysis on the surface of the DLPC membrane in the last frame of the trajectory.

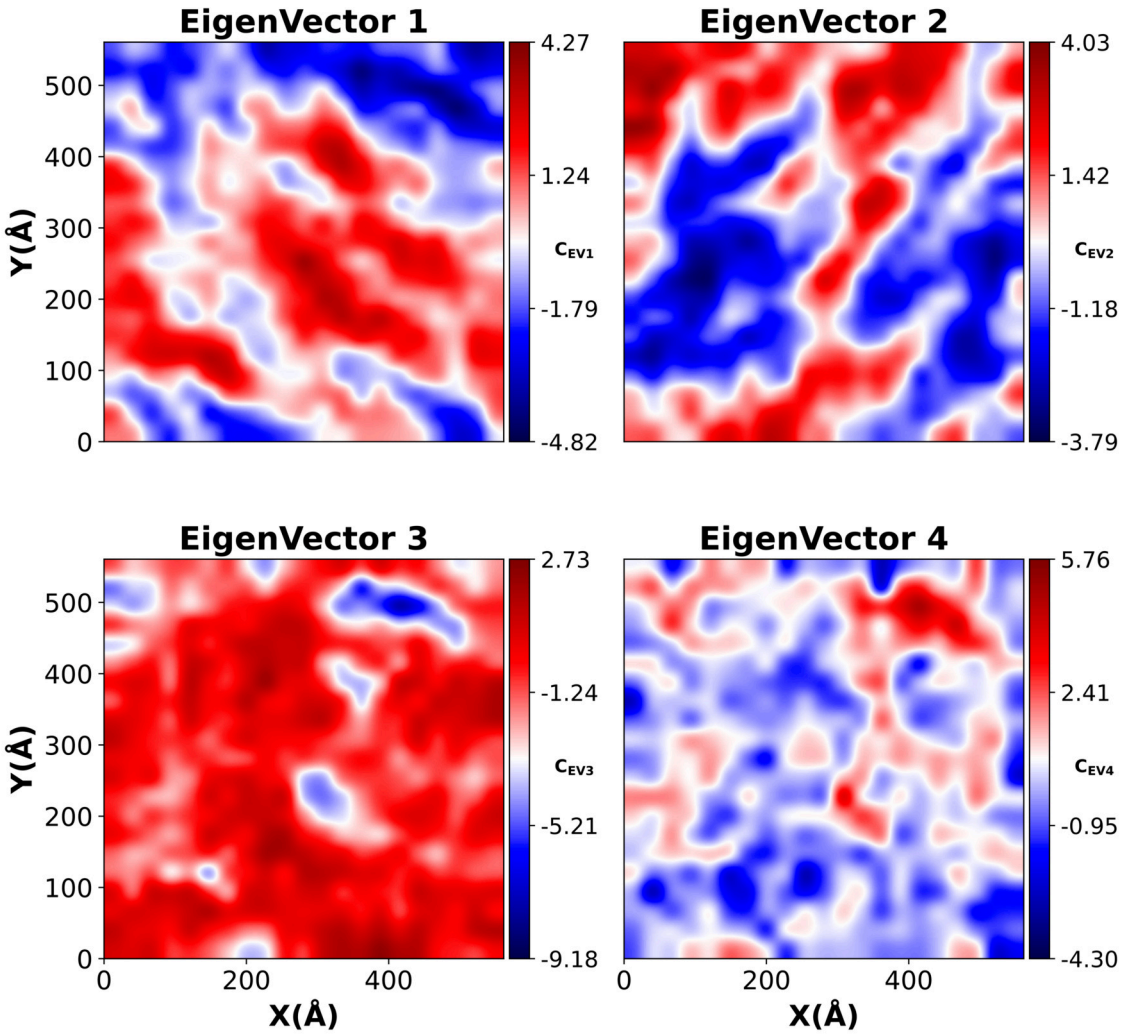

Figure S41: Projection of the first four eigenvectors resultant of the reduced SVD analysis on the surface of the POPE:POPG membrane in the last frame of the trajectory.

A.4 Supplementary Figures for Section 4.3

A.4.1 Radial Distribution Functions

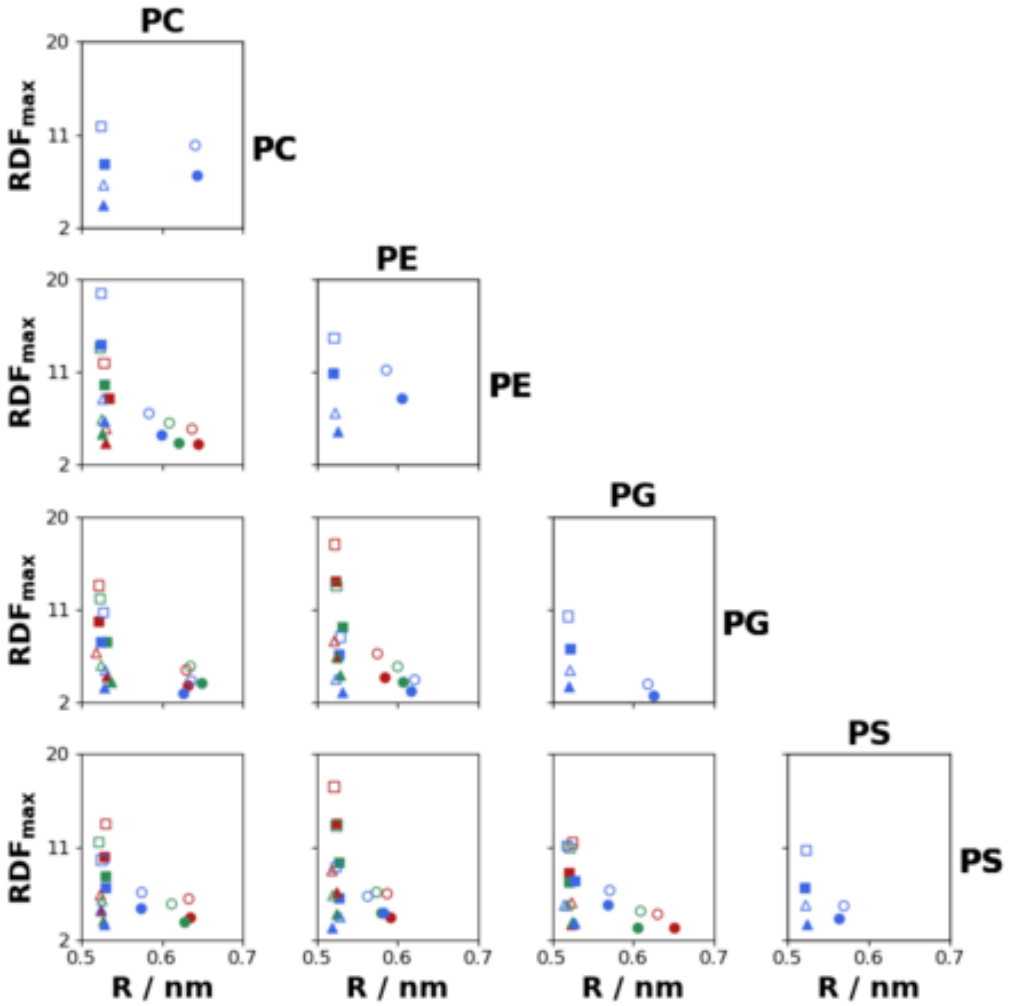

Figure S42: Intensity of the first peak in the radial distribution function (RDF) as a function of the distance to the peak. The RDF was calculated for three types of simulations: coarse-grained without ions (squares), coarse-grained with ions (triangles) and atomistic (circles). The colours used to represent the RDF correspond to the type of lipids: green for different types (row-column), red for the same type (columns) and blue for the same type (rows). The hollow symbols represent the minimum pressure, and the solid symbols represent the maximum pressure.

A.4.2 Intensity of Oscillation Box Plots

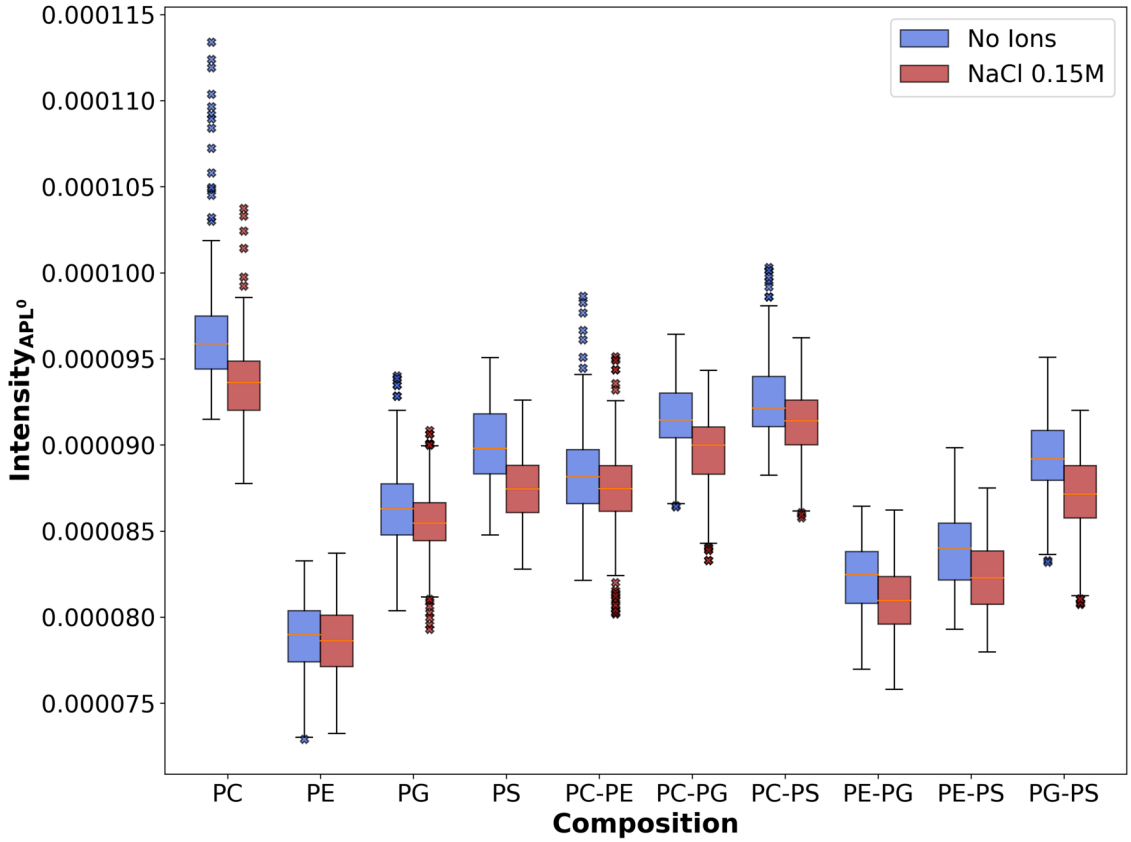

Figure S43: Box plots showing the Area per Lipid response to the US wave of all the simulated systems. The different lipid compositions are indicated in the abscissa, without the 'PO' prefix. The box areas represent the inter-quartile range (iqr = Q3 Q1) for the simulations without additional ions (blue) and with added salt (red), the yellow horizontal line represents the mean, and the whiskers are calculated as Q1 1.5·iqr and Q3+1.5·iqr, respectively. Outliers are represented by an "x" marker.

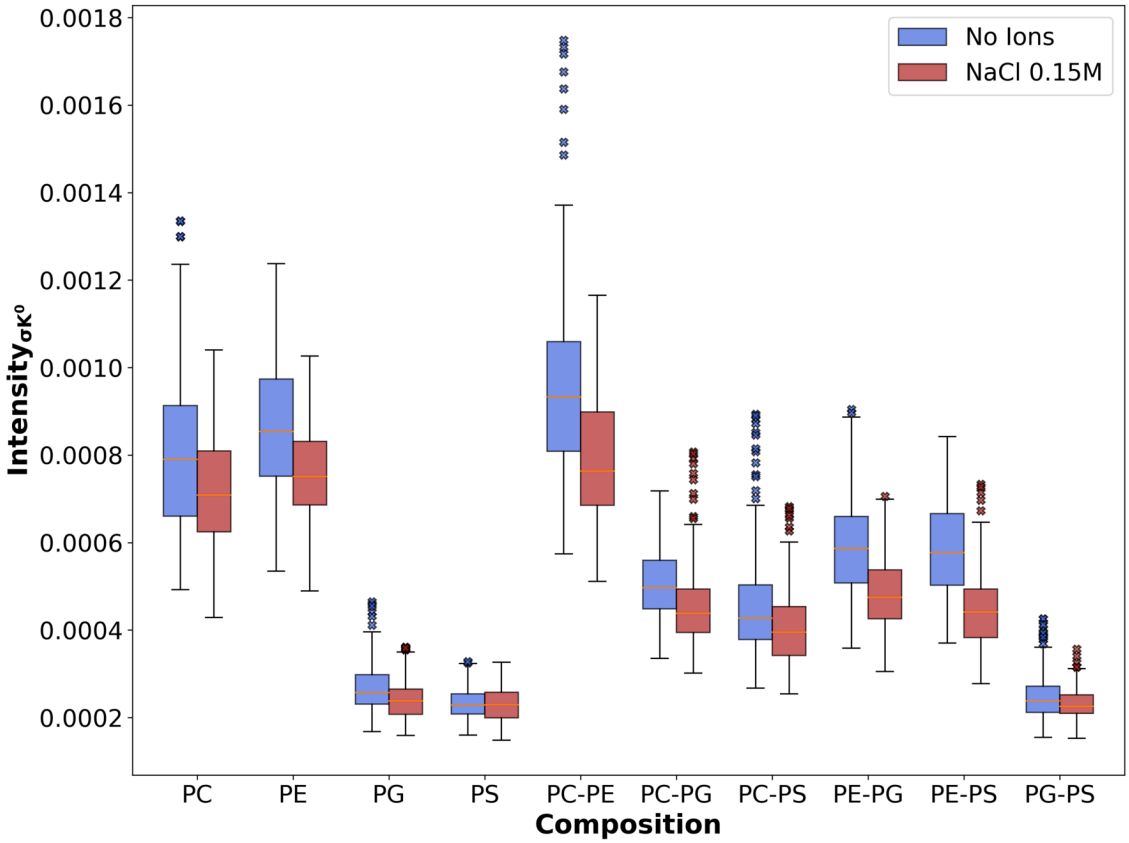

Figure S44: Box plots showing the Curvature response to the US wave of all the simulated systems. The different lipid compositions are indicated in the abscissa, without the 'PO' prefix. The box areas represent the inter-quartile range (iqr = Q3 Q1) for the simulations without additional ions (blue) and with added salt (red), the yellow horizontal line represents the mean, and the whiskers are calculated as Q1 1.5·iqr and Q3+1.5·iqr, respectively. Outliers are represented by an "x" marker.

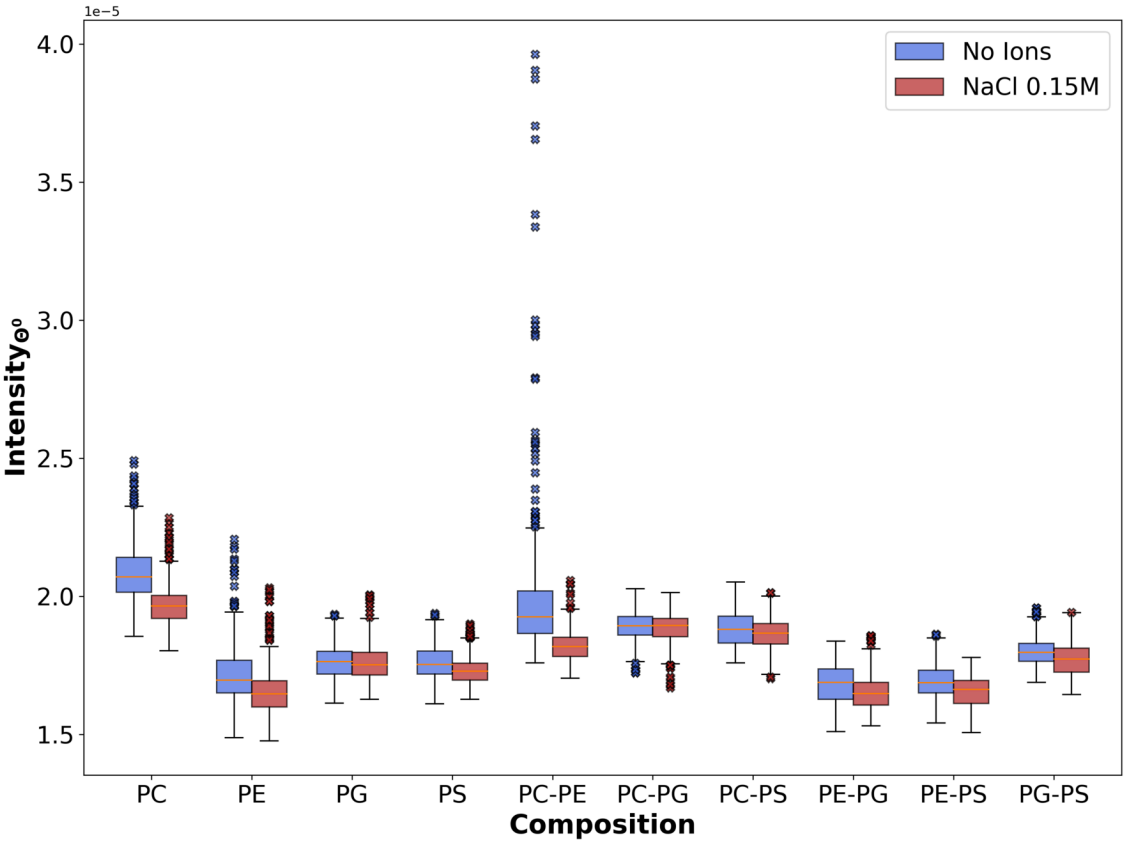

Figure S45: Box plots showing the Tail Tilt response to the US wave of all the simulated systems. The different lipid compositions are indicated in the abscissa, without the 'PO' prefix. The box areas represent the inter-quartile range (iqr = Q3 Q1) for the simulations without additional ions (blue) and with added salt (red), the yellow horizontal line represents the mean, and the whiskers are calculated as Q1 1.5·iqr and Q3+1.5·iqr, respectively. Outliers are represented by an "x" marker.

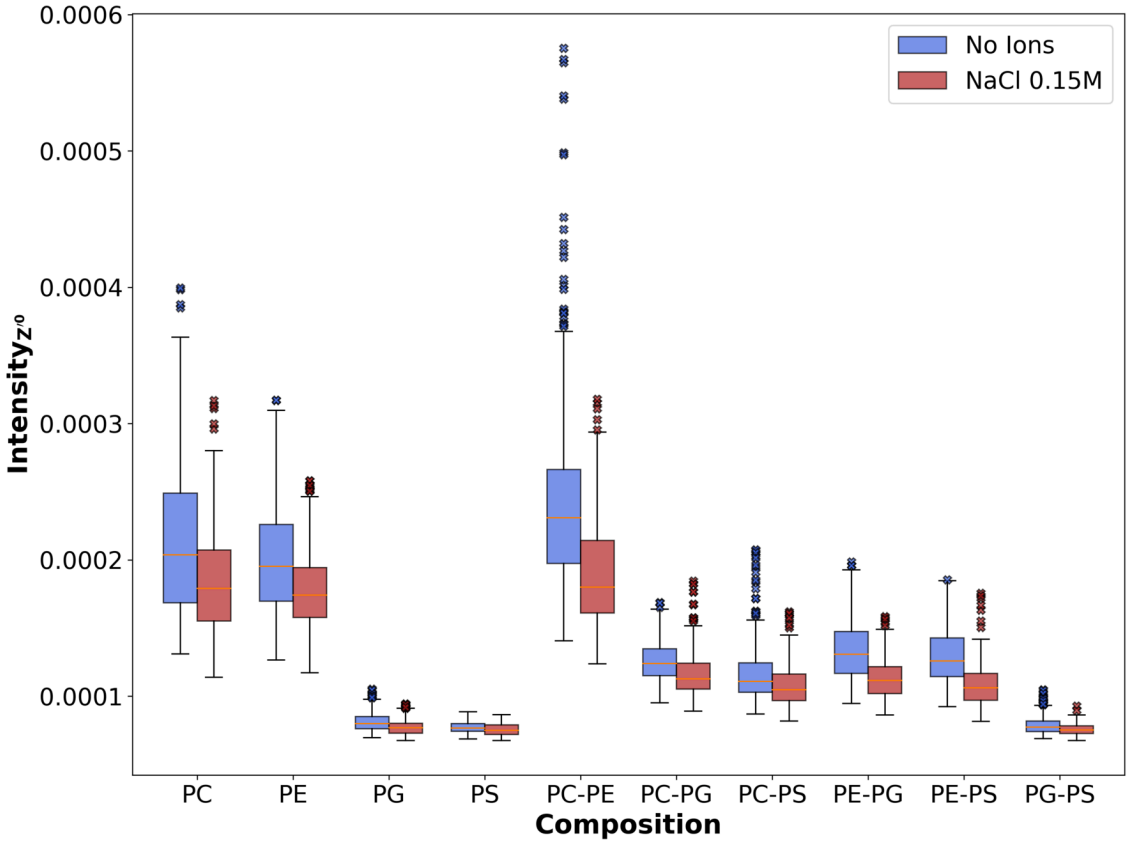

Figure S46: Box plots showing the Thickness response to the US wave of all the simulated systems. The different lipid compositions are indicated in the abscissa, without the 'PO' prefix. The box areas represent the inter-quartile range (iqr = Q3 Q1) for the simulations without additional ions (blue) and with added salt (red), the yellow horizontal line represents the mean, and the whiskers are calculated as Q1 1.5·iqr and Q3+1.5·iqr, respectively. Outliers are represented by an "x" marker.

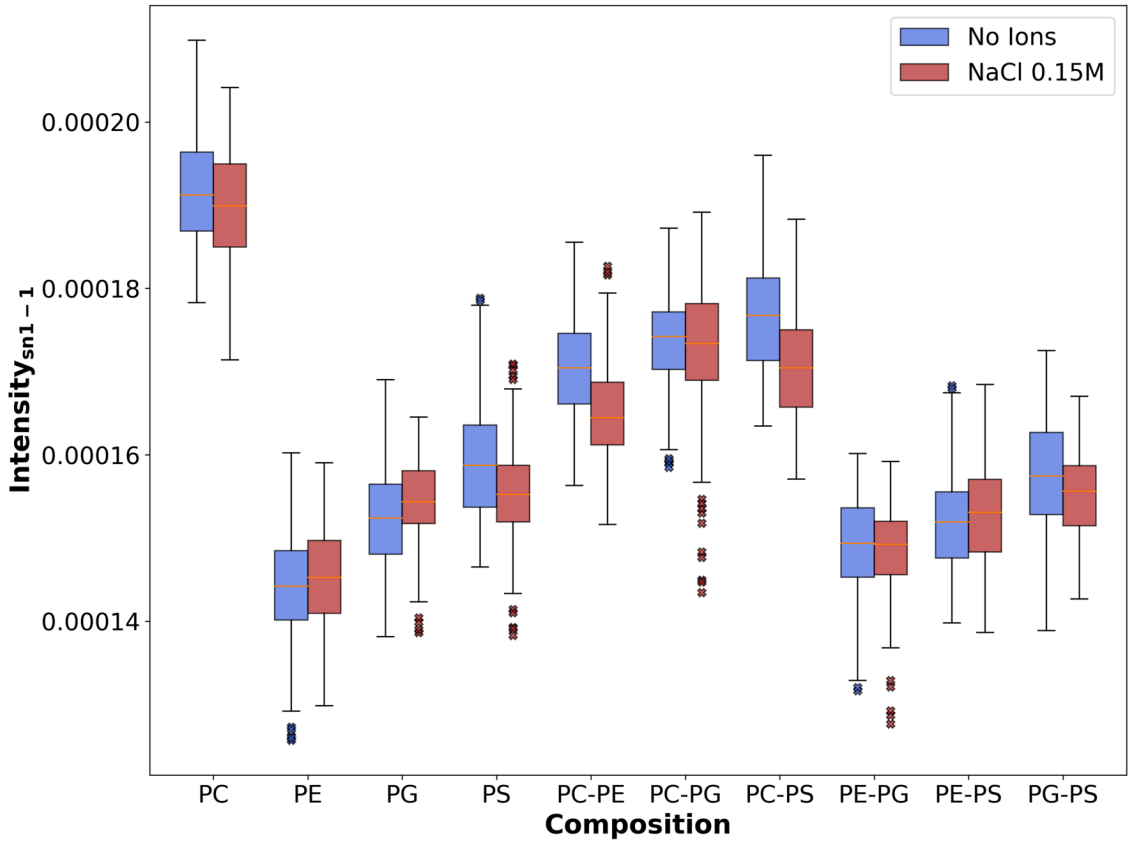

Figure S47: Box plots showing the Segmental Order Parameter, *sn-1* tail first bead, response to the US wave of all the simulated systems. The different lipid compositions are indicated in the abscissa, without the 'PO' prefix. The box areas represent the interquartile range (iqr = Q3 Q1) for the simulations without additional ions (blue) and with added salt (red), the yellow horizontal line represents the mean, and the whiskers are calculated as Q1 1.5·iqr and Q3+1.5·iqr, respectively. Outliers are represented by an "x" marker.

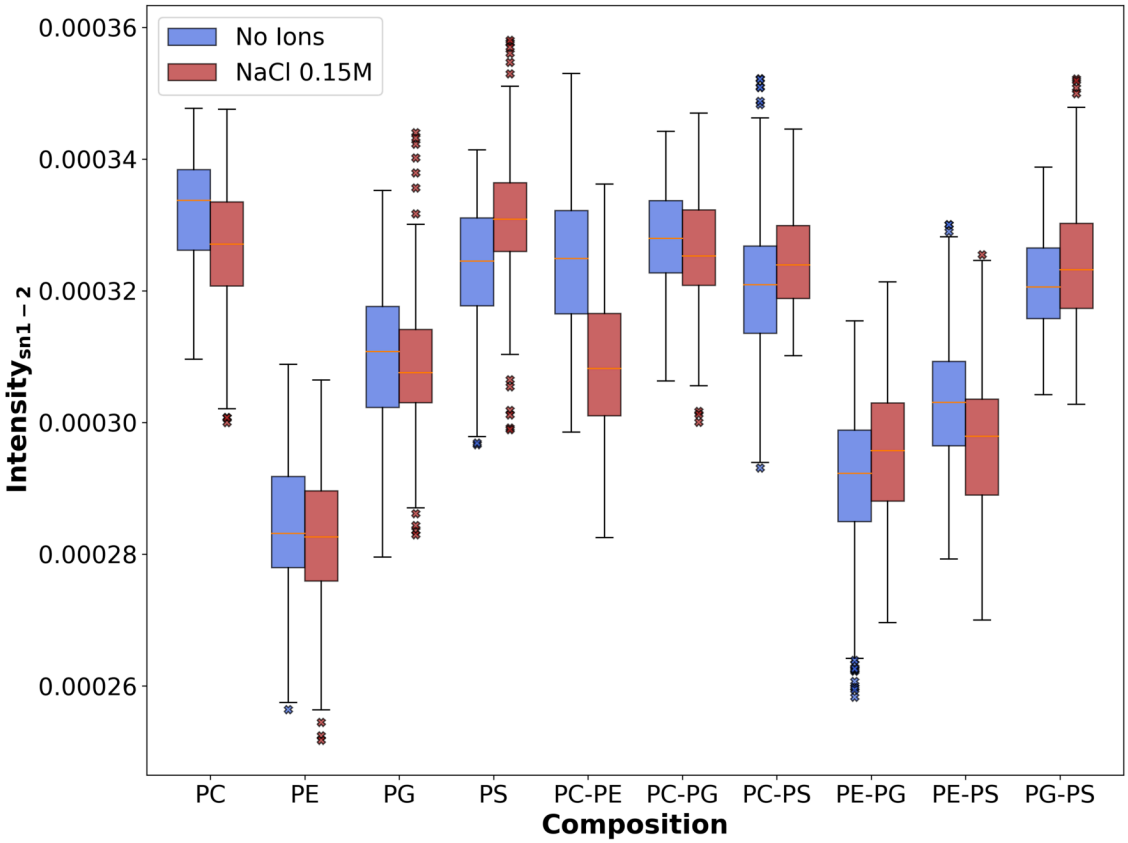

Figure S48: Box plots showing the Segmental Order Parameter, *sn-1* tail second bead, response to the US wave of all the simulated systems. The different lipid compositions are indicated in the abscissa, without the 'PO' prefix. The box areas represent the inter-quartile range (iqr = Q3 Q1) for the simulations without additional ions (blue) and with added salt (red), the yellow horizontal line represents the mean, and the whiskers are calculated as Q1 1.5·iqr and Q3+1.5·iqr, respectively. Outliers are represented by an "x" marker.

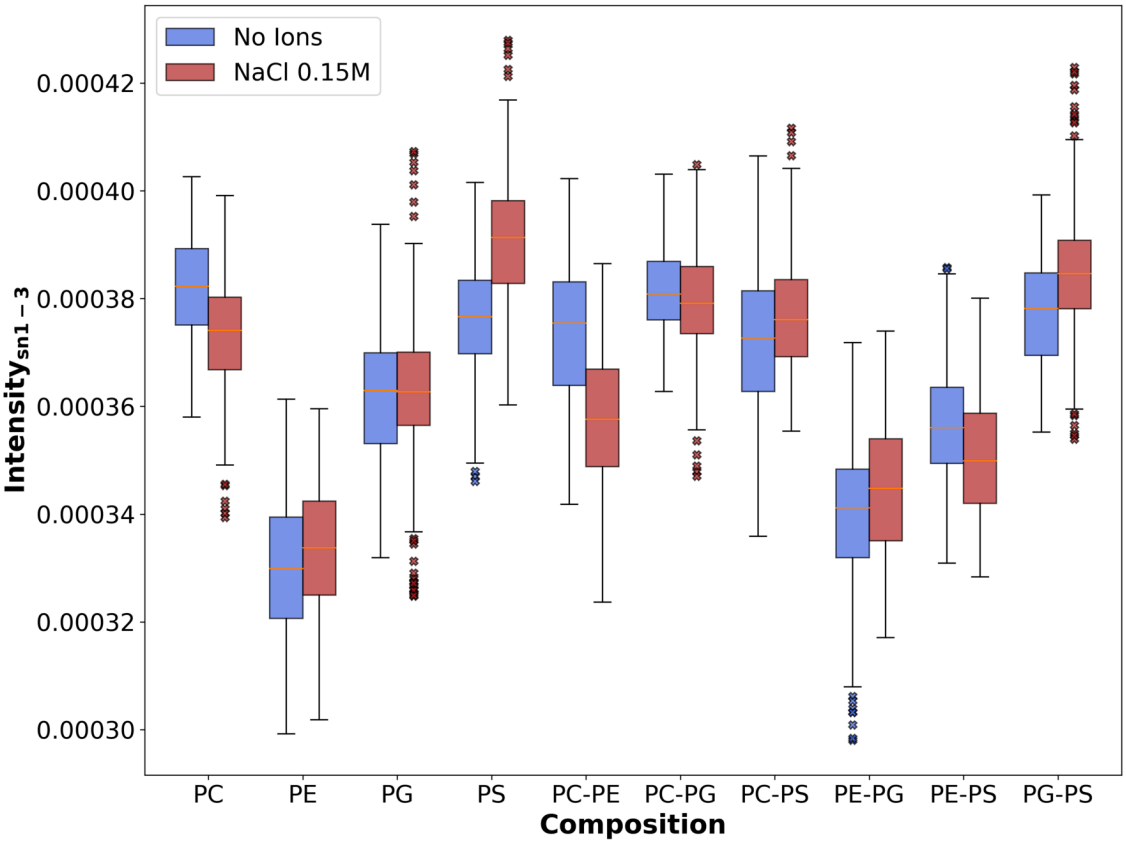

Figure S49: Box plots showing the Segmental Order Parameter, *sn-1* tail third bead, response to the US wave of all the simulated systems. The different lipid compositions are indicated in the abscissa, without the 'PO' prefix. The box areas represent the interquartile range (iqr = Q3 Q1) for the simulations without additional ions (blue) and with added salt (red), the yellow horizontal line represents the mean, and the whiskers are calculated as Q1 1.5·iqr and Q3+1.5·iqr, respectively. Outliers are represented by an "x" marker.

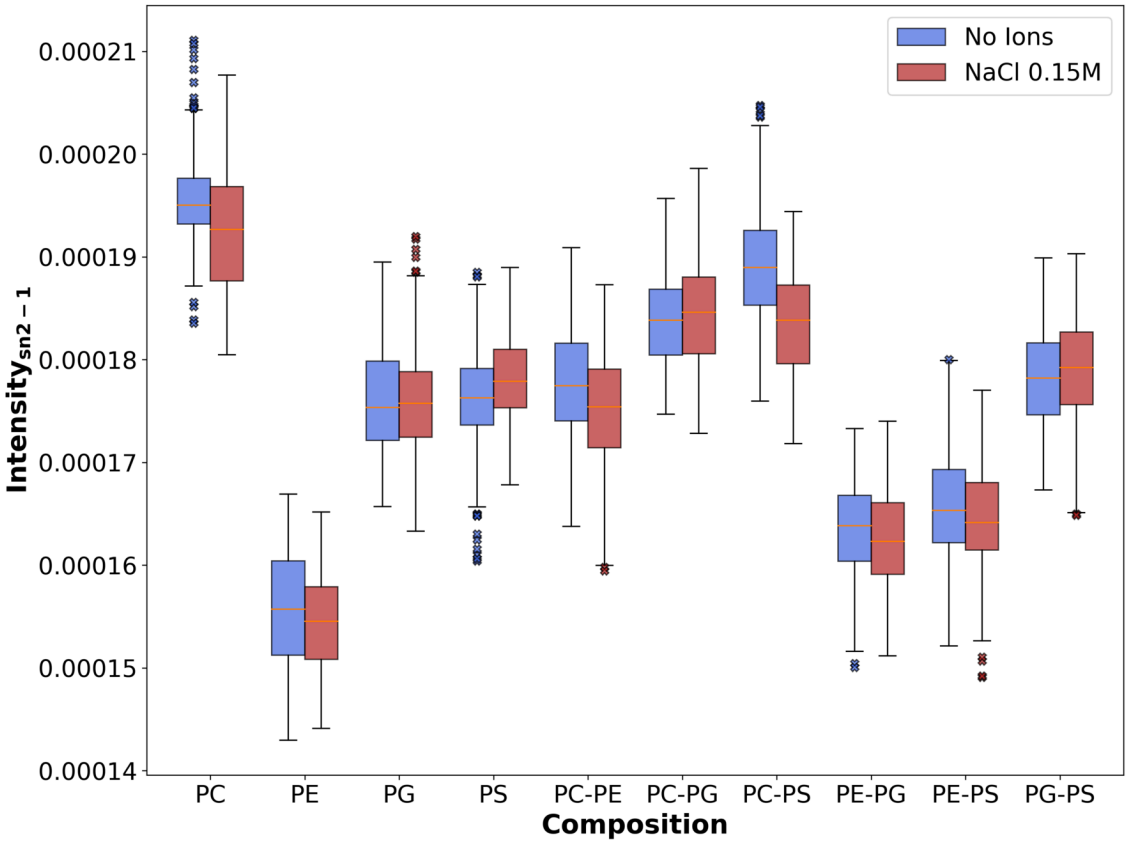

Figure S50: Box plots showing the Segmental Order Parameter, *sn-2* tail first bead, response to the US wave of all the simulated systems. The different lipid compositions are indicated in the abscissa, without the 'PO' prefix. The box areas represent the interquartile range (iqr = Q3 Q1) for the simulations without additional ions (blue) and with added salt (red), the yellow horizontal line represents the mean, and the whiskers are calculated as Q1 1.5·iqr and Q3+1.5·iqr, respectively. Outliers are represented by an "x" marker.

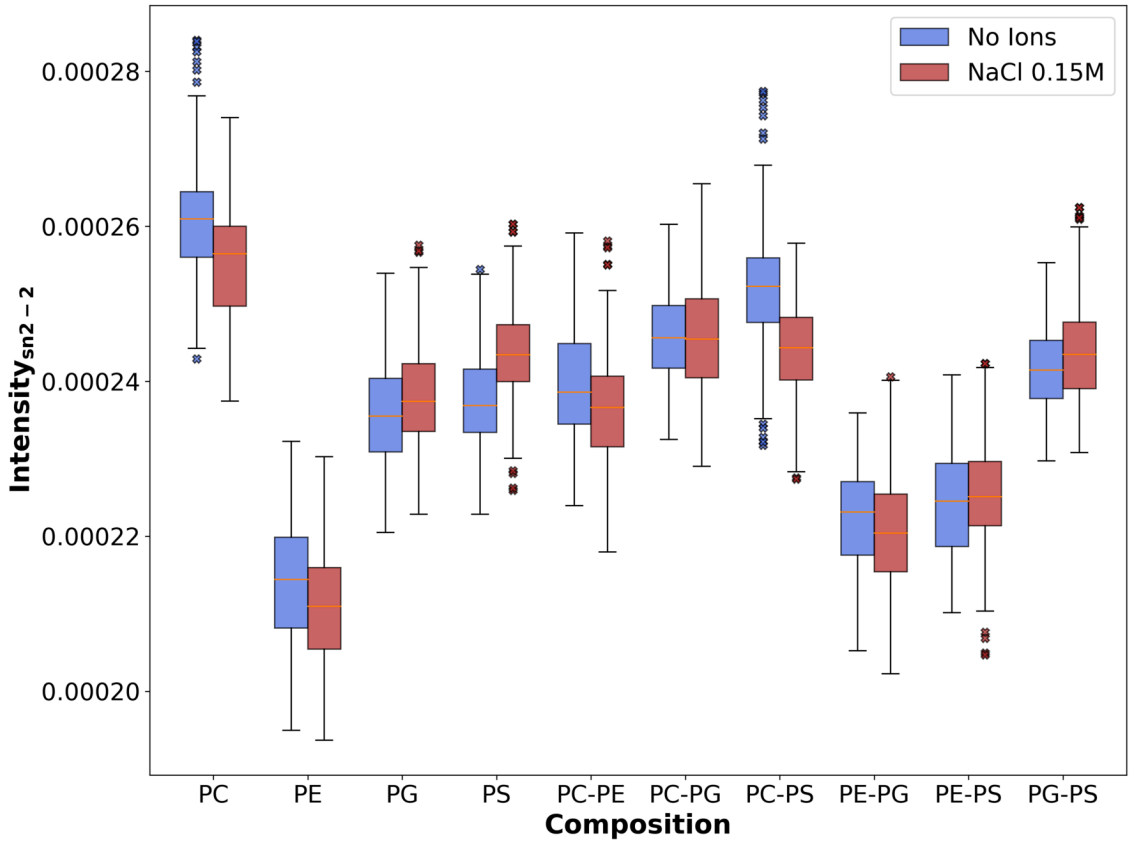

Figure S51: Box plots showing the Segmental Order Parameter, *sn-2* tail second bead, response to the US wave of all the simulated systems. The different lipid compositions are indicated in the abscissa, without the 'PO' prefix. The box areas represent the inter-quartile range (iqr = Q3 Q1) for the simulations without additional ions (blue) and with added salt (red), the yellow horizontal line represents the mean, and the whiskers are calculated as Q1 1.5·iqr and Q3+1.5·iqr, respectively. Outliers are represented by an "x" marker.

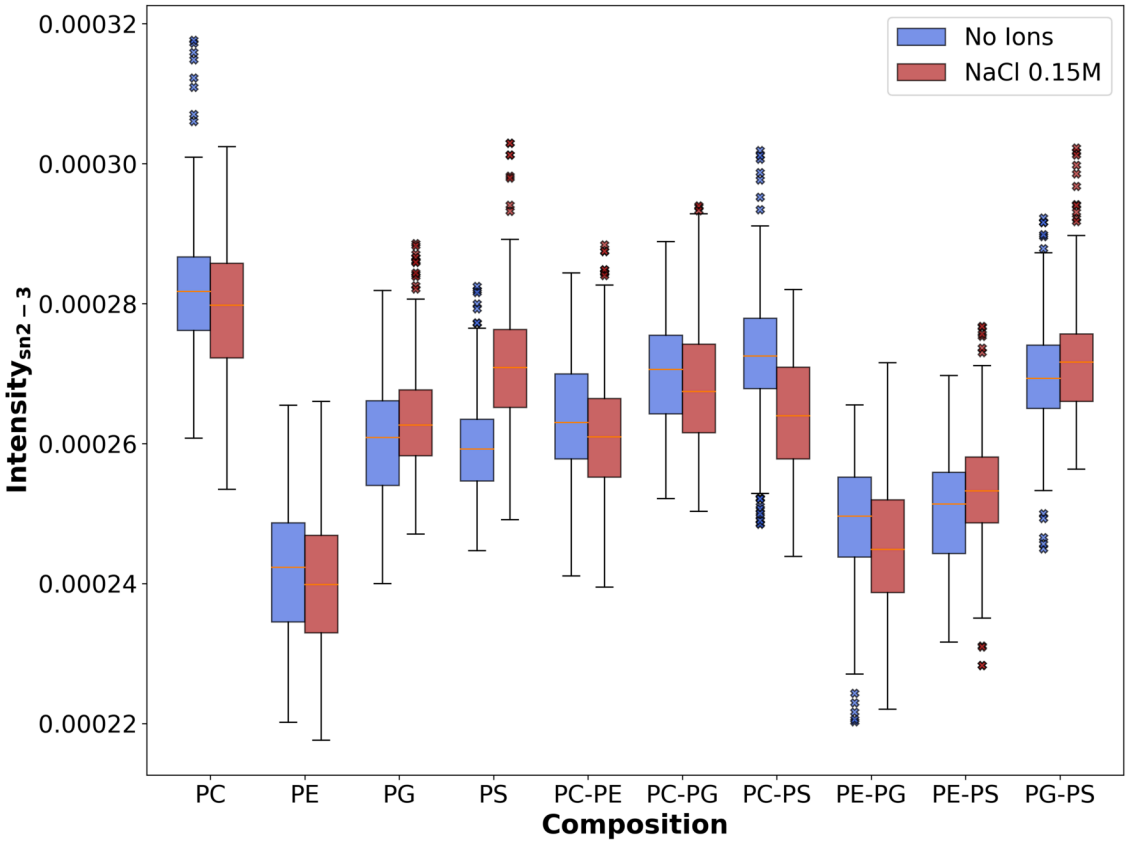

Figure S52: Box plots showing the Segmental Order Parameter, *sn-2* tail third bead, response to the US wave of all the simulated systems. The different lipid compositions are indicated in the abscissa, without the 'PO' prefix. The box areas represent the interquartile range (iqr = Q3 Q1) for the simulations without additional ions (blue) and with added salt (red), the yellow horizontal line represents the mean, and the whiskers are calculated as Q1 1.5·iqr and Q3+1.5·iqr, respectively. Outliers are represented by an "x" marker.

A.4.3 Clustering Analysis

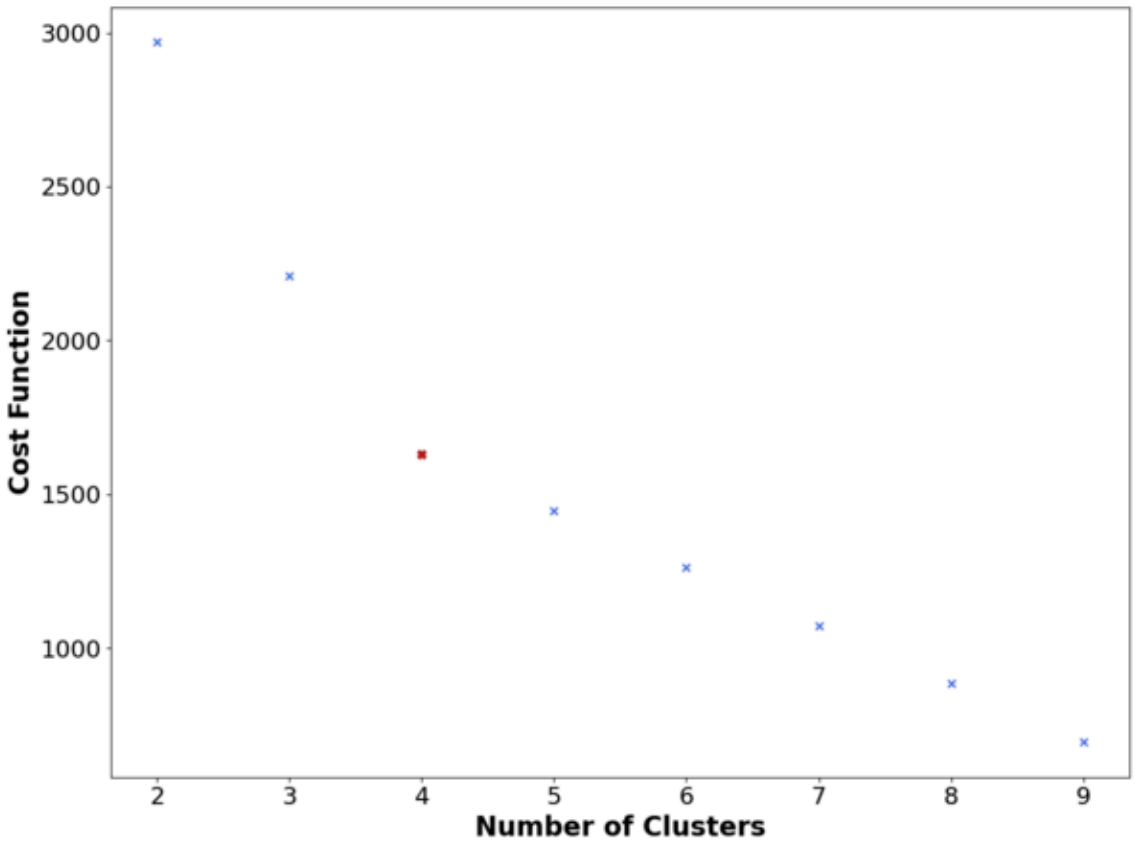

Figure S53: Cost function of the algorithm against number of clusters. The knee of the function was found at 4 clusters, shown as a red 'x' marker.

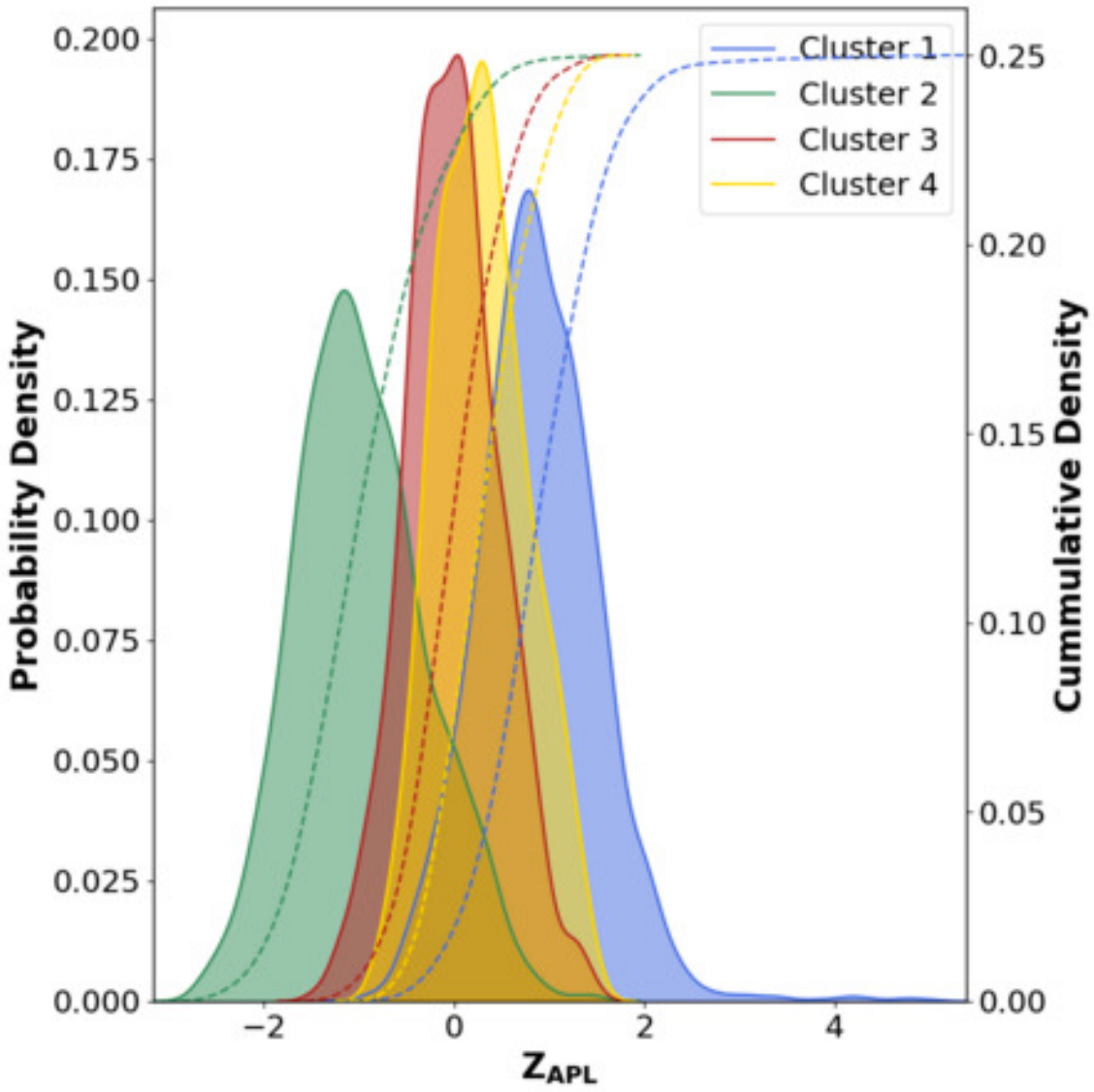

Figure S54: Estimation of the Probability Density Functions for the normalized Area per Lipid, calculated for each cluster separately. Each cluster is shown in one color. The Probability Density Function is shown as a solid line with a shaded area beneath. The Cumulative Density Function is shown as a dashed line.

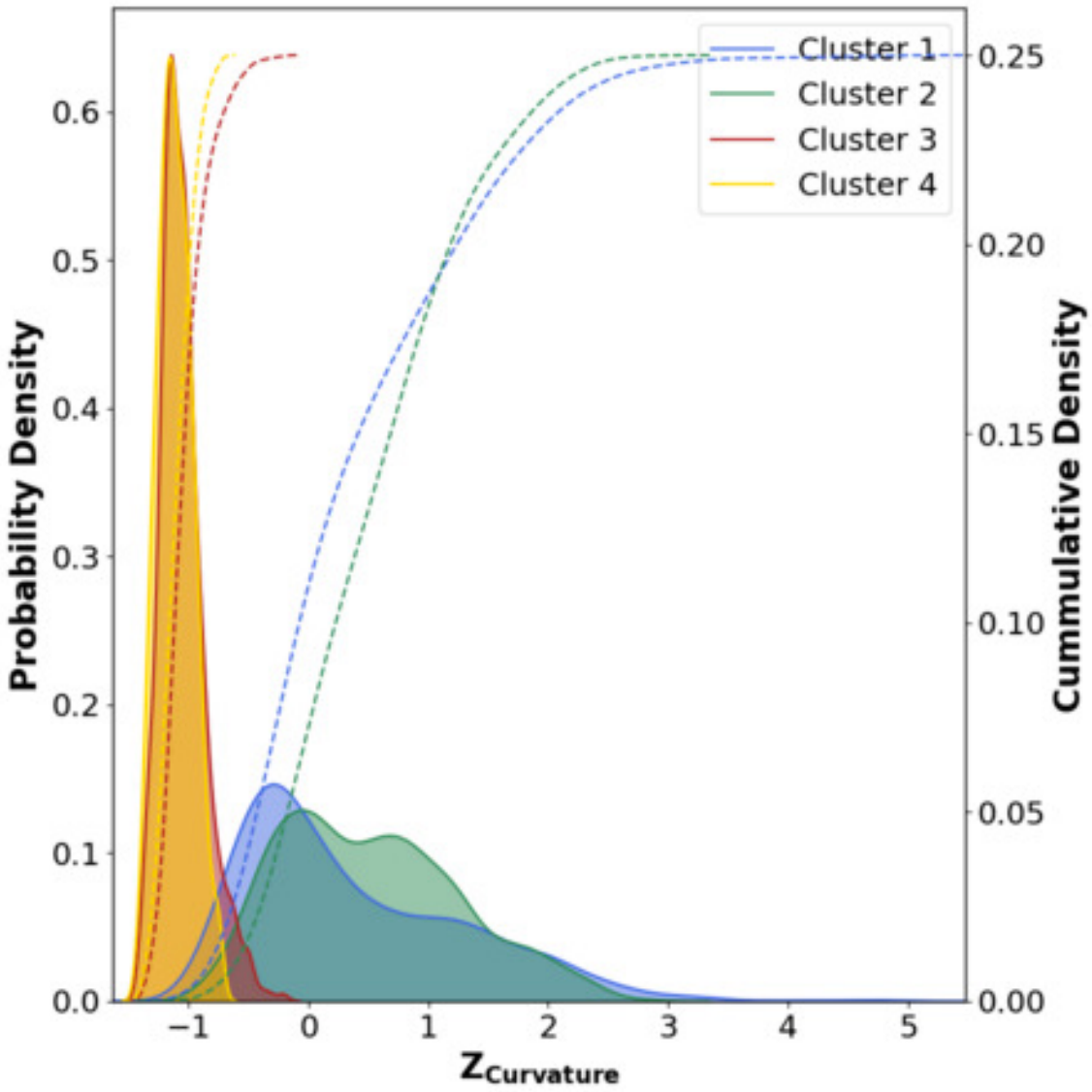

Figure S55: Estimation of the Probability Density Functions for the normalized Curvature, calculated for each cluster separately. Each cluster is shown in one color. The Probability Density Function is shown as a solid line with a shaded area beneath. The Cumulative Density Function is shown as a dashed line.

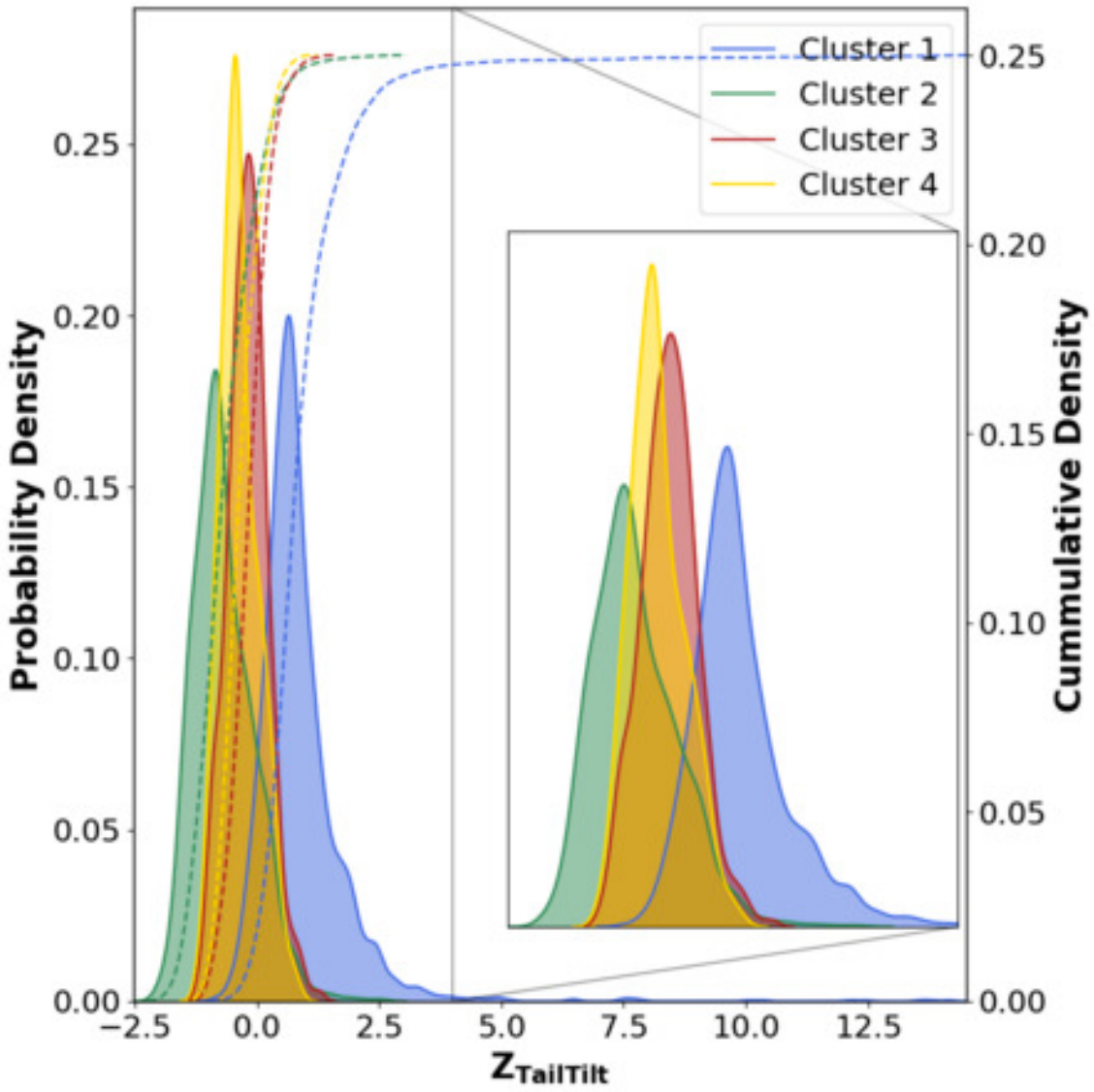

Figure S56: Estimation of the Probability Density Functions for the normalized Tail Tilt, calculated for each cluster separately. Each cluster is shown in one color. The Probability Density Function is shown as a solid line with a shaded area beneath. The Cumulative Density Function is shown as a dashed line.

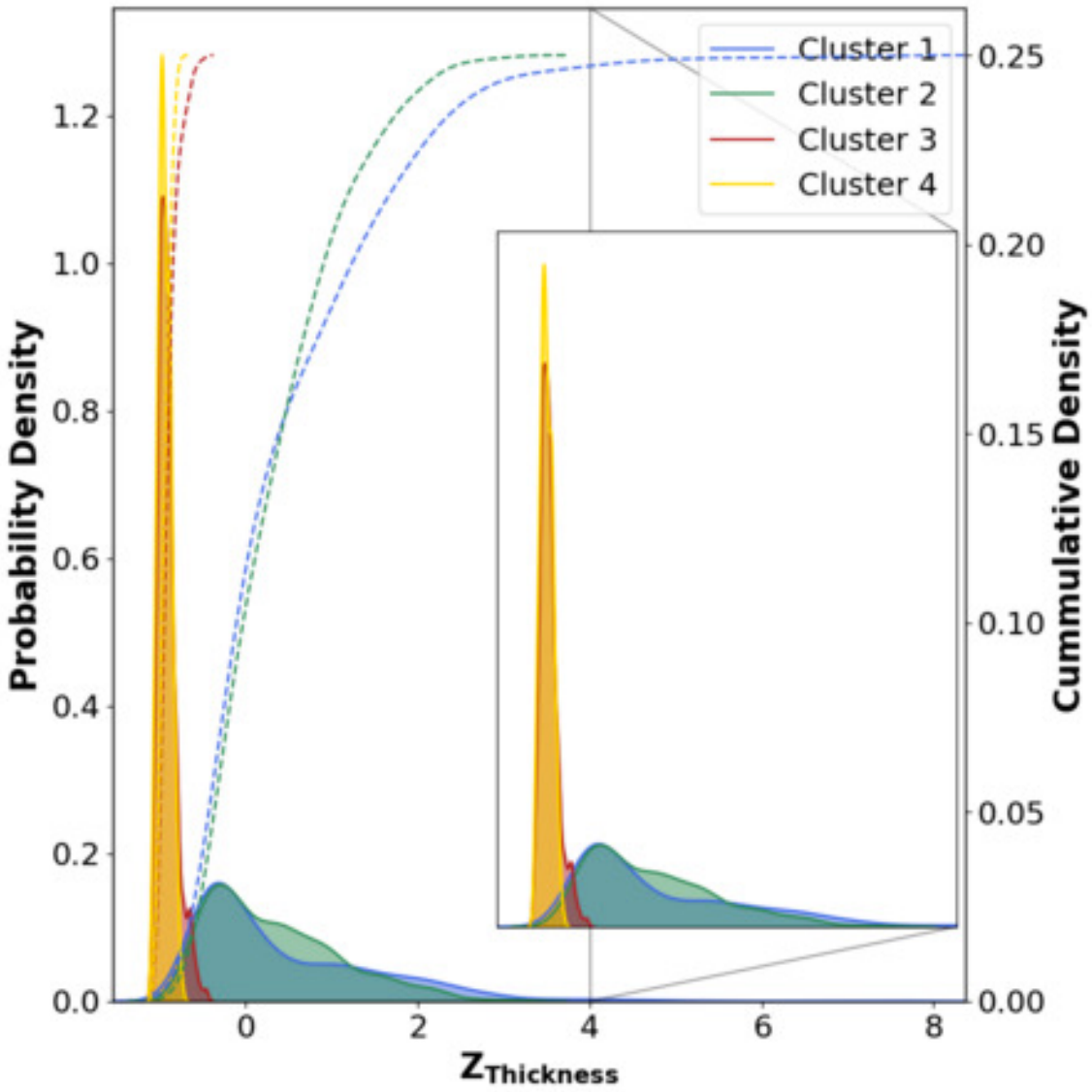

Figure S57: Estimation of the Probability Density Functions for the normalized Area per Lipid, calculated for each cluster separately. Each cluster is shown in one color. The Probability Density Function is shown as a solid line with a shaded area beneath. The Cumulative Density Function is shown as a dashed line.

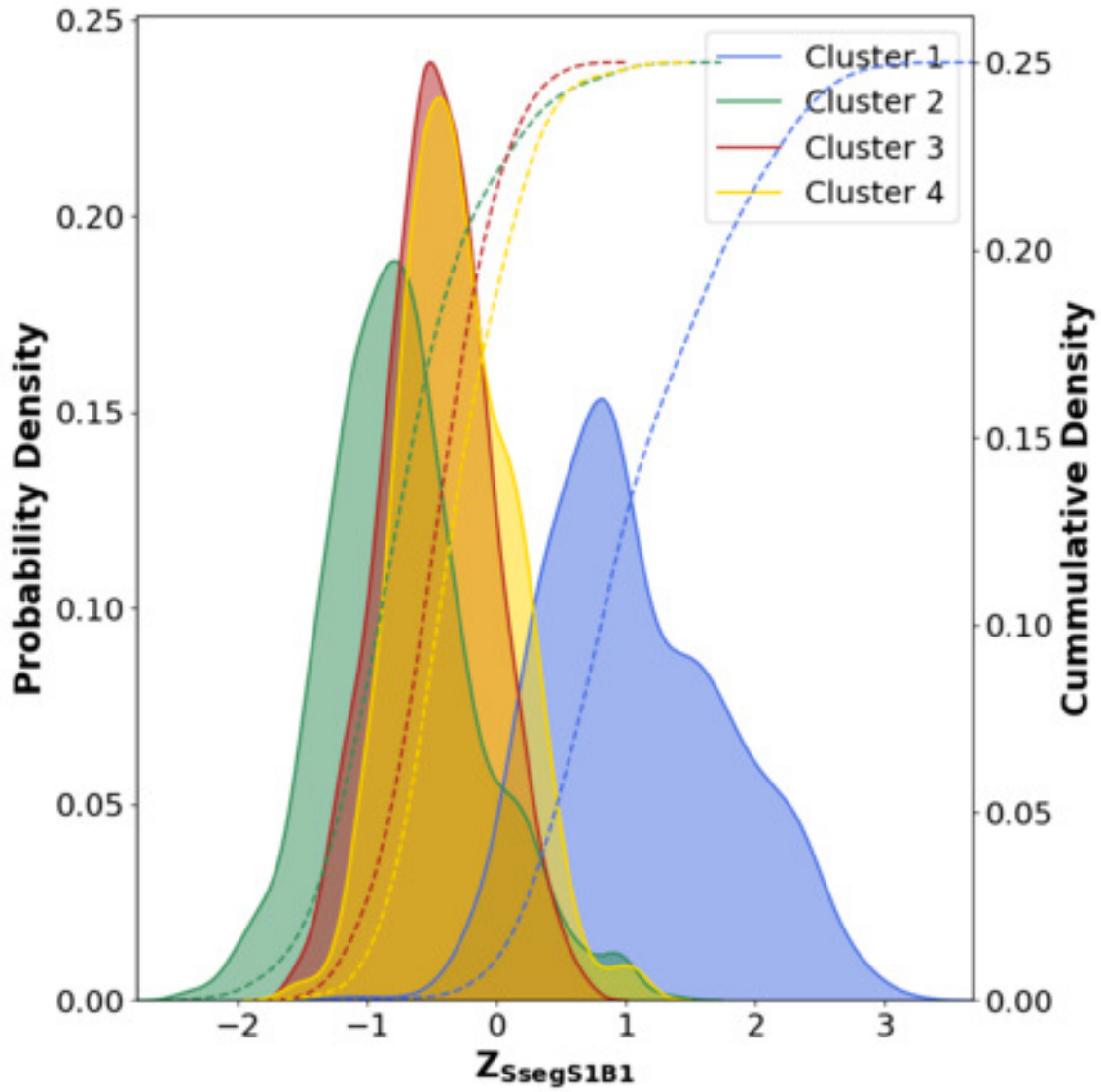

Figure S58: Estimation of the Probability Density Functions for the normalized Segmental Order Parameter for the first bead of the *sn-1* tail, calculated for each cluster separately. Each cluster is shown in one color. The Probability Density Function is shown as a solid line with a shaded area beneath. The Cumulative Density Function is shown as a dashed line.

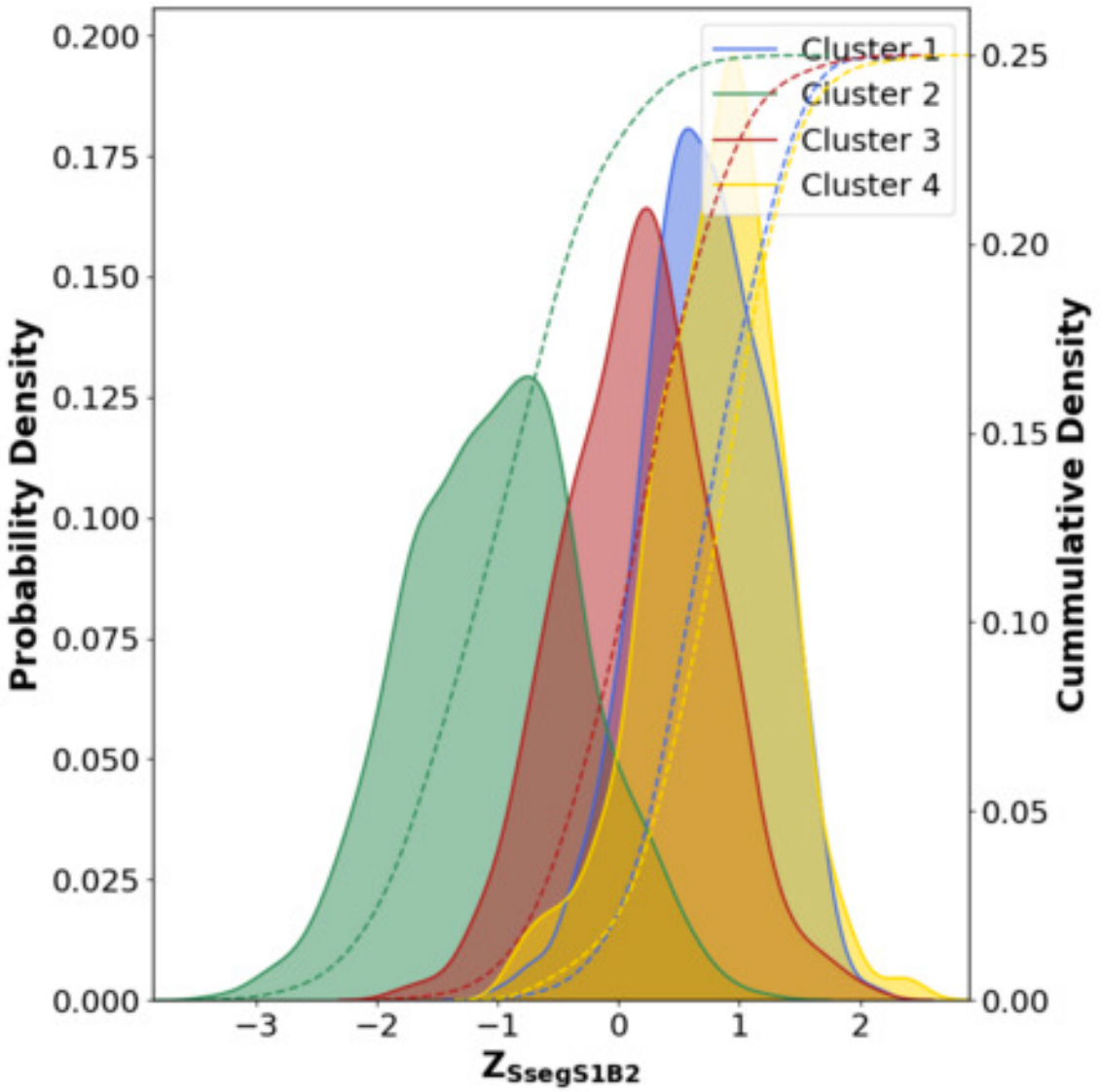

Figure S59: Estimation of the Probability Density Functions for the normalized Segmental Order Parameter for the second bead of the *sn-1* tail, calculated for each cluster separately. Each cluster is shown in one color. The Probability Density Function is shown as a solid line with a shaded area beneath. The Cumulative Density Function is shown as a dashed line.

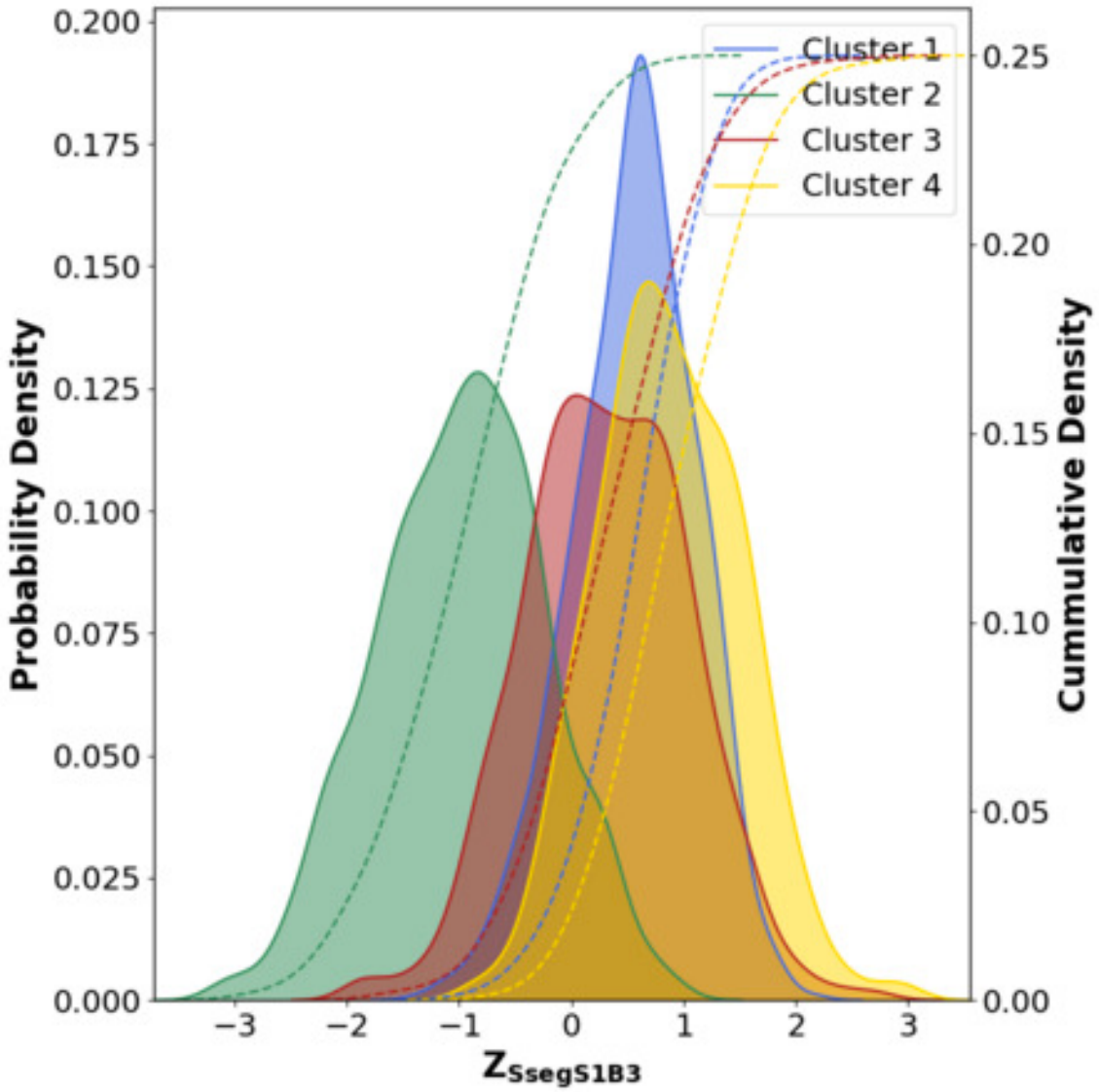

Figure S60: Estimation of the Probability Density Functions for the normalized Segmental Order Parameter for the third bead of the *sn-1* tail, calculated for each cluster separately. Each cluster is shown in one color. The Probability Density Function is shown as a solid line with a shaded area beneath. The Cumulative Density Function is shown as a dashed line.

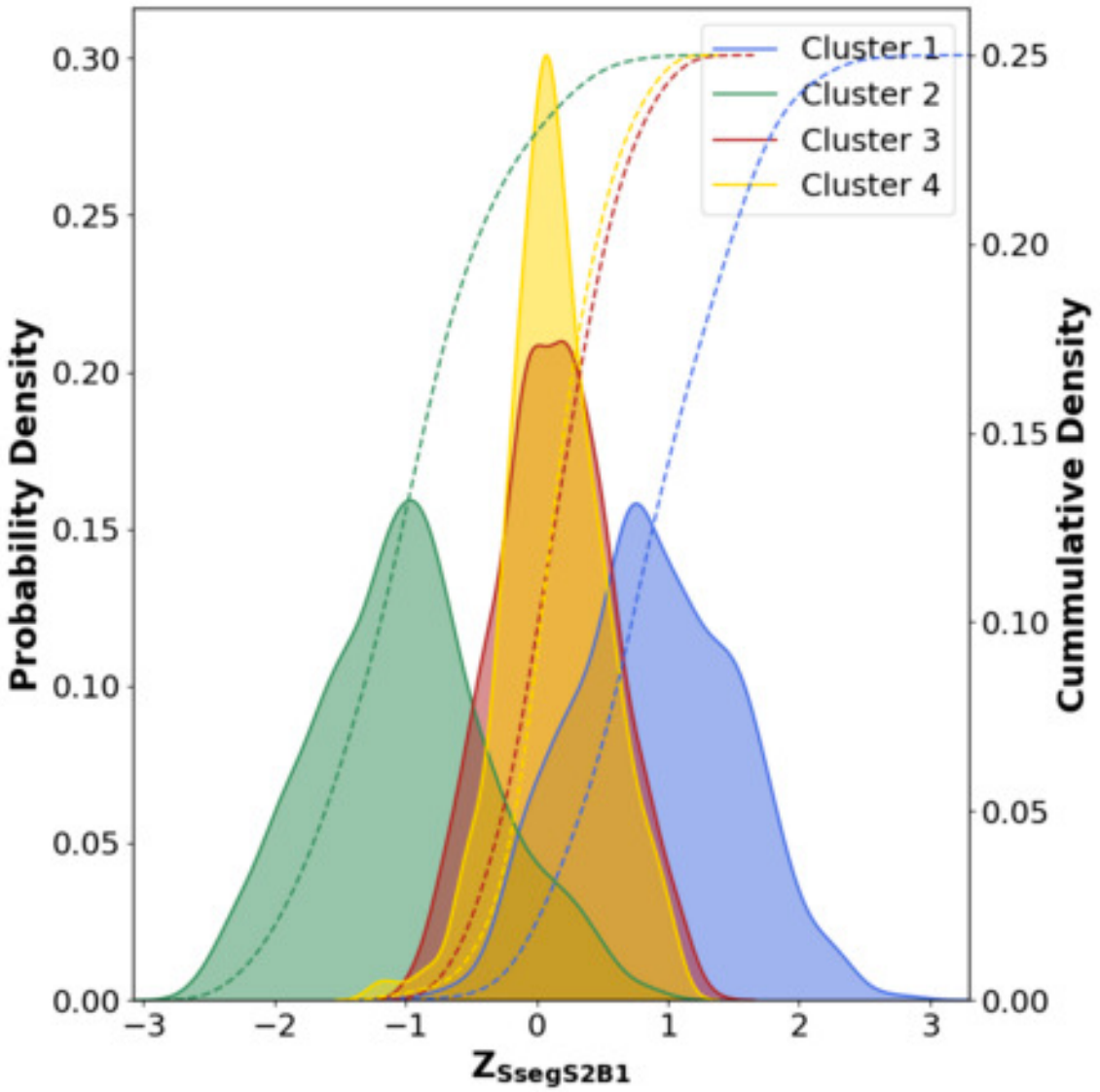

Figure S61: Estimation of the Probability Density Functions for the normalized Segmental Order Parameter for the first bead of the *sn-2* tail, calculated for each cluster separately. Each cluster is shown in one color. The Probability Density Function is shown as a solid line with a shaded area beneath. The Cumulative Density Function is shown as a dashed line.

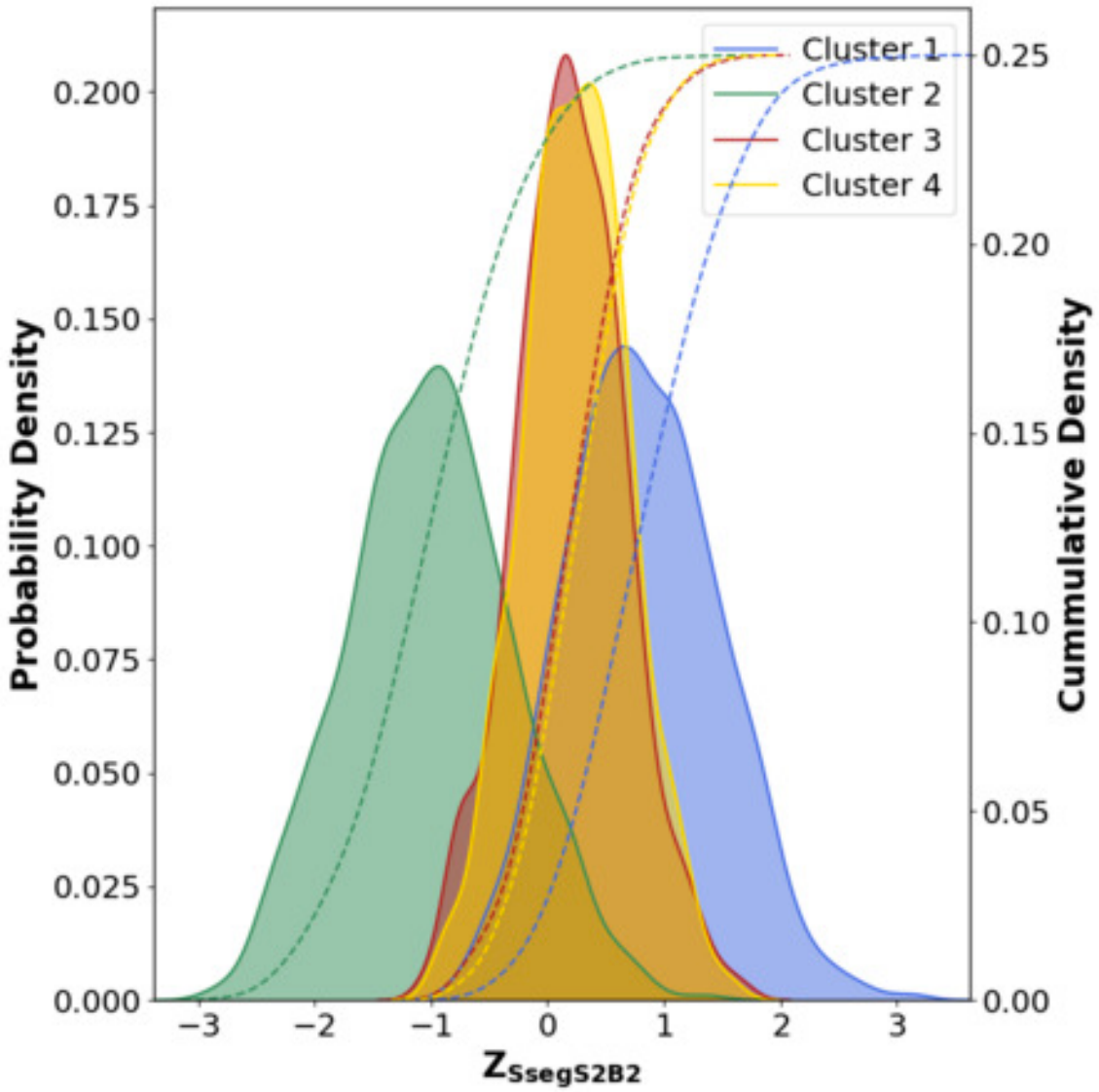

Figure S62: Estimation of the Probability Density Functions for the normalized Segmental Order Parameter for the second bead of the *sn-2* tail, calculated for each cluster separately. Each cluster is shown in one color. The Probability Density Function is shown as a solid line with a shaded area beneath. The Cumulative Density Function is shown as a dashed line.

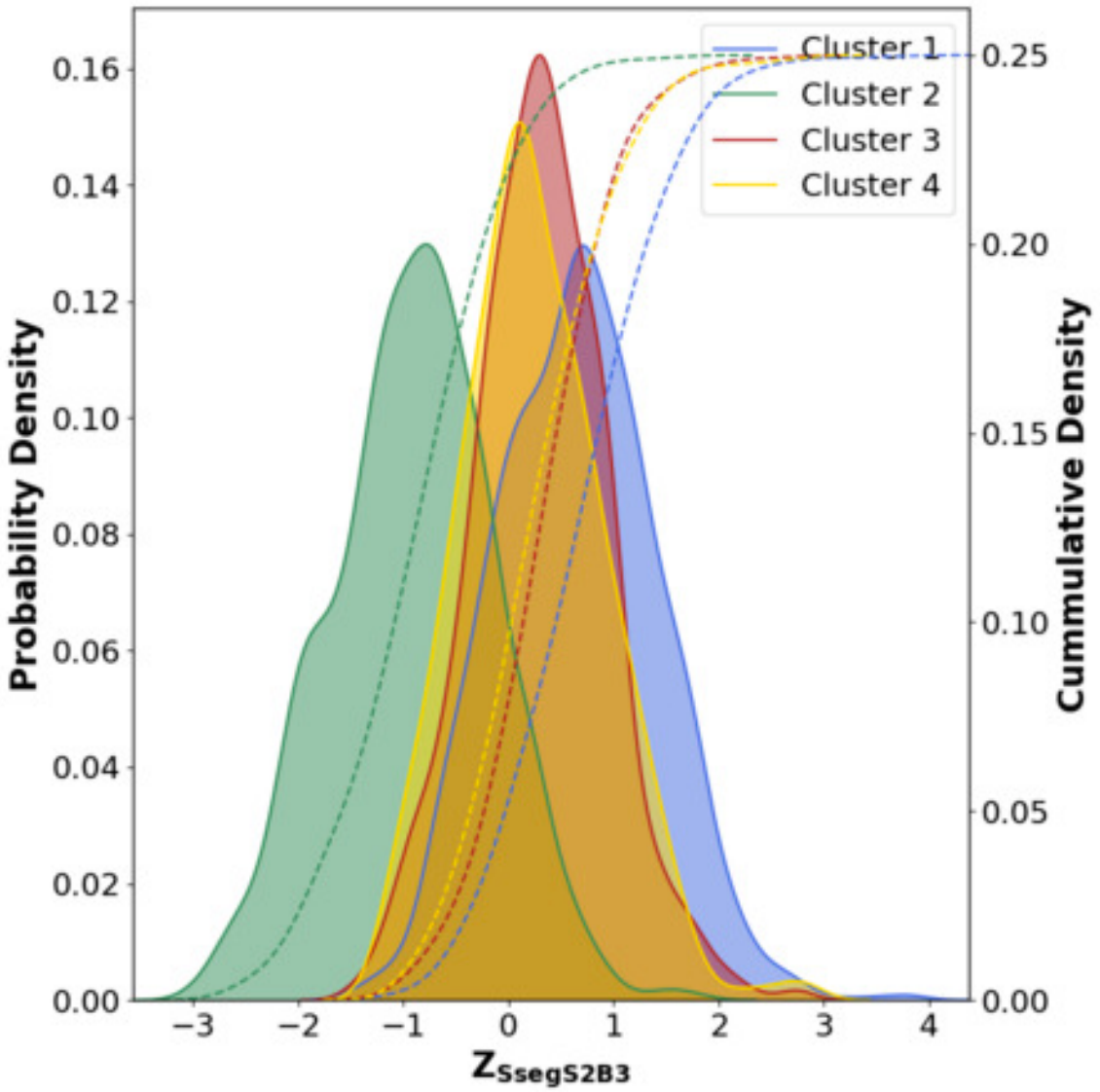

Figure S63: Estimation of the Probability Density Functions for the normalized Segmental Order Parameter for the third bead of the *sn-2* tail, calculated for each cluster separately. Each cluster is shown in one color. The Probability Density Function is shown as a solid line with a shaded area beneath. The Cumulative Density Function is shown as a dashed line.

A.5 Supplementary Figures for Section 4.4

A.5.1 Response Surfaces for Order Parameters

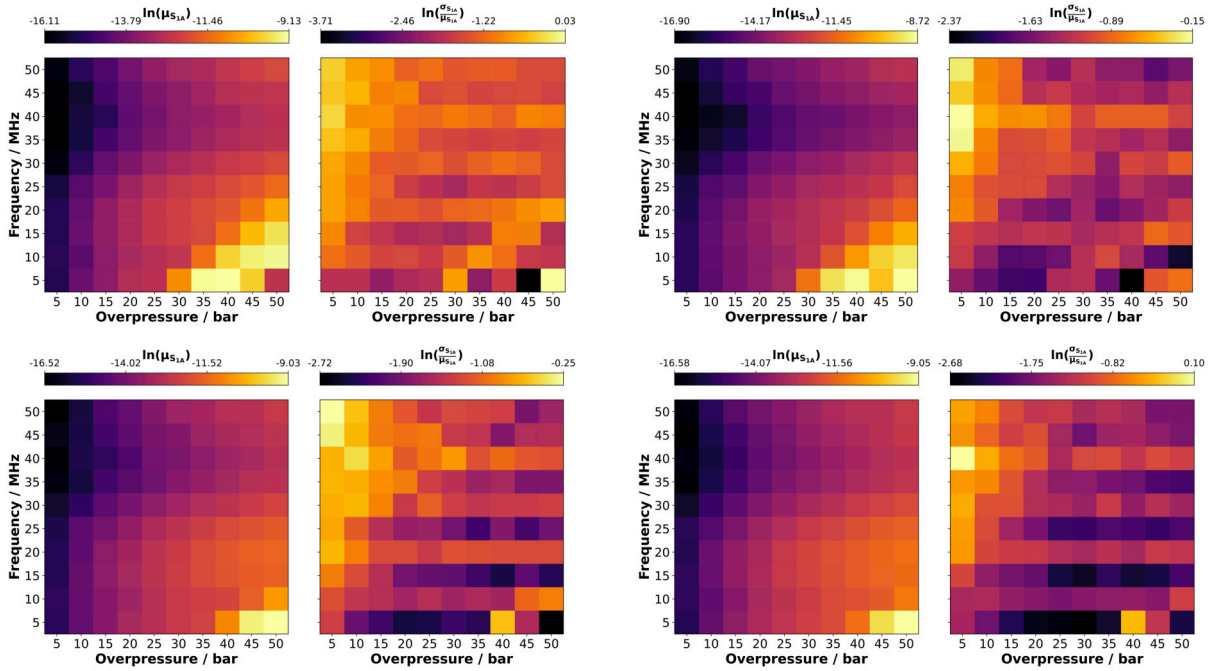

Figure S64: Order Parameters of the *sn-1* tail, first bead, (S_{1A}) response for the studied systems (starting in top left and going clockwise: POPC, POPE, POPG and POPS) under varying ultrasound conditions. Two heatmaps are plotted for each lipid bilayer: Logarithm of mean S_{1A}, $\ln(\mu_{S_{1A}})$, showing average membrane expansion or compression (left); and Logarithm of relative APL fluctuations, $\ln\left(\frac{\sigma_{S_{1A}}}{\mu_{S_{1A}}}\right)$, indicating the magnitude of APL variations relative to its average value (right). The logarithmic representation is used to improve the visibility of the figures.

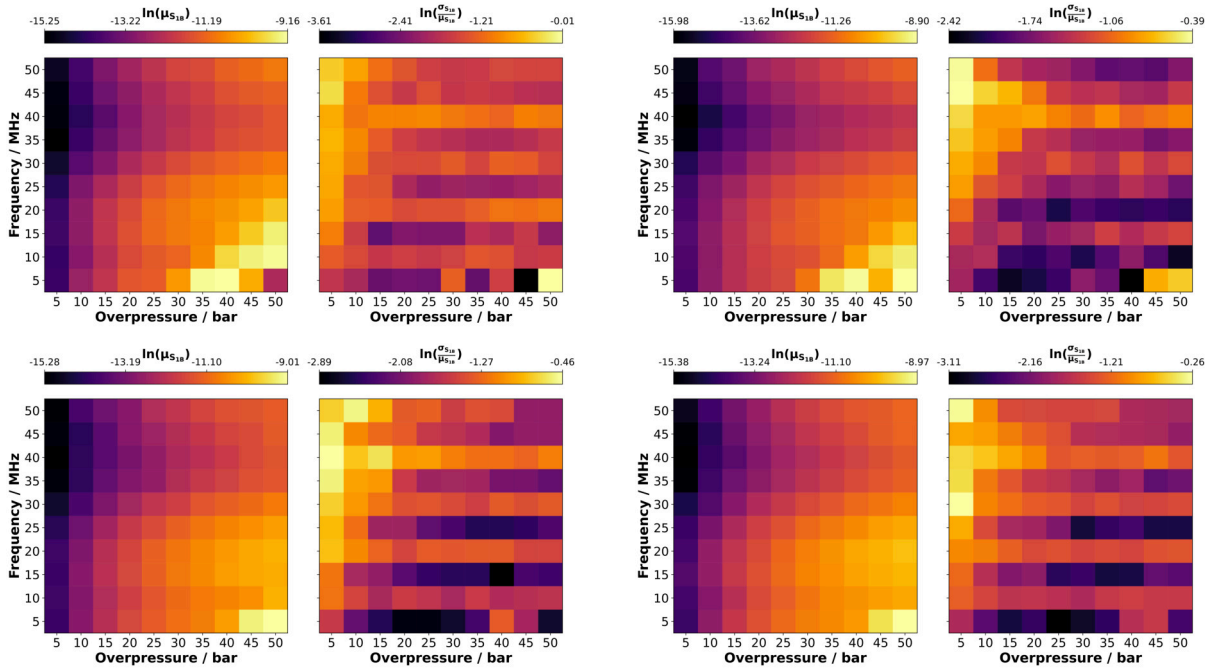

Figure S65: Order Parameters of the *sn-1* tail, second bead, (S_{1B}) response for the studied systems (starting in top left and going clockwise: POPC, POPE, POPG and POPS) under varying ultrasound conditions. Two heatmaps are plotted for each lipid bilayer: Logarithm of mean S_{1B}, $\ln(\mu_{S_{1B}})$, showing average membrane expansion or compression (left); and Logarithm of relative APL fluctuations, $\ln\left(\frac{\sigma_{S_{1B}}}{\mu_{S_{1B}}}\right)$, indicating the magnitude of APL variations relative to its average value (right). The logarithmic representation is used to improve the visibility of the figures.

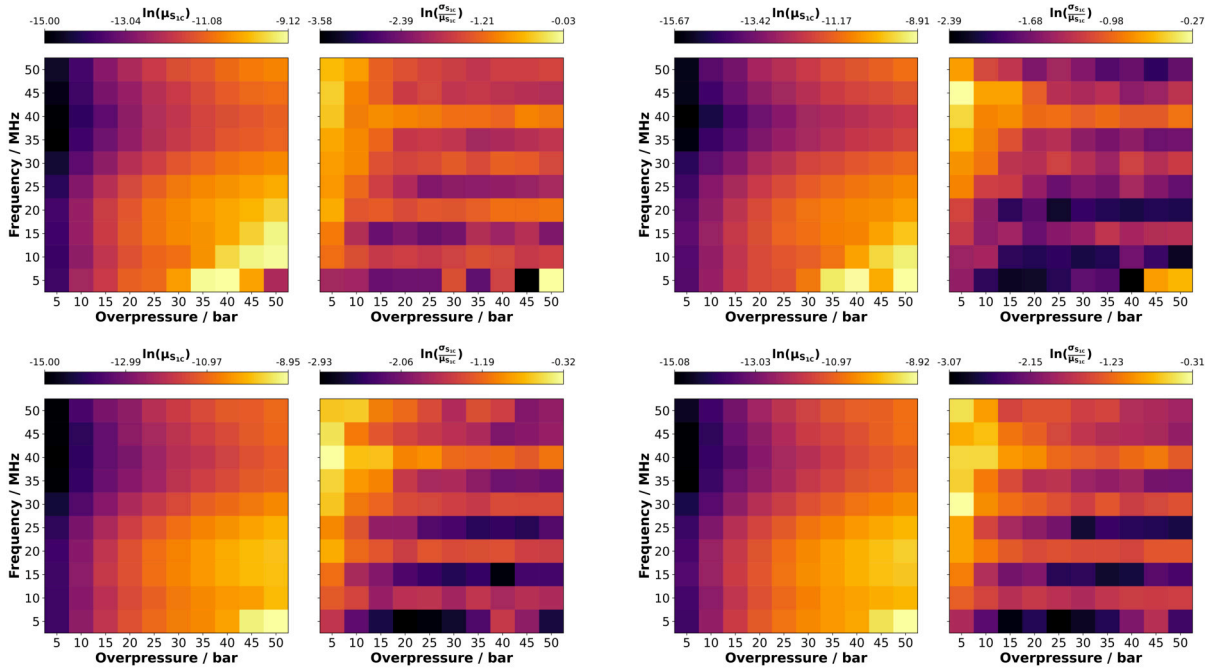

Figure S66: Order Parameters of the *sn-1* tail, third bead, (S_{1C}) response for the studied systems (starting in top left and going clockwise: POPC, POPE, POPG and POPS) under varying ultrasound conditions. Two heatmaps are plotted for each lipid bilayer: Logarithm of mean S_{1C}, $\ln(\mu_{S_{1C}})$, showing average membrane expansion or compression (left); and Logarithm of relative APL fluctuations, $\ln\left(\frac{\sigma_{S_{1C}}}{\mu_{S_{1C}}}\right)$, indicating the magnitude of APL variations relative to its average value (right). The logarithmic representation is used to improve the visibility of the figures.

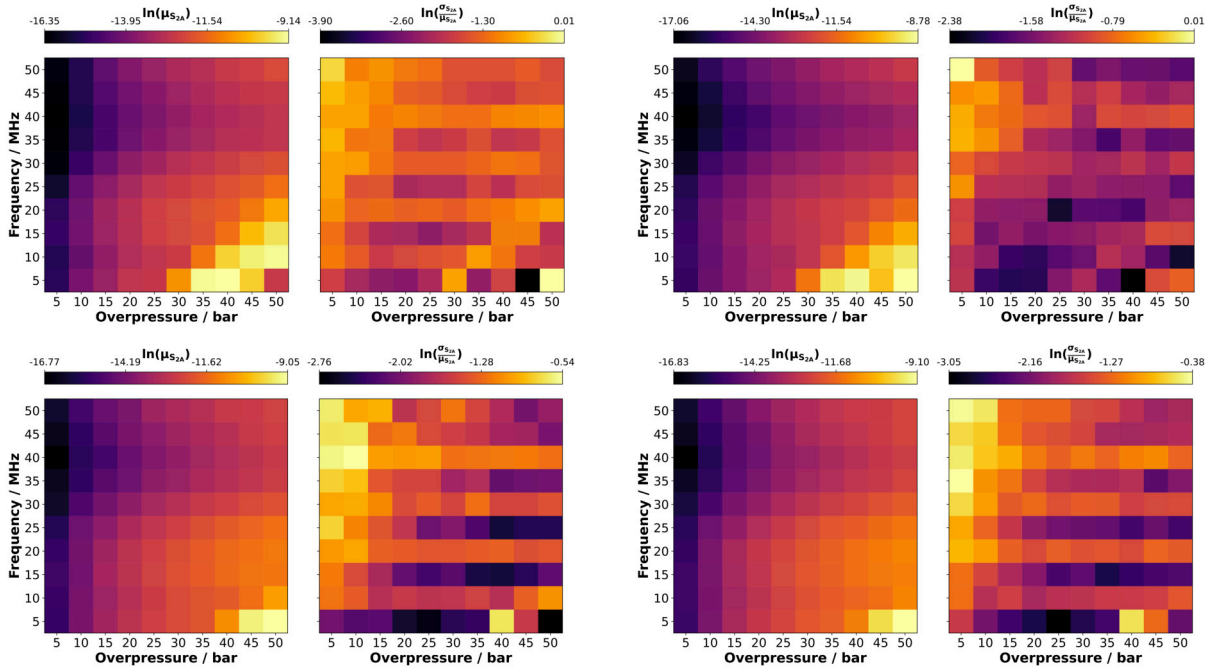

Figure S67: Order Parameters of the *sn-2* tail, first bead, (S_{2A}) response for the studied systems (starting in top left and going clockwise: POPC, POPE, POPG and POPS) under varying ultrasound conditions. Two heatmaps are plotted for each lipid bilayer: Logarithm of mean S_{2A}, $\ln(\mu_{S_{2A}})$, showing average membrane expansion or compression (left); and Logarithm of relative APL fluctuations, $\ln\left(\frac{\sigma_{S_{2A}}}{\mu_{S_{2A}}}\right)$, indicating the magnitude of APL variations relative to its average value (right). The logarithmic representation is used to improve the visibility of the figures.

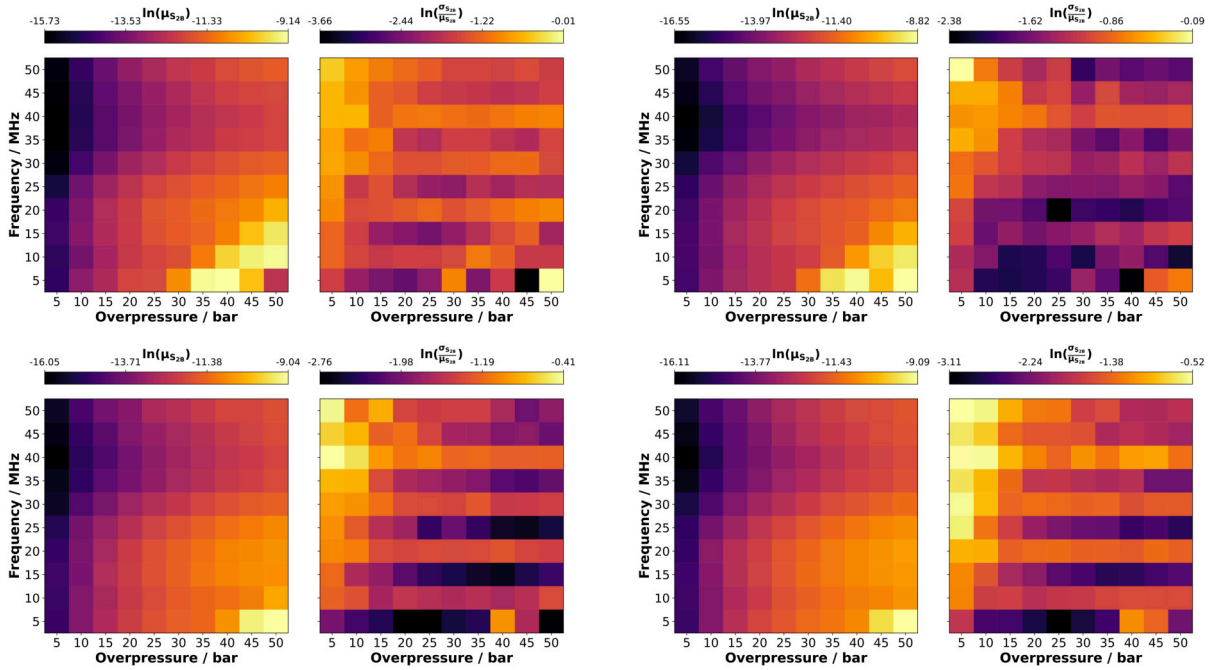

Figure S68: Order Parameters of the *sn-2* tail, second bead, (S_{2B}) response for the studied systems (starting in top left and going clockwise: POPC, POPE, POPG and POPS) under varying ultrasound conditions. Two heatmaps are plotted for each lipid bilayer: Logarithm of mean S_{2B}, $\ln(\mu_{S_{2B}})$, showing average membrane expansion or compression (left); and Logarithm of relative APL fluctuations, $\ln\left(\frac{\sigma_{S_{2B}}}{\mu_{S_{2B}}}\right)$, indicating the magnitude of APL variations relative to its average value (right). The logarithmic representation is used to improve the visibility of the figures.

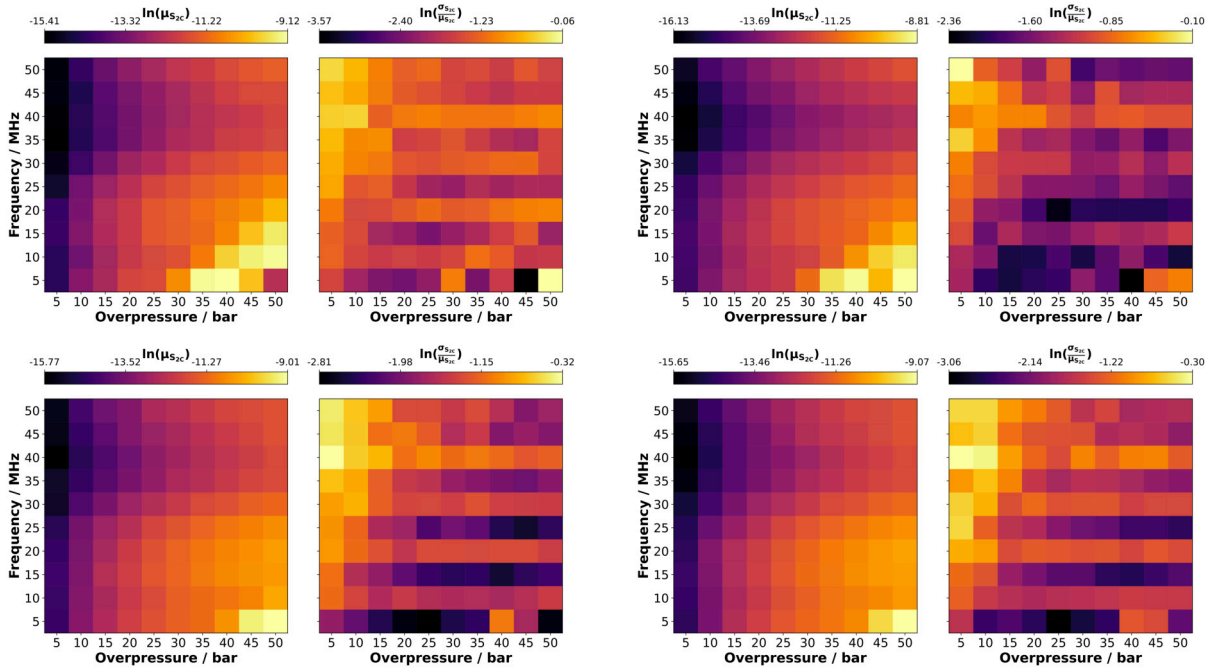

Figure S69: Order Parameters of the *sn-2* tail, third bead, (S_{2C}) response for the studied systems (starting in top left and going clockwise: POPC, POPE, POPG and POPS) under varying ultrasound conditions. Two heatmaps are plotted for each lipid bilayer: Logarithm of mean S_{2C}, $\ln(\mu_{S_{2C}})$, showing average membrane expansion or compression (left); and Logarithm of relative APL fluctuations, $\ln\left(\frac{\sigma_{S_{2C}}}{\mu_{S_{2C}}}\right)$, indicating the magnitude of APL variations relative to its average value (right). The logarithmic representation is used to improve the visibility of the figures.

A.5.2 Difference Matrices for Order Parameters

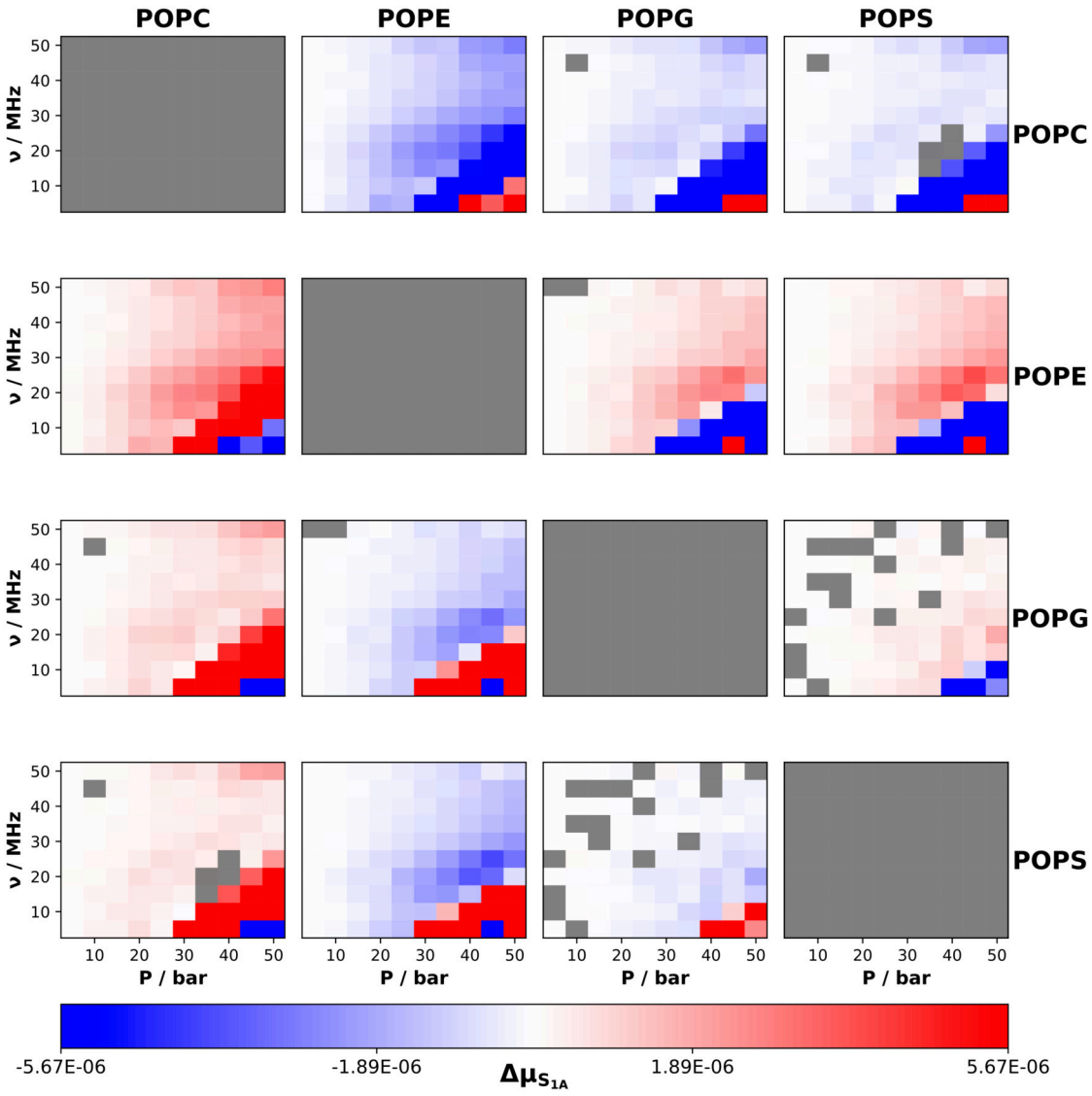

Figure S70: Pairwise difference matrix of the Order Parameters of the *sn-1* tail, first bead (S_{1A}), response surfaces for the studied membranes under varying ultrasound conditions. Each subplot shows ΔS_{1A} (column lipid minus row lipid) across frequencies (ν) and overpressures (P). Red indicates positive differences, blue negative, with intensity proportional to magnitude. Gray areas represent differences not statistically significant at the 99.9% confidence level.

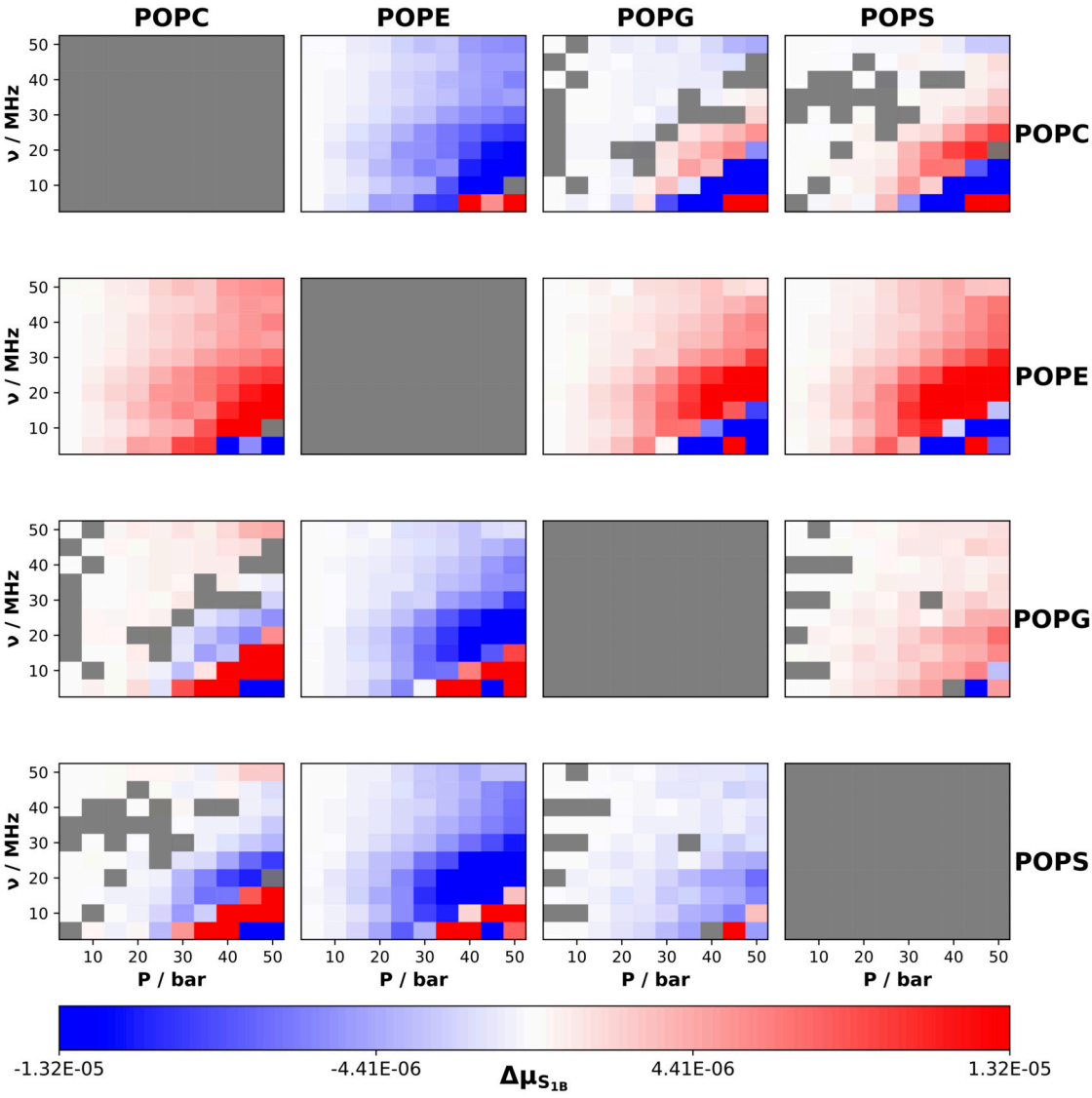

Figure S71: Pairwise difference matrix of the Order Parameters of the *sn-1* tail, second bead (S_{1B}), response surfaces for the studied membranes under varying ultrasound conditions. Each subplot shows ΔS_{1B} (column lipid minus row lipid) across frequencies (ν) and overpressures (P). Red indicates positive differences, blue negative, with intensity proportional to magnitude. Gray areas represent differences not statistically significant at the 99.9% confidence level.

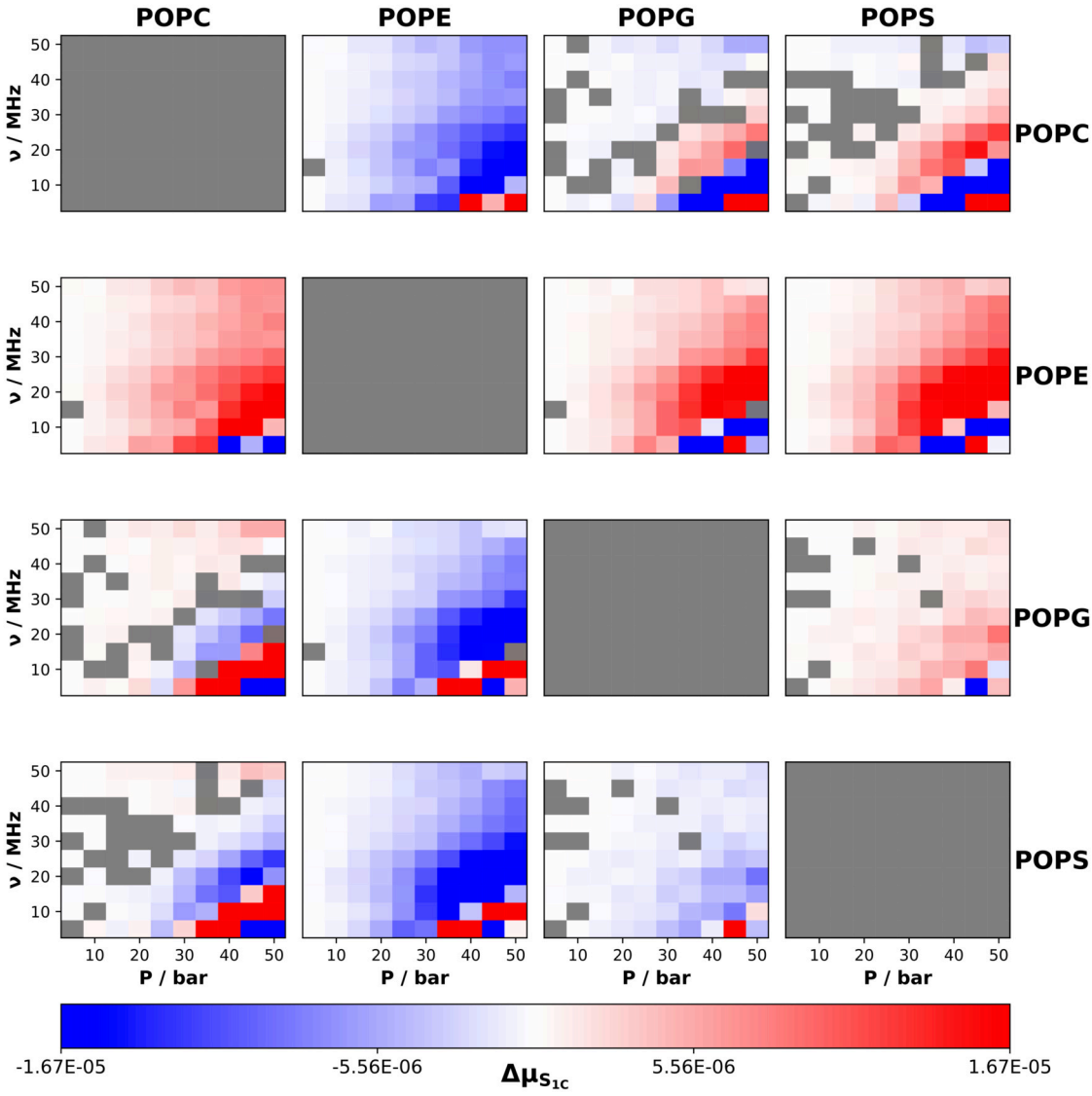

Figure S72: Pairwise difference matrix of the Order Parameters of the *sn-1* tail, third bead (S_{1C}), response surfaces for the studied membranes under varying ultrasound conditions. Each subplot shows ΔS_{1C} (column lipid minus row lipid) across frequencies (ν) and overpressures (P). Red indicates positive differences, blue negative, with intensity proportional to magnitude. Gray areas represent differences not statistically significant at the 99.9% confidence level.

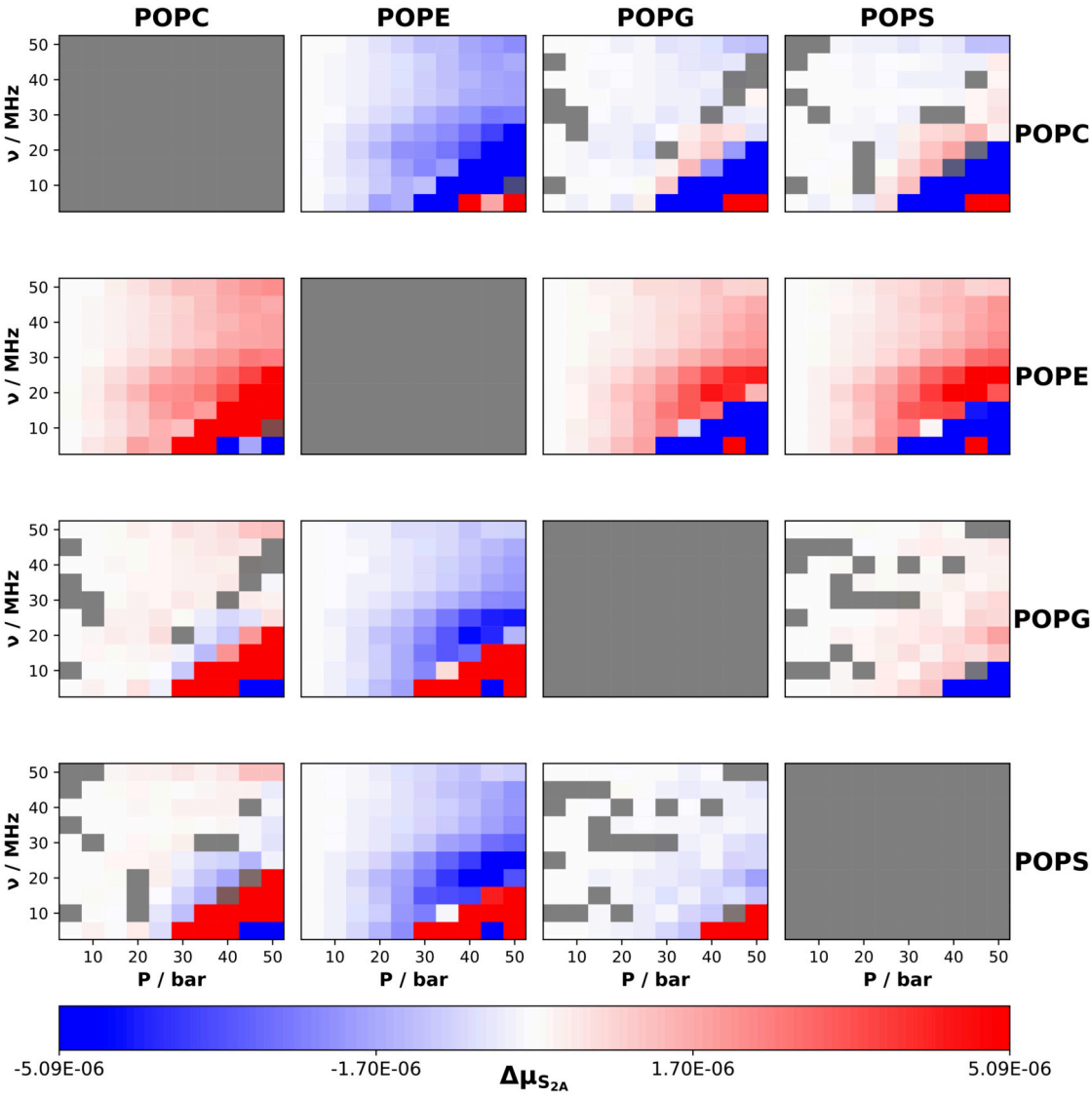

Figure S73: Pairwise difference matrix of the Order Parameters of the *sn-2* tail, first bead (S_{2A}), response surfaces for the studied membranes under varying ultrasound conditions. Each subplot shows ΔS_{2A} (column lipid minus row lipid) across frequencies (ν) and overpressures (P). Red indicates positive differences, blue negative, with intensity proportional to magnitude. Gray areas represent differences not statistically significant at the 99.9% confidence level.

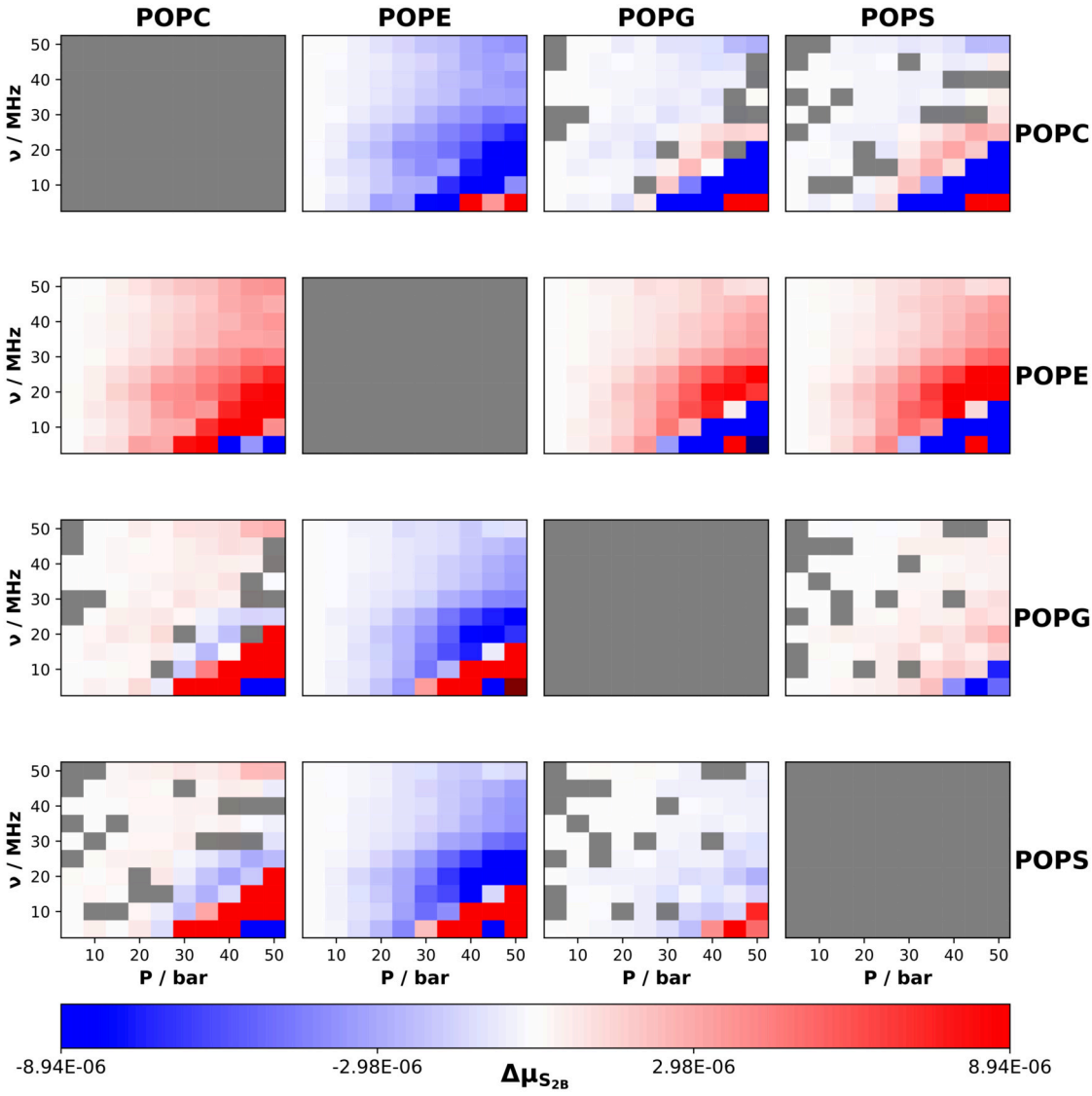

Figure S74: Pairwise difference matrix of the Order Parameters of the *sn-2* tail, second bead (S_{2B}), response surfaces for the studied membranes under varying ultrasound conditions. Each subplot shows ΔS_{2B} (column lipid minus row lipid) across frequencies (ν) and overpressures (P). Red indicates positive differences, blue negative, with intensity proportional to magnitude. Gray areas represent differences not statistically significant at the 99.9% confidence level.

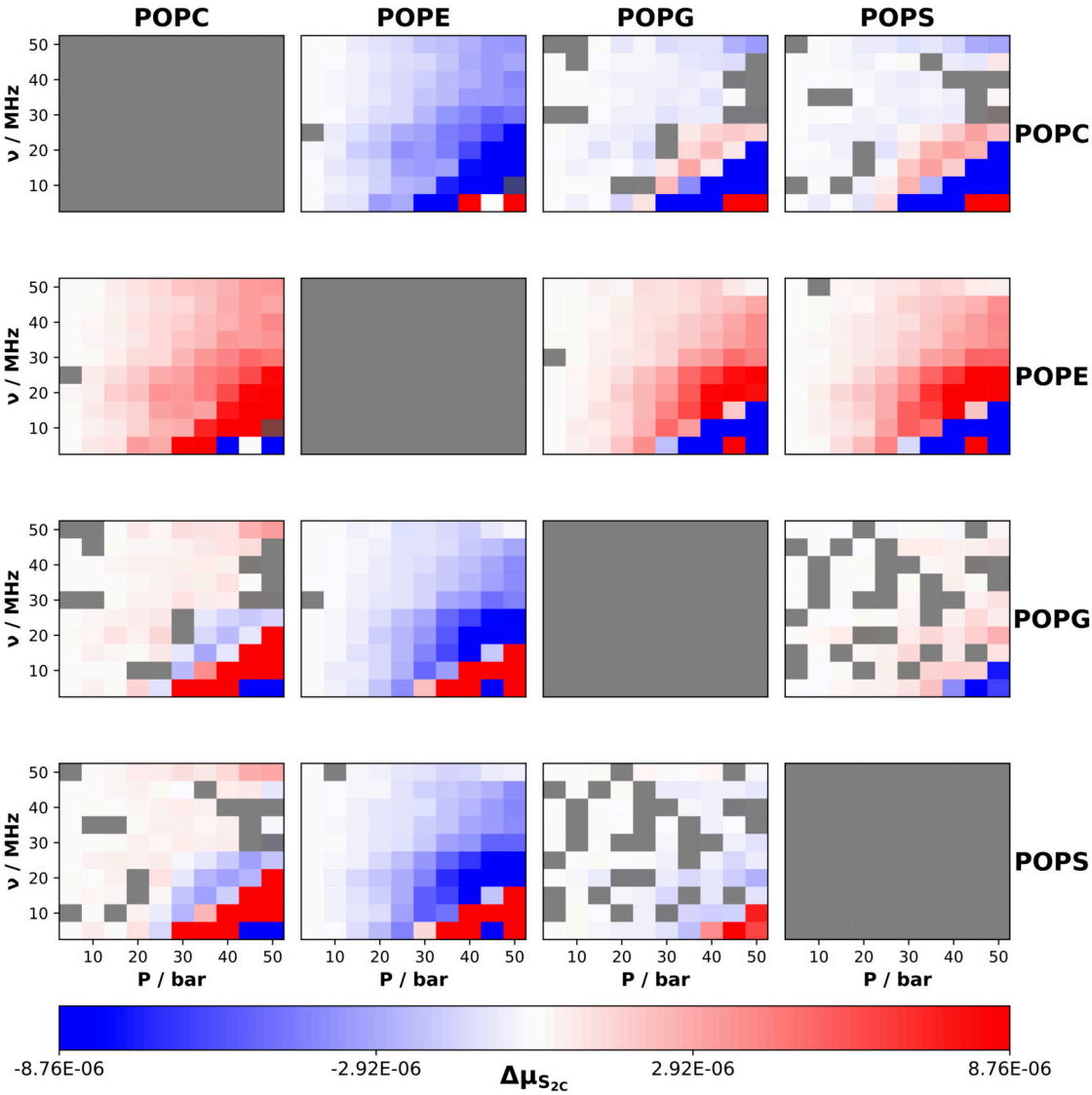

Figure S75: Pairwise difference matrix of the Order Parameters of the *sn-2* tail, first bead (S_{2C}), response surfaces for the studied membranes under varying ultrasound conditions. Each subplot shows ΔS_{2C} (column lipid minus row lipid) across frequencies (ν) and overpressures (P). Red indicates positive differences, blue negative, with intensity proportional to magnitude. Gray areas represent differences not statistically significant at the 99.9% confidence level.

B RELATION OF PUBLICATIONS

B.1 Works and Contributions

We give here a comprehensive list of published works carried out during this Thesis. We also give information about several quality metrics of the journals in which they were published.

B.1.1 Published Work for Section 4.1

The results presented in Section 4.1 can be also consulted in the journal article 'Simulating Bacterial Membrane Models at the Atomistic Level: A Force Field Comparison'[491], published in the Journal of Chemical Theory and Computation, ISSN 1549-9618. The 2023 Journal Impact Factor was of 5.7, and ranked 5/40, first quartile, in the area of Physics, Atomic, Molecular & Chemical science, as per Journal Citation Reports[517]. For this work, the author of this Thesis performed the simulations, analysed them, and contributed to the writing of the final manuscript.

B.1.2 Published Work for Section 4.2

The results presented in Section 4.2 can be also consulted in the journal article 'Unravelling hierarchical levels of structure in lipid membranes'[506], published in the Computational and Structural Biotechnology Journal, ISSN 2001-0370. The 2022 Journal Impact Factor was of 6.0, and ranked 60/285, first quartile, in the area of Biochemistry & Molecular Biology, as per Journal Citation Reports[518]. For this work, the author of this Thesis performed the simulations, analysed them, and contributed to the writing of the final manuscript.

B.1.3 Published Work for Section 4.3

The results presented in Section 4.1 can be also consulted in the journal article 'Molecular insights into the effects of focused ultrasound mechanotherapy on lipid bilayers: Unlocking the keys to design effective treatments'[480], published in the Journal of Colloid and Interface Science, ISSN 0021-9797. The 2023 Journal Impact Factor was of 9.4, and ranked 32/178, first quartile, in the area of Physical Chemistry, as per Journal Citation Reports[519]. For this study, the author of this Thesis patched the MD engine source code in order to allow simulation of an US wave, performed the simulations, analysed them, and contributed to the writing of the final manuscript.

C RIGHTS AND PERMISSIONS

C.1 Rights for Reproduced Figures from Third-Party Articles

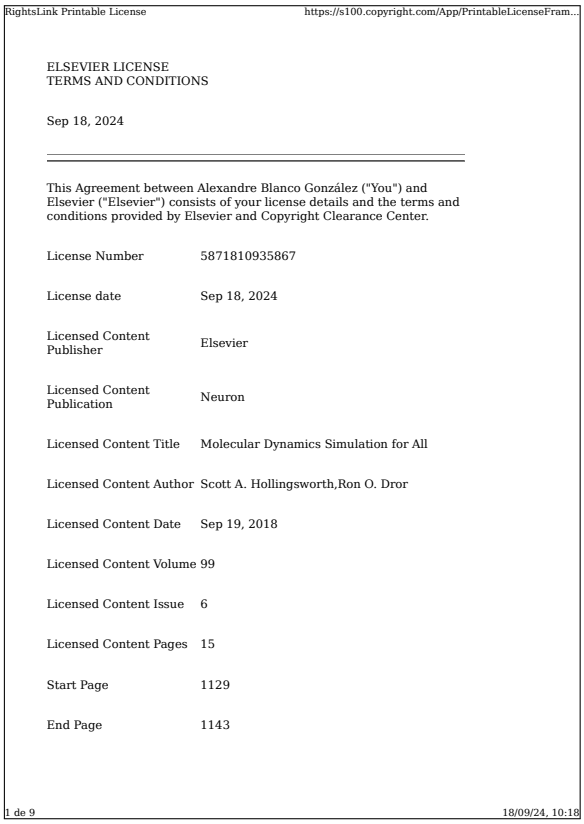

RightsLink Printable License https://s100.copyright.com/App/PrintableLicenseFram...

ELSEVIER LICENSE
TERMS AND CONDITIONS

Sep 18, 2024

This Agreement between Alexandre Blanco González ("You") and Elsevier ("Elsevier") consists of your license details and the terms and conditions provided by Elsevier and Copyright Clearance Center.

License Number	5871810935867
License date	Sep 18, 2024
Licensed Content Publisher	Elsevier
Licensed Content Publication	Neuron
Licensed Content Title	Molecular Dynamics Simulation for All
Licensed Content Author	Scott A. Hollingsworth,Ron O. Dror
Licensed Content Date	Sep 19, 2018
Licensed Content Volume	99
Licensed Content Issue	6
Licensed Content Pages	15
Start Page	1129
End Page	1143

1 de 9 18/09/24, 10:18

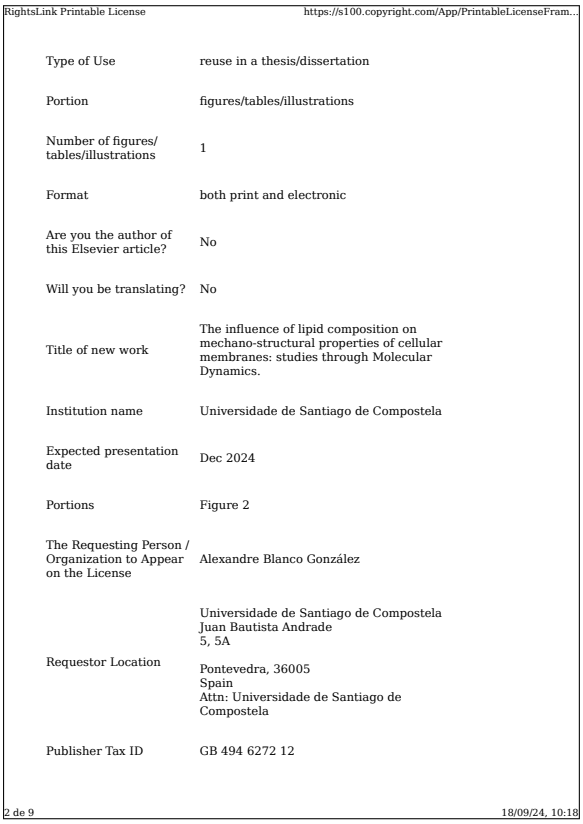

RightsLink Printable License https://s100.copyright.com/App/PrintableLicenseFram...

Type of Use	reuse in a thesis/dissertation
Portion	figures/tables/illustrations
Number of figures/ tables/illustrations	1
Format	both print and electronic
Are you the author of this Elsevier article?	No
Will you be translating?	No
Title of new work	The influence of lipid composition on mechano-structural properties of cellular membranes: studies through Molecular Dynamics.
Institution name	Universidade de Santiago de Compostela
Expected presentation date	Dec 2024
Portions	Figure 2
The Requesting Person / Organization to Appear on the License	Alexandre Blanco González
Requestor Location	Universidade de Santiago de Compostela Juan Bautista Andrade 5, 5A Pontevedra, 36005 Spain Attn: Universidade de Santiago de Compostela
Publisher Tax ID	GB 494 6272 12

2 de 9 18/09/24, 10:18

Licence L1: Licence of reproduction for Figure 1.11.

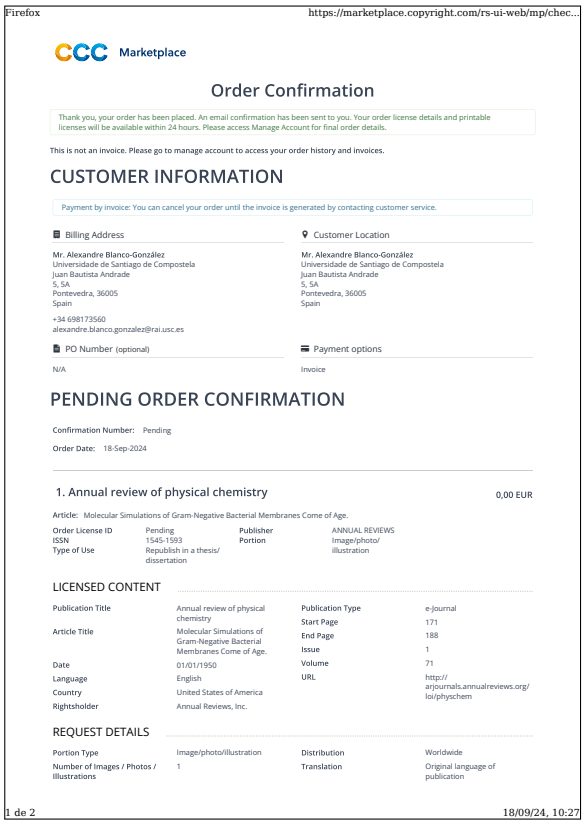

Firefox https://marketplace.copyright.com/rs-ui-web/mp/chec...

CCC Marketplace

Order Confirmation

Thank you, your order has been placed. An email confirmation has been sent to you. Your order license details and printable licenses will be available within 24 hours. Please access Manage Account for final order details.

This is not an invoice. Please go to manage account to access your order history and invoices.

CUSTOMER INFORMATION

Payment by invoice: You can cancel your order until the invoice is generated by contacting customer service.

Billing Address

Mr. Alexandre Blanco-González
Universidade de Santiago de Compostela
Juan Bautista Andrade
5, 5A
Pontevedra, 36005
Spain

+34 698173560
alexandre.blanco.gonzalez@rai.usc.es

Customer Location

Mr. Alexandre Blanco-González
Universidade de Santiago de Compostela
Juan Bautista Andrade
5, 5A
Pontevedra, 36005
Spain

PO Number (optional)

N/A

Payment options

Invoice

PENDING ORDER CONFIRMATION

Confirmation Number: Pending

Order Date: 18-Sep-2024

1. Annual review of physical chemistry 0,00 EUR

Article: Molecular Simulations of Gram-Negative Bacterial Membranes Come of Age.

Order License ID	Pending	Publisher	ANNUAL REVIEWS
ISSN	1545-1593	Portion	Image/photo/ illustration
Type of Use	Republish in a thesis/ dissertation		

LICENSED CONTENT

Publication Title	Annual review of physical chemistry	Publication Type	e-journal
Article Title	Molecular Simulations of Gram-Negative Bacterial Membranes Come of Age.	Start Page	171
		End Page	188
		Issue	1
Date	01/01/1950	Volume	71
Language	English	URL	http://arjournals.annualreviews.org/loi/physchem
Country	United States of America		
Rightsholder	Annual Reviews, Inc.		

REQUEST DETAILS

Portion Type	Image/photo/illustration	Distribution	Worldwide
Number of Images / Photos / Illustrations	1	Translation	Original language of publication

1 de 2 18/09/24, 10:27

Firefox https://marketplace.copyright.com/rs-ui-web/mp/chec...

Format (select all that apply)	Print, Electronic	Copies for the Disabled?	No
Who Will Republish the Content?	Academic institution	Minor Editing Privileges?	Yes
Duration of Use	Life of current and all future editions	Incidental Promotional Use?	No
		Currency	EUR
Lifetime Unit Quantity	Up to 499		
Rights Requested	Main product		

NEW WORK DETAILS

Title	The influence of lipid composition on mechano-structural properties of cellular membranes: studies through Molecular Dynamics.	Institution Name	Universidade de Santiago de Compostela
		Expected Presentation Date	2024-12-20
Instructor Name	Alexandre Blanco González		

ADDITIONAL DETAILS

Order Reference Number	N/A	The Requesting Person / Organization to Appear on the License	Alexandre Blanco González

REQUESTED CONTENT DETAILS

Title, Description or Numeric Reference of the Portion(s)	Figure 5	Title of the Article / Chapter the Portion Is From	Molecular Simulations of Gram-Negative Bacterial Membranes Come of Age.
Editor of Portion(s)	Im, Wonpil; Khalid, Syma		
Volume / Edition	71	Author of Portion(s)	Im, Wonpil; Khalid, Syma
Page or Page Range of Portion	171-188	Issue, if Republishing an Article From a Serial	1
		Publication Date of Portion	2020-04-20

Total Items: 1 Total Due: 0,00 EUR

Accepted: Marketplace Permissions General Terms and Conditions and any applicable Publisher Terms and Conditions

2 de 2 18/09/24, 10:27

Licence L2: Licence of reproduction for Figure 1.13.

Licence L3: Licence of reproduction for Figure 1.15.

Licence L4: Licence of reproduction for Figure 1.16.

Licence L5: Licence of reproduction for Figure 1.17.

Licence L6: Licence of reproduction for Figure 1.18.

C.2 Rights for Reproduced Content of Published Articles by the Author

Licence L7: Licence of reproduction for the contents of section 4.1.

BIBLIOGRAPHY

1. *NAMA Machine d'Anticythère 1* https://commons.wikimedia.org/wiki/File:NAMA_Machine_d%27Anticyth%C3%A8re_1.jpg.
2. Ifrah, G. *The universal history of computing: From the abacus to quantum computing* (John Wiley & Sons, Inc., 2000).
3. Arndt, A. Al-Khwarizmi. *The Mathematics Teacher* **76,** 668–670 (1983).
4. Marguin, J. *Histoire des instruments et machines à calculer: trois siècles de mécanique pensante, 1642-1942* ISBN: 9782705661663 (Hermann, 1994).
5. Gerard & O'Regan. *A brief history of computing* (Springer, 2008).
6. Ragsxl. *IQM Quantum Computer in Espoo Finland* https://commons.wikimedia.org/wiki/File:IQM_Quantum_Computer_Espoo_Finland.jpg.
7. Bromley, A. G. Charles babbage's analytical engine, 1838. *Annals of the History of Computing* **4,** 196–217 (1982).
8. Boole, G. The calculus of logic (1848).
9. Durao, F., Carvalho, J. F. S., Fonseka, A. & Garcia, V. C. A systematic review on cloud computing. *The Journal of Supercomputing* **68,** 1321–1346 (2014).
10. Ali, M., Khan, S. U. & Vasilakos, A. V. Security in cloud computing: Opportunities and challenges. *Information sciences* **305,** 357–383 (2015).
11. Johnson, K. B. *et al.* Precision medicine, AI, and the future of personalized health care. *Clinical and translational science* **14,** 86–93 (2021).
12. Zhou, J. *et al.* Graph neural networks: A review of methods and applications. *AI open* **1,** 57–81 (2020).
13. Shinde, P. P. & Shah, S. *A review of machine learning and deep learning applications* in *2018 Fourth international conference on computing communication control and automation (ICCUBEA)* (2018), 1–6.
14. Booch, G. *et al. Thinking fast and slow in AI* in *Proceedings of the AAAI Conference on Artificial Intelligence* **35** (2021), 15042–15046.
15. Kambhampati, S. Can large language models reason and plan? *Annals of the New York Academy of Sciences* (2024).
16. Andrews, M. The immortal science of ML: Machine learning & the theory-free ideal. *Preprint at https://rgdoi. net/10.13140/RG* **2** (2023).
17. Andrews, M., Smart, A. & Birhane, A. The reanimation of pseudoscience in machine learning and its ethical repercussions. *Patterns* (2024).
18. Borenstein, J. & Howard, A. Emerging challenges in AI and the need for AI ethics education. *AI and Ethics* **1,** 61–65 (2021).
19. Deng, L., Li, G., Han, S., Shi, L. & Xie, Y. Model compression and hardware acceleration for neural networks: A comprehensive survey. *Proceedings of the IEEE* **108,** 485–532 (2020).
20. Gill, S. S. *et al.* Quantum computing: A taxonomy, systematic review and future directions. *Software: Practice and Experience* **52,** 66–114 (2022).

21. Katz, E. Biocomputing—Tools, aims, perspectives. *Current opinion in biotechnology* **34,** 202–208 (2015).
22. Saint-Pol, B. *Physician treating a patient. Red-figure Attic aryballos, ca. 480–470 BC.* https://commons.wikimedia.org/wiki/File:Medicine_aryballos_Louvre_CA1989-2183.jpg.
23. Henschen, F. *The Human Skull: A Cultural History* ISBN: 9787420001657 (Thames & Hudson, 1966).
24. Restak, R. *Mysteries of the mind* (National Geographic Society, 2000).
25. Larson, G. *et al.* Current perspectives and the future of domestication studies. *Proceedings of the National Academy of Sciences* **111,** 6139–6146 (2014).
26. Magner, L. *A History of the Life Sciences, Revised and Expanded* ISBN: 9780203911006. https://books.google.es/books?id=YKJ6gVYbrGwC (CRC Press, 2002).
27. Mayr, E. *The Growth of Biological Thought: Diversity, Evolution, and Inheritance* ISBN: 9780674364462. https://books.google.es/books?id=pHThtE2R0UQC (Belknap Press, 1982).
28. Kilgour, F. G. GALEN. *Scientific American* **196,** 105–117. ISSN: 00368733, 19467087. http://www.jstor.org/stable/24940775 (2024) (1957).
29. Magnus, A. *The book of Minerals* (Dalcassian Publishing Company, 1967).
30. Magnus, A., Kitchell, K. F. & Resnick, I. M. *Albertus Magnus On Animals V1 2: A Medieval Summa Zoologica Revised Edition* ISBN: 9780814213599. http://www.jstor.org/stable/j.ctv1jq5qp2 (2024) (Ohio State University Press, 2018).
31. Salzberg, R. *The Renaissance on the Road: Mobility, Migration and Cultural Exchange* (Cambridge University Press, 2023).
32. Ball, P. *Spreading It Around: Mobility, Disease and Epidemics* in *Why Society is a Complex Matter: Meeting Twenty-first Century Challenges with a New Kind of Science* (2012), 28–32.
33. Mesquita, E. T., Souza Júnior, C. V. d. & Ferreira, T. R. Andreas Vesalius 500 years-A Renaissance that revolutionized cardiovascular knowledge. *Brazilian Journal of Cardiovascular Surgery* **30,** 260–265 (2015).
34. Lasky, I. I. The martyrdom of doctor Andreas Vesalius. *Clinical Orthopaedics and Related Research®* **259,** 304–311 (1990).
35. Ribatti, D. William Harvey and the discovery of the circulation of the blood. *Journal of angiogenesis research* **1,** 1–2 (2009).
36. Fay, B. Learned societies in Europe and America in the eighteenth century. *The American Historical Review* **37,** 255–266 (1932).
37. Robertson, L. A. Antoni van Leeuwenhoek 1723–2023: a review to commemorate Van Leeuwenhoek's death, 300 years ago: For submission to Antonie van Leeuwenhoek journal of microbiology. *Antonie van Leeuwenhoek* **116,** 919–935 (2023).
38. De Lavoisier, A., de Lavoisier, M. & Cuchet, G. *Traité élémentaire de chimie, présenté dans un ordre nouveau et d'après les découvertes modernes ; avec figures : par M. Lavoisier,... Tome premier [-second].* (Chez Cuchet, Libraire, rue & hôtel Serpente, 1789).
39. De Morveau, L. *et al. Méthode de nomenclature chimique* (Chez Cuchet, libraire, 1787).
40. Burkhardt Jr, R. W. Lamarck, evolution, and the inheritance of acquired characters. *Genetics* **194,** 793–805 (2013).
41. Goodsell, D. S., Voigt, M., Zardecki, C. & Burley, S. K. Integrative illustration for coronavirus outreach. *PLoS biology* **18,** e3000815 (2020).

42. Darwin, C., West, W., Clowes, W. & Sons. *On the Origin of Species by Means of Natural Selection, Or The Preservation of Favoured Races in the Struggle for Life* ISBN: 9781530766161. https://books.google.es/books?id=jTZbAAAAQAAJ (John Murray, Albemarle Street., 1859).

43. Gayon, J. From Mendel to epigenetics: History of genetics. *Comptes rendus biologies* **339,** 225–230 (2016).

44. Harrison, A. John Dalton's atomic theory: Using the history and nature of science to teach particle concepts? (2002).

45. Kaji, M. Mendeleev's discovery of the periodic law: The origin and the reception. *Foundations of Chemistry* **5,** 189–214 (2003).

46. University of Berkeley. *Random Mutations and Evolutionary Change: Ronald Fisher, JBS Haldane, & Sewall Wright* Accessed April 12, 2024. https://evolution.berkeley.edu/the-history-of-evolutionary-thought/1900-to-present/random-mutations-and-evolutionary-change-ronald-fisher-jbs-haldane-sewall-wright/ (2024).

47. Franklin, R. E. & Gosling, R. G. Evidence for 2-chain Helix in crystalline structure of sodium deoxyribonucleate. *Nature* **172,** 156–157. ISSN: 00280836. https://www.nature.com/articles/172156a0 (4369 1953).

48. Watson, J. D. & Crick, F. H. Molecular structure of nucleic acids: A structure for deoxyribose nucleic acid. *Nature* **171,** 737–738. ISSN: 00280836. https://www.nature.com/articles/171737a0 (4356 Apr. 1953).

49. Klug, A. Rosalind Franklin and the discovery of the structure of DNA. *Nature* **219,** 808–844. ISSN: 00280836. https://www.nature.com/articles/219808a0 (5156 Aug. 1968).

50. Stretton, A. O. W. The First Sequence: Fred Sanger and Insulin. *Genetics* **162,** 527–532. ISSN: 1943-2631. eprint: https://academic.oup.com/genetics/article-pdf/162/2/527/42046134/genetics0527.pdf. https://doi.org/10.1093/genetics/162.2.527 (Oct. 2002).

51. Choudhuri, S. The Path from Nuclein to Human Genome: A Brief History of DNA with a Note on Human Genome Sequencing and Its Impact on Future Research in Biology. *Bulletin of Science, Technology & Society* **23,** 360–367. https://api.semanticscholar.org/CorpusID:84467931 (2003).

52. Stillwell, W. *An introduction to biological membranes: composition, structure and function* (Elsevier, 2016).

53. Kleinzeller, A. William Hewson's studies of red blood corpuscles and the evolving concept of a cell membrane. *American Journal of Physiology-Cell Physiology* **271,** C1–C8 (1996).

54. Benos, D. J., Deamer, D. W., Kleinzeller, A. & Fambrough, D. M. *Membrane permeability: 100 years since Ernest Overton* (Academic Press, 1999).

55. Gorter, E. & Grendel, F. On bimolecular layers of lipoids on the chromocytes of the blood. *The Journal of experimental medicine* **41,** 439 (1925).

56. Dowhan, W. Molecular basis for membrane phospholipid diversity: why are there so many lipids? *Annual review of biochemistry* **66,** 199–232 (1997).

57. Borchman, D., Foulks, G. N., Yappert, M. C., Tang, D. & Ho, D. V. Spectroscopic evaluation of human tear lipids. *Chemistry and physics of lipids* **147,** 87–102 (2007).

58. Yeagle, P. L. *The structure of biological membranes* (CRC press, 2004).

59. Fahy, E. *et al.* A comprehensive classification system for lipids. *Journal of lipid research* **46,** 839–861 (2005).

60. Wenk, M. R. The emerging field of lipidomics. *Nature reviews Drug discovery* **4,** 594–610 (2005).

61. Helenius, A. & Simons, K. Solubilization of membranes by detergents. *Biochimica et Biophysica Acta (BBA)-Reviews on Biomembranes* **415,** 29–79 (1975).

62. Cavitch, S. M. & Susan, M. The Natural Soap Book. *Pownal, VT: Storey Commu* (1994).

63. The Elder, P. *Historia Naturalis* (I DC).

64. Vance, J. E. & Steenbergen, R. Metabolism and functions of phosphatidylserine. *Progress in lipid research* **44,** 207–234 (2005).

65. Vivanco, I. & Sawyers, C. L. The phosphatidylinositol 3-kinase–AKT pathway in human cancer. *Nature Reviews Cancer* **2,** 489–501 (2002).

66. Ferguson, M. & Williams, A. F. Cell-surface anchoring of proteins via glycosyl-phosphatidylinositol structures. *Annual review of biochemistry* **57,** 285–320 (1988).

67. Houtkooper, R. & Vaz, F. Cardiolipin, the heart of mitochondrial metabolism. *Cellular and Molecular Life Sciences* **65,** 2493–2506 (2008).

68. Yeagle, P. *The Structure of Biological Membranes, Third Edition* ISBN: 9781439809570. `https://books.google.es/books?id=JVCAB1WwDmYC` (Taylor & Francis, 2011).

69. Foobar. *Schematic representation of the different types of interaction between polytopic membrane proteins and the cell membrane* `https://commons.wikimedia.org/wiki/File:Polytopic_membrane_protein.png`.

70. Marsh, D., Horváth, L. I., Swamy, M. J., Mantripragada, S. & Kleinschmidt, J. H. Interaction of membrane-spanning proteins with peripheral and lipid-anchored membrane proteins: perspectives from protein-lipid interactions. *Molecular membrane biology* **19,** 247–255 (2002).

71. Boggs, J. *Myelin Basic Protein* ISBN: 9781604566994. `https://books.google.es/books?id=VeePNAAACAAJ` (Nova Science Publishers, 2008).

72. Ozols, J., Gerard, C. & Nobrega, F. Proteolytic cleavage of horse liver cytochrome b5. Primary structure of the heme-containing moiety. *Journal of Biological Chemistry* **251,** 6767–6774 (1976).

73. Sakmar, T. P. Twenty years of the magnificent seven: with decades of discovery on seven transmembrane receptors, why haven't we saved the day? *The Scientist* **19,** 22–24 (2005).

74. Wimley, W. C. The versatile β-barrel membrane protein. *Current opinion in structural biology* **13,** 404–411 (2003).

75. Farazi, T. A., Waksman, G. & Gordon, J. I. The biology and enzymology of proteinN-myristoylation* 210. *Journal of biological chemistry* **276,** 39501–39504 (2001).

76. Bijlmakers, M.-J. & Marsh, M. The on–off story of protein palmitoylation. *Trends in cell biology* **13,** 32–42 (2003).

77. Johnson, J. E. & Cornell, R. B. Amphitropic proteins: regulation by reversible membrane interactions. *Molecular membrane biology* **16,** 217–235 (1999).

78. Jones, M. *Overview of LPS structure.* `https://commons.wikimedia.org/wiki/File:LPS.svg`.

79. Nikaido, H. & Vaara, M. Molecular basis of bacterial outer membrane permeability. *Microbiological reviews* **49,** 1–32 (1985).

80. Shearer, J., Marzinek, J. K., Bond, P. J. & Khalid, S. Molecular dynamics simulations of bacterial outer membrane lipid extraction: Adequate sampling? *The Journal of Chemical Physics* **153** (2020).

81. Berglund, N. A. *et al.* Interaction of the antimicrobial peptide polymyxin B1 with both membranes of E. coli: a molecular dynamics study. *PLoS computational biology* **11,** e1004180 (2015).

82. Villarreal, M. R. *Phospholipids aqueous solution structure.* `https://commons.wikimedia.org/wiki/File:Phospholipids_aqueous_solution_structures.svg`.

83. Tanford, C. *The Hydrophobic Effect: Formation of Micelles and Biological Membranes* ISBN: 9780894646218. `https://books.google.es/books?id=pv0bQAAACAAJ` (Krieger, 1991).

84. De Weer, P. A century of thinking about cell membranes. *Annual review of physiology* **62,** 919 (2000).

85. Danielli, J. F. & Davson, H. A contribution to the theory of permeability of thin films. *Journal of cellular and comparative physiology* **5,** 495–508 (1935).

86. Robertson, J. *The cell membrane concept* in *Journal Of Physiology-london* **140** (1958), P58–P59.

87. Robertso, J. The molecular structure and contact relationships of cell membranes. *Progress in biophysics and molecular biology* **10,** 343–418 (1960).

88. Benson, A. On the orientation of lipids in chloroplast and cell membranes. *Journal of the American Oil Chemists Society* **43,** 265–270 (1966).

89. Vanderkooi, G. & Green, D. E. Biological membrane structure, I. The protein crystal model for membranes. *Proceedings of the National Academy of Sciences* **66,** 615–621 (1970).

90. Singer, S. J. & Nicolson, G. L. The Fluid Mosaic Model of the Structure of Cell Membranes: Cell membranes are viewed as two-dimensional solutions of oriented globular proteins and lipids. *Science* **175,** 720–731 (1972).

91. Karnovsky, M. J., Kleinfeld, A. M., Hoover, R. L. & Klausner, R. D. The concept of lipid domains in membranes. *The Journal of cell biology* **94,** 1–6 (1982).

92. Devaux, P. F. & Morris, R. Transmembrane asymmetry and lateral domains in biological membranes. *Traffic* **5,** 241–246 (2004).

93. Villarreal, M. R. *Cell membrane detailed diagram.* `https://commons.wikimedia.org/wiki/File:Cell_membrane_detailed_diagram_en.svg`.

94. Demel, R., Jansen, J., Van Dijck, P. & Van Deenen, L. The preferential interaction of cholesterol with different classes of phospholipids. *Biochimica et biophysica acta* **465,** 1–10 (1977).

95. Estep, T., Mountcastle, D., Barenholz, Y., Biltonen, R. & Thompson, T. Thermal behavior of synthetic sphingomyelin-cholesterol dispersions. *Biochemistry* **18,** 2112–2117 (1979).

96. Simons, K. & Ikonen, E. Functional rafts in cell membranes. *nature* **387,** 569–572 (1997).

97. Pike, L. J. Rafts defined: a report on the Keystone Symposium on Lipid Rafts and Cell Function. *Journal of lipid research* **47,** 1597–1598 (2006).

98. Levental, I., Levental, K. R. & Heberle, F. A. Lipid rafts: controversies resolved, mysteries remain. *Trends in cell biology* **30,** 341–353 (2020).

99. Shaw, A. S. Lipid rafts: now you see them, now you don't. *Nature immunology* **7,** 1139–1142 (2006).

100. lgkoch, L. K. *Lipid Raft.* `https://commons.wikimedia.org/wiki/File:Lipid_Raft.png`.

101. Schenck, M., Carpinteiro, A., Grassmé, H., Lang, F. & Gulbins, E. Ceramide: physiological and pathophysiological aspects. *Archives of biochemistry and biophysics* **462,** 171–175 (2007).

102. Wassall, S. R. & Stillwell, W. Docosahexaenoic acid domains: the ultimate non-raft membrane domain. *Chemistry and physics of lipids* **153,** 57–63 (2008).

103. Wassall, S. R. & Stillwell, W. Polyunsaturated fatty acid–cholesterol interactions: domain formation in membranes. *Biochimica et Biophysica Acta (BBA)-Biomembranes* **1788,** 24–32 (2009).

104. Casares, D., Escribá, P. V. & Rosselló, C. A. Membrane lipid composition: effect on membrane and organelle structure, function and compartmentalization and therapeutic avenues. *International journal of molecular sciences* **20,** 2167 (2019).

105. Andersson, G., Karlberg, O., Canbäck, B. & Kurland, C. G. On the origin of mitochondria: a genomics perspective. *Philosophical Transactions of the Royal Society of London. Series B: Biological Sciences* **358,** 165–179 (2003).

106. Whatley, J. M. in *International review of cytology* 259–299 (Elsevier, 1993).

107. Massana, R. The nitroplast: A nitrogen-fixing organelle. *Science* **384,** 160–161 (2024).

108. Corradi, V. *et al.* Emerging diversity in lipid–protein interactions. *Chemical reviews* **119,** 5775–5848 (2019).

109. Sciacca, M. F. *et al.* Lipid-chaperone hypothesis: A common molecular mechanism of membrane disruption by intrinsically disordered proteins. *ACS chemical neuroscience* **11,** 4336–4350 (2020).

110. Hinderliter, A., Biltonen, R. L. & Almeida, P. F. Lipid modulation of protein-induced membrane domains as a mechanism for controlling signal transduction. *Biochemistry* **43,** 7102–7110 (2004).

111. Nussinov, R., Tsai, C.-J. & Jang, H. Ras assemblies and signaling at the membrane. *Current opinion in structural biology* **62,** 140–148 (2020).

112. Südhof, T. C. Towards an understanding of synapse formation. *Neuron* **100,** 276–293 (2018).

113. Stieger, B., Steiger, J. & Locher, K. P. Membrane lipids and transporter function. *Biochimica et Biophysica Acta (BBA)-Molecular Basis of Disease* **1867,** 166079 (2021).

114. Parisio, G., Stocchero, M. & Ferrarini, A. Passive membrane permeability: beyond the standard solubility-diffusion model. *Journal of Chemical Theory and Computation* **9,** 5236–5246 (2013).

115. Campellone, K. G. & Welch, M. D. A nucleator arms race: cellular control of actin assembly. *Nature reviews Molecular cell biology* **11,** 237–251 (2010).

116. Sens, P. & Plastino, J. Membrane tension and cytoskeleton organization in cell motility. *Journal of Physics: Condensed Matter* **27,** 273103 (2015).

117. Welte, M. A. & Gould, A. P. Lipid droplet functions beyond energy storage. *Biochimica et Biophysica Acta (BBA)-Molecular and Cell Biology of Lipids* **1862,** 1260–1272 (2017).

118. Parrales, A. & Iwakuma, T. p53 as a regulator of lipid metabolism in cancer. *International journal of molecular sciences* **17,** 2074 (2016).

119. Harayama, T. & Riezman, H. Understanding the diversity of membrane lipid composition. *Nature reviews Molecular cell biology* **19,** 281–296 (2018).

120. Sohlenkamp, C. & Geiger, O. Bacterial membrane lipids: diversity in structures and pathways. *FEMS microbiology reviews* **40,** 133–159 (2016).

121. De Kroon, A. I., Rijken, P. J. & De Smet, C. H. Checks and balances in membrane phospholipid class and acyl chain homeostasis, the yeast perspective. *Progress in lipid research* **52,** 374–394 (2013).

122. Perczyk, P., Wójcik, A., Wydro, P. & Broniatowski, M. The role of phospholipid composition and ergosterol presence in the adaptation of fungal membranes to harsh environmental conditions–membrane modeling study. *Biochimica et Biophysica Acta (BBA)-Biomembranes* **1862,** 183136 (2020).

123. Szlasa, W., Zendran, I., Zalesińska, A., Tarek, M. & Kulbacka, J. Lipid composition of the cancer cell membrane. *Journal of bioenergetics and biomembranes* **52,** 321–342 (2020).

124. Ketter, E. & Randall, G. Virus impact on lipids and membranes. *Annual review of virology* **6,** 319–340 (2019).

125. Miller, S. & Krijnse-Locker, J. Modification of intracellular membrane structures for virus replication. *Nature Reviews Microbiology* **6,** 363–374 (2008).

126. Svennerholm, L., Boström, K., Jungbjer, B. & Olsson, L. Membrane lipids of adult human brain: lipid composition of frontal and temporal lobe in subjects of age 20 to 100 years. *Journal of neurochemistry* **63,** 1802–1811 (1994).

127. Egawa, J., Pearn, M. L., Lemkuil, B. P., Patel, P. M. & Head, B. P. Membrane lipid rafts and neurobiology: age-related changes in membrane lipids and loss of neuronal function. *The Journal of physiology* **594,** 4565–4579 (2016).

128. Choe, M., Jackson, C. & Yu, B. P. Lipid peroxidation contributes to age-related membrane rigidity. *Free Radical Biology and Medicine* **18,** 977–984 (1995).

129. Albouery, M. *et al.* Age-related changes in the gut microbiota modify brain lipid composition. *Frontiers in Cellular and Infection Microbiology* **9,** 444 (2020).

130. Douglas-Escobar, M., Elliott, E. & Neu, J. Effect of intestinal microbial ecology on the developing brain. *JAMA pediatrics* **167,** 374–379 (2013).

131. Foster, J. A., Lyte, M., Meyer, E. & Cryan, J. F. Gut microbiota and brain function: an evolving field in neuroscience. *International Journal of Neuropsychopharmacology* **19,** pyv114 (2016).

132. Escribá, P. V. Membrane-lipid therapy: a new approach in molecular medicine. *Trends in molecular medicine* **12,** 34–43 (2006).

133. Escribá, P. V. Membrane-lipid therapy: A historical perspective of membrane-targeted therapies—From lipid bilayer structure to the pathophysiological regulation of cells. *Biochimica et Biophysica Acta (BBA)-Biomembranes* **1859,** 1493–1506 (2017).

134. Bahar, A. A. & Ren, D. Antimicrobial peptides. *Pharmaceuticals* **6,** 1543–1575 (2013).

135. Jenssen, H., Hamill, P. & Hancock, R. E. Peptide antimicrobial agents. *Clinical microbiology reviews* **19,** 491–511 (2006).

136. Loeffler, J. M., Nelson, D. & Fischetti, V. A. Rapid killing of Streptococcus pneumoniae with a bacteriophage cell wall hydrolase. *Science* **294,** 2170–2172 (2001).

137. Madani, F., Lindberg, S., Langel, Ü., Futaki, S. & Gräslund, A. Mechanisms of cellular uptake of cell-penetrating peptides. *Journal of biophysics* **2011,** 414729 (2011).

138. Barceló-Coblijn, G. *et al.* Sphingomyelin and sphingomyelin synthase (SMS) in the malignant transformation of glioma cells and in 2-hydroxyoleic acid therapy. *Proceedings of the National Academy of Sciences* **108,** 19569–19574 (2011).

139. Escribá, P. V. *et al.* Membrane lipid therapy: Modulation of the cell membrane composition and structure as a molecular base for drug discovery and new disease treatment. *Progress in lipid research* **59,** 38–53 (2015).

140. Terés, S. *et al.* 2-Hydroxyoleate, a nontoxic membrane binding anticancer drug, induces glioma cell differentiation and autophagy. *Proceedings of the National Academy of Sciences* **109,** 8489–8494 (2012).

141. Terés, S. *et al.* Normalization of sphingomyelin levels by 2-hydroxyoleic acid induces autophagic cell death of SF767 cancer cells. *Autophagy* **8,** 1542–1544 (2012).

142. Erazo, T. *et al.* The new antitumor drug ABTL0812 inhibits the Akt/mTORC1 axis by upregulating tribbles-3 pseudokinase. *Clinical Cancer Research* **22,** 2508–2519 (2016).

143. Cacabelos, D. *et al.* Interplay between TDP-43 and docosahexaenoic acid-related processes in amyotrophic lateral sclerosis. *Neurobiology of Disease* **88,** 148–160 (2016).

144. Murphy, E. J., Schapiro, M. B., Rapoport, S. I. & Shetty, H. U. Phospholipid composition and levels are altered in Down syndrome brain. *Brain research* **867,** 9–18 (2000).

145. Martins, I. C. *et al.* Lipids revert inert Aβ amyloid fibrils to neurotoxic protofibrils that affect learning in mice. *The EMBO journal* **27,** 224–233 (2008).

146. Plourde, M. *et al.* Unresolved issues in the link between docosahexaenoic acid and Alzheimer's disease. *Prostaglandins, leukotrienes and essential fatty acids* **77,** 301–308 (2007).

147. Prasad, M. R., Lovell, M. A., Yatin, M., Dhillon, H. & Markesbery, W. R. Regional membrane phospholipid alterations in Alzheimer's disease. *Neurochemical research* **23,** 81–88 (1998).

148. Söderberg, M., Edlund, C., Kristensson, K. & Dallner, G. Fatty acid composition of brain phospholipids in aging and in Alzheimer's disease. *Lipids* **26,** 421–425 (1991).

149. Díaz, M. *et al.* Biophysical alterations in lipid rafts from human cerebral cortex associate with increased BACE1/AβPP interaction in early stages of Alzheimer's disease. *Journal of Alzheimer's Disease* **43,** 1185–1198 (2015).

150. Yang, X., Sun, G. Y., Eckert, G. P. & Lee, J. C. Cellular membrane fluidity in amyloid precursor protein processing. *Molecular neurobiology* **50,** 119–129 (2014).

151. Fiol-deRoque, M. A. *et al.* Cognitive recovery and restoration of cell proliferation in the dentate gyrus in the 5XFAD transgenic mice model of Alzheimer's disease following 2-hydroxy-DHA treatment. *Biogerontology* **14,** 763–775 (2013).

152. Torres, M. *et al.* Membrane lipid modifications and therapeutic effects mediated by hydroxydocosahexaenoic acid on Alzheimer's disease. *Biochimica et Biophysica Acta (BBA)-Biomembranes* **1838,** 1680–1692 (2014).

153. Marion-Letellier, R., Savoye, G. & Ghosh, S. Polyunsaturated fatty acids and inflammation. *IUBMB life* **67,** 659–667 (2015).

154. Lopez, D. H. *et al.* 2-Hydroxy arachidonic acid: a new non-steroidal anti-inflammatory drug. *PloS one* **8,** e72052 (2013).

155. Alaarg, A. *et al.* Docosahexaenoic acid liposomes for targeting chronic inflammatory diseases and cancer: an in vitro assessment. *International journal of nanomedicine,* 5027–5040 (2016).

156. Da Silva-Santi, L. G. *et al.* Liver fatty acid composition and inflammation in mice fed with high-carbohydrate diet or high-fat diet. *Nutrients* **8,** 682 (2016).

157. Bouwens, M. *et al.* Fish-oil supplementation induces antiinflammatory gene expression profiles in human blood mononuclear cells. *The American journal of clinical nutrition* **90,** 415–424 (2009).

158. Teres, S. *et al.* Oleic acid content is responsible for the reduction in blood pressure induced by olive oil. *Proceedings of the National Academy of Sciences* **105,** 13811–13816 (2008).

159. Escribá, P. V., Sánchez-Dominguez, J. M., Alemany, R., Perona, J. S. & Ruiz-Gutiérrez, V. Alteration of lipids, G proteins, and PKC in cell membranes of elderly hypertensives. *Hypertension* **41,** 176–182 (2003).

160. Trapani, L., Segatto, M. & Pallottini, V. Regulation and deregulation of cholesterol homeostasis: The liver as a metabolic "power station". *World journal of hepatology* **4,** 184 (2012).

161. Alemany, R. *et al.* 2-Hydroxyoleic acid: a new hypotensive molecule. *Hypertension* **43,** 249–254 (2004).

162. Mori, T. A. Omega-3 fatty acids and hypertension in humans. *Clinical & Experimental Pharmacology & Physiology* **33** (2006).

163. Gawrisch, K., Soubias, O. & Mihailescu, M. Insights from biophysical studies on the role of polyunsaturated fatty acids for function of G-protein coupled membrane receptors. *Prostaglandins, Leukotrienes and Essential Fatty Acids* **79,** 131–134 (2008).

164. Kremmyda, L.-S., Tvrzicka, E., Stankova, B. & Zak, A. Fatty acids as biocompounds: their role in human metabolism, health and disease - A review. Part 2: Fatty acid phisiological roles and applications in human health and disease. *Biomedical Papers of the Medical Faculty of Palacky University in Olomouc* **155** (2011).

165. Schmidt, M. *et al.* Obesity in young men, and individual and combined risks of type 2 diabetes, cardiovascular morbidity and death before 55 years of age: a Danish 33-year follow-up study. *BMJ open* **3,** e002698 (2013).

166. Sloan, F. A., Bethel, M. A., Ruiz, D., Shea, A. H. & Feinglos, M. N. The growing burden of diabetes mellitus in the US elderly population. *Archives of Internal Medicine* **168,** 192–199 (2008).

167. López-Miranda, J. *et al.* Olive oil and health: summary of the II international conference on olive oil and health consensus report, Jaén and Córdoba (Spain) 2008. *Nutrition, metabolism and cardiovascular diseases* **20,** 284–294 (2010).

168. Vögler, O. *et al.* Structure–effect relation of C18 long-chain fatty acids in the reduction of body weight in rats. *International journal of obesity* **32,** 464–473 (2008).

169. Perez-Martinez, P., Garcia-Rios, A., Delgado-Lista, J., Perez-Jimenez, F. & Lopez-Miranda, J. Mediterranean diet rich in olive oil and obesity, metabolic syndrome and diabetes mellitus. *Current pharmaceutical design* **17,** 769–777 (2011).

170. Salas-Salvadó, J., Martinez-González, M., Bulló, M. & Ros, E. The role of diet in the prevention of type 2 diabetes. *Nutrition, Metabolism and Cardiovascular Diseases* **21.** Role of Macronutrient Distribution on Weight Loss, B32–B48. ISSN: 0939-4753. `https://www.sciencedirect.com/science/article/pii/S0939475311000895` (2011).

171. Anoop Misra, N. S. & Khurana, L. Obesity, the Metabolic Syndrome, and Type 2 Diabetes in Developing Countries: Role of Dietary Fats and Oils. *Journal of the American College of Nutrition* **29.** PMID: 20823489, 289S–301S (2010).

172. Weijers, R. N. M. Lipid composition of cell membranes and its relevance in type 2 diabetes mellitus. *Current diabetes reviews* **8,** 390–400. ISSN: 1573-3998 (Sept. 2012).

173. Perona, J. S. *et al.* Consumption of Virgin Olive Oil Influences Membrane Lipid Composition and Regulates Intracellular Signaling in Elderly Adults With Type 2 Diabetes Mellitus. *The Journals of Gerontology: Series A* **62,** 256–263. ISSN: 1079-5006 (Mar. 2007).

174. Kien, C. L. Dietary interventions for metabolic syndrome: role of modifying dietary fats. *Current diabetes reports* **9,** 43–50 (2009).

175. Song, G. *et al.* Mechanical stretch promotes proliferation of rat bone marrow mesenchymal stem cells. *Colloids and Surfaces B: Biointerfaces* **58,** 271–277 (2007).

176. Luu, Y. K. *et al.* Mechanical stimulation of mesenchymal stem cell proliferation and differentiation promotes osteogenesis while preventing dietary-induced obesity. *Journal of bone and mineral research* **24,** 50–61 (2009).

177. Hajra, L. *et al.* The NF-κB signal transduction pathway in aortic endothelial cells is primed for activation in regions predisposed to atherosclerotic lesion formation. *Proceedings of the National Academy of Sciences* **97,** 9052–9057 (2000).

178. Anishkin, A., Loukin, S. H., Teng, J. & Kung, C. Feeling the hidden mechanical forces in lipid bilayer is an original sense. *Proceedings of the National Academy of Sciences* **111,** 7898–7905 (2014).

179. Nyholm, T. K., Özdirekcan, S. & Killian, J. A. How protein transmembrane segments sense the lipid environment. *Biochemistry* **46,** 1457–1465 (2007).

180. Janmey, P. A. & McCulloch, C. A. Cell mechanics: integrating cell responses to mechanical stimuli. *Annu. Rev. Biomed. Eng.* **9,** 1–34 (2007).

181. Lim, C.-G., Jang, J. & Kim, C. Cellular machinery for sensing mechanical force. *BMB reports* **51,** 623 (2018).

182. Haswell, E. S., Phillips, R. & Rees, D. C. Mechanosensitive channels: what can they do and how do they do it? *Structure* **19,** 1356–1369 (2011).

183. Ogawa, R. in *In Situ Tissue Regeneration* 165–181 (Elsevier, 2016).

184. Ng, J. L., Kersh, M. E., Kilbreath, S. & Knothe Tate, M. Establishing the basis for mechanobiology-based physical therapy protocols to potentiate cellular healing and tissue regeneration. *Frontiers in Physiology* **8,** 303 (2017).

185. Li, R. S. *et al.* Transformable nano-antibiotics for mechanotherapy and immune activation against drug-resistant Gram-negative bacteria. *Science Advances* **9,** eadg9601 (2023).

186. Orgill, D. P. & Bayer, L. R. Update on negative-pressure wound therapy. *Plastic and reconstructive surgery* **127,** 105S–115S (2011).

187. Kurita, M., Okazaki, M., Fujino, T., Takushima, A. & Harii, K. Cyclic stretch induces upregulation of endothelin-1 with keratinocytes in vitro: possible role in mechanical stress-induced hyperpigmentation. *Biochemical and Biophysical Research Communications* **409,** 103–107 (2011).

188. Qureshi, A. A., Ross, K. M., Ogawa, R. & Orgill, D. P. Shock wave therapy in wound healing. *Plastic and Reconstructive Surgery* **128,** 721e–727e (2011).

189. Selvamurugan, N., Kwok, S., Vasilov, A., Jefcoat, S. C. & Partridge, N. C. Effects of BMP-2 and pulsed electromagnetic field (PEMF) on rat primary osteoblastic cell proliferation and gene expression. *Journal of orthopaedic research* **25,** 1213–1220 (2007).

190. Petecchia, L. *et al.* Electro-magnetic field promotes osteogenic differentiation of BM-hMSCs through a selective action on Ca2+-related mechanisms. *Scientific reports* **5,** 13856 (2015).

191. d'Agostino, M., Craig, K., Tibalt, E. & Respizzi, S. Shock wave as biological therapeutic tool: From mechanical stimulation to recovery and healing, through mechanotransduction. *International journal of surgery* **24,** 147–153 (2015).

192. Vahdatpour, B., Sajadieh, S., Bateni, V., Karami, M. & Sajjadieh, H. Extracorporeal shock wave therapy in patients with plantar fasciitis. A randomized, placebo-controlled trial with ultrasonographic and subjective outcome assessments. *Journal of research in medical sciences: the official journal of Isfahan University of Medical Sciences* **17,** 834 (2012).

193. Kisch, T. *et al.* Repetitive shock wave therapy improves muscular microcirculation. *journal of surgical research* **201,** 440–445 (2016).

194. Rosso, F., Bonasia, D. E., Marmotti, A., Cottino, U. & Rossi, R. Mechanical stimulation (pulsed electromagnetic fields "PEMF" and extracorporeal shock wave therapy "ESWT") and tendon regeneration: a possible alternative. *Frontiers in aging neuroscience* **7,** 211 (2015).

195. Knothe Tate, M. L., O'Leary, J., McNamara, E., Cai, L. & Knothe, U. R. Lithotripsy stimulates new bone formation and mitigates loss of bone due to disuse in aged rats. *Technology and Health Care* **21,** 587–597 (2013).

196. Lentacker, I., De Cock, I., Deckers, R., De Smedt, S. & Moonen, C. Understanding ultrasound induced sonoporation: definitions and underlying mechanisms. *Advanced drug delivery reviews* **72,** 49–64 (2014).

197. Miller, D. L., Bao, S. & Morris, J. E. Sonoporation of cultured cells in the rotating tube exposure system. *Ultrasound in medicine & biology* **25,** 143–149 (1999).

198. Ward, M., Wu, J. & Chiu, J.-F. Ultrasound-induced cell lysis and sonoporation enhanced by contrast agents. *The Journal of the Acoustical Society of America* **105,** 2951–2957 (1999).

199. VanBavel, E. Effects of shear stress on endothelial cells: possible relevance for ultrasound applications. *Progress in biophysics and molecular biology* **93,** 374–383 (2007).

200. Wu, J. Theoretical study on shear stress generated by microstreaming surrounding contrast agents attached to living cells. *Ultrasound in medicine & biology* **28,** 125–129 (2002).

201. Postema, M., Van Wamel, A., Lancée, C. T. & De Jong, N. Ultrasound-induced encapsulated microbubble phenomena. *Ultrasound in medicine & biology* **30,** 827–840 (2004).

202. Postema, M., van Wamel, A., ten Cate, F. J. & de Jong, N. High-speed photography during ultrasound illustrates potential therapeutic applications of microbubbles. *Medical physics* **32,** 3707–3711 (2005).

203. Rich, J., Tian, Z. & Huang, T. J. Sonoporation: Past, present, and future. *Advanced materials technologies* **7,** 2100885 (2022).

204. Bhutto, D. F. *et al.* Effect of molecular weight on sonoporation-mediated uptake in human cells. *Ultrasound in Medicine & Biology* **44,** 2662–2672 (2018).

205. Karki, A. *et al.* Sonoporation as an Approach for siRNA delivery into T cells. *Ultrasound in Medicine & Biology* **45,** 3222–3231 (2019).

206. Qin, J., Wang, T.-Y. & Willmann, J. K. Sonoporation: Applications for cancer therapy. *Therapeutic Ultrasound,* 263–291 (2016).

207. Kamimura, H. A. *et al.* Focused ultrasound neuromodulation of cortical and subcortical brain structures using 1.9 MHz. *Medical physics* **43,** 5730–5735 (2016).

208. Downs, M. E. *et al.* Non-invasive peripheral nerve stimulation via focused ultrasound in vivo. *Physics in Medicine & Biology* **63,** 035011 (2018).

209. Sorum, B., Rietmeijer, R. A., Gopakumar, K., Adesnik, H. & Brohawn, S. G. Ultrasound activates mechanosensitive TRAAK K+ channels through the lipid membrane. *Proceedings of the National Academy of Sciences* **118,** e2006980118 (2021).

210. Kubanek, J. *et al.* Ultrasound modulates ion channel currents. *Scientific reports* **6,** 24170 (2016).

211. Phenix, C. P., Togtema, M., Pichardo, S., Zehbe, I. & Curiel, L. High intensity focused ultrasound technology, its scope and applications in therapy and drug delivery. *Journal of Pharmacy & Pharmaceutical Sciences* **17,** 136–153 (2014).

212. Bachu, V. S., Kedda, J., Suk, I., Green, J. J. & Tyler, B. High-intensity focused ultrasound: a review of mechanisms and clinical applications. *Annals of biomedical engineering* **49,** 1975–1991 (2021).

213. Izadifar, Z., Izadifar, Z., Chapman, D. & Babyn, P. An introduction to high intensity focused ultrasound: systematic review on principles, devices, and clinical applications. *Journal of clinical medicine* **9,** 460 (2020).

214. Wu, F. *et al.* Pathological changes in human malignant carcinoma treated with high-intensity focused ultrasound. *Ultrasound in medicine & biology* **27,** 1099–1106 (2001).

215. Wu, F. *et al.* A randomised clinical trial of high-intensity focused ultrasound ablation for the treatment of patients with localised breast cancer. *British journal of cancer* **89,** 2227–2233 (2003).

216. McDannold, N., Clement, G. T., Black, P., Jolesz, F. & Hynynen, K. Transcranial magnetic resonance imaging–guided focused ultrasound surgery of brain tumors: initial findings in 3 patients. *Neurosurgery* **66,** 323–332 (2010).

217. Stewart, E. A. *et al.* Clinical outcomes of focused ultrasound surgery for the treatment of uterine fibroids. *Fertility and sterility* **85,** 22–29 (2006).

218. Peek, M. C., Ahmed, M., Pinder, S. E. & Douek, M. A review of ablative techniques in the treatment of breast fibroadenomata. *Journal of therapeutic ultrasound* **4,** 1–8 (2016).

219. Chang, W. S. *et al.* Unilateral magnetic resonance guided focused ultrasound thalamotomy for essential tremor: practices and clinicoradiological outcomes. *Journal of Neurology, Neurosurgery & Psychiatry* **86,** 257–264 (2015).

220. Magara, A. *et al.* First experience with MR-guided focused ultrasound in the treatment of Parkinson's disease. *Journal of Therapeutic Ultrasound* **2,** 1–8 (2014).

221. Zhou, Y.-F. High intensity focused ultrasound in clinical tumor ablation. *World journal of clinical oncology* **2,** 8 (2011).

222. Karplus, M. & McCammon, J. A. Molecular dynamics simulations of biomolecules. *Nature structural biology* **9,** 646–652 (2002).

223. Alder, B. J. & Wainwright, T. E. Phase transition for a hard sphere system. *The Journal of chemical physics* **27,** 1208–1209 (1957).

224. McCammon, J. A., Gelin, B. R. & Karplus, M. Dynamics of folded proteins. *nature* **267,** 585–590 (1977).

225. Hollingsworth, S. A. & Dror, R. O. Molecular dynamics simulation for all. *Neuron* **99,** 1129–1143 (2018).

226. Jumper, J. *et al.* Highly accurate protein structure prediction with AlphaFold. *nature* **596,** 583–589 (2021).

227. Varadi, M. *et al.* AlphaFold Protein Structure Database in 2024: providing structure coverage for over 214 million protein sequences. *Nucleic acids research* **52,** D368–D375 (2024).

228. Team, G. *Gromacs WebPage* `https://www.gromacs.org/`.

229. Team, A. *The Amber Home Page* `https://ambermd.org/`.

230. Team, C. *Chemistry at HARvard Macromolecular Mechanics* `https://academiccharmm.org/`.

231. Stone, J. E. *et al. Evaluation of emerging energy-efficient heterogeneous computing platforms for biomolecular and cellular simulation workloads* in *2016 IEEE International Parallel and Distributed Processing Symposium Workshops (IPDPSW)* (2016), 89–100.

232. Berneche, S. & Roux, B. Energetics of ion conduction through the K+ channel. *Nature* **414,** 73–77 (2001).

233. Khafizov, K. *et al.* Investigation of the sodium-binding sites in the sodium-coupled betaine transporter BetP. *Proceedings of the National Academy of Sciences* **109,** E3035–E3044 (2012).

234. Li, J. *et al.* Transient formation of water-conducting states in membrane transporters. *Proceedings of the National Academy of Sciences* **110,** 7696–7701 (2013).

235. Brunger, A. T. & Adams, P. D. Molecular dynamics applied to X-ray structure refinement. *Accounts of chemical research* **35,** 404–412 (2002).

236. Trabuco, L. G., Villa, E., Mitra, K., Frank, J. & Schulten, K. Flexible fitting of atomic structures into electron microscopy maps using molecular dynamics. *Structure* **16,** 673–683 (2008).

237. Zhao, G. *et al.* Mature HIV-1 capsid structure by cryo-electron microscopy and all-atom molecular dynamics. *Nature* **497,** 643–646 (2013).

238. Lindorff-Larsen, K., Best, R. B., DePristo, M. A., Dobson, C. M. & Vendruscolo, M. Simultaneous determination of protein structure and dynamics. *Nature* **433,** 128–132 (2005).

239. Dror, R. O. *et al.* Structural basis for modulation of a G-protein-coupled receptor by allosteric drugs. *Nature* **503,** 295–299 (2013).

240. Wacker, D. *et al.* Crystal structure of an LSD-bound human serotonin receptor. *Cell* **168,** 377–389 (2017).

241. Cordero-Morales, J. F. *et al.* Molecular driving forces determining potassium channel slow inactivation. *Nature structural & molecular biology* **14,** 1062–1069 (2007).

242. Fields, J. B. *et al.* Calmodulin gates aquaporin 0 permeability through a positively charged cytoplasmic loop. *Journal of Biological Chemistry* **292,** 185–195 (2017).

243. Liu, Y., Ke, M. & Gong, H. Protonation of Glu135 facilitates the outward-to-inward structural transition of fucose transporter. *Biophysical Journal* **109,** 542–551 (2015).

244. Delemotte, L., Tarek, M., Klein, M. L., Amaral, C. & Treptow, W. Intermediate states of the Kv1. 2 voltage sensor from atomistic molecular dynamics simulations. *Proceedings of the National Academy of Sciences* **108,** 6109–6114 (2011).

245. Yang, Y. I., Shao, Q., Zhang, J., Yang, L. & Gao, Y. Q. Enhanced sampling in molecular dynamics. *The Journal of chemical physics* **151** (2019).

246. Torrie, G. M. & Valleau, J. P. Nonphysical sampling distributions in Monte Carlo free-energy estimation: Umbrella sampling. *Journal of computational physics* **23,** 187–199 (1977).

247. Laio, A. & Parrinello, M. Escaping free-energy minima. *Proceedings of the national academy of sciences* **99,** 12562–12566 (2002).

248. Invernizzi, M. & Parrinello, M. Rethinking metadynamics: from bias potentials to probability distributions. *The journal of physical chemistry letters* **11,** 2731–2736 (2020).

249. Invernizzi, M., Piaggi, P. M. & Parrinello, M. Unified approach to enhanced sampling. *Physical Review X* **10,** 041034 (2020).

250. Sugita, Y. & Okamoto, Y. Replica-exchange molecular dynamics method for protein folding. *Chemical physics letters* **314,** 141–151 (1999).

251. Zhang, J., Yang, Y. I. & Noé, F. Targeted adversarial learning optimized sampling. *The journal of physical chemistry letters* **10,** 5791–5797 (2019).

252. Marrink, S. J. *et al.* Computational modeling of realistic cell membranes. *Chemical reviews* **119,** 6184–6226 (2019).

253. Enkavi, G., Javanainen, M., Kulig, W., Róg, T. & Vattulainen, I. Multiscale simulations of biological membranes: the challenge to understand biological phenomena in a living substance. *Chemical reviews* **119,** 5607–5774 (2019).

254. Van der Ploeg, P. & Berendsen, H. Molecular dynamics simulation of a bilayer membrane. *The Journal of Chemical Physics* **76,** 3271–3276 (1982).

255. Egberts, E. & Berendsen, H. Molecular dynamics simulation of a smectic liquid crystal with atomic detail. *The Journal of chemical physics* **89,** 3718–3732 (1988).

256. Feller, S. E. Molecular dynamics simulations of lipid bilayers. *Current opinion in colloid & interface science* **5,** 217–223 (2000).

257. Essmann, U. & Berkowitz, M. L. Dynamical properties of phospholipid bilayers from computer simulation. *Biophysical journal* **76,** 2081–2089 (1999).

258. Pasenkiewicz-Gierula, M., Takaoka, Y., Miyagawa, H., Kitamura, K. & Kusumi, A. Charge pairing of headgroups in phosphatidylcholine membranes: a molecular dynamics simulation study. *Biophysical journal* **76,** 1228–1240 (1999).

259. Lindahl, E. & Edholm, O. Mesoscopic undulations and thickness fluctuations in lipid bilayers from molecular dynamics simulations. *Biophysical journal* **79,** 426–433 (2000).

260. Feller, S. E. & Pastor, R. W. Constant surface tension simulations of lipid bilayers: the sensitivity of surface areas and compressibilities. *The Journal of chemical physics* **111,** 1281–1287 (1999).

261. Feller, S. E., Huster, D. & Gawrisch, K. Interpretation of NOESY cross-relaxation rates from molecular dynamics simulation of a lipid bilayer. *Journal of the American Chemical Society* **121,** 8963–8964 (1999).

262. Petrache, H. I., Tu, K. & Nagle, J. F. Analysis of simulated NMR order parameters for lipid bilayer structure determination. *Biophysical journal* **76,** 2479–2487 (1999).

263. Smondyrev, A. & Berkowitz, M. Molecular dynamics study of Sn-1 and Sn-2 chain conformations in dipalmitoylphosphatidylcholine membranes. *The Journal of chemical physics* **110,** 3981–3985 (1999).

264. Chakraborty, S. *et al.* How cholesterol stiffens unsaturated lipid membranes. *Proceedings of the National Academy of Sciences* **117,** 21896–21905 (2020).

265. Pogozheva, I. D. *et al.* Comparative molecular dynamics simulation studies of realistic eukaryotic, prokaryotic, and archaeal membranes. *Journal of chemical information and modeling* **62,** 1036–1051 (2022).

266. Miettinen, M. S. & Ollila, O. S. NMRlipids databank. *Biophysical Journal* **121,** 531a (2022).

267. Kiirikki, A. *et al.* NMRlipids Databank makes data-driven analysis of biomembrane properties accessible for all (2023).

268. Dickson, C. J., Walker, R. C. & Gould, I. R. Lipid21: complex lipid membrane simulations with AMBER. *Journal of chemical theory and computation* **18,** 1726–1736 (2022).

269. Grote, F. & Lyubartsev, A. P. Optimization of slipids force field parameters describing headgroups of phospholipids. *The Journal of Physical Chemistry B* **124,** 8784–8793 (2020).

270. Hossein, A. & Deserno, M. Spontaneous curvature, differential stress, and bending modulus of asymmetric lipid membranes. *Biophysical Journal* **118,** 624–642 (2020).

271. Drabik, D., Chodaczek, G., Kraszewski, S. & Langner, M. Mechanical properties determination of DMPC, DPPC, DSPC, and HSPC solid-ordered bilayers. *Langmuir* **36,** 3826–3835 (2020).

272. Fiorin, G., Marinelli, F. & Faraldo-Gómez, J. D. Direct derivation of free energies of membrane deformation and other solvent density variations from enhanced sampling molecular dynamics. *Journal of computational chemistry* **41,** 449–459 (2020).

273. Risselada, H. J. & Marrink, S. J. The molecular face of lipid rafts in model membranes. *Proceedings of the National Academy of Sciences* **105,** 17367–17372 (2008).

274. Carpenter, T. S. *et al.* Capturing phase behavior of ternary lipid mixtures with a refined martini coarse-grained force field. *Journal of chemical theory and computation* **14,** 6050–6062 (2018).

275. Wang, Y., Gkeka, P., Fuchs, J. E., Liedl, K. R. & Cournia, Z. DPPC-cholesterol phase diagram using coarse-grained Molecular Dynamics simulations. *Biochimica et Biophysica Acta (BBA)-Biomembranes* **1858,** 2846–2857 (2016).

276. Risselada, H. J., Marrink, S. J. & Müller, M. Curvature-dependent elastic properties of liquid-ordered domains result in inverted domain sorting on uniaxially compressed vesicles. *Physical review letters* **106,** 148102 (2011).

277. Schäfer, L. V. *et al.* Lipid packing drives the segregation of transmembrane helices into disordered lipid domains in model membranes. *Proceedings of the National Academy of Sciences* **108,** 1343–1348 (2011).

278. De Jong, D. H., Lopez, C. A. & Marrink, S. J. Molecular view on protein sorting into liquid-ordered membrane domains mediated by gangliosides and lipid anchors. *Faraday discussions* **161,** 347–363 (2013).

279. Contreras, F.-X. *et al.* Molecular recognition of a single sphingolipid species by a protein's transmembrane domain. *Nature* **481,** 525–529 (2012).

280. Lee, J. Y., Patel, R. & Lyman, E. Ligand-dependent cholesterol interactions with the human A2A adenosine receptor. *Chemistry and physics of lipids* **169,** 39–45 (2013).

281. Cang, X. *et al.* Mapping the functional binding sites of cholesterol in β2-adrenergic receptor by long-time molecular dynamics simulations. *The Journal of Physical Chemistry B* **117,** 1085–1094 (2013).

282. Sengupta, D., Prasanna, X., Mohole, M. & Chattopadhyay, A. Exploring GPCR–lipid interactions by molecular dynamics simulations: excitements, challenges, and the way forward. *The Journal of Physical Chemistry B* **122,** 5727–5737 (2018).

283. Sengupta, D. & Chattopadhyay, A. Identification of cholesterol binding sites in the serotonin1A receptor. *The journal of physical chemistry B* **116,** 12991–12996 (2012).

284. Rouviere, E., Arnarez, C., Yang, L. & Lyman, E. Identification of two new cholesterol interaction sites on the A2A adenosine receptor. *Biophysical journal* **113,** 2415–2424 (2017).

285. Yen, H.-Y. *et al.* PtdIns (4, 5) P2 stabilizes active states of GPCRs and enhances selectivity of G-protein coupling. *Nature* **559,** 423–427 (2018).

286. Niemela, P. S. *et al.* Membrane proteins diffuse as dynamic complexes with lipids. *Journal of the American Chemical Society* **132,** 7574–7575 (2010).

287. Apajalahti, T. *et al.* Concerted diffusion of lipids in raft-like membranes. *Faraday discussions* **144,** 411–430 (2010).

288. Duneau, J.-P., Khao, J. & Sturgis, J. N. Lipid perturbation by membrane proteins and the lipophobic effect. *Biophysical Journal* **112,** 326a (2017).

289. Guixà-González, R. *et al.* Membrane omega-3 fatty acids modulate the oligomerisation kinetics of adenosine A2A and dopamine D2 receptors. *Scientific reports* **6,** 19839 (2016).

290. Periole, X., Knepp, A. M., Sakmar, T. P., Marrink, S. J. & Huber, T. Structural determinants of the supramolecular organization of G protein-coupled receptors in bilayers. *Journal of the American Chemical Society* **134,** 10959–10965 (2012).

291. Ghosh, A., Sonavane, U. & Joshi, R. Multiscale modelling to understand the self-assembly mechanism of human β2-adrenergic receptor in lipid bilayer. *Computational biology and chemistry* **48,** 29–39 (2014).

292. Mondal, S. *et al.* Membrane driven spatial organization of GPCRs. *Scientific reports* **3,** 2909 (2013).

293. Castillo, N., Monticelli, L., Barnoud, J. & Tieleman, D. P. Free energy of WALP23 dimer association in DMPC, DPPC, and DOPC bilayers. *Chemistry and physics of lipids* **169,** 95–105 (2013).

294. Grau, B. *et al.* The role of hydrophobic matching on transmembrane helix packing in cells. *Cell stress* **1,** 90 (2017).

295. Simunovic, M. & Bassereau, P. Reshaping biological membranes in endocytosis: crossing the configurational space of membrane-protein interactions. *Biological chemistry* **395,** 275–283 (2014).

296. Kozlov, M. M. *et al.* Mechanisms shaping cell membranes. *Current opinion in cell biology* **29,** 53–60 (2014).

297. Baumgart, T., Capraro, B. R., Zhu, C. & Das, S. L. Thermodynamics and mechanics of membrane curvature generation and sensing by proteins and lipids. *Annual review of physical chemistry* **62,** 483–506 (2011).

298. Dos Santos Soares, R. d. O., Bortot, L. O., van Der Spoel, D. & Caliri, A. Membrane vesiculation induced by proteins of the dengue virus envelope studied by molecular dynamics simulations. *Journal of Physics: Condensed Matter* **29,** 504002 (2017).

299. Woo, H.-J. & Wallqvist, A. Spontaneous buckling of lipid bilayer and vesicle budding induced by antimicrobial peptide magainin 2: a coarse-grained simulation study. *The journal of physical chemistry B* **115,** 8122–8129 (2011).

300. Sodt, A. J. & Pastor, R. W. Molecular modeling of lipid membrane curvature induction by a peptide: more than simply shape. *Biophysical journal* **106,** 1958–1969 (2014).

301. Patel, D. S. *et al.* Influence of ganglioside GM1 concentration on lipid clustering and membrane properties and curvature. *Biophysical journal* **111,** 1987–1999 (2016).

302. Wu, Q.-Y. & Liang, Q. Interplay between curvature and lateral organization of lipids and peptides/proteins in model membranes. *Langmuir* **30,** 1116–1122 (2014).

303. Baoukina, S., Ingólfsson, H. I., Marrink, S. J. & Tieleman, D. P. Curvature-induced sorting of lipids in plasma membrane tethers. *Advanced Theory and Simulations* **1,** 1800034 (2018).

304. Fuhrmans, M., Marelli, G., Smirnova, Y. G. & Müller, M. Mechanics of membrane fusion/pore formation. *Chemistry and physics of lipids* **185,** 109–128 (2015).

305. Beaven, A. H., Sapp, K. & Sodt, A. J. Simulated dynamic cholesterol redistribution favors membrane fusion pore constriction. *Biophysical Journal* **122,** 2162–2175 (2023).

306. Smirnova, Y. G., Marrink, S.-J., Lipowsky, R. & Knecht, V. Solvent-exposed tails as prestalk transition states for membrane fusion at low hydration. *Journal of the American Chemical Society* **132,** 6710–6718 (2010).

307. Kawamoto, S. & Shinoda, W. Free energy analysis along the stalk mechanism of membrane fusion. *Soft matter* **10,** 3048–3054 (2014).

308. Jahn, R., Cafiso, D. C. & Tamm, L. K. Mechanisms of SNARE proteins in membrane fusion. *Nature Reviews Molecular Cell Biology* **25,** 101–118 (2024).

309. Case, D. A. *et al.* The Amber biomolecular simulation programs. *Journal of computational chemistry* **26,** 1668–1688 (2005).

310. Dickson, C. J., Rosso, L., Betz, R. M., Walker, R. C. & Gould, I. R. GAFFlipid: a General Amber Force Field for the accurate molecular dynamics simulation of phospholipid. *Soft Matter* **8,** 9617–9627 (2012).

311. Dickson, C. J. *et al.* Lipid14: the amber lipid force field. *Journal of chemical theory and computation* **10,** 865–879 (2014).

312. Jorgensen, W. L. & Tirado-Rives, J. The OPLS [optimized potentials for liquid simulations] potential functions for proteins, energy minimizations for crystals of cyclic peptides and crambin. *Journal of the American Chemical Society* **110,** 1657–1666 (1988).

313. Jorgensen, W. L., Maxwell, D. S. & Tirado-Rives, J. Development and testing of the OPLS all-atom force field on conformational energetics and properties of organic liquids. *Journal of the american chemical society* **118,** 11225–11236 (1996).

314. Pluhackova, K. *et al.* A critical comparison of biomembrane force fields: structure and dynamics of model DMPC, POPC, and POPE bilayers. *The Journal of Physical Chemistry B* **120,** 3888–3903 (2016).

315. Chandrasekhar, I. *et al.* A consistent potential energy parameter set for lipids: dipalmitoylphosphatidylcholine as a benchmark of the GROMOS96 45A3 force field. *European Biophysics Journal* **32,** 67–77 (2003).

316. Oostenbrink, C., Villa, A., Mark, A. E. & Van Gunsteren, W. F. A biomolecular force field based on the free enthalpy of hydration and solvation: the GROMOS force-field parameter sets 53A5 and 53A6. *Journal of computational chemistry* **25,** 1656–1676 (2004).

317. Poger, D., Van Gunsteren, W. F. & Mark, A. E. A new force field for simulating phosphatidylcholine bilayers. *Journal of computational chemistry* **31,** 1117–1125 (2010).

318. Reif, M. M., Hünenberger, P. H. & Oostenbrink, C. New interaction parameters for charged amino acid side chains in the GROMOS force field. *Journal of chemical theory and computation* **8,** 3705–3723 (2012).

319. Piggot, T. J., Pineiro, A. & Khalid, S. Molecular dynamics simulations of phosphatidylcholine membranes: a comparative force field study. *Journal of chemical theory and computation* **8,** 4593–4609 (2012).

320. Orsi, M. & Essex, J. W. The ELBA force field for coarse-grain modeling of lipid membranes. *PloS one* **6,** e28637 (2011).

321. Jong, D. H. D. *et al.* Improved parameters for the martini coarse-grained protein force field. *Journal of Chemical Theory and Computation* **9,** 687–697. ISSN: 15499618. `https://pubs.acs.org/doi/abs/10.1021/ct300646g` (1 Jan. 2013).

322. Souza, P. C. *et al.* Martini 3: a general purpose force field for coarse-grained molecular dynamics. *Nature Methods* **18,** 382–388. ISSN: 15487105. `http://dx.doi.org/10.1038/s41592-021-01098-3` (4 2021).

323. Marrink, S. J. *et al.* Two decades of Martini: Better beads, broader scope. *Wiley Interdisciplinary Reviews: Computational Molecular Science* **13,** e1620. ISSN: 1759-0884. `https://onlinelibrary.wiley.com/doi/full/10.1002/wcms.1620%20https://onlinelibrary.wiley.com/doi/abs/10.1002/wcms.1620%20https://wires.onlinelibrary.wiley.com/doi/10.1002/wcms.1620` (1 Jan. 2023).

324. Arnarez, C. *et al.* Dry Martini, a coarse-grained force field for lipid membrane simulations with implicit solvent. *Journal of chemical theory and computation* **11,** 260–275 (2015).

325. Yesylevskyy, S. O., Schäfer, L. V., Sengupta, D. & Marrink, S. J. Polarizable Water Model for the Coarse-Grained MARTINI Force Field. *PLoS Computational Biology* **6** (ed Levitt, M.) e1000810. ISSN: 1553-7358. `http://dx.doi.org/10.1371/journal.pcbi.1000810` (June 2010).

326. Paloncýová, M. *et al.* Benchmarking of force fields for molecule–membrane interactions. *Journal of Chemical Theory and Computation* **10,** 4143–4151 (2014).

327. Siani, P., de Souza, R., Dias, L., Itri, R. & Khandelia, H. An overview of molecular dynamics simulations of oxidized lipid systems, with a comparison of ELBA and MARTINI force fields for coarse grained lipid simulations. *Biochimica et Biophysica Acta (BBA)-Biomembranes* **1858,** 2498–2511 (2016).

328. Antila, H. S. *et al.* Evaluating polarizable biomembrane simulations against experiments. *Journal of Chemical Theory and Computation* (2024).

329. Kiirikki, A. M. *et al.* Overlay databank unlocks data-driven analyses of biomolecules for all. *Nature Communications* **15,** 1136 (2024).

330. Im, W. & Khalid, S. Molecular simulations of Gram-negative bacterial membranes come of age. *Annual review of physical chemistry* **71,** 171–188 (2020).

331. Ingólfsson, H. I. *et al.* Lipid organization of the plasma membrane. *Journal of the american chemical society* **136,** 14554–14559 (2014).

332. Koldsø, H., Shorthouse, D., Hélie, J. & Sansom, M. S. Lipid clustering correlates with membrane curvature as revealed by molecular simulations of complex lipid bilayers. *PLoS computational biology* **10,** e1003911 (2014).

333. Duncan, A. L. *et al.* Protein crowding and lipid complexity influence the nanoscale dynamic organization of ion channels in cell membranes. *Scientific Reports* **7,** 16647 (2017).

334. Koldsø, H. & Sansom, M. S. Organization and dynamics of receptor proteins in a plasma membrane. *Journal of the American Chemical Society* **137,** 14694–14704 (2015).

335. Hedger, G., Sansom, M. S. & Koldsø, H. The juxtamembrane regions of human receptor tyrosine kinases exhibit conserved interaction sites with anionic lipids. *Scientific reports* **5,** 9198 (2015).

336. Shorthouse, D., Hedger, G., Koldsø, H. & Sansom, M. S. Molecular simulations of glycolipids: Towards mammalian cell membrane models. *Biochimie* **120,** 105–109 (2016).

337. Andoh, Y., Okazaki, S. & Ueoka, R. Molecular dynamics study of lipid bilayers modeling the plasma membranes of normal murine thymocytes and leukemic GRSL cells. *Biochimica et Biophysica Acta (BBA)-Biomembranes* **1828,** 1259–1270 (2013).

338. Daum, G. Lipids of mitochondria. *Biochimica et Biophysica Acta (BBA)-Reviews on Biomembranes* **822,** 1–42 (1985).

339. Arnarez, C., Marrink, S. J. & Periole, X. Molecular mechanism of cardiolipin-mediated assembly of respiratory chain supercomplexes. *Chemical Science* **7,** 4435–4443 (2016).

340. Duncan, A. L., Robinson, A. J. & Walker, J. E. Cardiolipin binds selectively but transiently to conserved lysine residues in the rotor of metazoan ATP synthases. *Proceedings of the National Academy of Sciences* **113,** 8687–8692 (2016).

341. Róg, M. V. T. P. T. How Cardiolipin Peroxidation Alters the Properties of. *Cell. Mol. Life Sci* **65,** 2493–2506 (2008).

342. Van Eerden, F. J., de Jong, D. H., de Vries, A. H., Wassenaar, T. A. & Marrink, S. J. Characterization of thylakoid lipid membranes from cyanobacteria and higher plants by molecular dynamics simulations. *Biochimica et Biophysica Acta (BBA)-Biomembranes* **1848,** 1319–1330 (2015).

343. Ray, A., Gräter, F. & Thukral, L. Probing molecular forces in multi-component physiological membranes. *Physical Chemistry Chemical Physics* **20,** 2155–2161 (2018).

344. Monje-Galvan, V. & Klauda, J. B. Modeling yeast organelle membranes and how lipid diversity influences bilayer properties. *Biochemistry* **54,** 6852–6861 (2015).

345. Silhavy, T. J., Kahne, D. & Walker, S. The bacterial cell envelope. *Cold Spring Harbor perspectives in biology* **2,** a000414 (2010).

346. Lins, R. D. & Straatsma, T. Computer simulation of the rough lipopolysaccharide membrane of Pseudomonas aeruginosa. *Biophysical journal* **81,** 1037–1046 (2001).

347. Dias, R. P., da Hora, G. C., Ramstedt, M. & Soares, T. A. Outer membrane remodeling: the structural dynamics and electrostatics of rough lipopolysaccharide chemotypes. *Journal of chemical theory and computation* **10,** 2488–2497 (2014).

348. Piggot, T. J., Holdbrook, D. A. & Khalid, S. Electroporation of the E. coli and S. aureus membranes: molecular dynamics simulations of complex bacterial membranes. *The journal of physical chemistry B* **115,** 13381–13388 (2011).

349. Hsu, P.-C., Jefferies, D. & Khalid, S. Molecular dynamics simulations predict the pathways via which pristine fullerenes penetrate bacterial membranes. *The journal of physical chemistry B* **120,** 11170–11179 (2016).

350. Piggot, T. J., Holdbrook, D. A. & Khalid, S. Conformational dynamics and membrane interactions of the E. coli outer membrane protein FecA: a molecular dynamics simulation study. *Biochimica et Biophysica Acta (BBA)-Biomembranes* **1828,** 284–293 (2013).

351. Lim, J. B. & Klauda, J. B. Lipid chain branching at the iso-and anteiso-positions in complex chlamydia membranes: A molecular dynamics study. *Biochimica et Biophysica Acta (BBA)-Biomembranes* **1808,** 323–331 (2011).

352. Pandit, K. R. & Klauda, J. B. Membrane models of E. coli containing cyclic moieties in the aliphatic lipid chain. *Biochimica et Biophysica Acta (BBA)-Biomembranes* **1818,** 1205–1210 (2012).

353. Boags, A. T., Samsudin, F. & Khalid, S. Binding from both sides: TolR and full-length OmpA bind and maintain the local structure of the E. coli cell wall. *Structure* **27,** 713–724 (2019).

354. Guigas, G. & Weiss, M. Effects of protein crowding on membrane systems. *Biochimica et Biophysica Acta (BBA)-Biomembranes* **1858,** 2441–2450 (2016).

355. Jeon, J.-H., Javanainen, M., Martinez-Seara, H., Metzler, R. & Vattulainen, I. Protein crowding in lipid bilayers gives rise to non-Gaussian anomalous lateral diffusion of phospholipids and proteins. *Physical Review X* **6,** 021006 (2016).

356. Javanainen, M., Martinez-Seara, H., Metzler, R. & Vattulainen, I. Diffusion of integral membrane proteins in protein-rich membranes. *The journal of physical chemistry letters* **8,** 4308–4313 (2017).

357. Wu, E. L. *et al. CHARMM-GUI membrane builder toward realistic biological membrane simulations* 2014.

358. Doktorova, M. & Weinstein, H. Accurate in silico modeling of asymmetric bilayers based on biophysical principles. *Biophysical Journal* **115,** 1638–1643 (2018).

359. Reddy, T. *et al.* Nothing to sneeze at: a dynamic and integrative computational model of an influenza A virion. *Structure* **23,** 584–597 (2015).

360. Marzinek, J. K., Holdbrook, D. A., Huber, R. G., Verma, C. & Bond, P. J. Pushing the envelope: dengue viral membrane coaxed into shape by molecular simulations. *Structure* **24,** 1410–1420 (2016).

361. Marzinek, J. K. *et al.* Characterizing the conformational landscape of flavivirus fusion peptides via simulation and experiment. *Scientific reports* **6,** 19160 (2016).

362. Reddy, T. & Sansom, M. S. The role of the membrane in the structure and biophysical robustness of the dengue virion envelope. *Structure* **24,** 375–382 (2016).

363. Dommer, A. *et al.* # COVIDisAirborne: AI-enabled multiscale computational microscopy of delta SARS-CoV-2 in a respiratory aerosol. *The international journal of high performance computing applications* **37,** 28–44 (2023).

364. Singharoy, A. *et al.* Atoms to phenotypes: molecular design principles of cellular energy metabolism. *Cell* **179,** 1098–1111 (2019).

365. Pezeshkian, W., König, M., Wassenaar, T. A. & Marrink, S. J. Backmapping triangulated surfaces to coarse-grained membrane models. *Nature communications* **11,** 2296 (2020).

366. Yu, I. *et al.* Biomolecular interactions modulate macromolecular structure and dynamics in atomistic model of a bacterial cytoplasm. *Elife* **5,** e19274 (2016).

367. Stevens, J. A. *et al.* Molecular dynamics simulation of an entire cell. *Frontiers in Chemistry* **11,** 1106495 (2023).

368. Helfrich, W. Elastic properties of lipid bilayers: theory and possible experiments. *Zeitschrift für Naturforschung c* **28,** 693–703 (1973).

369. Hamm, M. & Kozlov, M. Elastic energy of tilt and bending of fluid membranes. *The European Physical Journal E* **3,** 323–335 (2000).

370. Watson, M. C., Penev, E. S., Welch, P. M. & Brown, F. L. Thermal fluctuations in shape, thickness, and molecular orientation in lipid bilayers. *The Journal of chemical physics* **135** (2011).

371. Terzi, M. M. & Deserno, M. Novel tilt-curvature coupling in lipid membranes. *The Journal of chemical physics* **147** (2017).

372. Terzi, M. M., Ergüder, M. F. & Deserno, M. A consistent quadratic curvature-tilt theory for fluid lipid membranes. *The Journal of chemical physics* **151** (2019).

373. Feller, S. E., Zhang, Y. & Pastor, R. W. Computer simulation of liquid/liquid interfaces. II. Surface tension-area dependence of a bilayer and monolayer. *The Journal of chemical physics* **103,** 10267–10276 (1995).

374. Zhang, Y., Feller, S. E., Brooks, B. R. & Pastor, R. W. Computer simulation of liquid/liquid interfaces. I. Theory and application to octane/water. *The Journal of chemical physics* **103,** 10252–10266 (1995).

375. Doktorova, M., LeVine, M. V., Khelashvili, G. & Weinstein, H. A new computational method for membrane compressibility: Bilayer mechanical thickness revisited. *Biophysical journal* **116,** 487–502 (2019).

376. Venable, R. M., Brown, F. L. & Pastor, R. W. Mechanical properties of lipid bilayers from molecular dynamics simulation. *Chemistry and physics of lipids* **192,** 60–74 (2015).

377. Ergüder, M. F. & Deserno, M. Identifying systematic errors in a power spectral analysis of simulated lipid membranes. *The Journal of Chemical Physics* **154,** 214103. ISSN: 0021-9606. `https://doi.org/10.1063/5.0049448%20https://aip.scitation.org/doi/10.1063/5.0049448` (21 June 2021).

378. Safran, S. *Statistical thermodynamics of surfaces, interfaces, and membranes* (CRC Press, 1994).

379. Goetz, R., Gompper, G. & Lipowsky, R. Mobility and elasticity of self-assembled membranes. *Physical review letters* **82,** 221 (1999).

380. Watson, M. C., Brandt, E. G., Welch, P. M. & Brown, F. L. Determining biomembrane bending rigidities from simulations of modest size. *Physical review letters* **109,** 028102 (2012).

381. Levine, Z. A. *et al.* Determination of biomembrane bending moduli in fully atomistic simulations. *Journal of the American Chemical Society* **136,** 13582–13585 (2014).

382. Jablin, M. S., Akabori, K. & Nagle, J. Experimental support for tilt-dependent theory of biomembrane mechanics. *Physical review letters* **113,** 248102 (2014).

383. Nagle, J. F. Experimentally determined tilt and bending moduli of single-component lipid bilayers. *Chemistry and physics of lipids* **205,** 18–24 (2017).

384. Erguder, M. F., Deserno, M. & Nagle, J. F. Measuring the splay-tilt modulus of lipid bilayers by diffuse X-ray scattering. *Biophysical Journal* **123,** 233a (2024).

385. Tieleman, D. P., Leontiadou, H., Mark, A. E. & Marrink, S.-J. Simulation of pore formation in lipid bilayers by mechanical stress and electric fields. *Journal of the American Chemical Society* **125,** 6382–6383 (2003).

386. Tarek, M. Membrane electroporation: a molecular dynamics simulation. *Biophysical journal* **88,** 4045–4053 (2005).

387. Ting, C. L., Awasthi, N., Müller, M. & Hub, J. S. Metastable prepores in tension-free lipid bilayers. *Physical review letters* **120,** 128103 (2018).

388. Wang, Z.-J. & Frenkel, D. Pore nucleation in mechanically stretched bilayer membranes. *The Journal of chemical physics* **123** (2005).

389. Wohlert, J., den Otter, W. K., Edholm, O. & Briels, W. J. Free energy of a trans-membrane pore calculated from atomistic molecular dynamics simulations. *The Journal of chemical physics* **124** (2006).

390. Mirjalili, V. & Feig, M. Density-biased sampling: a robust computational method for studying pore formation in membranes. *Journal of chemical theory and computation* **11,** 343–350 (2015).

391. Awasthi, N. & Hub, J. S. Simulations of pore formation in lipid membranes: reaction coordinates, convergence, hysteresis, and finite-size effects. *Journal of chemical theory and computation* **12,** 3261–3269 (2016).

392. Hub, J. S. & Awasthi, N. Probing a continuous polar defect: A reaction coordinate for pore formation in lipid membranes. *Journal of Chemical Theory and Computation* **13,** 2352–2366 (2017).

393. Hub, J. S. Joint reaction coordinate for computing the free-energy landscape of pore nucleation and pore expansion in lipid membranes. *Journal of Chemical Theory and Computation* **17,** 1229–1239 (2021).

394. Starke, L. J., Allolio, C. & Hub, J. S. Free energy barriers against pore formation in complex membranes strongly depend on lipid composition. *Biophysical Journal* **123,** 93a–94a (2024).

395. Murphy, M. *et al.* Molecular dynamics simulations showing 1-palmitoyl-2-oleoyl-phosphatidylcholine (POPC) membrane mechanoporation damage under different strain paths. *Journal of Biomolecular Structure and Dynamics* **37,** 1346–1359 (2019).

396. Shigematsu, T., Koshiyama, K. & Wada, S. Effects of stretching speed on mechanical rupture of phospholipid/cholesterol bilayers: molecular dynamics simulation. *Scientific reports* **5,** 15369 (2015).

397. Zhang, L. *et al.* Molecular dynamics simulations of heterogeneous cell membranes in response to uniaxial membrane stretches at high loading rates. *Scientific reports* **7,** 8316 (2017).

398. Oliveira, M. C., Yusupov, M., Bogaerts, A. & Cordeiro, R. M. Molecular dynamics simulations of mechanical stress on oxidized membranes. *Biophysical Chemistry* **254,** 106266 (2019).

399. Vo, A. T., Murphy, M. A., Phan, P. K., Prabhu, R. K. & Stone, T. W. Effect of Force Field Resolution on Membrane Mechanical Response and Mechanoporation Damage under Deformation Simulations. *Molecular Biotechnology* **66,** 865–875 (2024).

400. Koshiyama, K. *et al. Molecular delivery into a lipid bilayer with a single shock waves using molecular dynamic simulation* in *AIP Conference Proceedings* **754** (2005), 104–106.

401. Kodama, T. *et al. Interaction of impulsive pressures of cavitation bubbles with cell membranes during sonoporation* in *AIP Conference Proceedings* **829** (2006), 34–38.

402. Ganzenmüller, G., Hiermaier, S. & Steinhauser, M. Shock-wave induced damage in lipid bilayers: a dissipative particle dynamics simulation study. *Soft Matter* **7,** 4307–4317 (2011).

403. Holian, B. L. & Lomdahl, P. S. Plasticity induced by shock waves in nonequilibrium molecular-dynamics simulations. *Science* **280,** 2085–2088 (1998).

404. Sliozberg, Y. & Chantawansri, T. Damage in spherical cellular membrane generated by the shock waves: Coarse-grained molecular dynamics simulation of lipid vesicle. *The Journal of chemical physics* **141** (2014).

405. Ohl, C. & Ikink, R. Shock-wave-induced jetting of micron-size bubbles. *Physical review letters* **90,** 214502 (2003).

406. Ohl, C.-D. *et al.* Sonoporation from jetting cavitation bubbles. *Biophysical journal* **91,** 4285–4295 (2006).

407. Choubey, A. *et al.* Poration of lipid bilayers by shock-induced nanobubble collapse. *Applied Physics Letters* **98** (2011).

408. Santo, K. P. & Berkowitz, M. L. Shock wave interaction with a phospholipid membrane: Coarse-grained computer simulations. *The Journal of chemical physics* **140** (2014).

409. Wei, T. *et al.* Impact of Shock-Induced Cavitation Bubble Collapse on the Damage of Cell Membranes with Different Lipid Peroxidation Levels. *The Journal of Physical Chemistry B* **125,** 6912–6920 (2021).

410. Fu, H., Comer, J., Cai, W. & Chipot, C. Sonoporation at small and large length scales: effect of cavitation bubble collapse on membranes. *The journal of physical chemistry letters* **6,** 413–418 (2015).

411. Man, V. H. *et al.* Molecular mechanism of the cell membrane pore formation induced by bubble stable cavitation. *The Journal of Physical Chemistry B* **123,** 71–78 (2018).

412. Man, V. H., Li, M. S., Derreumaux, P., Wang, J. & Nguyen, P. H. Molecular mechanism of ultrasound-induced structural defects in liposomes: a nonequilibrium molecular dynamics simulation study. *Langmuir* **37,** 7945–7954 (2021).

413. Man, V. H., Li, M. S., Wang, J., Derreumaux, P. & Nguyen, P. H. Interaction mechanism between the focused ultrasound and lipid membrane at the molecular level. *The Journal of Chemical Physics* **150** (2019).

414. Man, V. H. *et al.* Molecular mechanism of ultrasound interaction with a blood brain barrier model. *The Journal of Chemical Physics* **153** (2020).

415. Li, J., Xia, Z., Cai, S., Xia, S. & Zhang, X. The non-thermal influences of ultrasound on cell membrane: A molecular dynamics study. *Journal of Molecular Structure* **1299,** 137140 (2024).

416. Leimkuhler, B. & Matthews, C. *Molecular Dynamics: With Deterministic and Stochastic Numerical Methods* ISBN: 9783319163758. https://books.google.es/books?id=AGF1CQAAQBAJ (Springer International Publishing, 2015).

417. Frenkel, D. & Smit, B. *Understanding molecular simulation: from algorithms to applications* (Elsevier, 2023).

418. GROMACS Team. *GROMACS Reference Manual* Accessed April 25, 2024. https://manual.gromacs.org/current/reference-manual/ (2024).

419. Darden, T., York, D. & Pedersen, L. Particle mesh Ewald: An N log (N) method for Ewald sums in large systems. *The Journal of chemical physics* **98,** 10089–10092 (1993).

420. Essmann, U. *et al.* A smooth particle mesh Ewald method. *The Journal of chemical physics* **103,** 8577–8593 (1995).

421. Huang, J. *et al.* CHARMM36m: An improved force field for folded and intrinsically disordered proteins. *Nature Methods* **14,** 71–73. ISSN: 15487105. https://www.nature.com/articles/nmeth.4067 (1 Nov. 2016).

422. F. Garrido, P., Calvelo, M., Garcia-Fandiño, R. & Piñeiro, Á. Rings, hexagons, petals, and dipolar moment sink-sources: The fanciful behavior of water around cyclodextrin complexes. *Biomolecules* **10,** 431 (2020).

423. Conde, D., Garrido, P. F., Calvelo, M., Piñeiro, Á. & Garcia-Fandino, R. Molecular Dynamics Simulations of Transmembrane Cyclic Peptide Nanotubes Using Classical Force Fields, Hydrogen Mass Repartitioning, and Hydrogen Isotope Exchange Methods: A Critical Comparison. *International Journal of Molecular Sciences* **23,** 3158 (2022).

424. Meza, J. C. Steepest descent. *Wiley Interdisciplinary Reviews: Computational Statistics* **2,** 719–722 (2010).

425. Nazareth, J. L. Conjugate gradient method. *Wiley Interdisciplinary Reviews: Computational Statistics* **1,** 348–353 (2009).

426. Byrd, R. H., Lu, P., Nocedal, J. & Zhu, C. A limited memory algorithm for bound constrained optimization. *SIAM Journal on scientific computing* **16,** 1190–1208 (1995).

427. Zhu, C., Byrd, R. H., Lu, P. & Nocedal, J. Algorithm 778: L-BFGS-B: Fortran subroutines for large-scale bound-constrained optimization. *ACM Transactions on mathematical software (TOMS)* **23,** 550–560 (1997).

428. Hockney, R. & Eastwood, J. *Computer Simulation Using Particles* ISBN: 9781439822050. https://books.google.es/books?id=nTOFkmnCQuIC (CRC Press, 2021).

429. Feenstra, K. A., Hess, B. & Berendsen, H. J. Improving efficiency of large time-scale molecular dynamics simulations of hydrogen-rich systems. *Journal of computational chemistry* **20,** 786–798 (1999).

430. Swope, W. C., Andersen, H. C., Berens, P. H. & Wilson, K. R. A computer simulation method for the calculation of equilibrium constants for the formation of physical clusters of molecules: Application to small water clusters. *The Journal of chemical physics* **76,** 637–649 (1982).

431. Bussi, G., Donadio, D. & Parrinello, M. Canonical sampling through velocity rescaling. *The Journal of chemical physics* **126** (2007).

432. Berendsen, H. J., Postma, J. v., Van Gunsteren, W. F., DiNola, A. & Haak, J. R. Molecular dynamics with coupling to an external bath. *The Journal of chemical physics* **81,** 3684–3690 (1984).

433. Wikipedia. *Wiener process* Accessed May 04, 2024. https://en.wikipedia.org/wiki/Wiener_process (2024).

434. Parrinello, M. & Rahman, A. Polymorphic transitions in single crystals: A new molecular dynamics method. *Journal of Applied physics* **52,** 7182–7190 (1981).

435. Nosé, S. & Klein, M. Constant pressure molecular dynamics for molecular systems. *Molecular Physics* **50,** 1055–1076 (1983).

436. Deserno, M. Fluid lipid membranes: From differential geometry to curvature stresses. *Chemistry and Physics of Lipids* **185,** 11–45. ISSN: 00093084. http://www.ncbi.nlm.nih.gov/pubmed/24835737%20https://linkinghub.elsevier.com/retrieve/pii/S000930841400053X (Jan. 2015).

437. Michaud-Agrawal, N., Denning, E. J., Woolf, T. B. & Beckstein, O. MDAnalysis: a toolkit for the analysis of molecular dynamics simulations. *Journal of computational chemistry* **32,** 2319–2327 (2011).

438. Gowers, R. J. *et al. MDAnalysis: a Python package for the rapid analysis of molecular dynamics simulations* tech. rep. (Los Alamos National Laboratory (LANL), Los Alamos, NM (United States), 2019).

439. Harris, C. R. *et al.* Array programming with NumPy. *Nature* **585,** 357–362 (2020).

440. Blanco-González, A. *HierarchyMem* 2022. https://github.com/allexandre97/HierarchyMem.

441. Blanco-González, A. *phd-scripts* 2024. https://github.com/allexandre97/phd-scripts.

442. Lam, S. K., Pitrou, A. & Seibert, S. *Numba: A llvm-based python jit compiler* in *Proceedings of the Second Workshop on the LLVM Compiler Infrastructure in HPC* (2015), 1–6.

443. Sigalotti, L. D. G., Klapp, J. & Gesteira, M. G. The mathematics of smoothed particle hydrodynamics (SPH) consistency. *Frontiers in Applied Mathematics and Statistics* **7,** 797455 (2021).

444. Pedregosa, F. *et al.* Scikit-learn: Machine Learning in Python. *Journal of Machine Learning Research* **12,** 2825–2830 (2011).

445. Blanco-González, A. *SurfParam* 2024. https://github.com/allexandre97/SurfParam.

446. Jonathan Barnoud Oliver Beckstein, I. *pyedr & panedr* 2024. https://github.com/MDAnalysis/panedr.

447. Bhatia, H., Ingólfsson, H. I., Carpenter, T. S., Lightstone, F. C. & Bremer, P. T. MemSurfer: A Tool for Robust Computation and Characterization of Curved Membranes. *Journal of Chemical Theory and Computation* **15,** 6411–6421. ISSN: 15499626. https://pubs.acs.org/sharingguidelines (11 Nov. 2019).

448. Kazhdan, M., Bolitho, M. & Hoppe, H. *Poisson surface reconstruction* in *Proceedings of the fourth Eurographics symposium on Geometry processing* **7** (2006).

449. Harris, C. R. *et al.* Array programming with NumPy. *Nature* **585,** 357–362. ISSN: 14764687. https://doi.org/10.1038/s41586-020-2649-2 (7825 Sept. 2020).

450. Lorensen, W. E. & Cline, H. E. in *Seminal graphics: pioneering efforts that shaped the field* 347–353 (1998).

451. Zhou, Q.-Y., Park, J. & Koltun, V. Open3D: A Modern Library for 3D Data Processing. *arXiv:1801.09847* (2018).

452. Zephyris. *Representation of the UV mapping of a cube.* https://commons.wikimedia.org/wiki/File:Cube_Representative_UV_Unwrapping.png.

453. Sheffer, A. & de Sturler, E. Parameterization of faceted surfaces for meshing using angle-based flattening. *Engineering with computers* **17,** 326–337 (2001).

454. Community, B. O. *Blender 4.1 Python API Documentation* Blender Foundation (2024). https://docs.blender.org/api/current/index.html.

455. Gjacquenot. *A Delaunay triangulation with circumcircles* `https://commons.wikimedia.org/wiki/File:Delaunay_circumcircles_vectorial.svg`.

456. Virtanen, P. *et al.* SciPy 1.0: Fundamental Algorithms for Scientific Computing in Python. *Nature Methods* **17,** 261–272 (2020).

457. Barber, C. B., Dobkin, D. P. & Huhdanpaa, H. The quickhull algorithm for convex hulls. *ACM Transactions on Mathematical Software (TOMS)* **22,** 469–483 (1996).

458. Izadifar, Z., Izadifar, Z., Chapman, D. & Babyn, P. An Introduction to High Intensity Focused Ultrasound: Systematic Review on Principles, Devices, and Clinical Applications. *Journal of Clinical Medicine* **9,** 460. ISSN: 2077-0383. `www.mdpi.com/journal/jcm` (2 2020).

459. Für Lasertechnik LLT, L. *Gaussian beam* Accessed August 31, 2024. `https://www.youtube.com/watch?v=MU4eOJw2sBQ` (2024).

460. Für Lasertechnik LLT, L. *Beam parameter product and beam quality* Accessed August 31, 2024. `https://www.youtube.com/watch?v=WB6S5qqhSUc` (2024).

461. Blanco-González, A. *GROMACS-OSC* 2024. `https://github.com/allexandre97/GROMACS-OSC`.

462. Schafer, R. W. What is a Savitzky-Golay filter?[lecture notes]. *IEEE Signal processing magazine* **28,** 111–117 (2011).

463. Portnoff, M. Time-frequency representation of digital signals and systems based on short-time Fourier analysis. *IEEE Transactions on Acoustics, Speech, and Signal Processing* **28,** 55–69 (1980).

464. Huang, Z. Extensions to the k-means algorithm for clustering large data sets with categorical values. *Data mining and knowledge discovery* **2,** 283–304 (1998).

465. De Vos, N. J. *Kmodes Categorical Clustering Library* 2015. `https://github.com/nicodv/kmodes`.

466. Satopaa, V., Albrecht, J., Irwin, D. & Raghavan, B. *Finding a' kneedle' in a haystack: Detecting knee points in system behavior* in *2011 31st international conference on distributed computing systems workshops* (2011), 166–171.

467. Ramamoorthy, A. *et al.* Deletion of all cysteines in tachyplesin I abolishes hemolytic activity and retains antimicrobial activity and lipopolysaccharide selective binding. *Biochemistry* **45,** 6529–6540 (2006).

468. Lee, J., Jung, S. W. & Cho, A. E. Molecular insights into the adsorption mechanism of human β-defensin-3 on bacterial membranes. *Langmuir* **32,** 1782–1790 (2016).

469. Jo, S., Kim, T., Iyer, V. G. & Im, W. CHARMM-GUI: a web-based graphical user interface for CHARMM. *Journal of computational chemistry* **29,** 1859–1865 (2008).

470. Lee, J. *et al.* CHARMM-GUI input generator for NAMD, GROMACS, AMBER, OpenMM, and CHARMM/OpenMM simulations using the CHARMM36 additive force field. *Biophysical journal* **110,** 641a (2016).

471. Jorgensen, W. L., Chandrasekhar, J., Madura, J. D., Impey, R. W. & Klein, M. L. Comparison of simple potential functions for simulating liquid water. *The Journal of chemical physics* **79,** 926–935 (1983).

472. Grote, F. & Lyubartsev, A. P. Optimization of slipids force field parameters describing headgroups of phospholipids. *The Journal of Physical Chemistry B* **124,** 8784–8793 (2020).

473. Bekker, H. *et al. Gromacs-a parallel computer for molecular-dynamics simulations* in *4th international conference on computational physics (PC 92)* (1993), 252–256.

474. Abraham, M. J. *et al.* GROMACS: High performance molecular simulations through multi-level parallelism from laptops to supercomputers. *SoftwareX* **1,** 19–25 (2015).

475. Team, G. D. *GROMACS 2018 Reference manual* Accessed September 02, 2024. `https://manual.gromacs.org/documentation/2018/manual-2018.pdf` (2024).

476. Hess, B., Bekker, H., Berendsen, H. J. & Fraaije, J. G. LINCS: a linear constraint solver for molecular simulations. *Journal of computational chemistry* **18,** 1463–1472 (1997).

477. Team, G. D. *GROMACS 2020.4 Reference manual* Accessed September 02, 2024. `https://manual.gromacs.org/documentation/2020.4/reference-manual/index.html` (2024).

478. Huang, C.-h., Li, S., Lin, H.-n. & Wang, G. On the bilayer phase transition temperatures for monoenoic phosphatidylcholines and phosphatidylethanolamines and the interconversion between them. *Archives of biochemistry and biophysics* **334,** 135–142 (1996).

479. Team, G. D. *GROMACS 2021.5 Reference manual* Accessed September 02, 2024. `https://manual.gromacs.org/documentation/2021.5/reference-manual/index.html` (2024).

480. Blanco-González, A., Marrink, S. J., Piñeiro, Á. & García-Fandiño, R. Molecular insights into the effects of focused ultrasound mechanotherapy on lipid bilayers: Unlocking the keys to design effective treatments. *Journal of Colloid and Interface Science* **650,** 1201–1210 (2023).

481. Lyubartsev, A. P. & Rabinovich, A. L. Force field development for lipid membrane simulations. *Biochimica et Biophysica Acta (BBA)-Biomembranes* **1858,** 2483–2497 (2016).

482. Klauda, J. B. Considerations of recent all-atom lipid force field development. *The Journal of Physical Chemistry B* **125,** 5676–5682 (2021).

483. Leonard, A. N., Wang, E., Monje-Galvan, V. & Klauda, J. B. Developing and testing of lipid force fields with applications to modeling cellular membranes. *Chemical reviews* **119,** 6227–6269 (2019).

484. Poger, D. & Mark, A. E. On the validation of molecular dynamics simulations of saturated and cis-monounsaturated phosphatidylcholine lipid bilayers: a comparison with experiment. *Journal of Chemical Theory and Computation* **6,** 325–336 (2010).

485. Poger, D., Caron, B. & Mark, A. E. Validating lipid force fields against experimental data: Progress, challenges and perspectives. *Biochimica et Biophysica Acta (BBA)-Biomembranes* **1858,** 1556–1565 (2016).

486. Janosi, L. & Gorfe, A. A. Simulating POPC and POPC/POPG bilayers: conserved packing and altered surface reactivity. *Journal of chemical theory and computation* **6,** 3267–3273 (2010).

487. Mills, T. T. *et al.* Order parameters and areas in fluid-phase oriented lipid membranes using wide angle X-ray scattering. *Biophysical journal* **95,** 669–681 (2008).

488. Bosse, M. *et al.* Shiga toxin binding alters lipid packing and the domain structure of Gb 3-containing membranes: a solid-state NMR study. *Physical Chemistry Chemical Physics* **21,** 15630–15638 (2019).

489. Vermeer, L. S., De Groot, B. L., Réat, V., Milon, A. & Czaplicki, J. Acyl chain order parameter profiles in phospholipid bilayers: computation from molecular dynamics simulations and comparison with 2 H NMR experiments. *European Biophysics Journal* **36,** 919–931 (2007).

490. Fischer, M., Schwarze, B., Ristic, N. & Scheidt, H. A. Predicting 2H NMR acyl chain order parameters with graph neural networks. *Computational Biology and Chemistry* **100,** 107750 (2022).

491. Blanco-González, A., Wurl, A., Mendes Ferreira, T., Piñeiro, Á. & Garcia-Fandino, R. Simulating Bacterial Membrane Models at the Atomistic Level: A Force Field Comparison. *Journal of Chemical Theory and Computation.* ISSN: 1549-9626. http://dx.doi.org/10.1021/acs.jctc.4c00204 (Sept. 2024).

492. Nagle, J. F. & Tristram-Nagle, S. Structure of lipid bilayers. *Biochimica et Biophysica Acta (BBA)-Reviews on Biomembranes* **1469,** 159–195 (2000).

493. Van Gunsteren, W. F., Dolenc, J. & Mark, A. E. Molecular simulation as an aid to experimentalists. *Current opinion in structural biology* **18,** 149–153 (2008).

494. Hyslop, P. A., Morel, B. & Sauerheber, R. D. Organization and interaction of cholesterol and phosphatidylcholine in model bilayer membranes. *Biochemistry* **29,** 1025–1038 (1990).

495. Piggot, T. J., Allison, J. R., Sessions, R. B. & Essex, J. W. On the calculation of acyl chain order parameters from lipid simulations. *Journal of chemical theory and computation* **13,** 5683–5696 (2017).

496. Wiedmann, T., Salmon, A. & Wong, V. Phase behavior of mixtures of DPPC and POPG. *Biochimica et Biophysica Acta (BBA)-Lipids and Lipid Metabolism* **1167,** 114–120 (1993).

497. Klauda, J. B. *et al.* Update of the CHARMM all-atom additive force field for lipids: validation on six lipid types. *The journal of physical chemistry B* **114,** 7830–7843 (2010).

498. Wurl, A., Saalwächter, K. & Mendes Ferreira, T. Time-domain proton-detected local-field NMR for molecular structure determination in complex lipid membranes. *Magnetic Resonance* **4,** 115–127 (2023).

499. Bacle, A. *et al.* Inverse conformational selection in lipid–protein binding. *Journal of the American Chemical Society* **143,** 13701–13709 (2021).

500. Polyansky, A. A., Volynsky, P. E., Nolde, D. E., Arseniev, A. S. & Efremov, R. G. Role of lipid charge in organization of water/lipid bilayer interface: insights via computer simulations. *The Journal of Physical Chemistry B* **109,** 15052–15059 (2005).

501. Murzyn, K., Róg, T. & Pasenkiewicz-Gierula, M. Phosphatidylethanolamine-phosphatidylglycerol bilayer as a model of the inner bacterial membrane. *Biophysical journal* **88,** 1091–1103 (2005).

502. Vögele, M., Köfinger, J. & Hummer, G. Hydrodynamics of diffusion in lipid membrane simulations. *Physical Review Letters* **120,** 268104 (2018).

503. Vögele, M. & Hummer, G. Divergent diffusion coefficients in simulations of fluids and lipid membranes. *The Journal of Physical Chemistry B* **120,** 8722–8732 (2016).

504. Camley, B. A., Lerner, M. G., Pastor, R. W. & Brown, F. L. Strong influence of periodic boundary conditions on lateral diffusion in lipid bilayer membranes. *The Journal of chemical physics* **143** (2015).

505. Garcia-Fandino, R., Pineiro, A., Trick, J. L. & Sansom, M. S. Lipid bilayer membrane perturbation by embedded nanopores: A simulation study. *ACS nano* **10,** 3693–3701 (2016).

506. Blanco-González, A., Piñeiro, Á. & García-Fandiño, R. Unravelling hierarchical levels of structure in lipid membranes. *Computational and Structural Biotechnology Journal* **20,** 2798–2806 (2022).

507. Sud, M. *et al.* Lmsd: Lipid maps structure database. *Nucleic acids research* **35,** D527–D532 (2007).

508. Eid, J., Razmazma, H., Jraij, A., Ebrahimi, A. & Monticelli, L. On calculating the bending modulus of lipid bilayer membranes from buckling simulations. *The journal of physical chemistry B* **124,** 6299–6311 (2020).

509. Pabst, G., Rappolt, M., Amenitsch, H. & Laggner, P. Structural information from multilamellar liposomes at full hydration: full q-range fitting with high quality x-ray data. *Physical Review E* **62,** 4000 (2000).

510. Kučerka, N., Nieh, M.-P. & Katsaras, J. Fluid phase lipid areas and bilayer thicknesses of commonly used phosphatidylcholines as a function of temperature. *Biochimica et Biophysica Acta (BBA)-Biomembranes* **1808,** 2761–2771 (2011).

511. Smaby, J. M., Momsen, M. M., Brockman, H. L. & Brown, R. E. Phosphatidylcholine acyl unsaturation modulates the decrease in interfacial elasticity induced by cholesterol. *Biophysical journal* **73,** 1492–1505 (1997).

512. Kučerka, N., Tristram-Nagle, S. & Nagle, J. F. Structure of fully hydrated fluid phase lipid bilayers with monounsaturated chains. *The Journal of membrane biology* **208,** 193–202 (2006).

513. Kučerka, N. *et al.* Molecular structures of fluid phosphatidylethanolamine bilayers obtained from simulation-to-experiment comparisons and experimental scattering density profiles. *The journal of physical chemistry B* **119,** 1947–1956 (2015).

514. Kucerka, N., Holland, B. W., Gray, C. G., Tomberli, B. & Katsaras, J. Scattering density profile model of POPG bilayers as determined by molecular dynamics simulations and small-angle neutron and X-ray scattering experiments. *The Journal of Physical Chemistry B* **116,** 232–239 (2012).

515. Mukherjee, S. *et al.* Accelerated molecular dynamics simulation analysis of MSI-594 in a lipid bilayer. *Physical chemistry chemical physics* **19,** 19289–19299 (2017).

516. Silva, T. *et al.* Unravelling a mechanism of action for a cecropin A-melittin hybrid antimicrobial peptide: the induced formation of multilamellar lipid stacks. *Langmuir* **34,** 2158–2170 (2018).

517. Reports, J. C. *Journal of Chemical Theory and Computation* Accessed September 12, 2024. `https://jcr.clarivate.com/jcr-jp/journal-profile?journal=J%20CHEM%20THEORY%20COMPUT&year=2023&fromPage=%2Fjcr%2Fhome` (2024).

518. Reports, J. C. *Computational and Structural Biotechnology Journal* Accessed September 12, 2024. `https://jcr.clarivate.com/jcr-jp/journal-profile?journal=COMPUT%20STRUCT%20BIOTEC&year=2023&fromPage=%2Fjcr%2Fhome` (2024).

519. Reports, J. C. *Journal of Colloid and Interface Science* Accessed September 12, 2024. `https://jcr.clarivate.com/jcr-jp/journal-profile?journal=J%20COLLOID%20INTERF%20SCI&year=2023&fromPage=%2Fjcr%2Fhome` (2024).

Lipid membranes are ubiquitous biochemical structures, crucial for the correct functioning of cells. As their name implies, lipids are a major constituent, of which several thousand types exist in nature. This gives rise to a wide variety of membranes, and this inherent variability can be exploited to design specific and targetted therapies.

Therefore, a detailed understanding of the behaviour of these cellular structures at the molecular level is of paramount importance. In this Thesis, we leverage the power of computational techniques, particularly of Molecular Dynamics, to study technical aspects such as the impact of simulation parameters on their outcome; as well as inherent phenomena to the membranes like their structural self-organisation and their responses to mechanical stimuli derived from ultrasounds.